Carlos Hernando López de Toledo



Escuela Internacional de Doctorado Escuela Técnica Superior de Ingeniería ICAI

Modeling And Experimental Research Of Cryogenic Magnetic Refrigeration For The 4-20 K Range

Autor: Carlos Hernando López de Toledo

Directores: Dr. Javier Munilla López

Dr. Luis García-Tabarés Rodriguez Dr. Juan Carlos del Real Romero



UNIVERSIDAD PONTIFICIA DE COMILLAS Escuela Internacional de Doctorado Escuela Técnica Superior de Ingenieros Industriales TESIS DOCTORAL Modeling And Experimental Research Of Cryogenic Magnetic Refrigeration For The 4-20 K Range Autor: Carlos Hernando López de Toledo Directores: Javier Munilla López Luis García-Tabarés Rodríguez Juan Carlos del Real Romero Tribunal nombrado por el Sr. Rector Magfco. de la Universidad Pontificia de Comillas, el día de de 20.... TRIBUNAL PRESIDENTE: D. Presidente: D. Vocal 1: **VOCALES**: D. Vocal 2: D. Vocal 3: SECRETARIO: D. Secretario: **SUPLENTES:** D. _____ Realizado el acto de defensa y lectura de la Tesis el día......de 20... en la Escuela técnica Superior de Ingeniería Industrial. Calificación

LOS VOCALES

EL SECRETARIO

EL PRESIDENTE





ABSTRACT

Cryogenics is an essential technology for advancing cutting-edge scientific and technological solutions. Among these applications is quantum computing, which requires temperatures below 1 K to mitigate qubit decoherence, as well as the development of a potential hydrogen-based economy, where transporting this gas in liquid form (at 20 K) is advantageous. Undoubtedly, one of the main beneficiaries of cryogenics is superconductivity applications, including magnetic confinement fusion and its use in other fields such as energy and medicine, particularly in magnetic resonance imaging (MRI) equipment.

Existing cryogenic systems are divided into two main categories: liquefaction plants, which use expansive cycles (Brayton/Claude), and cryocoolers, which employ regenerative cycles such as Stirling, Gifford-McMahon, or Pulse Tube. Due to their high capital cost and the complexity associated with their operation and maintenance, liquefaction plants are typically restricted to large-scale scientific facilities like the LHC in Geneva or ITER in Marseille. For other applications, such as MRI equipment, cryocoolers are used because they offer compact and easily adaptable refrigeration systems.

However, cryocoolers face critical limitations when operating at temperatures below 20 K, where both their cooling capacity and exergy efficiency are significantly reduced. This limitation is primarily attributed to the relationship between the volumetric heat capacities of helium—which increase near its critical point—and those of the materials comprising the regenerator, whose heat capacity properties decrease within this temperature range. Consequently, research into new regenerative materials has become a priority area in cryogenics.

Due to this limited cooling capacity and low efficiency, cryogenic systems often represent one of the highest costs in applications requiring extremely low temperatures. The development of advanced cryogenic refrigeration equipment that surpasses current capabilities would not only enhance the competitiveness of existing technologies but also enable new applications.

In this context, the present thesis explores the application of magnetic refrigeration to cryogenic environments by leveraging the magnetocaloric effect as an alternative to conventional methods. The study begins with a review of previous prototypes based on this technology, identifying various challenges and limitations such as the selection of suitable magnetocaloric materials—previous developments have used Gd₃Ga₅O₁₂—and the complexity of employing high-field magnetic systems. From this analysis, ErAl₂ emerges as a material with superior performance in the 4.2–20 K range. To evaluate its potential, a one-dimensional (1D) numerical model was developed to estimate key characteristics of the magnetic refrigeration system, including its cooling power and exergy efficiency.

To validate the numerical model, an experimental test bench was designed and constructed based on the single-blow method for regenerator characterization. This prototype was modified to analyze its behavior under cryogenic temperature conditions and the application of a magnetic field.

Using this infrastructure, a methodology was proposed for evaluating magnetocaloric regenerators by imposing thermal and magnetic transients. Under this approach, the performance of two regenerators (ErAl₂ and Gd₃Ga₅O₁₂) was studied. Although partial validation of the numerical model was achieved, several factors hindered full confirmation, including the sensitivity of the test bench to external losses and uncertainties regarding the actual properties of magnetocaloric materials.

The results obtained from both the model and experimental tests support a broader technological analysis that includes economic considerations and system-scale integration.

Notably, magnetic refrigeration demonstrates significant potential for substantially reducing costs associated with cryogenic cooling. Finally, a roadmap is presented outlining critical steps for advancing this technology while mitigating risks throughout its development process, thereby reinforcing its industrial and commercial viability.

RESUMEN

La criogenia es una tecnología esencial para promover el desarrollo de soluciones científicas y tecnológicas de vanguardia. Dentro de ellas se incluye la computación cuántica, que requiere temperaturas inferiores a 1 K para mitigar la decoherencia de los qubits, así como el impulso de una eventual economía basada en el hidrógeno, en la que resulta ventajoso transportar este gas en estado líquido (a 20 K). Sin duda uno de los claros usuarios son las aplicaciones de la superconductividad, entre las que se incluyen la fusión (por confinamiento magnético), y su aplicación en otras áreas de actividad como la energía y la medicina en equipos de resonancia magnetica ("MRI" por sus siglas en inglés).

Los sistemas criogénicos existentes se dividen en dos grandes categorías: por un lado, las plantas de licuefacción que utilizan ciclos expansivos (Brayton/Claude) y, por otro, los criorrefrigeradores o *cryocoolers*, que emplean ciclos regenerativos del tipo Stirling, Gifford-MacMahon o Pulse Tube. Dada su alto coste de capital y la complejidad asociada a su operación y mantenimiento, las plantas de licuefacción suelen restringirse a grandes instalaciones científicas, como el LHC en Ginebra o ITER en Marsella. Para el resto de aplicaciones, por ejemplo en equipos de MRI, se emplean *cryocoolers*, que ofrecen un sistema de refrigeración compacto y fácilmente adaptable.

No obstante, los *cryocoolers* presentan limitaciones cruciales cuando se requiere operar a temperaturas inferiores a 20 K, donde tanto su capacidad de refrigeración como su eficiencia exergética se ven afectadas. La causa principal de esta restricción se atribuye a la relación entre las capacidades caloríficas volumétricas del helio, que aumentan cerca de su punto crítico, y las de los materiales que conforman el regenerador, cuyas propiedades caloríficas disminuyen en ese rango de temperaturas. Por ello, la investigación de nuevos materiales regenerativos constituye un área prioritaria en criogenia.

Debido a esta capacidad de refrigeración limitada y a la baja eficiencia, el sistema criogénico suele representar uno de los mayores costes en aplicaciones que exigen temperaturas muy bajas. El desarrollo de equipos de refrigeración criogénica que superen las características de los actuales no solo incrementaría la competitividad de las tecnologías disponibles, sino que abriría la puerta a nuevas aplicaciones.

En este contexto, la presente tesis aborda la aplicación de la refrigeración magnética a entornos criogénicos, aprovechando el efecto magnetocalórico como vía alternativa a los métodos convencionales. Se inicia con la revisión de prototipos anteriores basados en esta tecnología, lo que permite identificar diversos desafíos y limitaciones, como la selección de materiales magnetocalóricos adecuados —en desarrollos previos se ha utilizado Gd₃Ga₅O₁₂— y la complejidad de emplear sistemas magnéticos de alto campo. A partir de este análisis, se observa que ErAl₂ posee mayores capacidades en el rango de 4,2 a 20 K. Para su evaluación, se ha desarrollado un modelo numérico unidimensional (1D) que permite estimar las principales características del sistema de refrigeración magnético, como su potencia de refrigeración y su eficiencia exergética.

Para validar el modelo numérico, se ha diseñado y construido un banco de pruebas experimental basado en el método *single-blow* para la caracterización de regeneradores. Este prototipo fue modificado con el fin de analizar su comportamiento en condiciones de temperatura criogénica y bajo la aplicación de un campo magnético.

Con esta infraestructura, se propone una metodología destinada a evaluar regeneradores magnetocalóricos mediante la imposición de transitorios térmicos y magnéticos. Bajo dicha estrategia, se estudia el rendimiento de dos regeneradores (ErAl₂ y Gd₃Ga₅O₁₂). Aunque el modelo numérico alcanza una validación parcial, existen factores que dificultan su confirmación completa, entre los que destacan la sensibilidad del banco de ensayos a

pérdidas externas y la incertidumbre en las propiedades reales de los materiales magnetocalóricos.

Los resultados obtenidos, tanto del modelo como de las pruebas experimentales, sustentan un análisis tecnológico más amplio, abarcando consideraciones económicas y la integración a escala de sistema. En particular, se identifica un elevado potencial en la refrigeración magnética para disminuir de forma notable los costes ligados al enfriamiento criogénico. Por último, se presenta una hoja de ruta con los pasos críticos para avanzar en esta tecnología y reducir el riesgo a lo largo de su desarrollo, refrendando así su viabilidad industrial y comercial.

ACKNOWLEDGEMENTS

I would like to express my deepest gratitude to my advisors for the continuous support provided during the completion of this thesis, without which it would not have been possible. First and foremost, to Luis, who gave me the opportunity to undertake this work after just a couple of phone conversations. Thank you so much for your patience, long-term vision, and the freedom to explore new ideas and paths that initially seemed challenging. I am also grateful to Javi for his ability to illuminate and resolve any problem, regardless of its origin. Thank you for your support and understanding, for serving as a balancing force during particularly complex moments, and for helping me maintain perspective. I also extend my gratitude to Juan Carlos for his support from the University, especially during the initial tests with the magnetocaloric material.

To the entire CYCLOMED team, thank you for your collaboration and contributions in enabling this thesis to move forward. Special thanks to Iván for your indispensable support with testing, schematics, and assembly. Without you, I would probably still be searching for helium leaks and extra hands to install the heat exchanger. This work would not have been possible without your help.

I am also grateful to the CIEMAT team: to Jose Manuel, for the trust placed in me from the very beginning. I wish to especially acknowledge the accelerators and magnets unit, particularly Conchi, Dani, and many others, especially Diego, who always found ways to overcome challenges when situations seemed insurmountable. Of course, my thanks also go to the MCBX team: Jose, Pablo, Cristóbal, Jesús(es), Oscar... with whom we shared the magnet laboratory during difficult days following the pandemic. A special mention goes to Fernando for your constant advice and support; together with Carla, we have shared experiences in opposite poles of American culture. Here's to another Kona Big Wave...

I would also like to acknowledge and thank the members of the superconductivity laboratory. To Luis, for helping professionalize data acquisition and for your patience when we turned the lab upside down; to Luismi and Antonio, for your collaboration in instrumentation and control; and to Pablo, for the brilliance and originality of your ideas.

Additionally, I express my gratitude to the electrical drives team: Marcoses (plural), Jorge, and especially Gustavo, for clarifying all my doubts and resolving every issue with the power supply.

To ANTEC, particularly Rafa and Borja, thank you for your dedication in finding solutions to manufacture the heat exchanger.

I owe an enormous debt of gratitude to my family—cousins, uncles, siblings, and grandparents—and most especially to my parents: none of this would have been possible without your support and sacrifice; you are an example of dedication.

Finally, to all my friends: I know I owe you a few rounds after these last few months!

AGRADECIMIENTOS

Quiero expresar mi profundo agradecimiento a mis directores por el apoyo continúo brindado durante la realización de esta tesis, sin el cual esta no hubiese sido posible. En primer lugar, a Luis, quien me ofreció la oportunidad de realizar este trabajo después de solo un par de conversaciones telefónicas. Muchas gracias por tu paciencia, visión a largo plazo y libertad para explorar nuevas ideas y caminos que, en un principio, parecían difíciles. También agradezco a Javi su habilidad para iluminar y resolver cualquier problema, sin importar su origen. Gracias por tu apoyo y comprensión, y por servir de balanza en momentos especialmente complejos y por saber ayudarme a conservar la perspectiva. Extiendo también mi agradecimiento a Juan Carlos por su respaldo desde la Universidad, sobre todo durante las primeras pruebas con el material magnetocalórico.

A todo el equipo de CYCLOMED, gracias por su colaboración y participación para que esta tesis pudiera avanzar. Especialmente a Iván por tu indispensable apoyo en los ensayos, los planos y el montaje. Sin ti, probablemente seguiría buscando fugas de helio y buscando manos donde no las hay para instalar el intercambiador de calor. Este trabajo no hubiera sido posible sin tu ayuda

Agradezco también al equipo de CIEMAT: a Jose Manuel por la confianza depositada desde el primer momento. Deseo especialmente mencionar a la unidad de aceleradores e imanes, en especial a Conchi, Dani, y tantos otros y sobre todo Diego, quien siempre encuentra la forma de sortear los problemas cuando la situación parecía insalvable. Por supuesto, también al equipo de MCBX: Jose, Pablo, Cristóbal, Jesús(s), Oscar... con quienes compartimos el laboratorio de imanes en días difíciles tras la pandemia. De manera especial, a Fernando, por tu consejo y apoyo constantes, que además con Carla, hemos compartido destino en polos opuestos en la cultura americana. Por una Kona Big Wave más...

También reconocer y agradecer la ayuda a los miembros del laboratorio de superconductividad. A Luis, por ayudar a profesionalizar la adquisición de medidas y por la paciencia mostrada cuando poníamos patas arriba el laboratorio; a Luismi y Antonio, por su colaboración en la instrumentación y el control; y a Pablo, por la brillantez y originalidad de tus ideas.

Por otra parte, expresar mi gratitud al equipo de accionamientos eléctricos, a los Marcos, Jorge y, de manera especial, a Gustavo, por aclarar todas mis dudas y resolver todos los problemas con la fuente de alimentación.

A ANTEC, especialmente a Rafa y Borja, gracias por el empeño que pusieron en encontrar soluciones para fabricar el intercambiador.

Guardo una deuda enorme con mi familia, primos, tíos, hermanos y abuelos. Y muy especialmente con mis padres: nada de esto habría sido posible sin vuestro apoyo y sacrificio, sois un ejemplo de dedicación.

Finalmente, a todos mis amigos, sé que os debo unas cuantas rondas después de estos últimos meses.

CONTENTS

CHAPTE	R 1 : INTRODUCTION	1
1.1	CRYOGENICS AND APPLICATIONS OF SUPERCONDUCTIVITY	1
1.1.1	Cryogenic refrigeration systems	2
1.1.2	Limitations of cryogenic systems	6
1.2 T	THESIS OUTLINE	8
1.2.1	Motivation	8
1.2.2	Objectives	8
1.2.3	Outline of the work	10
	R 2 : FUNDAMENTALS OF THE MAGNETOCALORIC EFFE	
AND DEV	ELOPMENT AND ANALYSIS OF A 1D NUMERICAL MODEL	.11
2.1 T	THE FUNDAMENTALS OF THE MAGNETOCALORIC EFFECT	.11
2.1.1	Thermodynamics of the MCE	.11
2.1.2	Carnot Cycle	13
2.2	CRYOGENIC MAGNETIC REFRIGERATION	14
2.2.1	Active Magnetic Regeneration (AMR)	14
2.2.2	Magnetocaloric materials for cryogenic applications	16
2.2.3	Magnetic field sources	
2.2.4	Relevant prototypes: Cryogenic Magnetic Refrigeration	19
2.2.5	General Analysis of Cryogenic Magnetic Refrigeration Technology	
2.3 1	D NUMERICAL MODEL	
2.3.1	Governing Equations	26
2.3.2	Compressible flow model	28
2.3.3	Experimental correlations: Heat transfer, Pressure drop and Thermal Conductivity	30
2.4 N	MODEL VERIFICATION AND ANALYSIS	
2.4.1	Material Properties	31
2.4.2	Cryomagnetic refrigerator	35
2.4.3	Impact of operational parameters	
2.5 E	EFFECT OF HELIUM COMPRESSIBILITY	
2.5.1	Incompressible model: Performance comparison	44
2.5.2	Numerical stability	
2.6 S	UMMARY: THE POTENTIAL OF MAGNETIC REFRIGERATION	46
CHAPTE	R 3 : DESIGN, MANUFACTURING AND COMMISSIONING (ЭF
EXPERIM	IENTAL TEST STAND	49
	CONCEPTUAL DESIGN	
3.2 N	AAGNETOCALORIC MATERIAL	51
3.2.1	Design of the test bed	52
3.2.2	Packed Bed manufacturing	
3.2.3	Packed Bed characteristics	55
3.2.4	Final Assembly and instrumentation	59
3.3 N	AAGNETIC SOURCE: SUPERCONDUCTING MAGNET	62
3.3.1	Electromagnetic Analysis	63
3.3.2	Electrical Circuit	
3.3.3	Superconducting Magnet Testing	67
3.3.4	Final Assembly	
3.4 F	HEAT TRANSFER CIRCUIT	71
3.4.1	Pumping circuit	71
3.4.2	Three-Fluid Heat Exchanger	
3.4.3	Commissioning of Three-Fluid Cryogenic Heat exchanger	

3.4.4 Final Assembly and Liquid Helium testing	87
3.5 SUMMARY: DEVELOPMENT OF TEST STAND	89
CHAPTER 4: EXPERIMENTAL PROCEDURE AND RESULT	ΓS 91
4.1 Experimental Procedure	
4.1.1 Heat Transfer Tests	91
4.1.2 Magnetocaloric Tests	
4.2 SUMMARY OF EXPERIMENTAL RUNS AND MODIFICATIONS	96
4.3 RAW EXPERIMENTAL RESULTS	98
4.3.1 Thermal: Single Blow Testing	98
4.3.2 Thermal: Periodic Blow Testing	102
4.3.3 Magnetic: No-Load Testing	105
4.3.4 Magnetic: Ramping Rate Testing	106
4.3.5 Magnetic: Variable Temperature Testing	
4.4 SUMMARY: EXPERIMENTAL PROCEDURE AND RESULTS	
CHAPTER 5 : ANALYSIS OF EXPERIMENTAL DATA AND	TECHNOLOGY
ASSESSMENT	
5.1 EXPERIMENTAL RESULTS ANALYSIS	115
5.1.1 Numerical model update	115
5.1.2 Thermal tests	
5.1.3 Magnetic tests	
5.1.4 Conclusions and recommendations for future testing	
5.2 TECHNOLOGY ASSESSMENT: ECONOMIC ANALYSIS	
5.2.1 Base comparison	
5.2.2 Cost of components: Magnetic Refrigerator	
5.2.3 Case 1: GM-Cryocooler with an AMR stage	
5.2.4 Case 2: Magnetic Cryocooler	
5.3 SUMMARY: TECHNOLOGY ASSESSMENT	
CHAPTER 6: CONCLUSIONS	
6.1 SUMMARY AND CONCLUSIONS	
6.2 Outlook	
6.3 LIST OF PUBLICATIONS	
REFERENCES	
APPENDICES	
APPENDIX 1: EXPERIMENTAL CORRELATIONS FOR	
REFRIGERATOR	173
APPENDIX 2: DERIVATION OF ERAL ₂ PROPERTIES	
APPENDIX 3: HEAT TRANSFER AND PRESSURE CORREL	
FLUID HEAT EXCHANGER	
APPENDIX 4: RAW EXPERIMENTAL RESULTS	
LIST OF TABLES	
LIST OF FIGURES	196

LIST OF ABBREVIATIONS AND ACRONYMS

1D One Dimensional AC Alternate Current

ADR Adiabatic Demagnetization Refrigeration

AMR Active Magnetic Regeneration

BC Boundary Conditions

BDF Backward Differentiation Formulas

BSCCO Bismuth Strontium Calcium Copper Oxide

CAPEX Capital Expenditures

CELF Constant Escalation Levelization Factor

CF ConFlat

COP Coefficient of Performance

CMRP Coefficient of Magnet-Refrigerant Performance

CRF Capital Recovery Factor

CRP Coefficient of Refrigerant Capacity

CSS Cryogenic Supply System

DC Direct Current
DR Dilution Refrigerators

ECOP Exergetic Coefficient of Performance

EIGA Electrode Induction Melting Gas Atomization

FOMT First Order Magnetocaloric Materials

GM Gifford-MacMahon HFC Hydrofluorocarbons

HP High Pressure

HTS High Temperature Superconductor

 $\begin{array}{lll} HX & Heat Exchanger \\ JT & Joule Thomson \\ LHe & Liquid Helium \\ LN_2 & Liquid Nitrogen \\ LP & Low Pressure \\ \end{array}$

LTS Low Temperature Superconductor

MC Magnetocaloric

MCM Magnetocaloric Material
MCE Magnetocaloric effect
MFC Mass Flow Controller
MR Magnetic Refrigeration
MRI Magnetic Resonance Imaging

NL No-Load

NMRSE Normalized Root Mean Square Error

NTU Number of Transfer Units
ODE Ordinary Differential Equation
OPEX Operational Expenditures

PB Periodic Blow

PDE Partial Differential Equation

PT Pulse Tube

RC Refrigerant Capacity
RCP Relative Cooling Power

REBCO Rare-Earth Barium Copper Oxide

RR Ramping-Rate

RRR Residual Resistance Ratio

SB Single Blow

SOMT Second Order Magnetocaloric Materials

VRC Volumetric Refrigerant Capacity VSVO Variable-Step, Variable-Order

VT Variable-Temperature

YBCO Yttrium Barium Copper Oxide

Chapter 1: Introduction

1.1 Cryogenics and applications of superconductivity

Cryogenics is an engineering branch that focuses on the production, use, and management of materials at extremely low temperatures, typically below 120 K, although there is not an established consensus temperature among the literature [1]. The applications of cryogenic technologies are numerous and can be roughly divided in the following domains:

- i) Industry: Liquefaction, storage, and transportation of gases
- ii) Medicine and biology
- iii) Research: Altering material properties at low temperatures
- iv) Superconductivity

This thesis emphasizes the applications of superconductivity and the refrigeration technologies essential for its implementation. Cryogenics plays a pivotal role in enabling superconductivity, as most materials require temperatures between 0 K and 80 K to achieve a superconducting state. Figure 1 provides an overview of key superconductivity applications, organized by their operational temperature ranges and associated refrigeration power requirements.

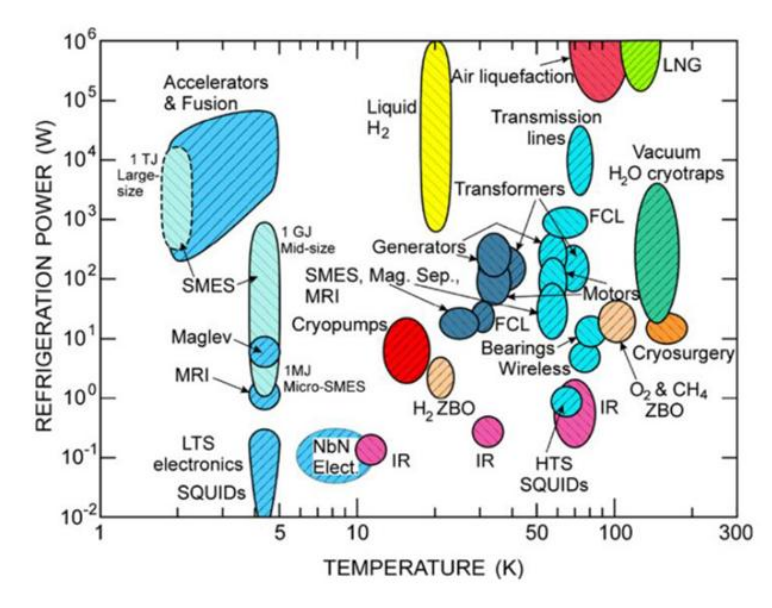


Figure 1. Cryogenic applications as function of typical cooling temperature and cooling power [2].

Figure 1 compiles the state of the art as of the early 2000s, while Table 1 provides an updated overview of certain applications, incorporating the latest advancements. Although a direct comparison reveals no substantial changes, a clear trend toward operating within the temperature range of 8–30 K is evident. This shift is primarily attributed to the development of MgB₂ wires and the adoption of high-temperature superconductors (HTS). The trend is particularly pronounced in applications related to biology and medicine, energy, and transportation. The continued advancement of efficient cooling systems within

this temperature range has the potential to further accelerate the growth and expansion of these fields.

Table 1. Cryogenic thermal demands of superconducting applications

Application	Temperature range (K)	Cooling power (W)	References
Biology and Medicine			
MRI	4.2-10	3-5	[3], [4]
Cyclotrons for RI production	4.2-10	1-5	[5]
NMR	4.2	1-10	[6]
Aerospace			[7], [8]
IR Detectors	4.2	10-500 mW	[9]
Microcalorimeters	4.2	10-50 mW	[9]
Bolometers	4.2	10-50 mW	[9]
EM propulsion systems	5-30	5-25 kW	[10]–[13]
Electronics			
Electronic components	< 4.2	10-500 mW	[14]–[17]
Quantum computing	< 4.2	10-500 mW	[18], [19]
Energy			[20]
Motor & Generators	20-50	0.1-5 kW	[21]–[24]
Fault current limiter	20-77	0.1-5 kW	[25]
SMES	20-77	0.5-5 kW	[26]
Transmission cable	65-77	0.5-3 W/m	[27]–[30]
Transformer	65-77	5-10 kW	[31]
Transport			
Maglev	5-30	2-5	[32], [33]
R&D			
Accelerator	< 4.2	0.5-100 kW	[34]
Fusion	< 4.2	0.5-100 kW	[35]

1.1.1 Cryogenic refrigeration systems

Before describing the refrigeration methods used in cryogenics, it is important to define two commonly used terms in the industry: the coefficient of performance (COP) and exergy efficiency.

The first term, the coefficient of performance or COP, is defined, in steady-state processes, as follows:

$$COP = \frac{Cooling\ Power\ (W)}{Power\ Input\ (W)} = \frac{\dot{Q}_c}{\dot{W}_l} \tag{1.1}$$

The specific power, or unit power, is the reciprocal of the COP, defined as:

$$p_{s} = \frac{Power\ Input\ (W)}{Cooling\ Power\ (W)} = \frac{\dot{W}_{t}}{\dot{Q}_{c}} \tag{1.2}$$

In an ideal refrigerator, where there are no irreversible processes, such as the Carnot cycle, the COP value is simplified to the following expression:

$$COP_{ideal} = \frac{T_c}{T_h - T_c} \tag{1.3}$$

where T_c and T_h are the cold and hot source temperature. The exergy or second-law efficiency computes the thermal efficiency relative to its performance in reversible conditions, and can be expressed as follows:

$$\eta_c = \frac{E\dot{x_{out}}}{E\dot{x}_{in}} = \frac{\dot{Q_c} \cdot (\frac{T_0}{T_c} - 1)}{\dot{W} + \dot{Q_h} \cdot (\frac{T_0}{T_h} - 1)}$$
(1.4)

where if T_h is equal to the ambient temperature (T_o) the relation can be expressed as the relation between the COP of the actual refrigeration cycle and the COP of an ideal refrigerator:

$$\eta_c = \frac{\dot{Q}_c \cdot (\frac{T_0}{T_c} - 1)}{\dot{W}} = \frac{COP(refrigeration \ cycle)}{COP(ideal \ cycle)}$$
(1.5)

A concise overview of cryogenic cooling methods is provided below. Figure 2 provides a classification method for refrigeration systems, these are first broadly categorized into open and closed systems. In an open system, both energy and matter can freely enter and exit, whereas a closed system is isolated from its surroundings. Open systems remain widely used in cryogenics, where the object being cooled is immersed in a bath of liquid cryogen [36]. However, there is increasing interest in transitioning to closed systems due to concerns over efficiency and cost.

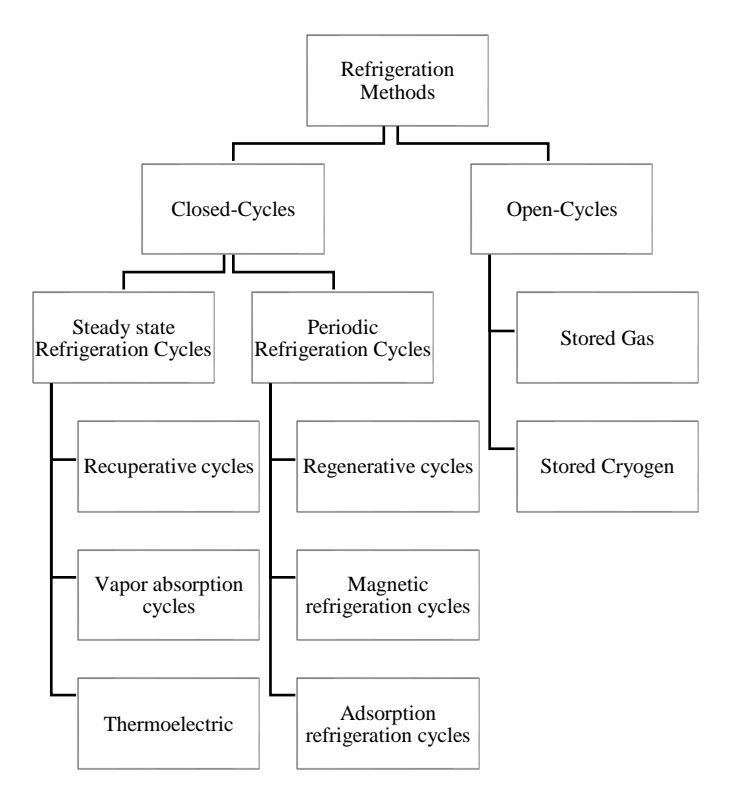


Figure 2. Refrigeration methods classification [37], [38].

Closed systems can be further categorized as either steady-state or periodic cycles [38], depending on the temporal variations in their operating parameters. In steady-state cycles, key parameters such as energy transfer, flow characteristics, or thermodynamic states remain constant during operation. In contrast, periodic cycles exhibit time-dependent fluctuations in these parameters, which may include pressure, mass flow rate, or other thermodynamic properties. This classification applies broadly across different types of

refrigeration cycles, encompassing gas-based systems as well as other cryogenic technologies.

Both steady-state and periodic closed-cycle methods are widely employed in cryogenics, with the choice depending on the specific application. In both approaches, gas cycles—classified as either recuperative or regenerative—are the most commonly utilized techniques.

For recuperative gas cycles, two primary types are employed:

- 1) Joule Thomson refrigerators: These systems achieve cooling through isenthalpic expansion of a fluid across a flow impedance, resulting in a temperature drop. To ensure reasonable cooling capacity and high efficiency, pressures exceeding 100 bars are typically required. Achieving such high pressures necessitates multiple compression stages, each equipped with an aftercooler to dissipate the heat generated during compression. Once the desired pressure is reached, the cryogen flows through a recuperative heat exchanger, transferring heat to the low-pressure stream. Finally, it passes through a throttling valve where it expands and reaches the target temperature.
- 2) Brayton and Claude refrigerators: In Brayton cycles, cooling is achieved through expansion in a turbine. Large-scale liquefaction plants utilizing this cycle can achieve efficiencies of approximately 30% relative to the Carnot limit. The Claude cycle integrates elements of both Brayton and JT cycles, enabling highly efficient gas liquefaction.

These gas cycles are often miniaturized into devices known as cryocoolers, which are refrigeration systems capable of achieving temperatures below 80 K. While the term "cryocooler" generally refers to compact, table-top devices, their development has been significantly influenced by the aeronautical and military industries [37], where size and weight are critical considerations (Figure 3 illustrates an example of a cryocooler).

JT cycles are particularly well-suited for miniaturization due to their lack of moving parts. Conversely, manufacturing small-scale expansion turbines for Brayton cycles poses significant challenges, restricting their use to large-scale liquefaction systems designed for high thermal load applications, such as accelerators or fusion reactors.

However, the application of recuperative gas cycles in cryocoolers is limited by the high effectiveness required of recuperative heat exchangers, which are often large and bulky. This constraint restricts their use to specialized applications where minimal interference is essential. In contrast, regenerative-based cryocoolers do not face this limitation and are therefore more broadly adopted across a wider range of cryogenic applications.

Typically used regenerative gas cycles in cryocoolers operate with oscillating pressures and mass flows. Three main cycles can be distinguished:

- 1) Stirling cycle: The Stirling cycle, invented by Robert Stirling in the early 19th century, was not applied to refrigeration until the mid-20th century, when it was first used to liquefy air. A basic Stirling cryocooler consists of a compressor (either a piston or another device) and a cold head. The cold head, shown in Figure 3, contains a displacer, a regenerator, and compression and expansion spaces. The cooling cycle is divided into four steps:
 - a. Compression: Helium gas is compressed in the warm compression space, and the heat generated is dissipated to the surroundings.
 - b. Displacement: The displacer moves up, allowing the helium to flow through the regenerator and into the cold expansion space, where it transfers heat to the regenerator.
 - c. Expansion: Helium expands in the cold space, extracting heat from the cold head heat exchanger, which provides the useful cooling power.
 - d. Return Flow: The displacer moves down, causing the helium to flow back through the regenerator, where it absorbs heat in the process.

At temperatures of 60-80 K, Stirling cryocoolers can achieve exergy efficiencies of approximately 15%. However, the high cost and technical complexity of pressure oscillators make their operation challenging and limit their widespread use.

2) Gifford-McMahon [39]: Gifford-McMahon (GM) refrigerators are based on the Stirling cycle, sharing the same cold head components. The primary difference lies in the pressure source. GM refrigerators use valved compressors, which allow the separation of the pressure source operation from the displacer. The displacer in a GM refrigerator operates at much lower frequencies (1-2 Hz compared to 30-60 Hz in Stirling cryocoolers), which significantly extends the lifetime of the cold head components. Additionally, GM refrigerators can utilize conventional oil-lubricated compressors, reducing the system's complexity and cost. However, the expected second law efficiency of GM refrigerators is lower compared to Stirling cryocoolers due to the increased irreversibility associated with the use of valves. Despite this, GM cryocoolers can achieve temperatures as low as 4 K and are widely used in industry. For example, they are commonly employed in the refrigeration of Magnetic Resonance Imaging (MRI) magnets [40]. Figure 3 shows a GM cryocooler.

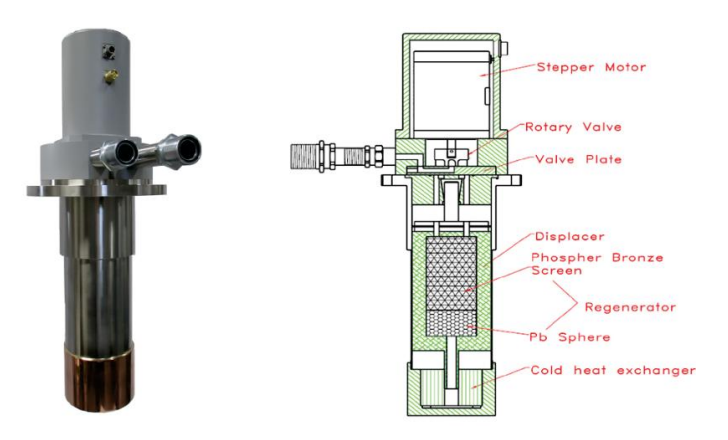


Figure 3. Image and schematic of a GM cryocooler.

3) Pulse tube [41]: Pulse tube (PT) refrigerators eliminate the displacer used in GM and Stirling cryocoolers. Instead, the necessary gas motion is achieved through the use of an orifice and a reservoir volume of gas at the warm end. The ideal PT cycle operates with adiabatic compression and expansion. During compression, the gas heats up and flows through the orifice to the reservoir, where it exchanges heat with the surroundings. Conversely, during expansion, the gas flows from the reservoir to the heat exchanger until the pressure equalizes.

Figure 4 (left), depicted from Radebaugh [42], illustrates the preferred cooling method for various combinations of temperature and cooling power. Generally, cooling systems with low cooling requirements are suited for cryocooler technology, while those requiring high cooling capacity employ Brayton/Claude expansion cycles in liquefaction plants.

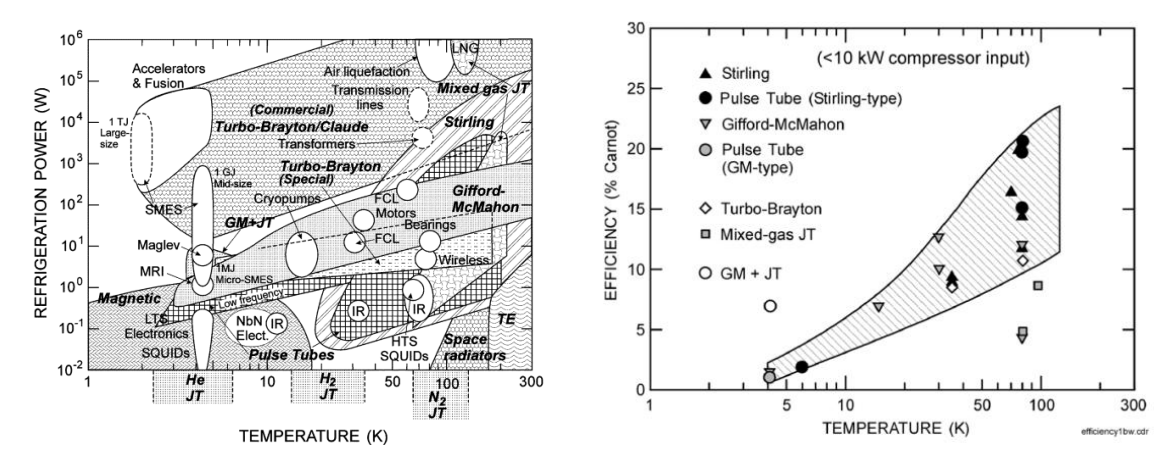


Figure 4. Preferable cooling method as function of temperature and cooling power (left), and exergy efficiency as function of refrigeration temperature for selected cooling methods (right). Radebaugh et al [42]

Figure 4 (right) depicts the exergy efficiency of various cooling techniques as a function of temperature, highlighting the significant efficiency penalties incurred at lower temperatures. As the cold source temperature decreases and the temperature difference between the hot and cold sources increases, the coefficient of performance (COP) of an ideal refrigerator declines. Additionally, the relative COP of a real refrigerator compared to an ideal one also diminishes under these conditions, further compounding inefficiencies.

The primary factor contributing to the low exergy efficiency of cryocoolers lies in the disparity between the volumetric heat capacities of helium and the regenerator material. At low temperatures, the heat capacity of the regenerator material decreases significantly, while helium's heat capacity increases near its critical point. This imbalance severely impacts the system's overall performance. Consequently, one of the key research priorities in cryogenics is the development and exploration of alternative regenerator materials with enhanced volumetric heat capacities at low temperatures. Figure 5 presents a comparison of the volumetric heat capacities of helium and various regenerator materials commonly employed in cryocooling systems [43].

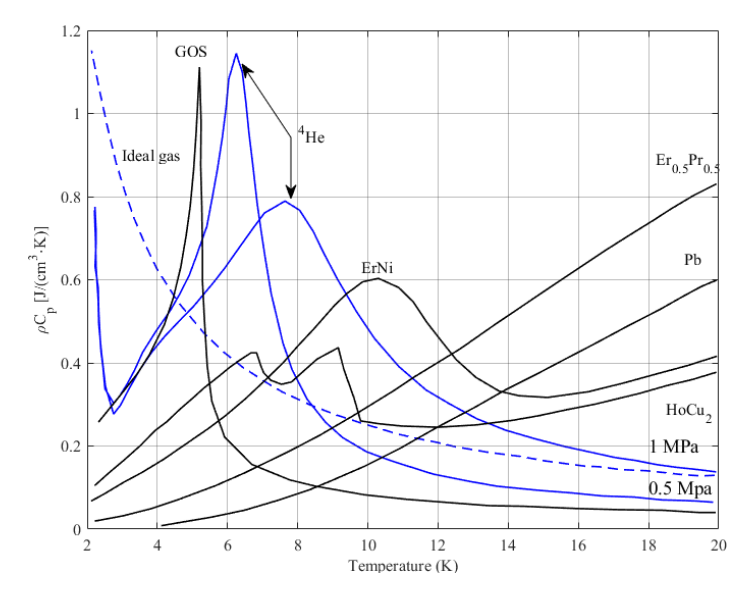


Figure 5. Volumetric heat capacity of various low temperature regenerator materials (in black), compared with that of helium at various pressures-0.5MPa, 1.0MPa.

Other refrigeration methods used in cryogenics, especially to reach lower temperatures are:

Adiabatic demagnetization: One of the first methods used to reach temperatures below 1 K [44]. Based on the magnetocaloric effect, an applied magnetic field interacts with the magnetic moment of a material reducing the total entropy. This method will be of special interest for the development of this thesis.

Dilution refrigerators (DR): which use a mixture of ³He and ⁴He to provide subKelvin temperatures, and capable of reaching the millikelvin. Four types of dilution refrigerators can be identified [44]: classical DR, Joule-Thomson DR, 'dry dilution', and 'no gravity' dilution.

Other less common alternatives are the Pomeranchuk refrigerator [45], the adiabatic nuclear demagnetization and the electronic refrigerator [46].

1.1.2 Limitations of cryogenic systems

In the design and development of a cryogenic system, several factors must be meticulously considered to ensure optimal performance and safety at low temperatures. The primary factors to evaluate and select the appropriate method for a cryogenic system are [2], [38]: 1) Heat Rejection Capacity/Cooling Power, 2) Efficiency: Higher efficiency translates to

lower operational costs, 3) Reliability, 4) Interference: Including electromagnetic, mechanical (vibration), and nuclear (activation), 5) Maintenance, 6) Size and Weight and 7) Economic factors.

The relative importance of each factor is dictated by the specific requirements of the application. However, as previously mentioned, the selection of a cryocooling technology can be broadly categorized based on the thermal demand of the application:

- 1) High thermal demand applications, predominantly employ recuperative expansion processes. These systems are well-suited for managing substantial thermal loads and are often designed to prioritize heat rejection capacity and operational efficiency. However, the capital investment required to establish a liquefaction facility for such applications is considerable. As a result, these facilities are generally limited to specialized uses, such as in advanced research infrastructure like the CERN particle accelerator.
- 2) Low thermal demand applications: in contrast regenerative cryocoolers are more frequently utilized in applications with lower thermal demands, such as those in the medical field, as well as military and aerospace sectors. For these applications, critical considerations include reliability, compact design, and minimal maintenance requirements. Moreover, regenerative cryocoolers show significant potential in the field of applied superconductivity, particularly in systems such as superconducting motors and generators.

While recuperative gas cycles can achieve an exergy efficiency of approximately 30%, currently available regenerative cryocoolers exhibit significantly lower efficiencies, typically ranging from 1–2% when operating at 4.2 K. These low efficiencies, combined with the substantial costs associated with cryogenic systems, make cooling infrastructure one of the primary cost drivers for applications requiring cryogenics.

Moreover, selecting an appropriate cooling method represents only an initial step in the development of a functional cryogenic system. Considerable adaptation is often required to meet the specific demands of the final application. For instance, modern MRI systems employ cryocoolers configured as thermosyphons to minimize electromagnetic interference [40]. Another example is the Cryogenic Supply System (CSS) designed for the refrigeration of a superconducting cyclotron [47], shown in Figure 6. In this case, a remote cooling solution based on cryocoolers was the only feasible approach due to system constraints and the thermal load range. Although this remote configuration offers advantages such as reduced interference and simplified maintenance, it also increases overall costs and reduces system efficiency, with cooling expenses accounting for over 30% of the total cost of the magnetic system.

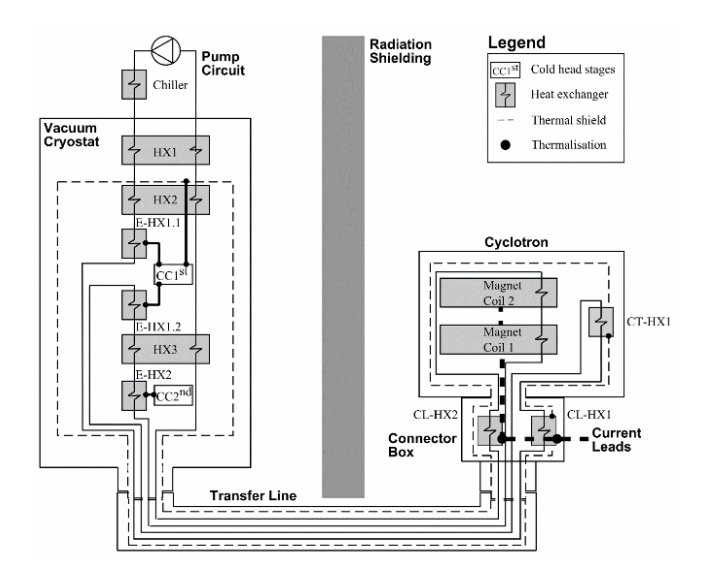


Figure 6. Cryogenic supply system (left) and CYCLOMED superconducting cyclotron (right).

These challenges significantly hinder the broader adoption of existing superconducting technologies and constrain the development of innovative applications in superconductivity and cryogenics. Addressing these limitations is essential to enable more widespread and cost-effective use of superconducting systems in various fields.

1.2 Thesis Outline

1.2.1 Motivation

The reliance on cryogenics has been a significant barrier to the widespread adoption of superconducting technologies. While superconductors have seen substantial advancements over the past two decades, progress in cryogenic technologies has been comparatively slower. Superconducting applications have largely adapted existing cryogenic methods with modifications tailored to specific requirements. These innovative configurations could potentially be applied to other systems, broadening their usability. However, two persistent challenges—high cost and low efficiency—continue to constrain the broader adoption of these technologies.

This project aims to address these challenges by analyzing cost-effective cryogenic techniques that could enhance the current state-of-the-art technologies within the operating temperature range of 4.2–20 K.

To establish a baseline for evaluation, data from commercial cryocoolers operating at various temperatures were analyzed. The analysis incorporated an electricity cost of 70 €/MWh and utilized performance data from leading cryocooler manufacturers, including Sumitomo, Cryomech (Bluefors), and ARS Cryogenic [48], [49]. For reference, the specifications of Sumitomo's latest 4 K model were used as a benchmark to assess cryocooler performance in low-temperature applications. The results are shown in Table 2.

By identifying and evaluating potential improvements in cryogenic efficiency and costeffectiveness, this project seeks to overcome key barriers limiting the development and deployment of superconducting technologies across diverse fields.

Temperature (K)	Capital Cost (per W)	Operational Cost (per W)	Exergy Efficiency
4.2	20-25.000 €	0.3-0.6 €/h	1-2%
10	3-6.000 €	0.05-0.12 €/h	5-7%
20	500-1000 €	0.015-0.05 €/h	10-12%
Sumitomo RDE- 418	43.000 € (ex VAT) 2W of cooling @ 4.2 K	8000 W electric consumption	1.8 %

Table 2. Cryocooler cost comparison for different operational temperatures

1.2.2 Objectives

The primary objective of this thesis is to identify and evaluate potential technological solutions for developing a cost-effective cryogenic system tailored to low thermal demand applications within the temperature range of 4.2–20 K. To assess the performance of the proposed system, three key metrics will be monitored: capital cost per watt, operational cost per watt, and exergy efficiency. These indicators will be benchmarked against baseline values provided in Table 2.

The research will focus on cryogenic magnetic refrigeration as a promising candidate due to its potential for achieving high exergy efficiency. Magnetic refrigeration theoretically operates near the Carnot efficiency limit and has garnered significant attention, particularly at room temperature, for its use of solid-state refrigerants in magnetic systems, eliminating the need for greenhouse gases such as hydrofluorocarbons (HFCs). While magnetic

refrigeration has been explored for low-temperature applications in the past, its renewed interest stems from its potential role in liquid hydrogen liquefaction. However, it is important to note that no commercial cryogenic magnetic refrigeration technology is currently available.

Given the ambitious nature of this research, the scope of the thesis has been carefully defined to ensure feasibility within the projected timeline. Table 3 shows the specific objectives that have been established to guide the investigation and focus efforts on critical aspects of system development. These objectives will serve as milestones to structure the research and evaluate progress toward creating a cost-effective cryogenic solution.

Table 3. Thesis Objectives

Objectives	Description	Milestones
Objective 1: Analysis of state-of-the-art cryocooling system. Investigate the potential of magnetic refrigeration for cryogenic purposes	This objective focuses on conducting a comprehensive review of existing cryocooling systems to establish a baseline for performance and efficiency. The analysis will evaluate the advantages and limitations of current technologies, with particular emphasis on identifying the potential of magnetic refrigeration as a viable alternative for cryogenic applications.	Milestone 1: MC material analysis Milestone 2: Magnetic field source analysis
Objective 2: Numerical analysis of a magnetic refrigeration stage.	The goal is to thoroughly define and predict the performance of a magnetic refrigeration system through numerical modeling and simulation. Computational tools, incorporating both analytical and empirical methods, will be developed to analyze key parameters such as cooling capacity, efficiency, and thermal behavior. This numerical analysis will serve as the foundation for optimizing the design and guiding subsequent experimental efforts.	Milestone 3: Complete evaluation of a magnetic refrigeration stage
Objective 3: Design, fabricate, and test a technology demonstrator.	A small-scale technology demonstrator will be designed, fabricated, and tested to validate the numerical model developed in Objective 2. This prototype will enable practical evaluation of the system's performance under controlled conditions, providing critical data to assess the feasibility of implementing magnetic refrigeration in cryogenic applications. The demonstrator will also help identify potential challenges in scaling up the technology.	Milestone 4: Design for manufacturing of the experimental set- up
Objective 4: Experimental validation of the multiphysics involved in a cryogenic magnetic refrigerator.	This objective aims to experimentally validate the multiphysics phenomena predicted by the numerical model, including thermal, magnetic, and fluid dynamics interactions within the system. Discrepancies between experimental results and model predictions will be analyzed to refine both the computational tools and the design of the system. This iterative process will ensure that the proposed design meets performance expectations under real-world conditions.	Milestone 5: Experimental validation at ambient temperatures Milestone 6: Working technology demonstrator and experimental validation of numerical model Milestone 7: Analysis of high efficiency magnetic refrigeration stage
Objective 5: Evaluate the technical performance and economic viability of magnetic refrigeration systems for cryogenic applications	This final objective focuses on assessing both technical and economic aspects of magnetic refrigeration for cryogenic purposes based on experimental outcomes from the technology demonstrator. Key performance indicators—capital cost per watt, operational cost per watt, and exergy efficiency—will be quantified and compared against baseline values established in Objective 1. The evaluation will determine whether magnetic refrigeration offers a competitive advantage over existing technologies in terms of cost-effectiveness, efficiency, and scalability for practical applications.	Milestone 8: Analysis of cost-effectiveness of a magnetic refrigeration cooling stage

1.2.3 Outline of the work

This introduction delineates the core research questions and objectives established in the thesis. The following chapters provide a structured exploration of the topic, combining theory, numerical modeling, and experimental validation to address these objectives:

Chapter 2, titled "Fundamentals Of The Magnetocaloric Effect And Development And Analysis Of A 1D Numerical Model", is divided in two parts, first a review of the state of the art of magnetic refrigeration with special dedication to the review of previous developed prototypes in cryogenic applications. The second part is dedicated to the creation and elaboration of a numerical model used to assess key refrigeration variables. This section discusses the potential of the technology and limitations inherent in current developments and justifies the need for constructing an experimental test stand based on these findings.

Chapter 3, "Design, Manufacturing and Commissioning of Experimental Test Stand", details the design process and specifications of the experimental test bench. It covers the rationale behind the design choices and the integration of each system component. It also addresses the commissioning phase of the test stand, including the validation of individual subsystems and the assembly of the complete system.

Chapter 4 focuses on the "Experimental Testing Procedure and Results". It outlines the methodology adopted during experimental testing, provides detailed descriptions and justifications for each test conducted, and presents the raw data obtained.

Chapter 5, "Analysis of Experimental Data And Technology Assessment", is divided in two main sections. The first section describes the data reduction techniques utilized in the analysis, followed by a comparison between experimental results and model predictions. Additionally, it includes a discussion on the broader implications of these findings for future advancements. The second section presents an economic analysis of a magnetic refrigeration stage, integrating insights from both the model and experimental results. Based on this analysis, potential directions for the future development of the technology are explored.

Chapter 6 concludes with a "Summary and Outlook", offering a synthesis of the research findings and an overview of potential future research directions.

Chapter 2: Fundamentals Of The Magnetocaloric Effect And Development And Analysis Of A 1D Numerical Model

2.1 The fundamentals of the magnetocaloric effect

The entropy of a magnetocaloric material (MCM) can be divided in three components [50], the magnetic entropy S_m , the entropy of the lattice S_l , and the electronic entropy of the material's free electrons S_e :

$$S_T(B,T) = S_m(B,T) + S_l(T) + S_e(T)$$
(2.1)

where the lattice and electronic entropy depend on the material temperature, and the magnetic entropy is dependent on both the magnetic field and the temperature.

If an external magnetic field is applied adiabatically to an MCM, the magnetic moments will tend to align with the field, thereby decreasing the magnetic entropy of the material while maintaining the value of S_T . As the process is isentropic, to compensate for the reduction in the magnetic entropy, lattice, and electronic entropy must increase, which causes an increase in the temperature of the sample. If the magnetic field is withdrawn, the process reverts, the magnetic moments will return to their original alignment capturing energy from the lattice and electronic system, thus reducing the temperature to its original value.

2.1.1 Thermodynamics of the MCE

A thermodynamic material can exchange energy with an external system through heat and work interactions, which can be expressed as a differential energy balance:

$$dU = TdS + dW (2.2)$$

Work interactions can be expressed more specifically if the energy is exchange in terms of mechanical, chemical or magnetic work:

$$dW = -PdV + \sum \mu_j dN_j + \mu_0 V_m H dM \tag{2.3}$$

For a magnetic refrigeration system, where the volume is not modified, i.e dV = 0, and there is no exchange of chemical energy, Eq. (2.3) is expressed as:

$$dU = TdS + \mu_0 V_m HdM \tag{2.4}$$

The total specific entropy change of the system can be represented as:

$$dS = \left(\frac{\partial s}{\partial T}\right)_{H} dT + \left(\frac{\partial s}{\partial H}\right)_{T} dH \tag{2.5}$$

Using the definition of specific heat, $C_{p,H} = T \left(\frac{\partial s}{\partial T} \right)_H$, and the Maxwell relation $\left(\frac{\partial s}{\partial H} \right)_T = \mu_0 \left(\frac{\partial m}{\partial T} \right)_{p,H}$, where m is the magnetization, Eq. (2.5) can be expressed as:

$$ds = \frac{C_{p,H}}{T}dT + \mu_0 \left(\frac{\partial m}{\partial T}\right)_{p,H} dH$$
 (2.6)

Under the condition that dS = 0, the following expression can be derived:

$$\Delta T_{ad} = -\mu_0 \int_{H_I}^{H_F} \frac{T}{C_{p,H}} \left(\frac{\partial m}{\partial T}\right)_{p,H} dH \tag{2.7}$$

Where H_F and H_I are the final and initial magnetic fields. The expression is denominated as adiabatic temperature change and is the reversible change of temperature that a magnetocaloric material undergoes in an adiabatic process under certain magnetization conditions.

When the MCM undergoes an isothermal process (dT = 0), Eq. (2.6) yields:

$$\Delta S_M = \mu_0 \int_{H_I}^{H_F} \left(\frac{\partial m}{\partial T}\right)_{p,H} dH \tag{2.8}$$

In this case, the change in entropy corresponds to the magnetic entropy change. Both Eq. (2.7) and (2.8) are employed to characterize the magnetocaloric effect of the material. These equations reveal that the maximum magnetocaloric effect occurs when a significant change in magnetization takes place. This explains why magnetocaloric materials are typically utilized near phase transitions, as this maximizes heat extraction. Figure 7 illustrates both key concepts: the adiabatic temperature change (ΔT_{ad}) and the isothermal magnetic entropy change (ΔS_M).

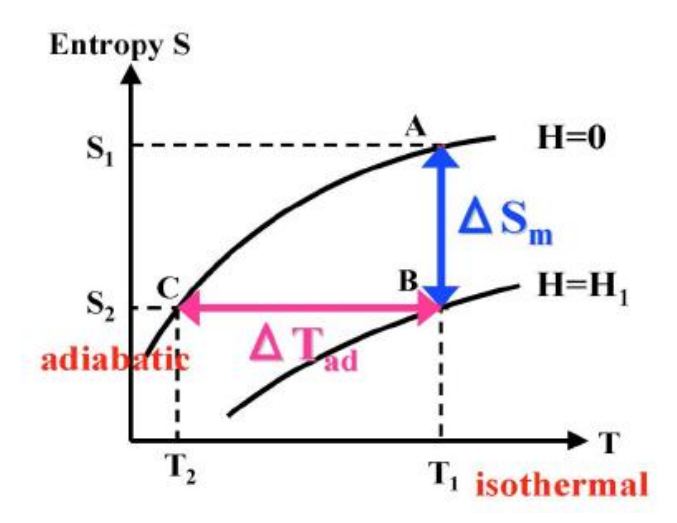


Figure 7. Isothermal magnetic entropy change, in blue, and adiabatic temperature change due to a varying magnetic field, in pink, of a generic magnetocaloric material. Depicted from [51].

To be able to compare among different materials a variable denominated refrigerant capacity (RC) is commonly used, which is defined as:

$$RC = \int_{T_{cold}}^{T_{hot}} \Delta S_m(T, H) dT$$
 (2.9)

Where T_{cold} and T_{hot} are the temperature of the cold and hot reservoirs. The advantages of using RC over other parameters is discussed in [52]. The calculation of RC requires the computation of the area under the curve defined by the variation of the magnetic entropy as function of temperature, as shown in Figure 8.

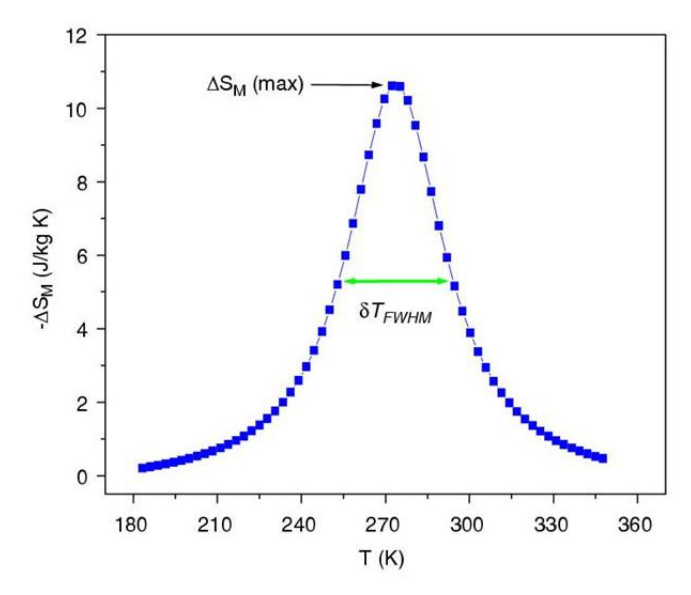


Figure 8. Magnetic entropy dependence on temperature of a generic magnetocaloric material. Depicted from [53].

A commonly used approximation in the literature is multiplying the peak entropy change, $\Delta S_m(\text{max})$ by the full width at half maximum, ∂T_{FWHM} , this is typically denominated as Relative Cooling Power (RCP):

$$RCP = \Delta S_m^{max} \cdot \partial T_{FWHM} \tag{2.10}$$

This definition could be deceiving in certain cases as kurtosis and skewness of the curve may differ substantially among materials, and if possible is always preferable to compute RC numerically.

2.1.2 Carnot Cycle

The Carnot cycle is the basis for any magnetocaloric refrigeration system. It consists of four processes: two adiabatic and two isothermal processes as illustrated in the T-S diagram of Figure 9.

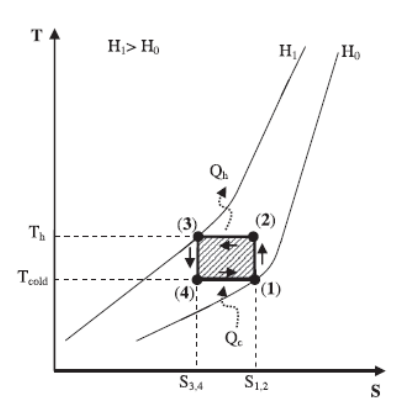


Figure 9. T–S diagram of an MR Carnot cycle.

The first step in the Carnot process (1-2) is an adiabatic magnetization where an external field is applied. The total entropy remains constant during the magnetization process, decreasing the magnetic entropy and increasing the thermal entropy. The second step (2-3) is an isothermal magnetization where the heat produced is rejected to the hot source. The third step is an adiabatic demagnetization process lowering the temperature of the MCM. Finally, in the last step, the sample is demagnetized isothermally absorbing heat from the cold source. The area (1-2-3-4) represents the work done during the process, and is equal to:

$$w = \int_{3}^{2} T dS - \int_{4}^{1} T dS = T_{h}(S_{2} - S_{3}) - T_{c}(S_{1} - S_{4})$$
 (2.11)

Where the first term of the right-hand side of the equation is the heat rejected to the hot source and the second term is the heat absorbed, i.e the cooling load of the refrigerator:

$$Q_c = \int_A^1 T dS = T_c(S_1 - S_4) \tag{2.12}$$

The cooling power of the cycle is proportional to the frequency:

$$\dot{Q}_c = f * Q_c = f * T_c * \Delta S_c \tag{2.13}$$

Maximizing the cycle frequency is a critical aspect of designing a magnetic refrigerator. However, this parameter is constrained by thermal losses that occur during heat exchange between the refrigerant and the hot and cold sources. Consequently, minimizing these thermal losses is essential for optimizing the system's performance, a topic that will be explored in greater detail later in this section. As introduced in Chapter 1, the performance of a refrigerator is typically evaluated using the Coefficient of Performance (COP) and exergy efficiency. These metrics provide a comprehensive assessment of the system's energy efficiency and thermodynamic effectiveness.

2.2 Cryogenic Magnetic Refrigeration

The preceding section established the fundamental principles of the magnetocaloric effect and its implementation in a Carnot cycle for magnetic refrigeration. This section introduces the Active Magnetic Regeneration (AMR) cycle, which has become the predominant approach in magnetic refrigeration systems, specially at room temperature. Subsequently, a comprehensive review of magnetocaloric materials and main magnetic field sources for cryogenic applications is presented. The section concludes with an analysis of significant cryogenic prototypes, drawing qualitative insights that form the foundation for the subsequent chapters of this thesis.

2.2.1 Active Magnetic Regeneration (AMR)

The temperature variation induced by a magnetic field change in a magnetocaloric material, is usually insufficient for direct refrigeration applications. Consequently, to achieve a temperature span adequate for practical refrigeration, a magnetic refrigeration device must employ a regenerative process, where the magnetocaloric material acts as both the refrigerant and the regenerator. The most used method for this purpose is Active Magnetic Regeneration (AMR) proposed by Stevert and Barclay in the 1970s [54].

The Active Magnetic Regenerator (AMR) cycle utilizes the magnetocaloric effect (MCE) to achieve efficient cooling through a regenerative process. This cycle is particularly distinguished by its ability to generate substantial temperature differences, which are essential for practical refrigeration applications. The AMR process involves a series of precisely coordinated steps that integrate a magnetocaloric material (MCM) with a heat transfer fluid within a regenerative framework. These steps, represented in Figure 10, are outlined as follows:

- 1. Magnetization: The cycle begins with the magnetization phase, during which the regenerator—comprising a porous matrix of the MCM—is exposed to a magnetic field. This field induces a temperature increase in the MCM due to the magnetocaloric effect. The resulting heat is transferred to the stationary heat transfer fluid within the regenerator during this phase.
- 2. Heat Displacement: The heated fluid is then displaced toward the hot heat exchanger, where it releases the absorbed heat to a high temperature sink. This step

- effectively removes heat from the fluid, preparing it for subsequent stages of the cycle.
- 3. Demagnetization: In this phase, the magnetic field is removed from the regenerator, causing the MCM to cool down through adiabatic demagnetization. As the MCM's temperature decreases, it absorbs heat from the previously warmed fluid, which has been displaced to facilitate this heat transfer. This cooling restores the MCM's capacity to absorb heat in subsequent cycles.
- 4. Heat Absorption: The cooled fluid is directed toward the cold heat exchanger, where it absorbs heat, achieving the desired cooling effect.

Through this regenerative process, the AMR cycle extends the temperature span beyond what could be achieved by the adiabatic temperature change of the MCM alone. The integration of magnetocaloric materials with a heat transfer fluid and the application of regenerative techniques enable the AMR system to produce significant temperature gradients, making it highly effective for various refrigeration applications.

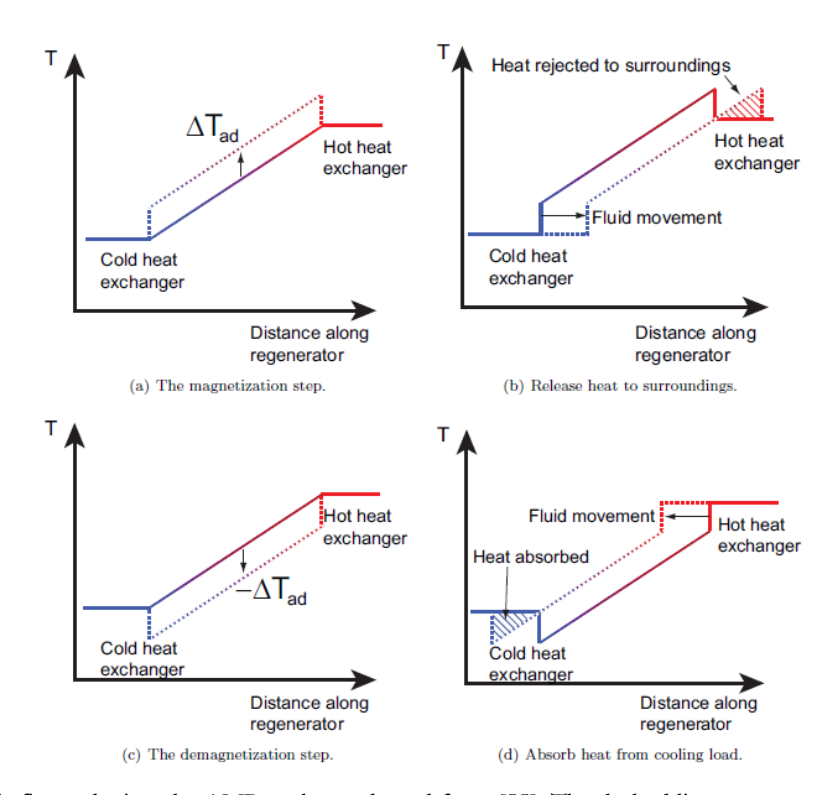


Figure 10. This figure depicts the AMR cycle as adapted from [55]. The dashed lines represent the temperature profiles, highlighting changes occurring during each step of the cycle. Between steps (b) and (c), the linear temperature profile is restored, a process similarly observed between steps (d) and (a).

Different thermodynamic cycles could be applied depending on the relation between the (de)magnetization phases and the heat transfer to the fluid phases. Figure 11, depicted from [56], shows the magnetic field and fluid profile for 3 different AMR cycles, a Brayton, an Ericsson and a combination of both, a Hybrid cycle. The Brayton-like AMR cycle is the most commonly applied thermodynamic cycle in magnetic refrigeration, especially at room temperature.

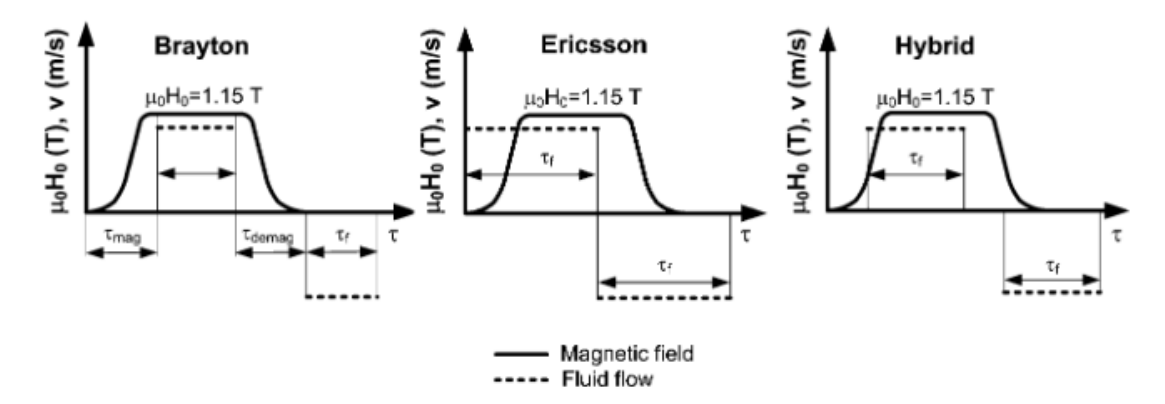


Figure 11. The magnetic field profiles and the corresponding fluid flow periods for the AMR thermodynamic cycles.

2.2.2 Magnetocaloric materials for cryogenic applications

The magnetocaloric material is an essential component on the design of a magnetic refrigerator. Two types can be distinguished regarding the order of the phase transition: first order magnetocaloric materials (FOMT), and second order magnetocaloric materials (SOMT). The former undergoes a discontinuous change in magnetization with temperatures, while the latter undergoes a continuous change. Comprehensive reviews regarding the different MCM exist within the literature [57] from low to ambient temperatures applications.

Some authors have provided a practical set of selection rules for picking a magnetic refrigerant depending on the application [56]. Some of these rules are:

- Suitable Curie temperature, which should be generalized to a suitable temperature of the phase transition since not all magnetocaloric materials transition from a ferromagnetic to a paramagnetic phase.
- Intensity of magnetocaloric effect: the greater the intensity of the magnetocaloric effect the better. It can be evaluated with the relative cooling power or RCP.
- Wide temperature range: the larger the temperature spans the better, as it could distance the cold and hot source.
- Near-Zero hysteresis: magnetocaloric materials suffer a small hysteresis during thermal and magnetic cycle, the smaller this hysteresis is the better as it directly affects the efficiency of the cycle. It is more predominant in first-order phase transition materials.
- High thermal conductivity and diffusivity: higher diffusivity favours a faster temperature response and improves the heat transfer between material and fluid. However, a very high thermal conductivity may reduce performance due to a higher heat flux along the regenerator.
- Good manufacturing properties: it is preferable that the materials have good manufacturing, mechanical and processing properties, as the geometrical properties of the material have a direct effect on the refrigerator performance.
- High electrical resistivity: it prevents the generation of eddy currents with the varying magnetic field, which could result in heat dissipation.
- Good corrosion properties

In addition to the characteristics mentioned, it is also preferable that the material has:

- Low price: the magnetocaloric material is one of the most expensive components in a magnetic refrigerator, especially for cryogenic applications, where the suitable materials are typically complex materials containing rare earths.

- High availability: the presence of critical raw materials, such as rare earths, may have an impact on the scalability of a refrigerator. It is preferable to use highly available materials.

Table 4 presents a selection of MC compounds suitable for cryogenic applications, along with an estimation of their RCP [51]. This estimation provides an initial framework for determining the required mass and operational frequency to achieve a targeted cooling capacity.

Table 4. Selection of compounds with giant MCE at low temperatures. Their properties are obtained under a magnetic field of 0-5 T

Compound	T _M (K)	$\Delta S_M^{max} \left(\frac{J}{kgK} \right)$	$RCP\left(\frac{J}{kg}\right)$	$\Delta T_{ad}^{max}(K)$	Reference
TmZn	8.4	26.9	269	8.6	[58]
$\mathrm{Er}_{4}\mathrm{PtMg}$	15	17.9	483	4.1	[59]
Er ₄ PdMg	21	15.5	457	3.7	[60]
Er ₄ NiCd	5.9	18.3	595	7.7	[61]
$TmMn_2Si_2 \\$	5.5	22.7	365	12.9	[62]
GdNiBC	15	19.8	474	9.9	[63]
$DyCo_3B_2$	22	12.6	397	11.6	[64]
GdPd	39	20.14	433	-	[65]
GGG	0.38	35	320	10.2	[66]–[69]
ErAl_2	12	45	464	12.8	[70]
HoAl ₂	28	29	445	14.4	[70]

Most of these compounds have been tested in laboratory conditions, moreover, most of their characteristics are derived from testing single crystals in ideal conditions. The actual properties for real-world applications may differ substantially from the data shown in Table 4. For this reason, it is necessary to analyze the properties of the commercially available MC materials and obtain an estimated price per kg range and expected cooling power.

2.2.2.1 Regenerator configurations

After selecting the magnetocaloric material, the subsequent step involves designing the test bed and containers that will house the material. The geometry of the regenerator plays a pivotal role in determining the performance of a magnetic refrigerator. An optimal regenerator geometry must ensure efficient heat transfer between the heat transfer fluid and the porous solid matrix, while also minimizing pressure drop and axial conduction. Among these factors, insufficient heat transfer and viscous dissipation represent two primary sources of energy loss, whereas axial conduction becomes particularly significant in short and bulky regenerators. Figure 12, adapted from [71], illustrates several alternative geometries commonly employed for regenerators. Two widely used regenerator geometries are the packed particle bed and the parallel plate matrix.

Packed particle beds are popular due to their straightforward construction and effective heat transfer performance. However, they are associated with a relatively high pressure drop and substantial viscous dissipation losses, which can compromise overall efficiency. In contrast, parallel plate matrices exhibit significantly lower frictional pressure drops. Nonetheless, achieving a high heat transfer coefficient in these systems poses challenges, primarily due to the difficulties involved in fabricating small channels [72].

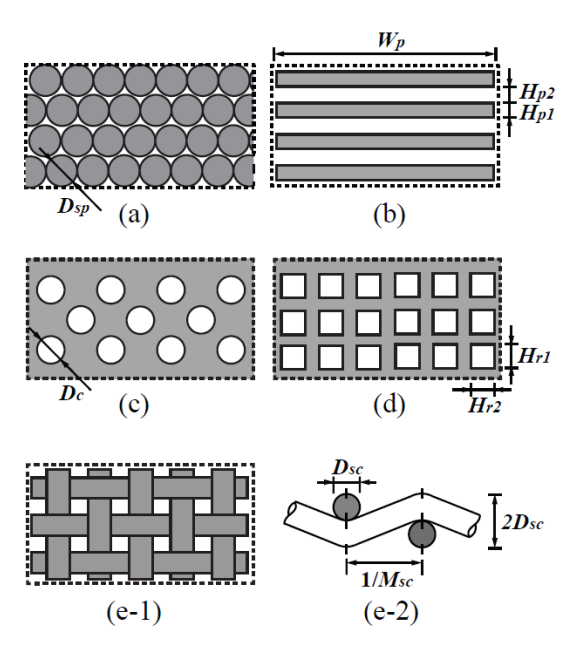


Figure 12. A schematic diagram illustrating various regenerator geometries, including: (a) a packed sphere bed, (b) a parallel plate matrix, (c) a circular micro-channel matrix, (d) a rectangular micro-channel matrix, and (e-1) and (e-2) top and side views of a packed screen bed. In all diagrams except (e-2), the flow direction is perpendicular to the plane of the diagram. The dark areas denote solid refrigerant, which is the magnetocaloric material, while the remaining areas represent the flow channels. Adapted from [71].

2.2.3 Magnetic field sources

The magnetic field is a crucial part of the magnetic refrigerator. There are two potential sources: electromagnets, or permanent magnet assemblies. Among the first, two types are recognized: superconducting or resistive electromagnets. Figure 13 (left) shows a magnetic refrigeration system with a superconducting magnet developed by Numazawa et al [73], and Figure 13 (right) shows a magnetic refrigeration system with a permanent magnet developed by Kiutra company [74].

The design of the magnetic field source is key, since along with the magnetocaloric material constitutes the most expensive components, representing in some cases over 90% of the cost [75]. In [56] a comprehensive review of the different magnetic field sources and their characteristics for MR is found.

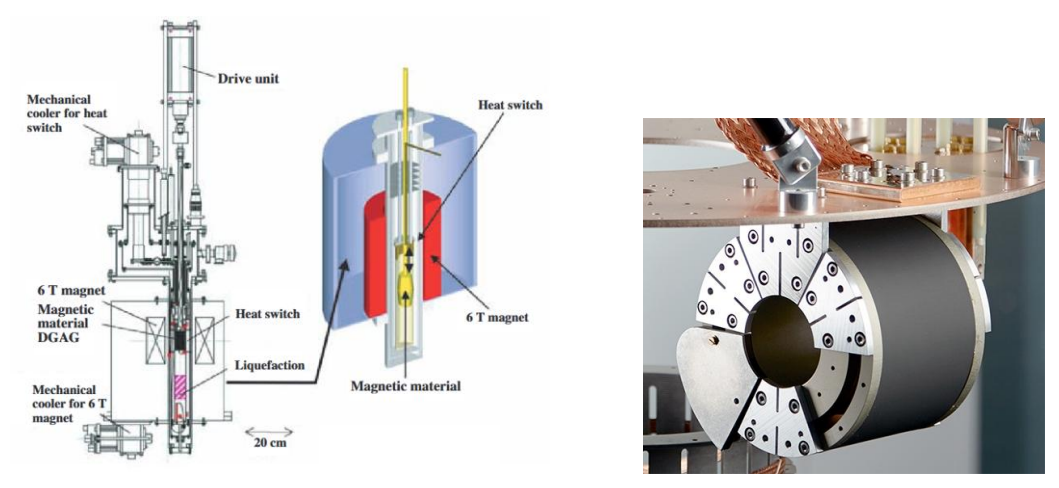


Figure 13. Two types of magnetic field sources: solenoid, a type of electromagnet from Numazawa et al [73] (left) and a Halbach cylinder made of permanent magnets by Kiutra company [74] (right).

Since the magnetic system is one of the key components of a magnetic refrigerator it is usual to define parameters, or figures of merit to compare different configurations.

Bjork et al [76] proposed the following figure of merit for a magnetic field source in magnetic refrigeration:

$$\Lambda_{cool} = \left(\mu_0 H_{high}^{\frac{2}{3}} - \mu_0 H_{low}^{\frac{2}{3}}\right) \frac{V_{field}}{V_{magnet}} P_{field}$$
(2.14)

where $\mu_0 H_{high}^{\frac{2}{3}}$ and $\mu_0 H_{low}^{\frac{2}{3}}$ represent the volume average magnetic fields during the magnetization and demagnetization phase respectively. V_{field} is the volume where the magnetic field is applied, usually the magnetocaloric material, and V_{magnet} is the total magnet volume. This figure of merit is focused on AMR cycles for room temperature applications which typically use permanent magnets. It may have certain limitations to other types of magnet assemblies, like superconducting magnets. Some of the limitations include: a) it does not take into account the work needed to perform a magnetic cycle, and b) does not include external losses like eddy currents.

Other figures of merit are proposed in the literature that maybe generalized to a broader range of applications. Wood and Potter [52] proposed alternative figures of merit for the evaluation and comparison of magnetic refrigerators.

The first metric is the Coefficient of Refrigerant Capacity (CRP), which is defined as the ratio of refrigerant capacity to the positive work of the system, being the positive work, the work done by the magnetic system on the refrigerant.

$$CRP = \frac{Refrigerant\ Capacity}{Positive\ Work} = \frac{\Delta S\Delta\ T_{max}}{V_{M}\int_{0}^{B}M(T_{c},B)dB} \tag{2.15}$$

The relation of the positive work to the total real work of the system is as follows:

$$W_{real} = W_{+} - W_{-} = \Delta S \Delta T - S_{irr} T_{h} - Q_{l} - Q_{f}$$
(2.16)

where W_{-} is the negative work of the system, or the work done by the magnetic refrigerant. The term $S_{irr}T_h$ represents the entropy produced by irreversible processes that must be expelled at the hot source. Q_l , and Q_f are terms associated with heat leaks and viscous dissipation.

Substituting Eq. (2.16) in Eq. (2.15) the CRP for real cycles can be defined as:

$$CRP_{real} = 1 - \frac{W_{-}}{W_{+}} - \frac{S_{irr}T_{h}}{W_{+}} - \frac{Q_{l}}{W_{+}}$$
 (2.17)

A second coefficient is defined in [52] called the Coefficient of Magnet-Refrigerant Performance (CMRP), which relates the refrigerant capacity to the energy of the applied field over the volume of the refrigerant:

$$CMRP = \frac{Refrigerant\ Capacity}{Magnetic\ Energy} = \frac{\Delta S\ T_{max}}{\frac{1}{2u_2} \int_{V} B^2 dV}$$
(2.18)

The combination of both parameters provides a good understanding of the performance of different magnetic refrigerators. Since, although CMRP does not account for the effort to cyclically produce a magnetic field, this effort can be evaluated in CRP_{real} . These parameters will be used in later sections to evaluate the system's performance.

2.2.4 Relevant prototypes: Cryogenic Magnetic Refrigeration

The quest for absolute zero saw its first significant breakthrough in the early 20th century. A pivotal moment occurred on July 9, 1908, when Kamerlingh Onnes achieved helium liquefaction. While this process could reach approximately 1 Kelvin through vapor pressure reduction over liquid helium, it hit a limitation with conventional gas cycles. A significant advancement came in 1926 when William Francis Giauque and Peter Debye independently

conceived magnetic cooling as a method to achieve sub-Kelvin temperatures. Their innovative approach employed gadolinium sulfate, a rare-earth salt that exhibits magnetocaloric properties at temperatures below 1K. Their method enabled Giauque to achieve a remarkable temperature of 0.25 K in 1933.

In 1954, Heer et al. [77] developed the first semi-continuous magnetic refrigerator, achieving temperatures around 0.2 K with low refrigeration power. Subsequent enhancements, including the use of a superconducting solenoid, improved performance, but these early systems were limited to low-power operation below 1 K. In 1966, Van Geuns [78] proposed the first magnetic refrigerator for use above 1 K, introducing a regenerative cycle with stabilized helium gas and a paramagnetic working material to address heat transfer and rising lattice heat capacity.

With the introduction of the active magnetic regeneration cycle in the late 1970s [54], the operating temperature range expanded, leading to developments in the 4.2 K to 20 K range, although most continue using non-regenerative cycles. These advancements were largely focused on the liquefaction of liquid helium and liquid hydrogen.

Before reviewing the main prototypes, we will distinguish between two main types of refrigerators: static and dynamic. In the first group there are no moving parts, and the magnetic field is modified by changing the magnet current. In the dynamic refrigerator type we again distinguish two groups based on the movement of the magnetic field relative to the refrigerant: reciprocating and rotary.

- 1. Reciprocating Magnetic Refrigerators: In these systems, the magnetic field is applied and removed in a linear, back-and-forth motion (reciprocating). The magnet and magnetocaloric material move relative to each other in a straight line, cycling through phases of magnetization (where heat is absorbed) and demagnetization (where heat is released).
- 2. Rotary Magnetic Refrigerators: These use a rotating mechanism to move the magnet relative to the magnetocaloric material. The material or the magnetic field rotates, allowing continuous cycles of magnetization and demagnetization. Rotary designs often allow for smoother and more continuous operation compared to reciprocating systems, which are more cyclical.

One of the seminal contributions to the field was made by Barclay et al. [79], who developed a Carnot-cycle magnetic refrigerator designed to operate in the temperature range of approximately 4 K to 15 K. In this section, the term "Carnot cycle" refers to a thermodynamic cycle comprising two isothermal and two adiabatic processes, as previously described. However, it is important to note that the efficiency of the developed prototypes did not approach the theoretical Carnot limit. In fact, in most cases, the exergy efficiency was below 2%.

The innovative cooling system developed by Barclay et al. employed gadolinium gallium garnet (GGG) as the refrigerant material, which was integrated into a rotating wheel rim configuration. The magnetic field, was generated by superconducting Helmholtz coils capable of producing magnetic fields up to 6 T. Helium gas was utilized as the heat-transfer medium to facilitate thermal exchange. The refrigerator demonstrated significant performance capabilities, achieving a cooling power exceeding one watt across a temperature span of several degrees. However, the system's overall thermodynamic efficiency was suboptimal, reaching only approximately 1% of the theoretical Carnot efficiency. The rotary design of this magnetic refrigerator represented a novel approach to continuous-cycle magnetic cooling. By incorporating the refrigerant material into a rotating wheel, the system allowed for a more efficient and continuous magnetization-demagnetization process. This pioneering work by Barclay et al. laid the foundation for subsequent research in low-temperature magnetic refrigeration and demonstrated the feasibility of achieving practical cooling power in the liquid helium temperature range using magnetocaloric materials. Figure 14 shows Barclay et al. first prototype.

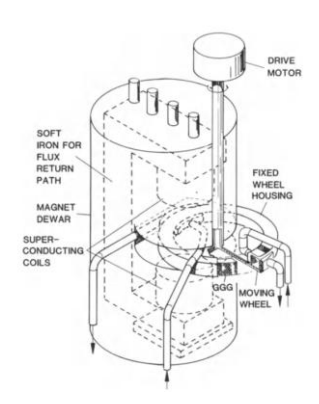


Figure 14. Schematic diagram of the 4-to-15 K magnetic refrigerator developed by Barclay et al [79].

Following the development of the rotating cryomagnetic refrigerator, Barclay et al, made a significant contribution by testing a reciprocating magnetic refrigerator for room temperature applications using gadolinium (Gd) as the magnetocaloric material. This work pioneered the development of magnetic refrigeration technology for ambient temperature applications. However, there is no available information regarding Barclay's further development of this principle for cryogenic applications.

In parallel, research in cryogenic magnetic refrigeration was carried out by Japanese institutions, including universities such as the Tokyo Institute of Technology and the Japan National Institute for Materials Science, often in collaboration with private sector entities like the Toshiba Development Center. These research groups have primarily focused on the liquefaction of cryogens, specifically helium and hydrogen, using Adiabatic Demagnetization Refrigeration (ADR) without regeneration.

One of the early significant developments in this field was a helium liquefier with a liquefaction capacity of approximately 3 W [80], employing a 10 kg gadolinium gallium garnet (GGG) crystal pill as the magnetocaloric material. This system demonstrated notable cooling power; however, its practical applicability was constrained by inefficiencies, particularly losses associated with the superconducting magnet. In recent years, research efforts have expanded to include the development of prototypes for hydrogen liquefaction, exploring the potential of alternative materials such as dysprosium gadolinium aluminum garnet (DGAG) and, more recently, holmium aluminum (HoAl₂). A recent publication by T. Numazawa et al. [81] provides a comprehensive overview of the advancements in magnetic refrigeration technology at cryogenic temperatures, with a particular focus on the potential for hydrogen liquefaction. Figure 15 illustrates the evolution of technology, presenting both the original helium liquefier prototype and the more recent hydrogen liquefier design [82].



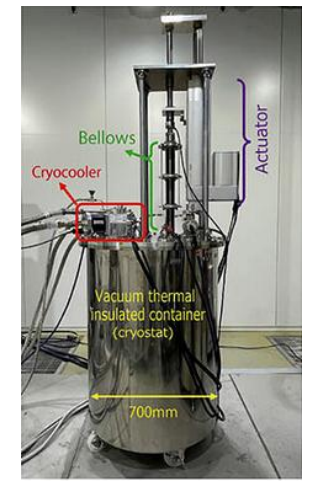


Figure 15. Helium liquefier magnetic refrigerator from Toshiba development center, and Tokyo University group [80] (left), and Hydrogen liquefier (20K) from Japan National Institute for Materials Science [83] (right).

The MIT Cryogenic Engineering Laboratory began its work on cryogenic magnetic refrigeration in the 1980s, culminating in the development of a pioneering prototype based on the AMR cycle in the late 1980s [84]. This prototype operated within the temperature range of 3.79 K to 5.51 K, delivering a cooling power of 0.4 W. These efforts bear similarities to other notable developments targeting sub-4.2 K temperatures, such as those by research groups in Grenoble and Los Alamos [69], [85], which marked some of the earliest applications of the AMR cycle.

Subsequent advancements by the MIT group represent a significant contribution to the temperature range of 4.2 K to 20 K. In his PhD thesis, Nellis et al. [86] introduced an experimental Gifford-McMahon/Magnetic Refrigerator, a hybrid cryocooler that combines the Gifford-McMahon cycle with the magnetic refrigeration cycle to reach temperatures as low as 5.6 K. This prototype employs helium and Gadolinium Gallium Garnet (GGG) as the thermodynamic working substances and incorporates a superconducting magnet capable of generating a magnetic field of 4 T.

Table 5 summarizes the characteristics of the mentioned prototypes in the 4.2-20 K range.

Authors	Year	Cycle	Magnetic source	MCM	Frequency (f)	T. Cooling (T_{cold})	T. Span (ΔT)	Cooling power $(Q_{cooling})$
Barclay et al.	1985	Carnot	SM (6 T)	GGG	<0.1Hz	5 K	6 K	~0.05 W
Japan group	1984	Carnot	SM (5.6 T)	GGG	<0.1Hz	4.2 K	>10 K*	<3 W
Japan group	1986	Carnot	SM (4.5 T)	GGG	0.38 Hz	4.2 K	>10 K*	0.95 W
Japan group	2007	Carnot	SM (6T)	DGAG (HoAl ₂)	0.5 Hz	20 K	-	25.3W
MIT	1000	AAMD	CM (4 T)	000	0.4.11.	2.70 1/	0.17	O 4 W/

Table 5. Magnetic refrigeration prototypes based on GGG operating between 4.2-20 K

2.2.5 General Analysis of Cryogenic Magnetic Refrigeration Technology

GGG

GGG

 $0.1~\mathrm{Hz}$

 $0.1~\mathrm{Hz}$

3.79 K

5.6 K

~2 K

~10 K

0.4 W

0.36 W

Previous prototypes of cryogenic magnetic refrigerators shared several common characteristics:

Magnetocaloric Material (MCM): the majority of the earlier developments relied on a single material, Gadolinium Gallium Garnet (GGG). This choice was primarily driven by limited knowledge and availability of alternative magnetocaloric materials. However, Japanese research groups were among the first to explore alternative materials such as Dysprosium Gallium Aluminum Garnet (DGAG) and, more recently, intermetallic compounds like Holmium Aluminum (HoAl₂). The magnetocaloric material is a critical component of a cryogenic magnetic refrigerator, as it directly influences the design and requirements of other system elements, including the magnetic source.

Magnetic Source: Superconducting magnets have been universally employed in previous prototypes for generating the magnetic field. While they enable the application of very high magnetic fields, they also increase the complexity of the system and introduce additional losses during alternating current (AC) operation. These losses significantly impact on the overall efficiency of the refrigerator.

1988

group MIT

group

AMR

GM/AMR

SM (4 T)

SM (4 T)

Thermodynamic Cycle: Most prototypes have operated using a quasi-Carnot cycle with a low operating frequency, typically around 0.1 Hz. A notable exception is the prototype developed by Nellis, which combines an AMR cycle with a GM cycle. Despite this innovative combination, the operating frequency remains relatively low at 0.1 Hz, especially when compared to modern commercial cryocoolers that typically operate at frequencies ranging from 1 to 3 Hz.

The reason behind these common characteristics resides in the selection of GGG as the MCM. Wood and Potter [52] addressed this issue in 1985. Their paper presents results from mean-field calculations of refrigerant capacity for ferromagnetic, paramagnetic, and antiferromagnetic refrigerants under various operating conditions. They argue that the optimum operating point of an antiferromagnetic material, like GGG, requires a magnetic field ratio to cold source temperature larger than 1, which for a cold source of 4.2 K it equals to a magnetic field of at least 4 T. This magnetic field can only be provided by a superconducting magnet. Figure 16 is a representation of Figure 8 in Wood and Potter [52] article exemplifying this problem, it shows the maximum refrigerant capacity per applied field as function of the applied field to cold source temperature ratio for different refrigerants (ferromagnetic, paramagnetic, and antiferromagnetic). It can be appreciated how ferromagnetic refrigerants can achieve higher refrigerant capacities per applied field at lower ratios of applied field to cold source temperature. The open data points are the results from real prototypes, the triangles from the Japanese group [80] and the squares from the Grenoble group [69].

The paper critiques the focus on using high magnetic fields and antiferromagnetic materials like GGG for low-temperature refrigeration, arguing that this approach may be suboptimal, and suggest that future development of low-temperature magnetic refrigeration should focus on finding and characterizing ferromagnetic refrigerants with appropriate Curie temperatures and developing regenerative magnetic cycles that can take full advantage of optimized ferromagnetic refrigerant cycles in fields below 1 Tesla.

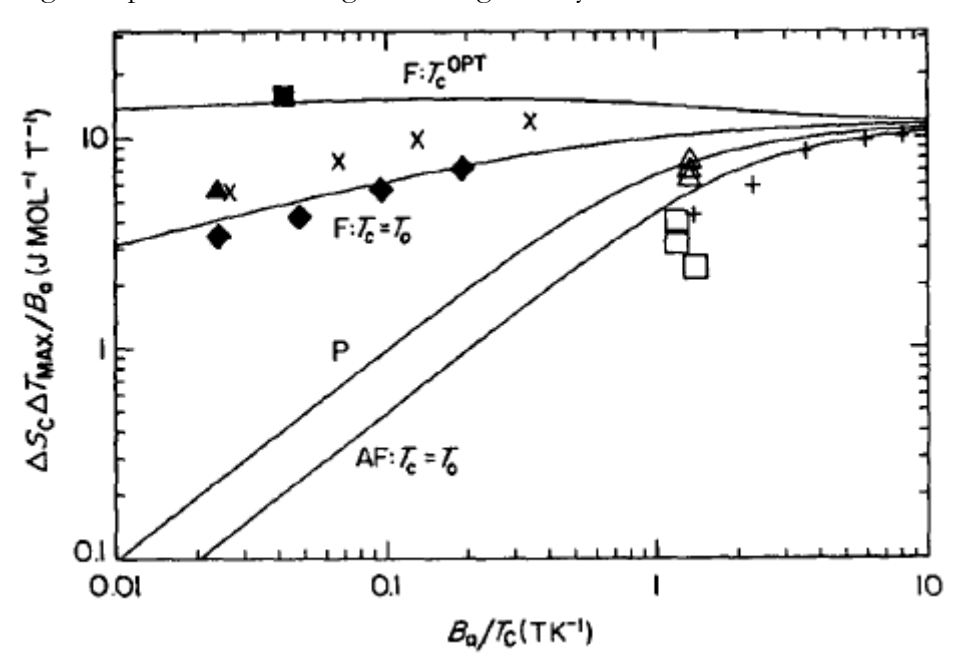


Figure 16. Representation of Figure 8 in Wood and Potter [52]. Solid lines show the calculated maximum allowed molar refrigerant capacity per applied field as a function of the field to temperature ratio. Solid data points are calculated from experimentally determined entropies. \blacksquare , Gd with $T_c = T_c^{OPT}$; \blacktriangle , Gd with $T_c = T_0$; +, GdCl₃ with $T_c = T_0$. Open data points are calculated from experimental refrigerator results using GGG as refrigerant. Δ , $T_c = 4.2~K$ and $B_a = 6.5~T$; \Box , $T_c = 1.8~K$ or 2.1~K and $B_a = 2.5~T$.

The conclusions of Wood and Potter generated considerable discussion within the field. In 1990, Tishin [87] argued that their hypothesis was not entirely accurate, as a significant number of magnetocaloric materials cannot be reliably modeled using mean-field theory. Tishin concluded that paramagnetic and antiferromagnetic materials should not be excluded from cryogenic magnetic refrigeration applications based solely on the Wood and Potter model.

However, while the hypothesis and calculations of Wood and Potter may not be universally applicable, some of their conclusions remain valid. For instance, GGG may not be the optimal refrigerant in the 4.2–20 K range. This is due to its dependence on very high magnetic fields and its limitations when applied to regenerative cycles. Nellis, in his doctoral thesis, reached a similar conclusion, emphasizing the need to focus efforts on identifying and analyzing alternative materials with more suitable regenerative properties.

Summarizing what has been discussed. The experience from previous findings underscores:

- The importance of exploring alternative refrigerants with characteristics that allow for efficient regenerative cycles and, ideally, require lower magnetic fields.
- Reducing field requirements can simplify magnet design and lower costs, potentially
 enabling the use of permanent magnets. Nevertheless, superconducting magnets
 cannot be disregarded, especially given the industrialization of high-temperature
 superconductors.
- There is a clear need to optimize refrigeration cycles and improve heat transfer performance. Exploring and combining alternative refrigeration cycles could pave the way for increasing the operating frequency of magnetic cycles to levels comparable to GM cryocoolers and room-temperature AMRs refrigerators.

The selection of appropriate magnetocaloric materials is a crucial step in overcoming existing limitations. The following subsection provides a qualitative analysis of the process used in this work to select two magnetocaloric materials. These materials are first employed in the numerical analysis presented in the subsequent section and afterward utilized in the development of a technology demonstrator, as described in the next chapters.

2.2.5.1 Preselection of magnetocaloric materials

With the established criteria in Section 2.2.2 and based on the previous discussion, two magnetocaloric materials have been preselected: ErAl₂ and GGG.

GGG is the straightforward choice, making it a natural choice as a baseline for comparison and a reliable option for constructing demonstrators. However, as previously discussed, its main limitation is that it is an antiferromagnet with a Néel temperature around 0.38 K, so it will be underutilized in most applications in the range of 4.2 to 20 K.

On the other hand, a REAl₂ compound such as ErAl₂ was selected. The selection process was tedious since there is limited information on the development of cryogenic magnetic refrigerators based on alternative materials to GGG. The main reason for this selection was the higher Curie temperature, around 12 K, its high refrigerant capacity in the 4.2-20 K range, and the possibility of acquiring high quality samples from a reliable supplier at a reasonable price.

To analyze the potential and the difference between GGG and ErAl₂, a qualitative analysis of the RC of both materials will be done. The first step is the determination of the magnetocaloric properties of each material. Although the derivation of their properties will be addressed in a later section, Figure 17 shows an advance of the entropy change of each of material.

We will analyze the potential of achieving 1 W of cooling power at 5 K with 1 kg. of both materials, with the following assumptions or idealizations: it is possible to operate at 1 Hz, 0 T is the low field, and 20 K will be used as the hot source.

From these assumptions it is straightforward to derive that an entropy change of 1 J/kg*K is needed to achieve 1 W of cooling power.

A horizontal line at 1 J/kg·K is traced in Figure 17, and the intersection with the vertical line at the cold source temperature yields the magnetic field needed to achieve the desire entropy change. This point is marked with a 1 in Figure 17. The magnetic field needed for GGG and ErAl₂ is 0.5 T and 0.7 T, respectively.

The next step is to close the cycle and reject heat to the hot source. For that purpose, the horizontal line is extended to the right. Having reached the temperature of 20 K, the following is observed:

- The entropy change of GGG decreases with increasing temperature. And since to fulfill the second law, which requires that $\Delta S_c \leq \Delta S_h$, the magnetic field needs to be increased to a minimum of 2 T.
- The entropy change of ErAl₂ increases first until its Curie Temperature, when it begins to decrease. However, at 20 K and 1 T the entropy change is still >6 J/kg·K, so the second law is still fulfilled and there is no need of increasing the magnetic field, in fact there is still a wide temperature margin.

The intersection of the horizontal line with the vertical line established by the hot source temperature of 20 K is marked with a 2. Two additional points are added at 0 T, 3 and 4. The process 3-2-1-4 describes a magnetic Carnot cycle. The process is difficult to implement in a real refrigerator, but helps in establishing the thermodynamic limits of each magnetocaloric material.

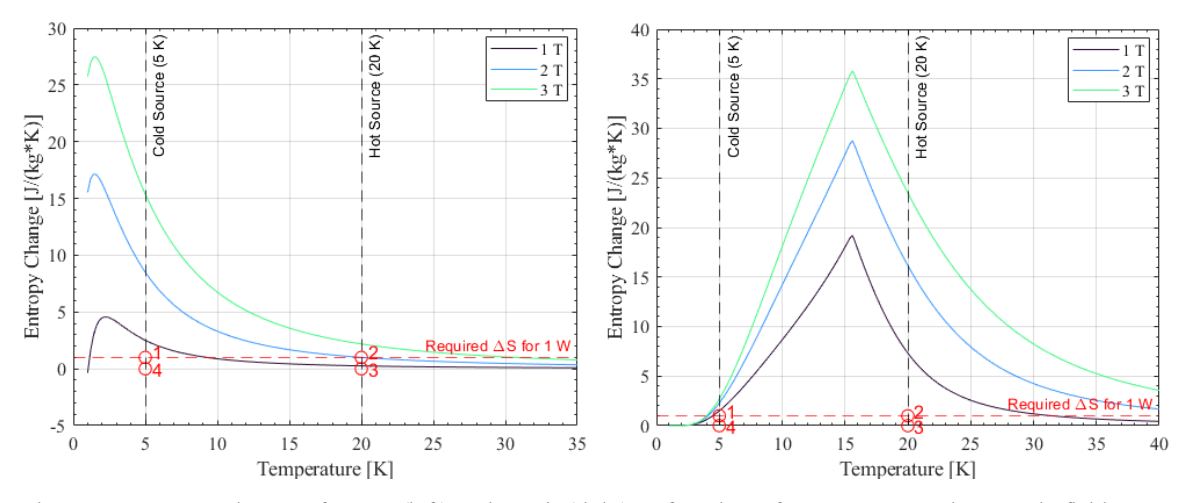


Figure 17. Entropy change of GGG (left) and ErAl₂ (right) as function of temperature and magnetic field.

This simple example describes what was discussed in the previous section, and highlights one of the conclusions of Wood and Potter: GGG properties limited their application above 4.2 K, as it requires high magnetic fields and has limited regeneration capabilities. On the other hand, the example has demonstrated the preliminary potential of $ErAl_2$ as a magnetic refrigerant.

Having selected two magnetocaloric materials, the evaluation of their potential requires accurate models to evaluate and predict the performance of various refrigerator configurations. The following section focuses on the development of a one-dimensional numerical model tailored for cryogenic applications. This model provides a tool for assessing and comparing the characteristics of different refrigerator designs.

Table 6 provides a summary of the main characteristics of each material based on the criteria established in previous sections.

Table 6. Summary of properties of selected magnetocaloric materials: ErAl₂ and GGG

	\mathbf{ErAl}_2	GGG	
Transition Temperature T _M (K)	12 K	0.38 K	
$RC\left(\frac{J}{kg}\right)$ (0-1T & 5-20K)	>25 J/kg	<1 J/kg	
Temperature Span: $\Delta T_{ad}^{max}(K)$	12.8 K	0.38 K	
Near-Zero hysteresis: $M = f(H, H)$	Both materials have second order transitions therefore hysteresis should be minimal		
Thermal Conductivity	Shown in Figure 23, GGG thermal conductivity is almost 50 times bigger than $\rm ErAl_2$		
Manufacturing properties	NA	Similar to glass [88]	
Electrical resistivity	No information reported in the literature		
Corrosion	NA	NA	
Price	4-5 k€/kg	6-7 k€/kg	

2.3 1D numerical model

In magnetic refrigeration modeling, one-dimensional (1D) models are commonly employed due to their computational efficiency, which allows for the exploration and optimization of various system parameters. For room-temperature applications, numerous 1D models have been developed [89]. These often use incompressible fluids, such as water, as the working fluid. This simplifies the mass conservation equation and reduces the momentum equation to a balance between pressure gradients and drag forces. Consequently, these models primarily focus on solving time-dependent thermal energy equations for both the fluid and solid components.

At cryogenic temperatures, however, the modeling approach becomes more complex due to the use of compressible gases like helium as the working fluid. Helium's compressibility results in significant density variations at cryogenic temperatures, particularly below 20 K. As a result, accurate modeling requires solving the full set of nonlinear compressible equations governing fluid motion and energy transfer within the porous regenerator structure.

The literature includes several prior attempts to model these systems. Some of the previously developed 1D models [90], [91] fail to fully account for helium compressibility, while 2D models have also been developed for hydrogen liquefaction although they are computationally intensive [92]. The most relevant foundational work is that of Nellis [88], which this study builds upon, and a recent contribution by Diamantopoulos et al. [93], which introduces an alternative approach for system resolution.

Developing such models remains particularly challenging, as highlighted by Diamantopoulos et al. [93], due to the limitations of certain numerical methodologies in handling these computations. This study adopts a similar approach to that of Nellis [88], incorporating certain modifications. Specifically, this work introduces additional considerations, including the influence of the housing wall, which will be elaborated upon in subsequent sections.

2.3.1 Governing Equations

For the developed 1D model the following assumptions are established:

- Magnetocaloric effect is a reversible process, and no hysteresis effect is accounted for in the model.

- The applied magnetic field (in the empty air gap of the magnetic field source) is equal to the internal magnetic field in the magnetocaloric material.
- The solid within the regenerator is uniformly distributed with no edge effects. No flow leakage or flow bypassing occurs. Any dead volume (the volume between the entry/exit of the AMR and valve/flow divider) is neglected.
- The system is adiabatic and no heat losses to the ambient are considered.

Having established the main assumptions, we continue to describe the physical system model. The general laws that describe the undergoing physics are: first, the continuity equation which describes the conservation of mass of the working fluid within the regenerator, which is given by:

$$\frac{d(\varepsilon \rho_f)}{dt} + \nabla(\rho_f u) = 0 \tag{2.19}$$

where ρ_f is the density of the fluid, ε is the porosity, and u is the superficial or Darcy fluid velocity, which differs from the interstitial or mean pore velocity defined as $u_p = u/\varepsilon$ [94]. The porosity, ε , is computed as follows:

$$\varepsilon = \frac{Void\ Volume}{Total\ Volume} = \frac{V_v}{V_T} \tag{2.20}$$

Second, the conservation of the fluid's momentum, in which viscous stresses and the convective terms are omitted, is given by:

$$\frac{1}{\varepsilon} \frac{d(\rho_f u)}{dt} = \nabla p - F_d \tag{2.21}$$

 F_d is the drag force exerted by the solid porous medium on the fluid. Third, the energy balance equation for a compressible fluid is given by:

$$\varepsilon \frac{d(\rho_f E)}{dt} + \nabla(u\rho_f h) + \frac{1}{\varepsilon^2} \nabla\left(\frac{u\rho_f u^2}{2}\right)$$

$$= \nabla(k_f^{eff} \nabla T_f) - h_m a_m (T_f - T_m) - h_w a_w (T_f - T_w)$$
(2.22)

where E is the total energy of the fluid, i.e., the sum of the internal and kinetic energy, h is the enthalpy of the fluid, k_f is the effective thermal conductivity of the fluid due to axial dispersion, h_m and h_w are the heat transfer coefficient between fluid-magnetocaloric and fluid-wall respectively, a_m and a_w are the specific surface area between fluid-magnetocaloric and fluid-wall, and T_f , T_m , T_w are the temperatures of the fluid, magnetocaloric and wall, respectively.

Fourth is the thermal equation for the magnetocaloric material:

$$(1 - \varepsilon)\rho_m \left(c_H \frac{\partial T_m}{\partial t} + T_s \left(\frac{\partial s_m}{\partial \mu H} \right)_{T_s} \frac{\partial \mu H}{\partial t} \right) = \nabla \cdot \left(k_m^{eff} \nabla T_m \right) + h_c a_m \left(T_f - T_m \right)$$
(2.23)

where ρ_m is the density of the material, c_H is the specific heat capacity, s_m is the specific entropy, $k_m^{\rm eff}$ is the axial effective thermal conductivity of the solid and μH is the applied magnetic field.

Finally, the thermal equation for the wall is:

$$\rho_w \left(c_{H,W} \frac{\partial T_w}{\partial t} \right) = \nabla \cdot (k_w \nabla T_w) + h_w a_w \left(T_f - T_w \right) \tag{2.24}$$

where ρ_w is the density of the wall, $c_{H,w}$ is the specific heat capacity of the wall, k_w is the axial thermal conductivity.

Figure 18 presents a schematic representation of the finite difference scheme for the one-dimensional model. It illustrates the spatial discretization of the system, where each division corresponds to a computational cell representing a segment of the fluid,

magnetocaloric material, or wall. The primary dependent variables for each subsystem are displayed on the right side of the schematic. The arrows within the schematic illustrate the conduction and convection processes, which establish spatial and temporal relationships among the subsystems.

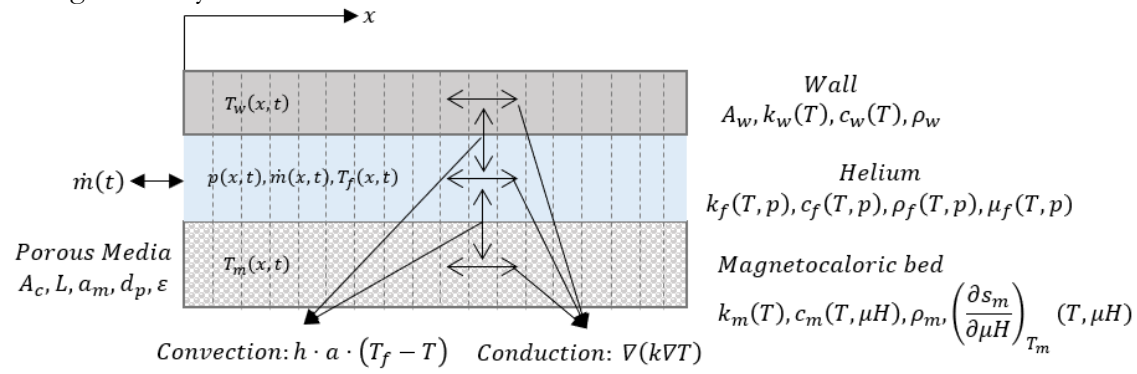


Figure 18. Conceptual drawing of a 1D AMR model showing the important parameters.

2.3.2 Compressible flow model

To resolve the model, Eqs. 2.19–2.24 are expanded, and the velocity (u) is substituted by the mass flow rate (\dot{m}) using the relation:

$$\dot{m} = \rho_f u A \tag{2.25}$$

where ρ_f is the fluid density, and A is the cross-sectional area. This substitution transforms the equations to be expressed in terms of mass flow rate instead of velocity.

Additionally, the density's partial derivative term in the mass conservation equation is expanded using the chain rule. The density (ρ_f) is treated as a function of temperature (T_f) and pressure (p), and its time derivative is expressed as:

$$\frac{d\rho_f}{dt} = \frac{d\rho_f}{dp}\frac{dp}{dt} + \frac{d\rho_f}{dT}\frac{dT}{dt}$$
 (2.26)

This modification yields a system of five equations with five variables: pressure (p), mass flow rate (m), fluid temperature (T_f) , magnetocaloric material temperature (T_m) , and wall temperature (T_w) . These equations form a coupled system governing the dynamics of the magnetic refrigeration process, accounting for compressible fluid flow, heat transfer, and magnetocaloric effects:

$$\frac{d\rho_f}{dt} + \frac{1}{\varepsilon AL} \frac{d\dot{m}}{d\bar{x}} = \left(\frac{d\rho_f}{dp} \frac{dp}{dt} + \frac{d\rho_f}{dT} \frac{dT}{dt}\right) + \frac{1}{\varepsilon AL} \frac{d\dot{m}}{d\bar{x}} = 0 \tag{2.27}$$

$$\frac{1}{\varepsilon A}\frac{d\dot{m}}{dt} = \frac{1}{L}\frac{dp}{d\bar{x}} - F_d \tag{2.28}$$

$$m_{f}c_{f}\frac{dT}{dt} + \dot{m}c_{p}\frac{dT}{d\bar{x}} = \frac{A_{f}k_{f}^{eff}}{L}\frac{d^{2}T}{d\bar{x}^{2}} - h_{c}a_{m}(T_{f} - T_{m}) - h_{w}a_{w}(T_{f} - T_{w}) + \frac{dp}{d\bar{x}}\frac{\dot{m}}{\rho_{f}}$$
(2.29)

$$m_m \left(c_H \frac{\partial T_m}{\partial t} \right) = \frac{A_m k_m^{eff}}{L} \frac{d^2 T}{d\bar{x}^2} + h_c a_m \left(T_f - T_m \right) - m_s T_m \left(\frac{\partial s_m}{\partial \mu H} \right)_{T_m} \frac{\partial \mu H}{\partial t}$$
 (2.30)

$$m_w c_w \frac{\partial T_w}{\partial t} = \frac{A_w k_w^{eff}}{L} \frac{d^2 T_w}{d\bar{x}^2} + h_w a_w (T_f - T_w)$$
(2.31)

Where the dimensionless variable $\bar{x} = \frac{x}{l}$ is used.

2.3.2.1 Boundary conditions

For the resolution of the numerical model the following boundary conditions are applied:

- Fluid temperatures: Mixed boundary conditions that alternate between Dirichlet and Neumann boundary conditions are applied to the left and right side of the regenerator.

$$\dot{m}_f > 0 \rightarrow T_f(x=0,t) = T_{hot}; \frac{\partial T_{cold}}{\partial x}(x=L) = 0$$
 (2.32)

$$\dot{m}_f < 0 \rightarrow T_f(x = L, t) = T_{cold}; \frac{\partial T_{hot}}{\partial x}(x = 0) = 0$$
 (2.33)

 Magnetocaloric temperature: Neumann boundary conditions are applied to the matrix.

$$\frac{\partial T_m}{\partial x}(x=0) = \frac{\partial T_m}{\partial x}(x=L) = 0 \tag{2.34}$$

- Wall temperature: Neumann boundary conditions are applied to the wall:

$$\frac{\partial T_w}{\partial x}(x=0) = \frac{\partial T_w}{\partial x}(x=L) = 0 \tag{2.35}$$

Different approaches can be considered depending on the real conditions of the operating cycle for the \dot{m}_f and p_f boundary conditions.

For example, applying a traditional AMR Brayton cycle, the boundary conditions for pressure and mass flow are:

 Pressure: A Dirichlet boundary conditions is applied to the left side and a Neumann boundary condition to the right:

$$p_f(x = 0, t) = p_{ref}; \frac{\partial p_f}{\partial x}(x = L) = 0;$$
 (2.36)

- Mass flow rate: Neumann boundary condition is applied to the left side of the regenerator and a Dirichlet boundary condition to the right:

$$\frac{\partial \dot{m}_f}{\partial x}(x=0) = 0; \dot{m}_f(x=L,t) = \dot{m}_{ref}(t); \tag{2.37}$$

Other combinations of boundary conditions could be valid for the same AMR. Furthermore, other cycles can be analyzed by varying the boundary and operating conditions, this not only includes Carnot cycles, or other types of AMR cycles, like Ericsson's, but also a combination of gas and magnetic cycles like the Stirling-Magnetic cycle proposed in [86].

The equipment outside of the bed, including the pumps, heat exchangers, and magnetic source, are not explicitly modeled. Rather, their effect on the bed is felt through an imposed time variation of the mass flow rate, pressure and the variation of the magnetic field in time and space. The interface between these boundary conditions for this regenerator model and these auxiliary pieces of equipment is handled by a system-level model that interacts with this component level model.

2.3.2.2 Numerical methodology

The system of PDEs is solved in MATLAB with pdepe and pde1m solvers. Both are based on the work of Skeel and Berzin [95]. The first solver, pdepe, is the standard MATLAB solver for PDEs, while the second solver was developed by Bill Greene [96] and provides relevant upgrades over pdepe. The most relevant for this application is that it allows for spatial vectorization during resolution which significantly improves computation time and allows for non-diagonal "c" matrices.

Both programs are designed to handle systems of PDEs in one spatial dimension and time, using a method of lines (MOL) approach for the numerical solution. This method is applied to systems of PDEs in the form:

$$c\left(x,t,u,\frac{\partial u}{\partial x}\right)\frac{\partial u}{\partial t} = x^{-m}\frac{\partial}{\partial x}\left(x^{m}f\left(x,t,u,\frac{\partial u}{\partial x}\right)\right) + s\left(x,t,u,\frac{\partial u}{\partial x}\right)$$
(2.38)

Where u(x,t) represents the solution vector, containing the dependent variables (pressure, mass flow and the temperatures), $c\left(x,t,u,\frac{\partial u}{\partial x}\right)$ is the time-dependent coefficient matrix, $f\left(x,t,u,\frac{\partial u}{\partial x}\right)$ denotes the flux vector, $s\left(x,t,u,\frac{\partial u}{\partial x}\right)$ denotes the source terms, and m is a geometric parameter indicating the symmetry of the problem, which in this case takes the value of 0.

The method of lines first discretizes the spatial variable while leaving the time derivative continuous. The spatial derivatives are approximated using finite-difference schemes. In that way the PDE is converted into an ODE at each point of the grid.

Once the system of PDEs has been discretized in space, it employs an ODE solver for the time integration of the resulting system of ODEs. The ODE system can be written as:

$$M\frac{dU}{dt} = F(U,t) \tag{2.39}$$

where U is the vector of all spatially discretized solution components, M is the mass matrix, and F(U,t) represents the fluxes and source terms in the discretized spatial form.

The time-stepping methods employed in both solvers are based on the ODE15s solver, which is particularly well-suited for stiff problems. This solver utilizes a variable-step, variable-order (VSVO) approach, dynamically adjusting both the step size and order to efficiently manage stiffness. The solver relies on Backward Differentiation Formulas (BDFs), a class of implicit methods renowned for their robust stability properties. The use of such a VSVO solver significantly reduces simulation time; however, careful attention must be paid to the definition of tolerances. Excessively small-time steps can introduce numerical instabilities, as discussed in Section 2.5.

2.3.3 Experimental correlations: Heat transfer, Pressure drop and Thermal Conductivity

This section describes the methodology employed to model heat transfer, pressure drop, and the effective thermal conductivity in the numerical framework. Detailed correlations utilized in this study are provided in the Appendix.

The transport and heat transfer phenomena are significantly influenced by fluid flow characteristics, necessitating the determination of the Reynolds number. For that, it is first necessary to define the hydraulic diameter, which from the general definition one can derive the following relation:

$$d_h = \frac{4V(Wetted\ Volume)}{A(Wetted\ Area)} = \frac{2\varepsilon}{3(1-\varepsilon)}d_p \tag{2.40}$$

However, Ergun [97] and Achenbach [94] omitted the 2/3 term in their correlations. With the hydraulic diameter defined, the Reynolds number can be expressed as:

$$Re_h = \frac{u_p d_h \rho_f}{u_f} = \frac{1}{1 - \varepsilon} Re_{dp} \tag{2.41}$$

Where Re_{dp} is defined as:

$$Re_{dp} = \frac{ud_p\rho_f}{\mu_f} = \frac{d_p \cdot \dot{m}_f}{A \cdot \mu_f} \tag{2.42}$$

where d_p is the particle diameter, and μ_f represents the dynamics viscosity of the fluid, A denotes the free flow area.

The heat transfer between the fluid and the magnetocaloric is modeled with a heat transfer coefficient (h_c), which can be derived from empirical Nusselt correlations from Achenbach [94]:

$$Nu_h = \frac{d_h \cdot h_c}{k_f} = \frac{\varepsilon}{1 - \varepsilon} Nu_{dp} \tag{2.43}$$

Where Nu_{dp} is defined as:

$$Nu_{dp} = \frac{d_p \cdot h_c}{k_f} \tag{2.44}$$

Heat transfer occurs across the entire surface area of the particle. The specific surface area (a_m) available for heat transfer is defined as follows [88]:

$$a_m = \frac{6}{d_n} \tag{2.45}$$

The heat transfer between the fluid and the wall is modelled in an analogous manner.

The parameter F_d in Eq. (2.21 & 2.28) is the drag force exerted by the magnetocaloric material in the fluid. For the purposes of this study F_d is computed under the Darcy-Forcheimer relation for a packed bed filled with spheres of uniform diameter:

$$F_d = \frac{\mu}{K}u + \frac{c_f \rho_f}{\sqrt{K}} |u|u \tag{2.46}$$

The fluid mixes along the direction of the flow due to the dispersion caused by the packed bed. This term can be treated as an axial conduction term. The total effective conductivity is a sum of the static thermal conductivity, and the axial conductivity caused by the dispersion. According to Kaviani [98], the total effective conductivity can be expressed as:

$$k_{eff} = k_{static} + k_f D^d (2.47)$$

2.4 Model verification and analysis

2.4.1 Material Properties

2.4.1.1 Fluid Properties

The main fluid used in this work is Helium-4, although Nitrogen properties are also utilized for the development of the test stand that will be presented in the next section.

The properties of Helium-4 at low temperature are highly nonideal. Representing these properties realistically is critical to the accuracy of the model. The properties of Helium-4 are obtained through bicubic spline interpolation on tables of properties in the dimensions of internal energy and pressure. This is in contrast to linear interpolation, where the second derivative is undefined at each abscissa and zero within each interval. Thermodynamically, this feature is very important. The higher order derivatives of the thermodynamic properties contain the second law consistency. In particular, the higher order derivatives guarantee the concavity of the fundamental relation with respect to energy and the convexity of the energy relation with respect to entropy. When numerical models based on thermodynamic principles employ a set of properties which is not self- consistent, they may converge to the point of greatest second law inconsistency.

These tables are constructed using a MATLAB code using the database provided by the NIST [99]. The helium property tables constructed in this fashion include: density, enthalpy, entropy, viscosity, Prandlt number, thermal conductivity and Joule Thomson

coefficient. Any other properties or property derivatives which are required can be obtained from this set of properties or their derivatives.

The generated properties are constructed to be compatible with MATLAB SIMSCAPE. These properties can extend from a two-phase mixture to a subcooled region to the supercritical region of the fluid.

In all cases the properties are defined by a normalized internal energy and the pressure value. In a subcooled liquid, the normalized internal energy definition is

$$\bar{u} = \frac{u - u_{min}}{u_{sar}^{L}(p) - u_{min}} - 1, \ u_{min} \le u < u_{sar}^{L}(p)$$
(2.48)

Where \bar{u} is the normalized internal energy of the fluid, u is the specific internal energy of the fluid, u_{\min} is the lowest specific internal energy allowed in the two-phase fluid network, u^L sat is the specific internal energy of the liquid phase at saturation.

In a superheated vapor, the normalized internal energy definition is:

$$\bar{u} = \frac{u - u_{max}}{u_{max} - u_{sat}^{V}(p)} + 2, \ u_{sar}^{V}(p) < u \le u_{max}$$
 (2.49)

Where u_{max} is the highest specific internal energy allowed in the two-phase fluid network, u^{V} sat is the specific internal energy of the vapor phase at saturation.

In a two-phase mixture, the normalized internal energy definition is

$$\bar{u} = \frac{u - u_{sat}^{L}(p)}{u_{sat}^{V}(p) - u_{sat}^{L}(p)}, \ u_{sat}^{L}(p) \le u \le u_{sat}^{V}(p)$$
(2.50)

These expressions correspond to a normalized internal energy that is at all pressures -1 at the minimum valid specific internal energy, 0 at the liquid saturation boundary, +1 at the vapor saturation boundary, and +2 at the maximum valid specific internal energy. For more information about the construction of the fluid database refer to [100].

2.4.1.2 Magnetocaloric Material Properties

The properties needed to define the magnetocaloric material behavior in a magnetic refrigeration stage are specific heat, entropy, and thermal conductivity, which are dependent on temperature and magnetic field. These properties can be reduced, to entropy and thermal conductivity, as the specific heat can be expressed as a function of temperature and entropy:

$$c_P = T \frac{dS}{dT} \tag{2.51}$$

In fact, adopting this expression, and having consistent datasets is essential to ensure a consistent solution. In the next subsections the adopted models for the computation of the magnetothermal properties of GGG and ErAl₂ will be revised.

2.4.1.2.1 Gadolinium Gallium Garnet (GGG)

The procedure reported by Murphy [101] has been adopted, and the reported FORTRAN code has been adapted to Matlab. The model adopts the method proposed by Price and Mastrup [102]. As this material has been widely covered and used in previous prototypes the adopted model will be quickly overview.

The Price and Mastrup model construct the magnetothermodynamic Gibbs function as the sum of electronic and lattice components. The electronic contribution is derived directly from the electronic partition function based on the crystal energy level structure. This structure accounts for: Energy levels resulting from crystal field splitting, Zeeman splitting effects in applied magnetic fields.

For the lattice contribution, the model uses the small compressibility assumption for solids to approximate the Gibbs free lattice energy using the Helmholtz free lattice energy.

It represents the lattice heat capacity using a variable Debye temperature form of the low-temperature Debye integral approximation. The model employs a quadratic temperature dependence for the Debye temperature, derived from zero-field heat capacity data.

For a comprehensive review of the methodology refer to [101] and [102].

The resulting entropy of GGG from this method is shown in Figure 19. The model has already been validated against experimental data from their own measurements. In this case, in Figure 19, the model data is compared against the experimental data from another source [67]. The model fits very well, although there are certain discrepancies in the high fields and high temperature region.

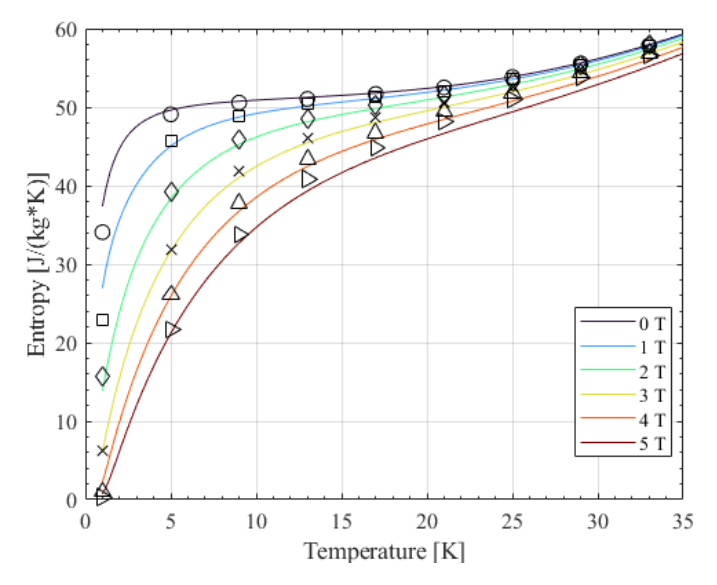


Figure 19. Entropy of GGG as function of temperature and magnetic field; in solid lines the results from the theoretical model, and the markers represent experimental data from [66]–[69].

Figure 20 shows the derived properties of GGG as function of temperature and magnetic field: the entropy change, and specific heat.

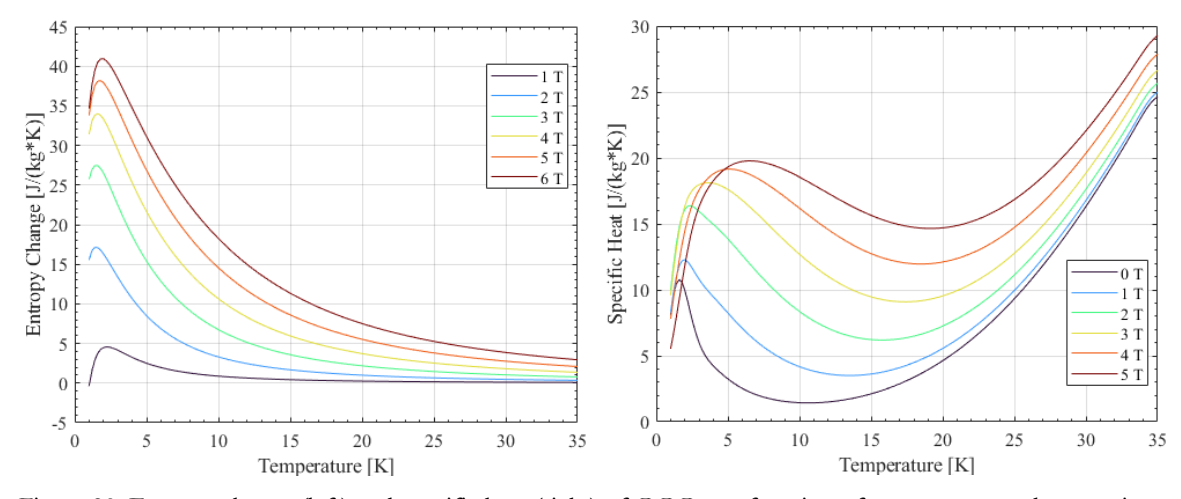


Figure 20. Entropy change (left) and specific heat (right) of GGG as a function of temperature and magnetic field.

2.4.1.2.2 Erbium Aluminum II (ErAl₂)

The theoretical model for computing the magnetothermodynamic properties of ErAl₂ is adopted from Oliveira et al [103]. Since ErAl₂ has not been adopted in any prototype, a more thorough review of the procedure is given in Appendix 1. For a detailed derivation refer to the original source.

The entropy of ErAl₂ obtained with the model for the easy direction <1,1,1> is shown in Figure 21. In the present study an average entropy of the three crystallographic directions: <1,1,1>, <1,1,0>, and <1,0,0> was used for the numerical model. It is noteworthy to highlight that the magnetic field represented in the following figures is the externally applied magnetic field.

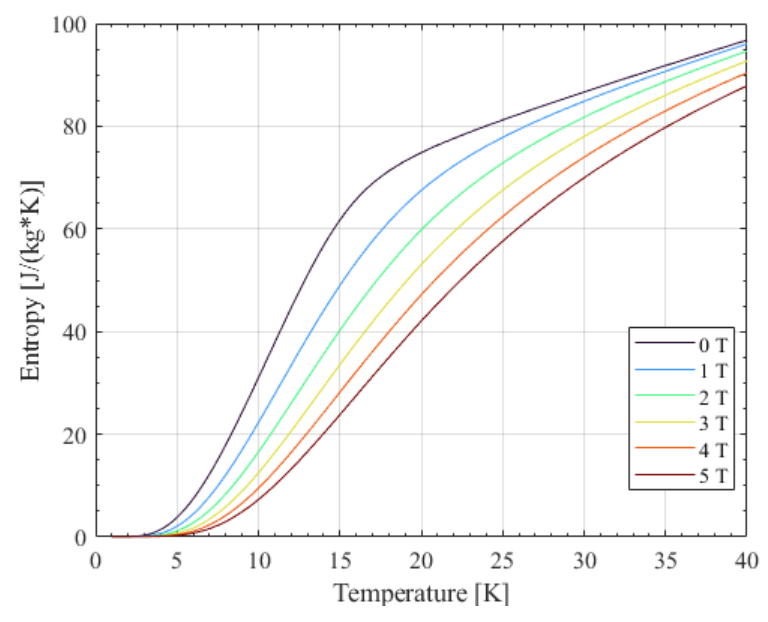


Figure 21. Entropy of ErAl₂ derived from the numerical model.

In this case the specific heat is compared against experimental measure data from a different source in the literature [104], maintaining the variables used in the experiments. The data from [104] differs from the data used in Oliveira et al [103], which adjusts to their model predicted data. Figure 22 shows the model and experimental results comparison for the specific heat (left), and the resulting entropy change (right). The model behaves reasonably well for values below 10 K, but certain discrepancies arise near the Curie Temperature. Discrepancies among experimental data has already been reported in [104], [105] and are evident here between the data from Oliveira et al [103] and Schelp et al [104]. There are alternative methods for ErAl₂ properties computation that appear to derive more accurate properties, which may adjust better to experimental measurements: Michalsky et al [106] reported the potential use of the ATOMIC MATTERS MFA software for intermetallic compounds like ErAl₂. However, it was not used in this study.

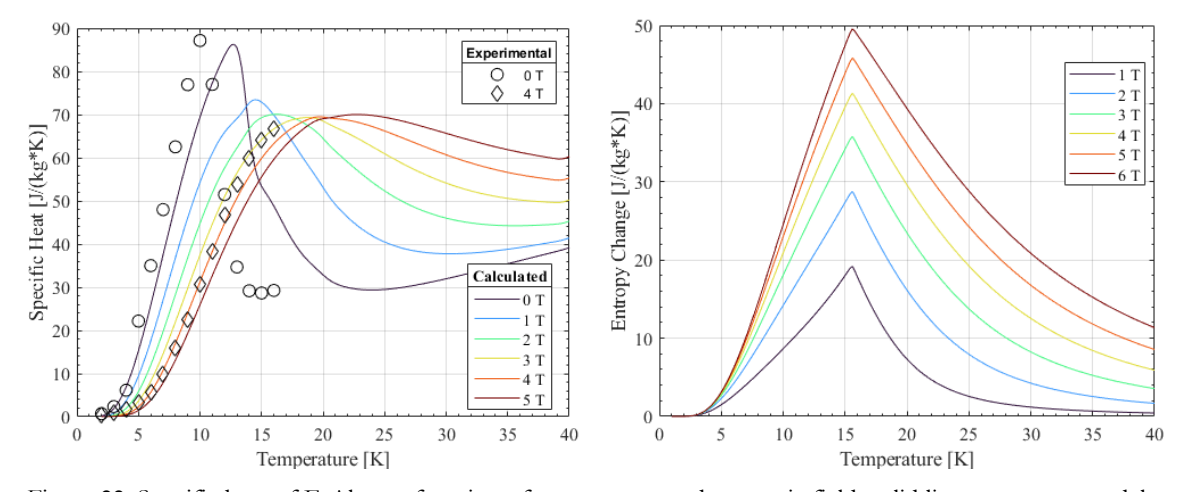


Figure 22. Specific heat of ErAl₂ as a function of temperature and magnetic field, solid lines represent model results, while markers represent data obtained from the literature [104] (left). Entropy change as function of temperature and magnetic field (right).

For the thermal conductivity of both materials, GGG and ErAl₂, only its temperature dependence has been used as there is limited information in the literature about their magnetic field dependence.

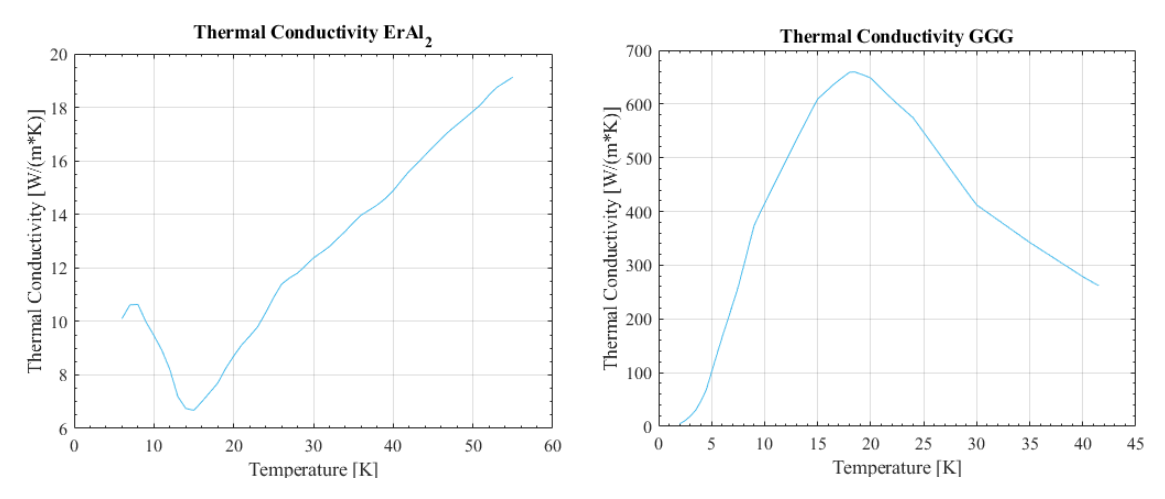


Figure 23. Thermal conductivity of ErAl₂ (left) GGG (right) as a function of temperature.

2.4.1.3 Other materials

Other materials used in this study include OFHC copper (C10200) and stainless steel 316 (S31600). Their cryogenics properties are derived from the NIST database [107].

2.4.2 Cryomagnetic refrigerator

2.4.2.1 Main Parameters

The potential of the AMR cycle in the cryogenic space is explored with the resolution of the proposed numerical methodology by applying the necessary pressure, mass flow and magnetic field conditions to perform an AMR Brayton cycle. Table 7 shows the main operating conditions of the analysed cycle. Other cycles could be applied using the same methodology and solver by varying the operating conditions.

Table 7. Operating conditions of the modelled AMR-Brayton cycle

Fluid profile		
Cycle	AMR Brayton	
T_{hot}	20 K	
$T_{ m cold}$	10 K	
Nominal Pressure	15 bar	
Mass flow range	$\pm 0.5 \text{ g/s}$	
$ au_f$	2.5 s	
Magnetic field profile		
Max. magnetic field	1 T	
Average ramp-rate	0.8 T/s	
$ au_m$	2.5 s	

Figure 24 illustrates the magnetic and fluid profiles corresponding to the applied cycle. The magnetic field is assumed to remain constant along the length of the regenerator, varying only with time. Notably, both profiles have been smoothed to eliminate

discontinuities in their derivatives, which could otherwise lead to convergence issues during numerical resolution.

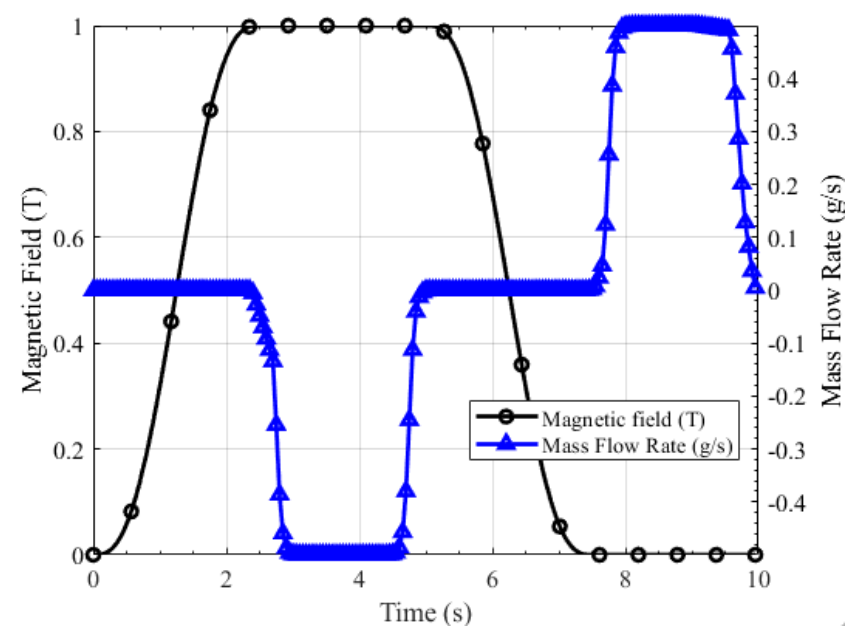


Figure 24. Magnetic field and pressure flow profile for the applied Brayton cycle.

Table 8 summarizes the main characteristic and geometry parameters of the packed bed.

Table 8. Regenerator characteristics

Characteristics			
Magnetocaloric Material	ErAl_2		
Geometry (radius x length)	35 mm. x 305 mm.		
Mass	1 kg.		
Sphere diameter	0.1 mm		
Shape factor	1		
Porosity	0.45		

In this analysis the wall has not been considered.

2.4.2.2 Model Convergence and Results

The model is initiated with a linear temperature gradient between the established hot and cold source temperatures. This helps in the initialization of the solver and reduces the computation time to reach a steady state and convergent solution. Figure 25 shows the establishment of the hot and cold source temperatures. Unlike traditional ambient temperature AMR simulations, the temperature profiles at the cold and hot sources readily stabilize in the studied model. However, achieving steady state operation at other locations within the regenerator requires multiple operational cycles. This convergence process is illustrated by the temperature evolution in the middle of the regenerator, as depicted in Figure 25.

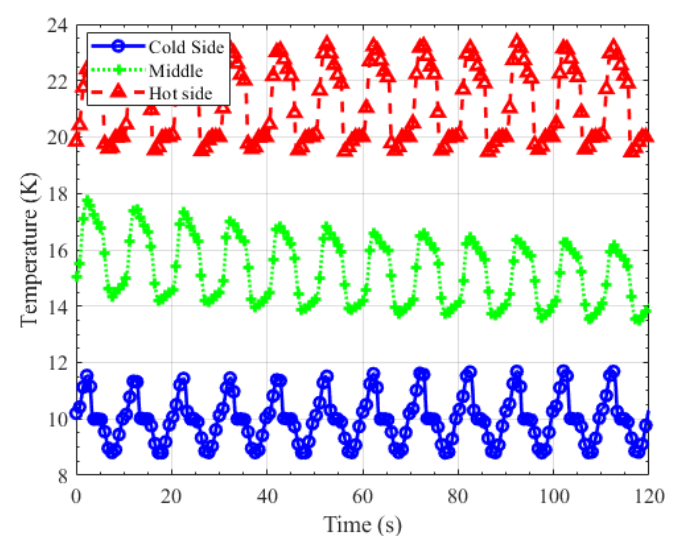


Figure 25. Establishment of the temperature profile between the magnetocaloric material at the hot and cold sides of the AMR.

One method to measure the convergence state of the refrigerator is to evaluate the net entropy change of the fluid over the course of a cycle. A similar method is adopted by Nellis et al [88]. Figure 26 (left) shows the fluid entropy change between the start of consecutive cycles at different positions of the regenerator. It is observed how the entropy change is being dumped to the hot and cold sources. Figure 26 (right) shows the sum of the entropy change along the regenerator for each cycle, and how the system reaches convergence once it has reached a value of entropy change near 0.

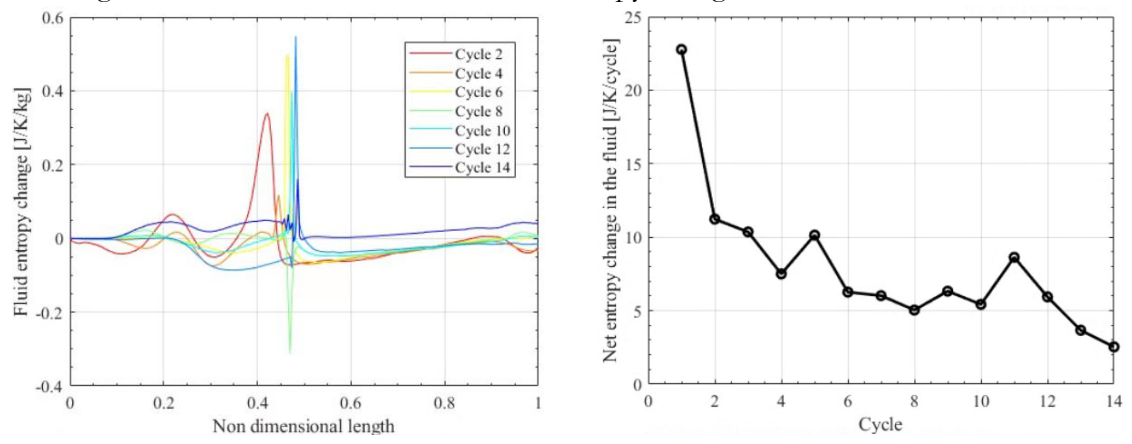


Figure 26. Fluid entropy change per cycle as function of non-dimensional length (left), and total entropy change per cycle (right).

Once the model has reached convergence, the key parameters, cooling power, or efficiency, can be computed. The heat rejection to the hot source and the cooling power of the system can be computed using the net heat flux carried by the fluid flowing through the hot and cold end. Eq. (2.52) and (2.53) show the numerical computation of these terms.

$$\dot{Q}_{cooling} = f \int_0^\tau \dot{m}_f \left(h_{f,c,in} \left(T_c, p_{ref} \right) - h_{f,c,out} \left(T_f, p \right) \right) dt \tag{2.52}$$

$$\dot{Q}_{rejected} = f \int_0^{\tau} \dot{m}_f \left(h_{f,h,out} \left(T_f, p \right) - h_{f,h,in} \left(T_h, p_{ref} \right) \right) dt \tag{2.53}$$

where $h_{f,c,\,\text{out}}$ and $h_{f,c,\,\text{in}}$ are the fluid enthalpies as it exits and enters the AMR at the cold side over the fluid flow period (τ_f) , while $h_{f,h,\,\text{in}}$ and $h_{f,h,\,\text{out}}$ are the fluid enthalpies as it enters and exits the AMR at the hot side over the fluid flow period, respectively. The values of $h_{f,c,\,\text{in}}$ and $h_{f,h,\,\text{in}}$ are evaluated at the reference source temperatures, T_c and T_h

respectively, and at the reference pressure. The f is the operational frequency, \dot{m}_f is the mass flow rate and $c_{p,f}$ is the specific heat of the fluid.

The efficiency of the system can be computed with the coefficient of performance, the ratio of cooling power to the input work. The main components of the input work are the magnet and pump work.

$$COP = \frac{\dot{Q}_{cooling}}{\dot{W}_{nump} + \dot{W}_{mag}} \tag{2.54}$$

The work needed to pump the fluid can be calculated with the following equation:

$$\dot{W}_{pump} = \frac{\dot{m}_f \Delta p}{\rho_f \eta_{pump}} \tag{2.55}$$

where η_{pump} is the pump's efficiency. For this first analysis a pumping efficiency of 70% has been considered.

In an ideal cycle, without dissipation losses, the magnetic work is given as the difference between the heat rejected and the refrigeration load [88], [108]:

$$\dot{W}_{mag} = \dot{Q}_{rejected} - \dot{Q}_{cooling} \tag{2.56}$$

Additionally, the work done by the magnet can be computed by summing the values for work input per unit length of the regenerator, i.e. by integrating the work done by each magnetocaloric particle using its T-s diagram:

$$\dot{W}_{mag} = \oint T ds = m_{mcm} f \int_{0}^{L} \int_{0}^{t} T_{s}(x, t) \frac{ds(x, t)}{dt} dt dx$$
 (2.57)

Eq. (2.57) relies on the assumption of internally reversible heat absorption. Figure 27 shows the temperature-entropy cycles undergone by the magnetocaloric material, and how each particle is acting like a heat pump, removing heat from a low temperature helium flow and rejecting it to a higher temperature stream.

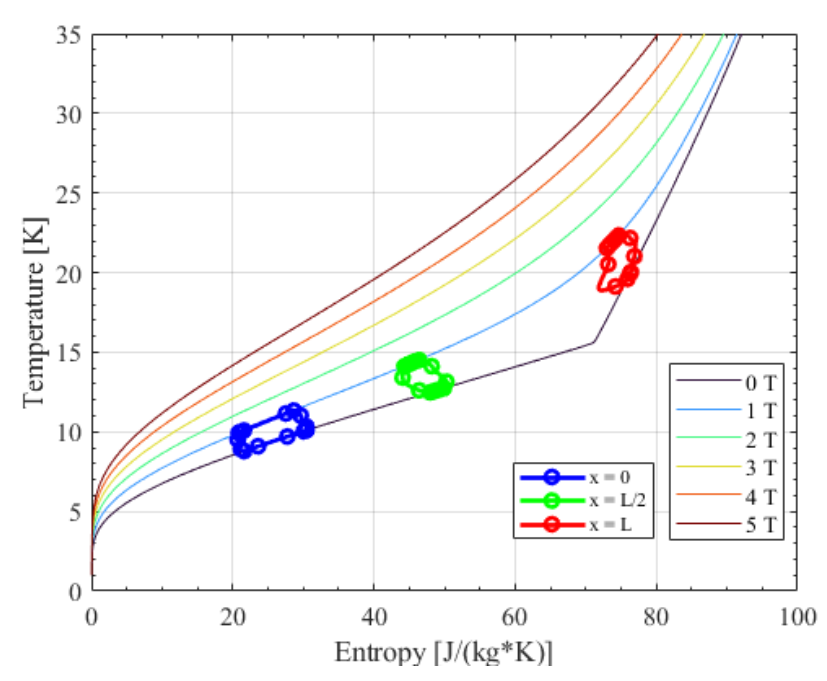


Figure 27 T-s diagram of AMR Brayton cycle. The entropy change through one cycle is shown for different positions of the regenerator, at the cold end (x = 0), in the middle (x=L/2), and in the hot end (x=L).

The thermodynamical convergence of the model is checked by comparing the independent computation of \dot{W}_{mag} using Eqns. (2.56) and (2.57). The origin of this

magnetic field and the real work needed to produce it has not been considered, in other words, $\eta_{magnet} = 100\%$.

To characterize the exergetic performance of the Active Magnetic Regenerator (AMR) stage, the Exergetic Coefficient of Performance (ECOP) is computed as follows:

$$ECOP = \frac{E\dot{x}_{out}}{\dot{W}} = \frac{\dot{Q}_{cooling} \cdot (\frac{T_h}{T_c} - 1)}{\dot{W}_{pump} + \dot{W}_{mag}}$$
(2.58)

The ECOP coincides with the exergy efficiency when the ambient temperature (T_0) is equal to the hot source temperature (T_h) . Alternatively, the ECOP represents the ratio of the COP of the real cycle and the COP of an ideal cycle operating between T_h and T_c :

$$ECOP = \frac{\dot{Q}_{cooling}}{\dot{W}_{pump} + \dot{W}_{mag}} \cdot \frac{T_h - T_c}{T_c} = \frac{COP}{COP_{ideal}^{T_h - T_c}}$$
(2.59)

This definition implies that, unlike the COP, the ECOP cannot exceed a value of 1. Therefore, expressing the ECOP as a percentage is often practical.

Table 9 details the principal parameters for the studied model. The model achieved a cooling power of 0.81 W and demonstrated an ECOP of 66%. This cooling power is comparable to the prototypes presented in Table 5, yet it is substantially lower than typical commercial cryocoolers. Subsequent sections investigate the effects of various parameters on the refrigerator's performance. Furthermore, Chapter 5 provides a systematic comparison of this technology with established commercial refrigeration methods

Table 9. Performance parameters of the AMR stage between 10-20 K

	Value
$\dot{Q}_{rejected}$	1.82 W
$\dot{Q}_{cooling}$	0.81W
\dot{W}_{mag} (Method 1)	1.01 W
\dot{W}_{mag} (Method 2)	0.99 W
$\dot{W}_{\rm pump}$	0.21 W
COP	0.66
ECOP	66%

2.4.3 Impact of operational parameters

The performance of a cryogenic magnetic refrigeration system is strongly dependent on the operational parameters of the system.

In this section an elementary review on the impact of the main system parameters is done to qualitatively and quantitively evaluate the potential of magnetic refrigeration. A more detailed optimization will be specific of the application and the established optimization variables: temperature span, cooling power, or efficiency (ECOP).

In the next subsections one variable will be changed and their effect on the cooling power and ECOP of the system will be analyzed.

2.4.3.1 Cold source temperature

The cold and hot source temperatures are fundamental inputs in the design of a refrigerator. This study focuses on the temperature range of 4.2–20 K, with a preliminary analysis of the feasibility of employing a conventional cooling system to achieve an intermediate temperature of 20 K. From this point, an Active Magnetic Regeneration (AMR) Brayton cycle is proposed to efficiently reach the target cold source temperature.

Using the baseline parameters established in the initial model, the cold source temperatures is systematically varied to evaluate their influence on cooling power and ECOP. Figure 28 illustrates the results of this analysis.

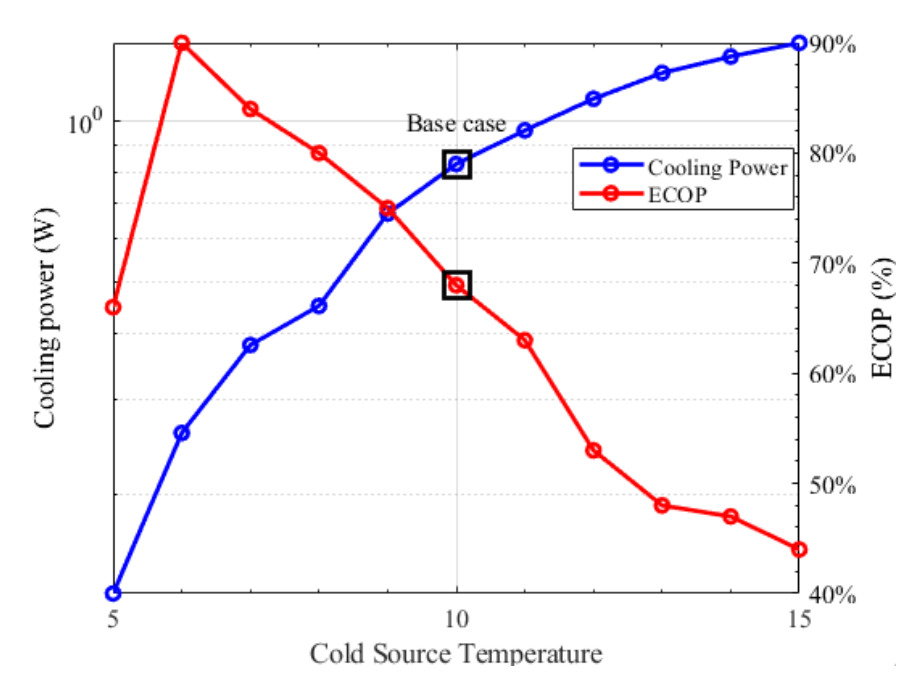


Figure 28. Cooling power and ECOP as a function of cold source temperature (5-15 K).

A direct relationship is observed between the cold source temperature and the cooling power. Specifically, for the system studied, the cooling power diminishes to negligible levels below 5 K. This reduction is attributed to the decreased magnetocaloric effect of ErAl₂ within that specific temperature range. Conversely, the ECOP shows an inverse relationship with temperature above 6 K, increasing as the temperature lowers. The primary reason for this behavior is the reduced work required for fluid pumping at lower temperatures. Below 6 K, however, the significant decline in cooling power results in a corresponding decrease in the ECOP.

This behavior is consistent with Wood and Potter [52] findings which show that the ECOP (defined as thermodynamic efficiency in Wood and Potter), is proportional to $\Delta \dot{S}_c \Delta T$:

$$ECOP = \frac{\dot{Q}_c/\dot{W}_{real}}{\dot{Q}_c/\dot{W}_{rev}} = \frac{1/\dot{W}_{real}}{1/\dot{W}_{rev}}$$
(2.60)

where \dot{W}_{rev} , is the reversible work, which Wood and Potter show is equivalent to the product of entropy change, and temperature change: $\Delta \dot{S}_c \Delta T$. And \dot{W}_{real} is the actual work of the system, generally given as:

$$\dot{W}_{real} = \Delta \dot{S}_c \Delta T + \dot{S}_{irr} \cdot T_h - \dot{Q}_l - \dot{Q}_f \tag{2.61}$$

where S_{irr} is the irreversible entropy generated in the heat transfer process, and \dot{Q}_{l} and \dot{Q}_{f} are the terms associated with entropy production due to heat leaks and friction or viscous effects respectively.

Therefore, it is deduced that the inverse of the ECOP is proportional to the inverse of the useful part of the real work $(\Delta \dot{S}_c \Delta T)$:

$$\frac{1}{ECOP} = 1 + \frac{1}{\Delta \dot{S}_c \Delta T} (\dot{S}_{irr} \cdot T_h - \dot{Q}_l - \dot{Q}_f)$$
 (2.62)

This is qualitative observed in Figure 28, as the cold source temperature reduces, increasing the useful work $(\Delta \dot{S}_c \Delta T)$, the ECOP increases, until $\Delta \dot{S}_c$ starts significantly reducing below 6 K due to the magnetocaloric properties of ErAl₂ (see Figure 22 right). The relation is not linear as certain terms, such as \dot{Q}_f , may not scale proportionately to ΔT .

2.4.3.2 Magnetic field

As discussed in previous sections, magnetic field is a key variable. Figure 29 highlights the influence of magnetic field on cooling power and ECOP. As expected, increasing the magnetic field enhances cooling power due to the stronger magnetocaloric effect, which allows more heat to be transferred during each cycle.

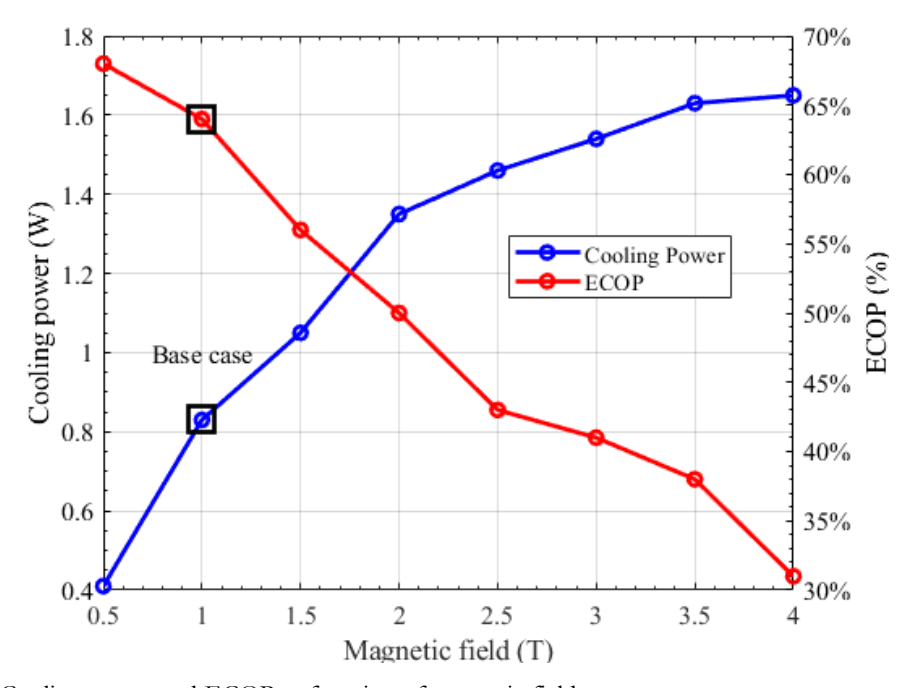


Figure 29. Cooling power and ECOP as function of magnetic field.

The analysis demonstrates the trade-offs between cooling power and system efficiency as magnetic field increases. Figure 29 shows that higher magnetic fields enhance cooling power, with diminishing returns at higher field. However, Figure 30 reveals that the Coefficient of Magnetic Refrigeration Performance (CMRP), calculated as the ratio of cooling power to energy demand, decreases significantly with increasing field. This decline indicates that the energy required for magnetization and demagnetization grows disproportionately compared to the gains in cooling power.

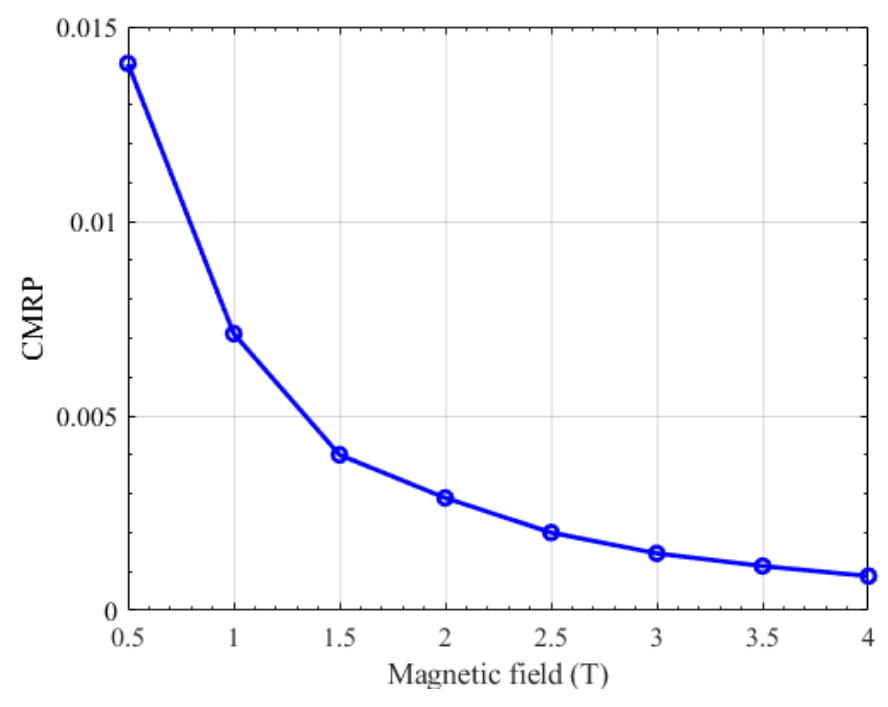


Figure 30. Coefficient of Magnet-Refrigerant performance as function of magnetic field.

2.4.3.3 Utilization factor and frequency

The frequency of the cycle is a crucial parameter to the performance of the cooling system. It is defined as the number of thermodynamic cycles per unit of time:

$$f = \frac{1}{2(\tau_{mag} + \tau_f)} \tag{2.63}$$

Increasing the cycle frequency can enhance cooling power by increasing the number of thermodynamic cycles per unit time. However, this increase must be carefully managed to avoid unbalancing the refrigerator, as excessively high frequencies can lead to inefficiencies in heat transfer and fluid flow.

To address this, the utilization factor is introduced as a key parameter. It represents the ratio of the amount of fluid contained in the regenerator to the amount of magnetocaloric material. The utilization factor ensures that the system remains balanced by optimizing fluid flow relative to the magnetocaloric material. This balance is essential for maintaining efficient heat transfer and avoiding performance degradation at higher frequencies. Defining the utilization factor in a cryogenic magnetic refrigerator is challenging due to the significant temporal and spatial variations in mass flow and specific heat. In this study, an average mass flow rate at the cold end of the regenerator was chosen, along with the average specific heats of both the fluid and the magnetocaloric material, calculated over the entire cycle and throughout the regenerator.

$$U = \frac{\int_0^{\tau} |m_f(t)| c_{p,f} dt}{2 \cdot m_{MCM} \cdot c_{p,MCM}}$$
(2.64)

where m_{MCM} and c_{MCM} are the mass and average specific heat of the magnetocaloric material.

When the utilization factor is too large, fluid is transported from the hot end to cold end decreasing the actual cooling power of the system. On the contrary, a small utilization factor limits the fluid capability to effectively transfer energy from the magnetocaloric effect.

Figure 31 illustrates the impact of the utilization factor on both cooling power and system efficiency.

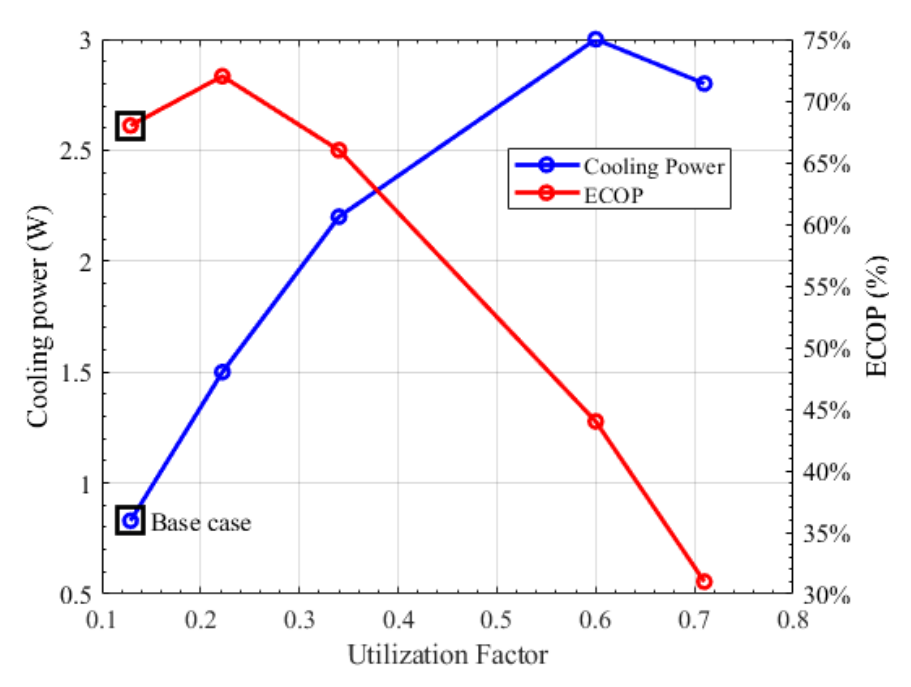


Figure 31. Cooling power and ECOP for different utilization factors.

The mass flow rate was increased while keeping all other parameters constant, as in the initial model. The figure demonstrates that, with a utilization factor of 0.125 in the initial model, much of the magnetocaloric material was underutilized in terms of cooling power. However, as the utilization factor increases, cooling power improves due to better utilization of the magnetocaloric material. At the same time, this increase negatively affects the system's ECOP, which declines rapidly as the utilization factor rises. This loss in the ECOP value is mainly due to the impact of increasing pumping work needed to move the fluid from the hot end to the cold end and viceversa.

This trade-off highlights the challenge of optimizing magnetic refrigeration systems, where maximizing cooling power often comes at the expense of efficiency. In order to increase the frequency to increase the number of cycles per unit of time, and therefore increasing the cooling power, the utilization factor must be also optimized. Figure 32 illustrates the cooling power and ECOP dependence on the utilization factor at various operating frequencies. Optimizing both cycle frequency and utilization factor enables the refrigerator to achieve cooling powers exceeding 10 W, comparable to current state-of-the-art technologies (even when operating at lower frequencies, 0.5 Hz vs 2 Hz for commercial GM cryocoolers). However, this optimization negatively impacts the ECOP, as higher utilization factors necessitate increased pumping work. Consequently, careful optimization is required to select the optimal operating point, balancing performance requirements against economic considerations for specific applications.

Simulating at higher frequencies (greater than 0.5 Hz) presents significant challenges due to the substantial increase in mesh density required to maintain convergence conditions. A finer mesh is essential for accurately resolving the governing equations under these conditions, but it also increases computational demands, including processing time and memory usage. This limitation, which impacts the efficiency and feasibility of high-frequency simulations, is further discussed in Section 2.6.

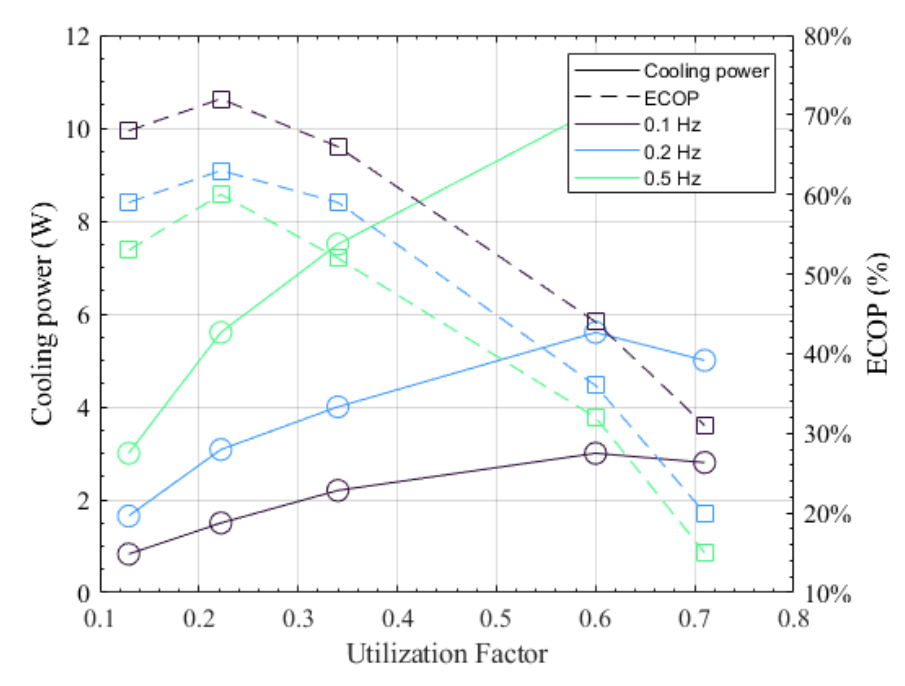


Figure 32. Cooling power and ECOP as function of utilization factor for different frequencies.

2.4.3.4 Other parameters

Other parameters that should be optimized are:

- Regenerator geometry: A detailed evaluation of packed bed regenerators compared to alternative configurations is essential. For packed beds, optimizing the particle diameter is critical as it directly influences the heat transfer area between the fluid and the magnetocaloric material, as well as the associated pressure drop. Smaller particles enhance heat transfer but result in higher pressure losses. Additionally, the shape factor of the particles should be optimized during manufacturing, with a target value close to 1 (perfect sphere), as this minimizes pressure losses.
 - The aspect ratio of the regenerator is another key parameter to optimize, particularly in real prototypes where wall effects influence performance.
- Thermodynamic cycle: Exploring variations of the Active Magnetic Regenerator (AMR) cycle can further enhance system performance. For instance, integrating the AMR cycle with other thermodynamic cycles, such as Gifford-McMahon or Stirling cycles, may yield efficiency improvements. The relationship between the magnetization/demagnetization time (τ_{mag}) and fluid flow time (τ_f) is particularly critical. As previously discussed, magnetization and demagnetization times do not contribute directly to the refrigerator's cooling performance and should therefore be minimized to improve overall efficiency.

2.5 Effect of Helium Compressibility

This section examines the effects of helium compressibility on system performance, focusing on cooling power and ECOP, and compares these results to an equivalent incompressible model. Additionally, the second part of the section evaluates the implications of helium compressibility for the numerical stability of the system.

2.5.1 Incompressible model: Performance comparison

The code developed in the previous section can be readily adapted to simulate the behavior of an equivalent refrigerator under the assumption of an incompressible fluid. This modification primarily impacts on the continuity equation:

Compressible
$$\rightarrow \frac{\delta \rho}{dt} + \nabla \cdot (\rho u) = 0$$
 (2.65)

$$Incompressible \to \nabla \cdot u = 0 \tag{2.66}$$

The model can be adapted to simulate incompressible flow by setting the partial derivative of density with respect to time to zero. The difference in performance between the two models can be compared by evaluating the cooling power and ECOP for different utilization factors. Figure 33 provides an update of Figure 31 comparing compressible and incompressible fluid.

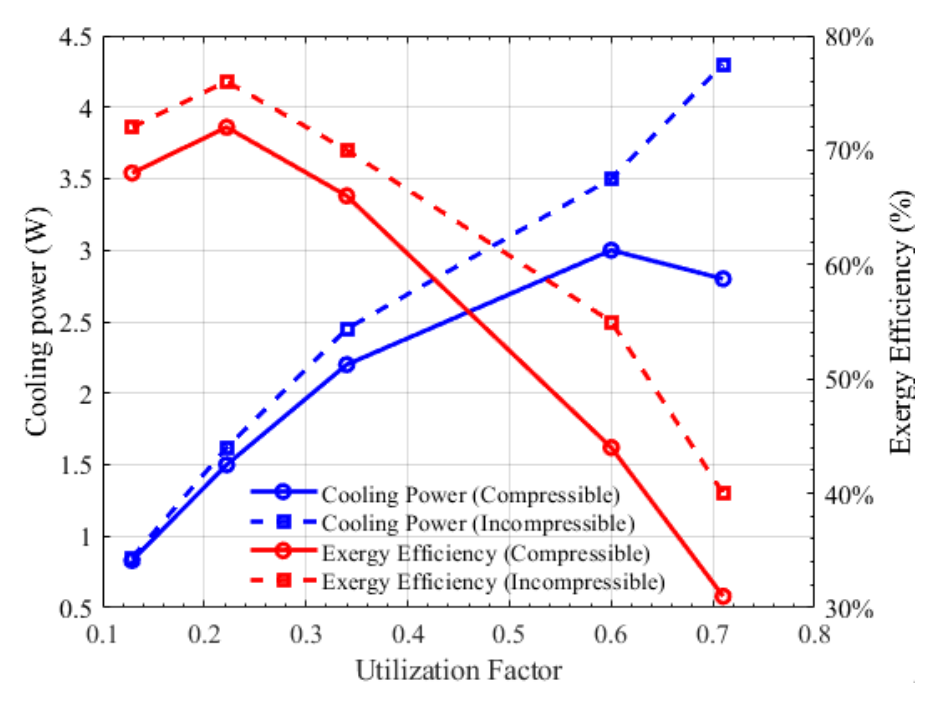


Figure 33. Comparison of cooling power and ECOP between compressible and incompressible models.

As shown in the figure, the incompressible model tends to overestimate the cooling power and ECOP of the refrigeration system, particularly at higher utilization factors. This performance divergence can be attributed to a key factor: during magnetization and demagnetization, fluid enters or exits the regenerator as pressure increases or decreases due to temperature variations in the magnetocaloric material. In the compressible flow simulation, this behavior has two significant effects. During magnetization, an additional heat load is transferred to the hot source, while during demagnetization, additional hot fluid enters the regenerator through the hot source. This results in an imbalance in fluid flow, causing hot fluid to enter the cold source during the cold blow phase.

2.5.2 Numerical stability

This section provides a concise discussion on the numerical stability of the model. Rather than offering a comprehensive analysis, the focus is to propose directions for future research, as the techniques employed here are not included in the thesis results.

From a theoretical perspective, within the system of PDEs, the presence of diffusion ensures that there exists a sufficiently refined computational mesh where the discretization method remains stable. As demonstrated in [88], Nellis estimated this critical ratio is proportional to:

$$r_{\sigma r} = \frac{\Delta t}{\Delta x} = \frac{\left[A \cdot (1 - \varepsilon) \cdot \rho_{M} \cdot T_{M} \cdot \left(\frac{\partial s_{M}}{\partial T} \right)_{\mu_{o}H} + A \cdot \varepsilon \cdot \left[\rho_{f} \cdot \left(\frac{\partial u_{f}}{\partial T} \right)_{p} - \frac{P}{\rho_{he}} \cdot \left(\frac{\partial \rho_{f}}{\partial T} \right)_{p} \right] \right]}{\dot{m}_{he} \cdot c_{p}}$$
(2.67)

The first term in the numerator represents the heat absorption by the magnetocaloric material, while the second term accounts for the heat absorbed by the entrained helium. Typically, the first term is dominant; however, below 10 K, the contribution of the second term increases significantly. This phenomenon is a key factor that adds complexity to solving real active magnetic regenerator (AMR) systems at cryogenic temperatures.

In order to achieve numerically stable and consistent simulations of a high-frequency AMR refrigerator, it is essential to ensure that spatial refinement increases proportionally with the system's requirements. In this case, since the coefficients of the PDE system are recomputed at each time step, computational costs rise significantly. Stabilization techniques can mitigate these challenges by enhancing stability without excessive mesh refinement.

Two primary sources of instability have been identified in this simulation:

- Boundary conditions: During the cold blow phase, the transition to Dirichlet boundary conditions for mass flow and temperature generates steep gradients near the boundaries.
- Pressure/Mass flow wave: The sharp gradients in temperature and velocity within the wake of the mass flow induce oscillations in the system.

Several stabilization strategies have been explored to address these issues:

- Local refinement of the mesh: Since instabilities predominantly arise near boundaries, refining the mesh in these regions—particularly on the cold side where density changes are more pronounced—can improve stability.
- Adding artificial diffusion: Adding small diffusion terms to the hyperbolic equations governing mass flow and momentum conservation has shown promise in stabilizing the solver. To maintain consistency, this artificial diffusion must be counterbalanced by subtracting it in the flux term.

The diffusion coefficient is defined as

$$\epsilon = \beta_m \cdot h \cdot |v_{char}| \tag{2.68}$$

where β_m is a tuning parameter, h is the mesh size, and v_{char} is a characteristic velocity. The characteristic velocity should scale differently for each equation, in the case of the mass flow equation it should scale proportionally to the velocity of the fluid, and in the pressure equation to the speed of sound.

While these measures have yielded partial success, further research is necessary to develop more effective methods that balance computational efficiency with thermodynamic consistency.

Recent studies propose alternative numerical schemes that merit exploration: In [93] two different numerical schemes are proposed: an implicit-explicit (IMEX) scheme for compressible Navier-Stokes equations, and a Pressure-Correction Scheme.

Other techniques worth exploring include the use of GPU-accelerated solvers, which have demonstrated promising results in specific fluid dynamics and heat transfer applications [109], as well as the application of machine learning methods, such as Physics-Informed Neural Networks (PINNs) [110].

2.6 Summary: The potential of magnetic refrigeration

This chapter has reviewed the fundamentals of magnetic refrigeration, with a particular focus on its applications in cryogenics. Key insights from the analysis of previously developed prototypes and the conducted study are summarized as follows:

• The performance of earlier prototypes in the 4.2-20 K range was constrained by the use of GGG (Gadolinium Gallium Garnet) as a magnetic refrigerant. There is a need to explore alternative refrigerants with properties better suited for efficient regenerative cycles.

- Reducing magnetic field requirements could simplify magnet design and lower costs, potentially enabling the use of permanent magnets, which would make the technology more practical and cost-effective.
- There is a clear need to optimize refrigeration cycles and enhance heat transfer performance. Combining and exploring alternative refrigeration cycles, such as Active Magnetic Regeneration (AMR), GM (Gifford-McMahon), or Stirling cycles, could yield significant improvements.

Erbium Aluminum II (ErAl₂) has been identified as a promising magnetocaloric material for operation in the 4.2–20 K temperature range.

A numerical model has been developed to account for helium compressibility and enable the parametrization of key variables. Using this model, the potential of ErAl₂ has been analyzed. Preliminary results confirm the material's suitability, reinforcing the idea that magnetic refrigeration is a promising technology for cryogenic applications with potential to meet proposed targets.

To validate these findings, it is crucial to develop a test stand to compare and validate the model's predictions with experimental data. This step will provide critical insights into the practical implementation and performance of magnetic refrigeration systems in cryogenic environments. The development of such test stand is addressed in the following chapter.

Chapter 3 : Design, Manufacturing and Commissioning of Experimental Test Stand

The previous chapter established a one-dimensional model for predicting the performance of a cryogenic magnetic regenerator, highlighting the potential of the magnetic refrigeration in cryogenic applications, but also the sensitivity of the system to operational parameters.

Although these theoretical and numerical findings offer valuable insights, purely analytical and numerical approaches are insufficient to capture all the complexities inherent in real-world applications. Consequently, an experimental investigation is essential to validate the predicted thermal behavior, pressure drop characteristics, and overall feasibility of the proposed design.

Table 10, presented below, outlines the specific objectives of this experimental phase.

Table 10. Objectives for the magnetocaloric test stand development.

Objectives

Objective 1: Acquire knowhow in the use of magnetocaloric materials, and establish a manufacturing procedure of a magnetocaloric packed bed

<u>Objective 2:</u> Technology demonstrator and proof of concept capable of operating under cryogenics conditions and magnetic field.

Objective 3: Validation of numerical model

Objective 3.1: Experimental evaluation of magnetocaloric effect in target temperature

Objective 3.2: Analyze heat transfer correlations at cryogenic temperatures

Building on these objectives, the following sections address the overall methodology, hardware design, manufacturing procedures, and commissioning steps required to confirm the system's functionality under both ambient and cryogenic operating conditions. The aim is to integrate magnetocaloric materials, superconducting magnets, and the associated cryogenic infrastructure into a cohesive setup capable of delivering robust data.

3.1 Conceptual Design

Before delving into the detailed engineering of each subsystem, it is crucial to outline the high-level vision for the experimental test stand. The guiding principle is to reproduce, at a laboratory scale, the core processes of magnetic refrigeration.

The work by Barclay et al. [111] significantly influenced the development of the experimental test stand described in this thesis. In their study, the authors investigated the thermodynamic behavior of a packed bed at cryogenic temperatures using the single-blow method. This technique involves imposing a temperature step at the inlet of the packed

bed and monitoring its transient temperature response along the bed. Further details about this testing methodology are provided in Chapters 4 and 5.

Although Barclay et al.'s findings were not entirely conclusive, their experimental framework offers a robust starting point for addressing the objectives of this thesis. With appropriate modifications, such as adapting the experimental setup to include magnetocaloric materials, a magnetic source, and operating at target temperatures between 4.2 K and 20 K, this framework can support the validation of numerical models and heat transfer correlations. Additionally, it provides a means to assess the magnetocaloric effect and packed bed performance under varying thermal and magnetic conditions.

Figure 34 illustrates the packed bed configuration used in Barclay et al.'s study, which is filled with Gd powder and Pb balls. The instrumentation includes three thermocouples positioned within the regenerator and two additional thermocouples at its inlet and outlet. The right side of Figure 34 shows the temperature evolution along the regenerator during an experiment conducted at liquid nitrogen temperature.

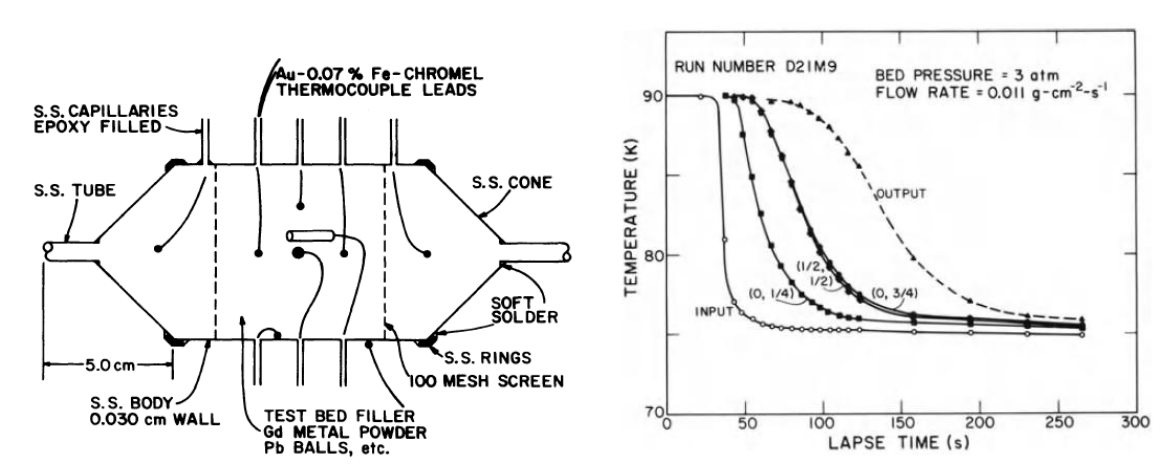


Figure 34. Schematic of the test bed Barclay et al test bed showing the thermocouple positions (left), and Response of lead-ball test bed to hot-to-cold step function (right). Figures are reproduced from [111].

To enable effective testing with the selected magnetocaloric materials GGG and ErAl₂, specific and challenging boundary conditions were required.

First, helium gas is needed to flow at temperatures below 20 K, as the magnetocaloric effect is not produced at higher temperatures. To achieve this, a system similar to the Cryogenic Supply System (CSS) developed for superconducting cyclotrons may be adapted. This system, described in Chapter 1, employs a closed-loop helium circuit capable of reaching liquid helium temperatures.

Second, a magnetic field of at least 2 T is necessary across a significant volume to induce sufficient magnetocaloric effects. Furthermore, the system needs to be designed to allow magnetic transients for dynamic testing.

Table 11 summarize these high-level requirements, and Figure 35 shows a conceptual design of the packed bed, inside the bore of a superconducting magnet. The following sections will specifically address how the system was designed to meet the established boundary conditions.

To reduce the development risk associated with the experimental test stand, its implementation was divided into two distinct phases: ambient temperature testing and cryogenic temperature testing.

During the first phase, the magnetocaloric packed bed was manufactured, and a test stand was developed to evaluate its performance under ambient conditions. This phase allowed for the preliminary validation of key components, such as the packed bed and the closed-loop helium circuit, which circulates helium gas through the magnetocaloric material. Figure 36 (left) illustrates the schematic of the test stand used in this stage. By

testing these components at ambient temperatures, potential design flaws could be identified early, ensuring a smoother transition to cryogenic operations.

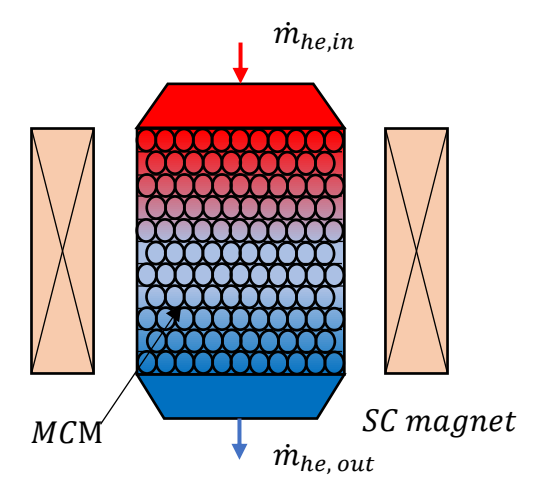


Table 11. Summary of technical requirements for the magnetic source of the magnetocaloric test stand

Requirements	Target Value
Thermal	$T_{fluid} \le 10K$
Magnetia	B >2 T
Magnetic	2 packed beds

Figure 35. Schematic of a packed bed placed in the bore of a superconducting magnet.

In the second phase, cryogenic temperature testing was conducted to evaluate system performance under target operating conditions. For this stage, the magnetocaloric materials were positioned within the bore of a superconducting magnet housed inside a cryostat and cooled using liquid helium. The evaporated helium gas from the cryostat was utilized to cool the closed-loop helium circuit via a heat exchanger. This setup enabled the system to reach and maintain the desired cryogenic temperature range while facilitating experimental evaluation of the magnetocaloric effect and heat transfer characteristics. The tests performed during this phase are detailed in Chapter 4.

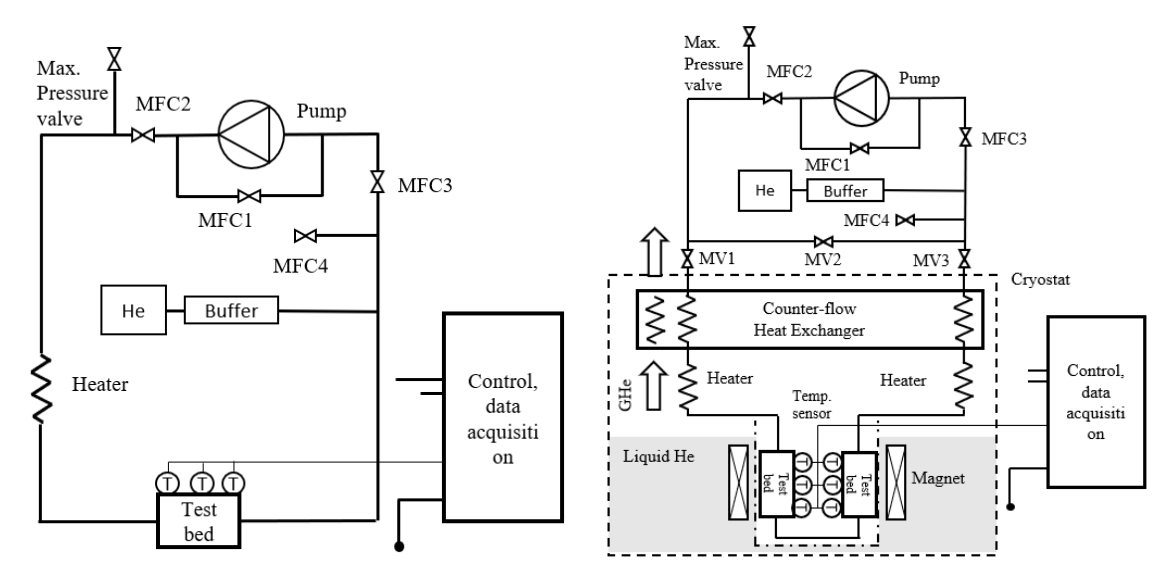


Figure 36. Configuration and schematic of apparatus and data acquisition system for the ambient test—Phase 1 (left) and cryogenic test—Phase 2 (Right). The portion enclosed by dashed lines, in the right-side figure, is inside a cryostat.

3.2 Magnetocaloric Material

As introduced in the previous chapter two magnetocaloric materials have been analysed and are used in the proposed test stand: GGG and ErAl₂. In the following subsections the engineering aspects of the design, manufacturing and commissioning of the packed bed development are addressed.

3.2.1 Design of the test bed

For this test stand, a packed sphere bed was adopted due to its good thermal performance and ease of manufacturing. The main variables that define a packed bed are:

- Particle size and shape: The size and shape of the particles affect the surface area available for heat transfer, as well as the flow characteristics. The shape factor (Φ) describes the 'irregularity' of the particles, and is defined as the ratio of the specific area of a spherical particle to the specific area of the particle in question.
- Porosity and packing arrangement and density: Porosity is the ratio of the void volume to the total volume of the packed bed, the packing arrangement refers to the relative position of each particle in the packed bed and the packing density refers to how tightly the particles are packed within the bed. All variables are related, and the type of packing determines the porosity of the packed bed.

Table 12 shows how the packing arrangement of the particle affects the porosity of the packed bed. In our case it will be assumed that all particles are distributed randomly.

Packing arrangement	Bed porosity
Spheres – rhombohedral	0.2595
Spheres – tetragonal	0.3019
Spheres – random	0.36-0.43
Spheres – orthorhombic	0.3954

Spheres - cubic

Table 12. Packed bed porosity for different packing arrangements [112]

To reduce porosity, pressure can be applied to the packed bed. However, if it is too high certain regions of the regenerator can become occluded and impede the flow of the fluid and isolate that region of the regenerator. Figure 37 shows the relation between packing pressure and porosity in Nellis work [88]. In their studies, porosities below 0.33 made the regenerator occluded.

0.4764

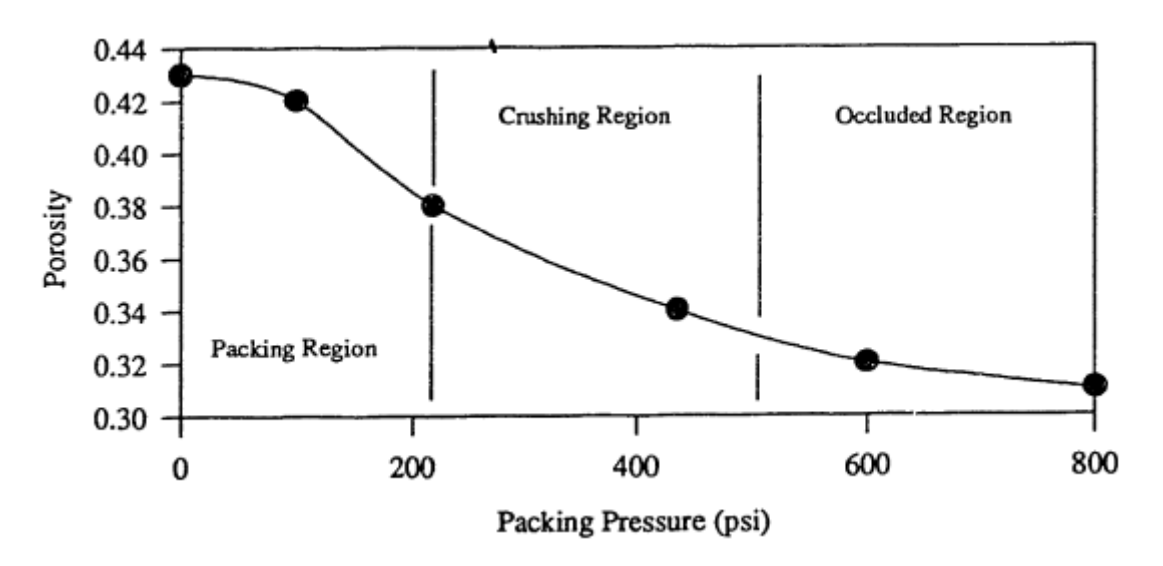


Figure 37. Regenerator porosity at varying packing pressure. Depicted from [88].

For the design and construction of the regenerator housing, the following parameters must be considered for functionality: media containment and replacement, working pressure, robust sealing, and minimum heat leak to the environment. Design parameters for material selection include minimized thermal mass, and thermal conductivity, cryogenic compatibility (leaks and thermal expansion), paramagnetic, sufficient strength for required

pressure, ease of machining, availability and cost [113]. Figure 38 shows the proposed schematic for the regenerator housing.

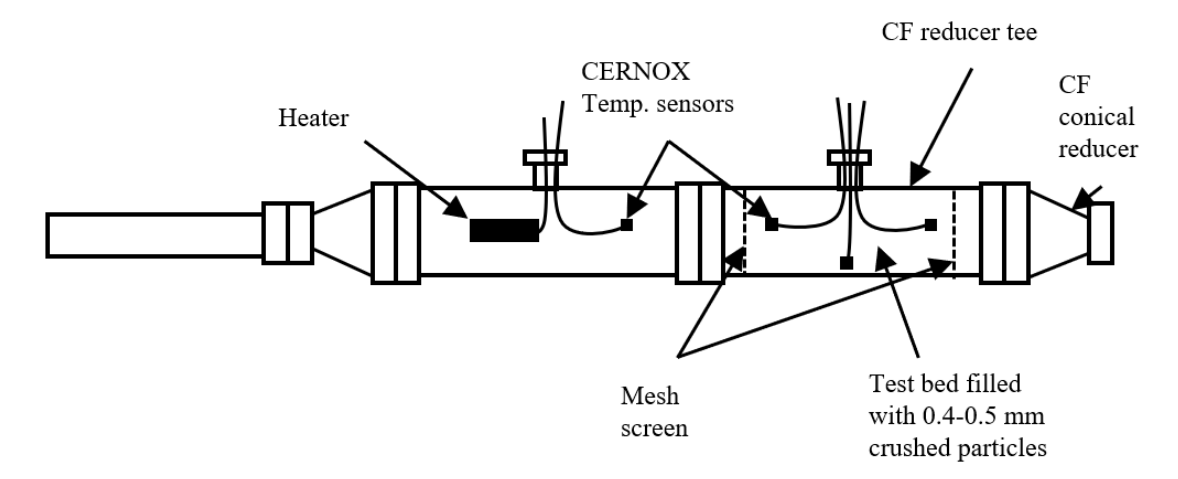


Figure 38. Schematic of instrumented GGG packed bed.

Having considered all parameters, the following selections were made:

- Regenerator housing: A commercial ConFlat Ultra High Vacuum (CF UHV) reducing tee was selected, with the small inlet designated for introducing the necessary instrumentation. This choice facilitates rapid and cost-effective development while ensuring reliable performance and minimal leakage at cryogenic temperatures. To contain the magnetocaloric material, mesh screens will be soldered to the CF copper gasket. However, this housing design may introduce certain inaccuracies during testing due to its high thermal mass and significant thermal conductivity, which could result in notable thermal leaks into the regenerator. Figure 39 shows the selected parts.
- Heater housing: an equal piece to the regenerator housing was used for the heater.
- Conical reducer: to reduce turbulence and backflow at the inlet and outlet of the test bed a conical reducer was included at both sides of the test bed.



Figure 39. ConFlat® (CF) UHV Reducing Tee (left) and ConFlat® (CF) conical reducer.

- Instrumentation

O Temperature sensors: Cernox temperature sensors were selected due to their high accuracy and reliability in cryogenic applications. They are made from a zirconium oxynitride thin film deposited on a sapphire substrate, providing excellent sensitivity and stability at low temperatures. They cover a wide temperature range, typically from 0.3 K to 310 K, and have low magnetic field-induced errors, making them ideal for environments with varying magnetic fields. These sensors also exhibit low heat dissipation, which minimizes self-heating effects.

O Heater: a cartridge heater was selected with 60W of power. Another typical source of error in regenerator testing is the ability to produce a quick temperature response, which is related among other things to the heater power, heat transfer area, and thermal mass.

Table 13 summarizes the main parameters of the magnetocaloric packed bed for the experimental test stand. There are certain parameters where a range has been established as the final value depends on the manufacturing process.

Table 13. Main parameters of each test bed for the experimental test stand

	Value
Regenerator Length	125 mm
Regenerator Diameter	35 mm
MC mass	0.3-0.5 kg
Particle Diameter	0.3-0.5 mm
Porosity	0.35-0.45
Shape Factor	0.9-1

3.2.2 Packed Bed manufacturing

Since the price of the magnetocaloric materials is high and its availability is limited, the manufacturing process was optimized first using glass spheres. The procedure followed described in [88],[114] was adopted:

1. Crush the material crystals: using a manual hydraulic press and in-house tooling the crystals were crushed to reduce their size. During the initial phase, with glass crystals, the quantity of material crushed per step and the pressure applied was optimized in order to reduce the waste material. Figure 40 shows the pre-crushed magnetocaloric material and the laboratory set-up during the preparation process.





Figure 40 Pre-crushed particles of ErAl₂ and GGG (left) and laboratory set up during manufacturing (right), which includes the hydraulic press, a sieve, a high precision weight scale and a computer for data acquisition.

2. Pass material through sieves: To achieve the chosen size the crushed crystals are passed through a series of sieves of unique dimensions. The sieves levels were 1, 0.5 and 0.3 mm. The target was to reduce the materials size to the 0.3-0.5 mm. range, which are in the range of previous prototypes [80], [86]. Any particle below 0.3 mm. was considered waste material. Figure 41 shows the sieves used during the manufacturing process.





Figure 41. Sieve used during manufacturing process (left) and detailed view of one sieve (right).

- 3. Repeat steps 1-2 with the material that did not pass through the sieve's higher levels.
- 4. Fill the regenerator housing with the crushed crystals with the desired size and apply certain packing pressure to achieve the chosen porosity. Figure 42 shows the packing process of the packed bed.



Figure 42. Application of pressure to the packed bed to achieve desired porosity.

3.2.3 Packed Bed characteristics

During the fabrication of the magnetocaloric packed bed, we aimed to reduce the uncertainty of the values established in Table 13 and inherent to the fabrication process, i.e., the particle size and shape factor, and the maximum achievable porosity without occluding the regenerator.

3.2.3.1 Particle size and shape factor

To characterize the resultant particles from the manufacturing process, we set apart a small batch and measured them under a microscope. Figure 43 shows a sample of both magnetocaloric materials under the microscope.

The microscope allowed us to create a 2D map establishing the size of each particle in the X and Y directions. Figure 44 shows a histogram analysis of each material's particles.

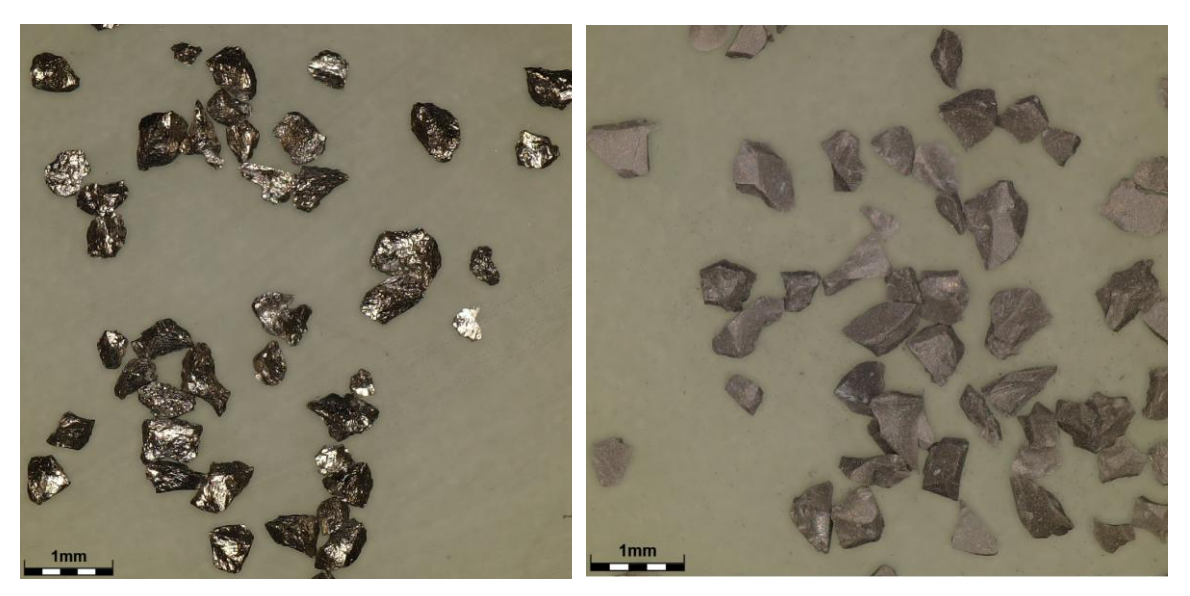


Figure 43. Microscope image of crushed particles of ErAl₂ (left) and GGG (right).

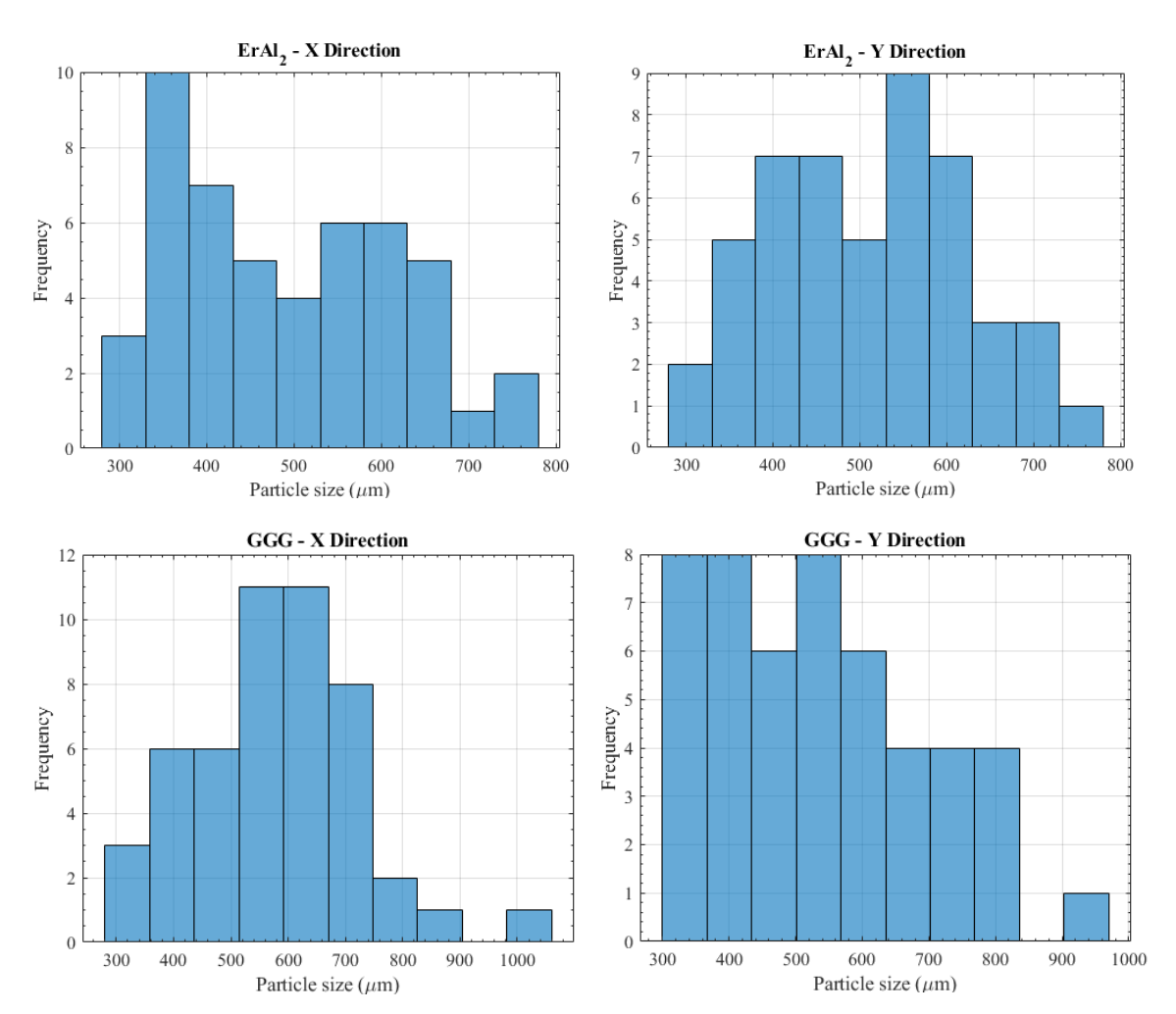


Figure 44. Particle size distribution of ErAl₂ and GGG samples in the X and Y direction obtained through microscope analysis.

It is noticeable that even if the minimum correctly adjusts to the minimum sieve value, 0.3 mm., the distribution has a long right tail, reaching values of 1 mm. Table 14 shows the statistical summary of Figure 44 highlighting this fact.

	ErAl ₂ -X	ErAl ₂ -Y	GGG-X	GGG-Y
Count	50	50	50	50
Average (µm.)	486.181	520.49	566.233	546.226
Max. (µm.)	775.227	890.375	1052.435	946.893
Min. (µm.)	287.457	316.13	298.711	281.473
Range (µm.)	487.77	574.245	753.724	665.42
σ (μm.)	124.941	134.67	143.029	157.622

Table 14. Statistical summary of particle size distribution of ErAl₂ and GGG samples

The explanation of this phenomenon is related to the shape factor of the crushed particles, which is defined as the ratio of the specific area of a spherical particle to the specific area of the real particle under consideration. The crushed particles resemble more an ellipsoid than a perfect sphere. Figure 45 shows the comparison between an ellipsoid and an actual particle.

The sieving process permits the passage of particles with semi-minor axes aa and cc smaller than 0.5 mm, regardless of whether the semi-major axis b exceeds this threshold. Furthermore, particle size measurements are inherently limited to two-dimensional mapping. Under microscopic observation, the semi-major axis b is typically measured because particles tend to orient themselves along this axis.

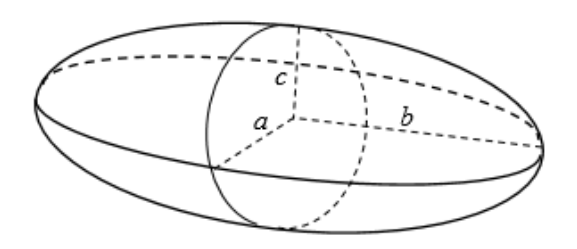




Figure 45. Image of an ellipsoid (left) and a ErAl₂ particle measured under the microscope (right).

For the full characterization of the packed bed the following will be assumed:

- Semi-minor axis "a" and "c" are equal and equal to the average measurement minus one standard deviation

$$a = c = \mu - \sigma \tag{3.1}$$

Semi-major axis is equal to the average measurement plus one standard deviation:

$$b = \mu + \sigma \tag{3.2}$$

- The average diameter is the geometric mean diameter:

$$D_p = (abc)^{\frac{1}{3}} \tag{3.3}$$

- Shape factor is:

$$\phi = \frac{A_{sph}}{A_{part}} = \frac{2D_p}{b + \frac{b^2}{\sqrt{b^2 - a^2}} ln\left(\frac{b + \sqrt{b^2 - a^2}}{b}\right)}$$
(3.4)

The packed beds are now fully characterized, and its values are summarized in Table 15. The values obtained for the shape factor appear to be reasonable when compared to other non-spherical objects [115]:

Table 15. Summary of mean geometric characteristics for ErAl2 and GGG samples

	ErAl ₂	GGG	Glass
Particle Diameter	0.45 mm	0.48 mm	0.75 mm
Shape Factor	0.95	0.95	0.9

3.2.3.2 Porosity: application of packing pressure

Porosity, the ratio between void volume to total volume, is a key factor in the definition of the packed bed, as it directly affects to the heat transfer area and the pressure drop of the packed bed. The main variables affecting the porosity are the packing arrangement and packing pressure, as was introduced in the previous section. In this section we will investigate the effect of packing pressure on the regenerator porosity.

The design target is to minimize porosity, reducing the void volume but without occluding the packed bed. To understand the relation of packing pressure, porosity and pressure drop a series of experiments were done at ambient temperature with the glass packed bed. Figure 46 shows an image of the test set-up during pressure drop testing, which is described more profoundly in Section 3.4.

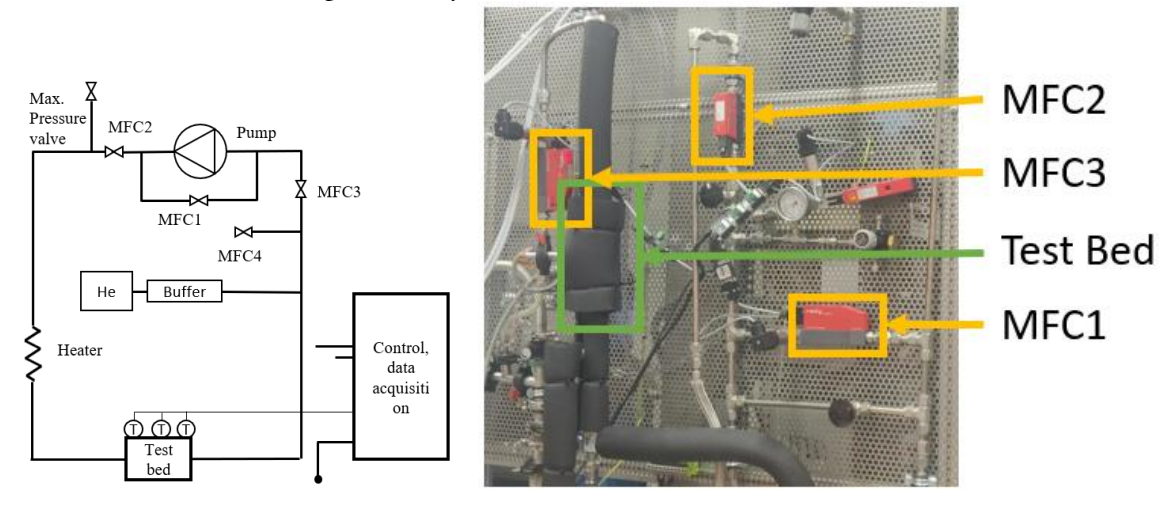


Figure 46. Schematic of ambient tests set up (left), and assembled test set-up during pressure drop measurements indicating main components of the fluid circuit

Figure 47 shows the theoretical and experimental pressure drop for different porosities, it can be observed how with porosities lower than 0.45, the regenerator becomes occluded, as there is a divergence between the theoretical, given by Ergun correlation [97], and experimental pressure drop.

This phenomenon has been reported by other researchers; however, the range of packing pressures at which it has been observed differs from those documented in previous studies. This discrepancy may be attributed to variations in particle diameter and shape factor, although this hypothesis has not yet been experimentally validated.

Based on the obtained results, it was determined that the fabrication of the ErAl₂ and GGG packed beds would be conducted using minimal packing pressure, aiming for a porosity of 0.45. Although this porosity may be considered high for an efficient refrigerator, the primary objective of these tests is to investigate the system's dynamics rather than to optimize its performance. Consequently, minimizing the risk of occlusion was deemed the safest approach.

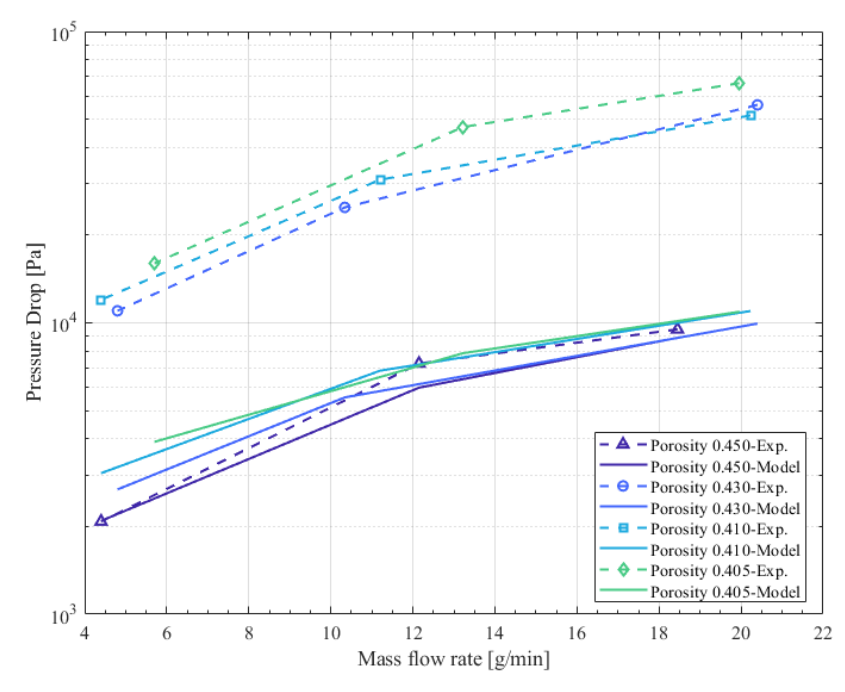


Figure 47. Pressure drop for glass packed bed, with different porosities of the regenerator. Solid lines represent simulation data, while discontinuous lines with open data points represent experimental data.

3.2.4 Final Assembly and instrumentation

The process described in the previous sections was employed to fabricate the magnetocaloric packed beds; however, several additional considerations were necessary.

First, the integration of the instrumentation involved positioning three temperature sensors along each packed bed. To route the sensor wires into the packed bed, a small inlet on the CF tee was utilized. A hole was drilled through a blank CF flange to allow the passage of wires, which were then sealed with 2850 Stycast to ensure hermeticity. After routing the wires, the CERNOX sensors were soldered and installed in the regenerator housing. Figure 48 shows both housings before the introduction of the magnetocaloric material, and Figure 49 shows the GGG packed bed after the introduction of the magnetocaloric material.





Figure 48. ErAl₂ and GGG packed bed housing with instrumentation placed before introducing the magnetocaloric material.

During the initial trials with ErAl₂ led to measurement errors due to insulation loss in the sensors. To address these, two corrective measures were implemented: first, a 1 mm.

kapton film was introduced between the wall and the magnetocaloric material, this measure also helps to reduce static losses to the ambient environment. Second, the CERNOX sensors in the ErAl₂ housing were sealed. Although the latter action compromised the temperature acquisition accuracy, no other tested alternatives provided reliable results.

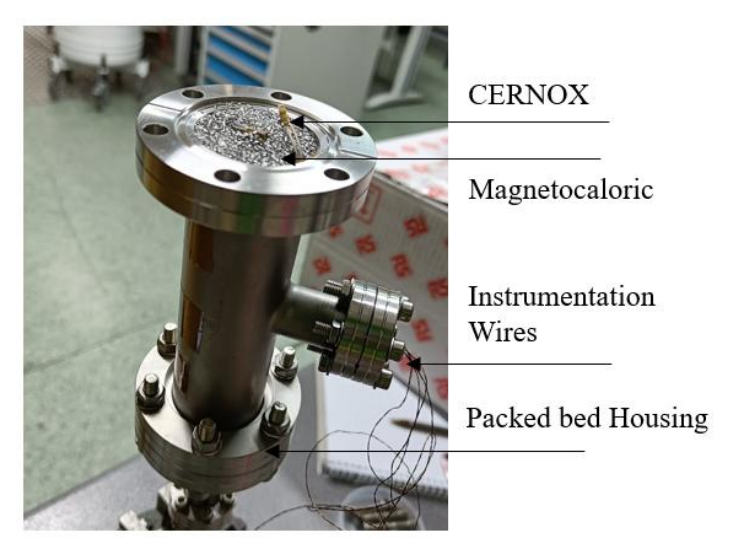


Figure 49. Packed bed after the introduction of GGG particles.

The final values of both packed beds are summarized Table 16.

Table 16. Main parameters of each test bed for the experimental test stand

	ErAl ₂	GGG
Length	125 mm	125 mm
Diameter	35 mm	35 mm
Volume	120.2 cm ³	120.2 cm ³
MC mass	346.51 g.	409.87 g.
Porosity	0.45	0.45
Particle Diameter	0.45 mm	0.48 mm
Shape Factor	0.95	0.95

To contain the magnetocaloric material within the regenerator housing a fine stainless steel mesh screen was soldered to the CF copper gasket. A nylon screen glued with analdite was also tested but with worse results. Figure 50 shows both trials.





Figure 50. Copper gasket with soldered stainless-steel mesh for packed bed containment.

The heater housing was prepared similarly to the packed bed, the inner diameter of the housing was covered with a Kapton film, and the wires for the heater and the temperature

sensor were routed in the same fashion. The heater was placed in the middle, with two inhouse pieces made from fiberglass to secure its position. Figure 51 left shows the heater housing with the heater and sensor in place.

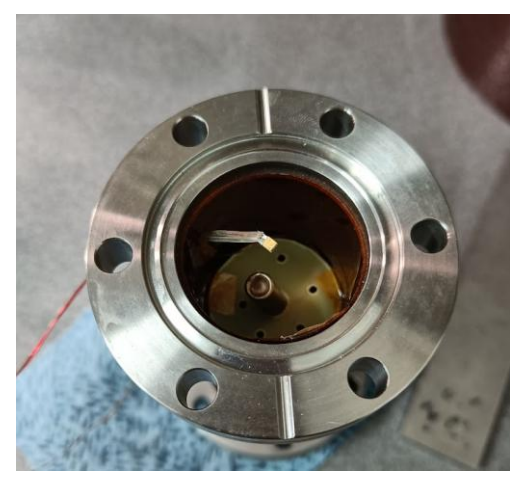






Figure 51. Stainless steel housing with heater and temperature sensor in place (left), brass block introduced inside stainless steel housing before entering the heater recipient (center and right).

To enhance the original design, an additional component was incorporated upstream of the heater. This component consists of a brass block designed to improve the thermal stability of the helium flow. Figure 52 shows the final assembly of the test bed.

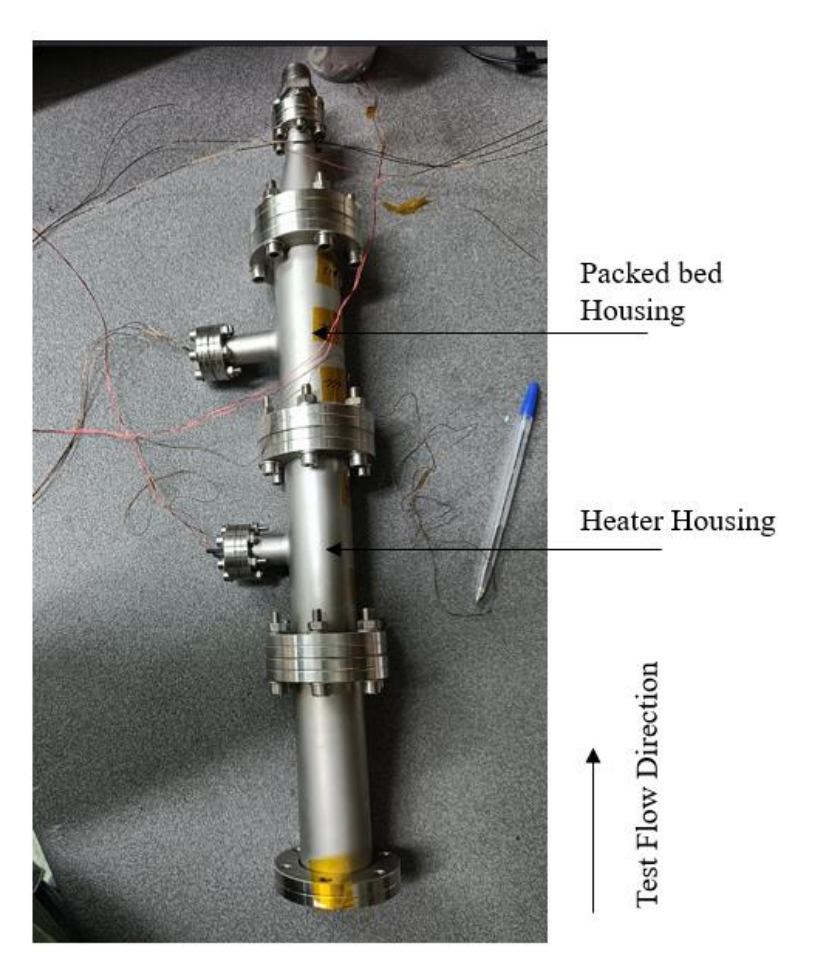


Figure 52. Final assembly of the test bed including brass container, heater and packed bed housing.

3.3 Magnetic Source: Superconducting magnet

As introduced at the beginning of this chapter, the selection of magnetocaloric materials directly influences the boundary conditions for the design of the remaining system components. Specifically, for the magnetic source, two key dependent variables were identified (Table 17): the magnetic field (T) and the magnetic field volume (m³).

The magnitude of the magnetic field is determined by the desired intensity of the magnetocaloric effect, which itself is strongly influenced by the operating temperature. A target operating temperature of 10 K was chosen based on preliminary calculations, which suggested that this temperature could be reasonably achieved in the regenerator. This aspect will be further detailed in the next subsection. For ErAl₂, the target temperature is near its transition point, allowing for a significant magnetocaloric effect even at relatively low magnetic fields. In contrast, GGG operates well above its transition temperature in this range, necessitating a magnetic field exceeding 2 T to adequately evaluate its refrigerant performance.

The second critical variable, magnetic field volume, is dictated by the spatial requirements of the packed bed regenerators. The bore diameter of the magnet must be large enough to accommodate two packed bed housings, each with a maximum diameter of 60 mm. Since simultaneous testing of both packed beds is planned, the bore diameter must exceed 120 mm to ensure sufficient space for instrumentation and flow management.

These considerations highlight the interplay between material properties and system design constraints, ensuring that both thermal and magnetic requirements are met for effective experimental evaluation of the selected magnetocaloric materials.

	Target Value	Description
Magnetic field	B >2 T	Figure 17 shows the entropy change of both magnetocaloric materials. At an operating temperature of 10 K, a magnetic field greater than 2 T is needed for an entropy difference of ~5 J/kg·K for GGG.
Bore volume	Volume: Diameter >120 mm Length >120 mm	The limits are imposed by both MC housing, each has a diameter of 60 mm and a length of 120 mm.

A superconducting magnet that fulfilled both conditions was available in CIEMAT facilities. This magnet, shown in Figure 53, was developed for the CRISA project, in which the power source of the antimatter spectrometer (AMS) experiment, a particle detector for the international space station (ISS), was tested [116]. Moreover, it was later used to perform a quench analysis in low temperature superconductors magnets, so it has demonstrated resilience. The characteristics of the CRISA magnet are summarized in Table 18.

The selection of this magnet was the most adequate for the test stand development, as it fulfilled all the target conditions with low development risk, as the magnet was available and previously tested. For other applications, or an optimized magnetic refrigerator, this magnet might not be the optimal option.

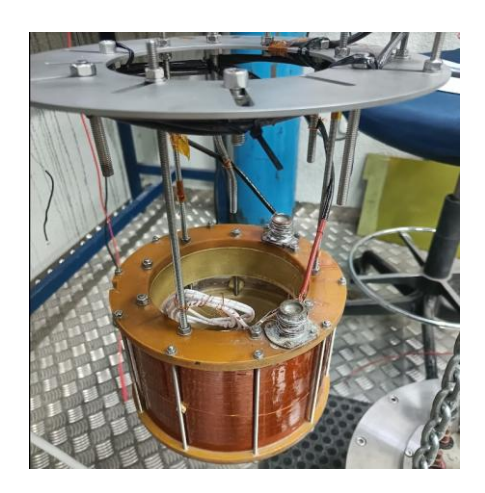


Table 18. Main electromagnetic properties of crisa magnet

Parameter	Value
Superconducting material	NbTi
Operating temperature	4.2 K
Nominal current	450 A
Critical current	$\sim 600~\mathrm{A}$
Superconductor field nominal (critical)	5.89 T (7.7 T)
Centre field nominal (critical)	4.25 T (5.88 T)
Inductance	0.56 H
Inner bore	$\Phi 180 \ x \ 125 \ mm$

Figure 53. CRISA superconducting magnet used as magnetic source in magnetocaloric test stand.

3.3.1 Electromagnetic Analysis

For the correct analysis of the performance of the magnetocaloric material it is important to have a precise map of the magnetic field, and to have a correct understanding of the performance and operation of the magnet in use.

The geometric characteristics of the coil and cable are defined in Table 19 and Table 20, which are used for the magnetic field computation.

Table 20. Superconductor cable information

Table 19 Geometry of CRISA magnet		
Geometry		
Int. radius	94.36	
Ext. radius	107.5	
Height	123.75	
Number of turns	1782	

Parameter	
Geometry	Rectangular
Dimensions (non- insulated)	0.61x1.13 mm
Dimensions (insulated)	0.73x1.25 mm
Cu/Sc ratio	1.65 mm
N° of filaments	7068
Filament diameter	7 μm
RRR	>100
Length	1200 m.

Figure 54 shows the positions of both packed beds inside the magnet bore. Figure 55 provides the magnetic field map and indicates the location of the packed beds at nominal current. The magnetic field is not constant along the packed beds, varying in both the axial and radial directions.

For the one-dimensional numerical model developed in the previous chapter, the magnetic field is assumed to vary along the axial length of the regenerator. To account for this variation, a mathematical function was formulated to relate the magnetic field to both the applied current and the axial position within the packed bed. This relationship is expressed as $B(I,x) = B_{nom}(x) * \frac{I}{I_{nom}}$, where $B_{nom}(x)$ represents a vector containing magnetic field values along the regenerator axis at the nominal current of 450 A. These values were computed using electromagnetic simulations performed in Ansys Maxwell.

In addition to axial variation, the magnetic field also exhibits radial non-uniformity. To address this, the average magnetic field at each axial position was calculated and used to define $B_{nom}(x)$. This approach ensures that the model captures the spatial distribution of the magnetic field while simplifying its integration into the governing equations.

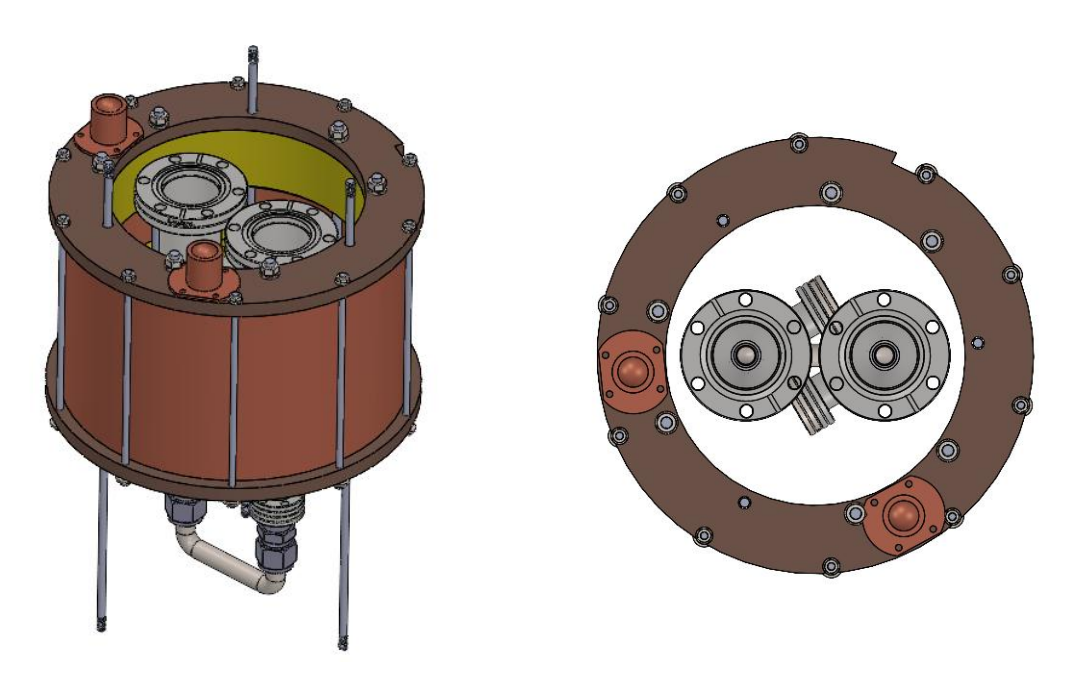


Figure 54. Position of the packed bed housing inside the CRISA magnet bore.

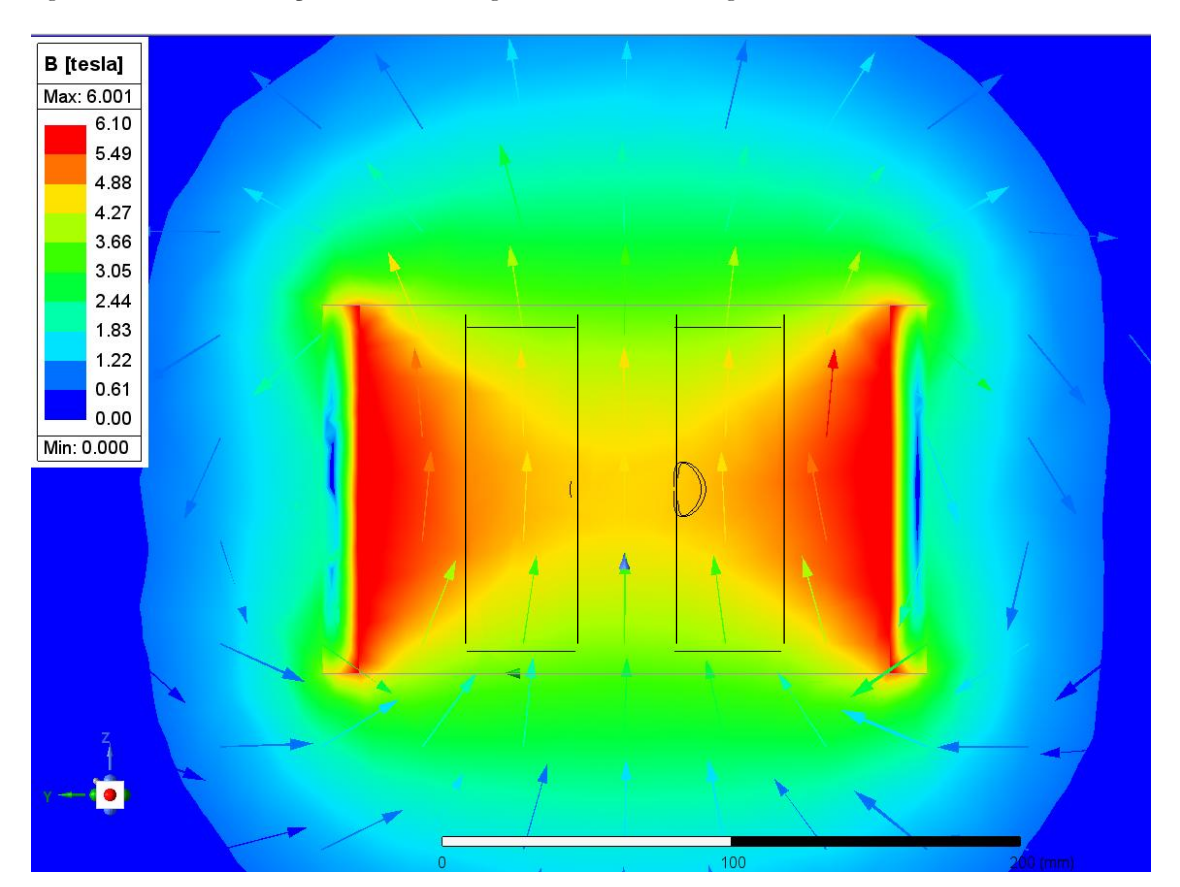


Figure 55. Map of the simulated magnetic field in the YZ plane of the CRISA magnet with both packed beds placed inside the magnet bore.

3.3.2 Electrical Circuit

Figure 56 shows the schematic of the test. A power source fed the superconducting magnet, and in parallel there is a resistor that allows to dissipate the energy of the magnet in case of quench (defined in Section 3.3.2.1). R_c is the resistance of the cables that power

the magnet, R_p is the protection resistance, R_{cl} is the resistance of the resistive part of the current leads, and finally L_{sc} represents the magnet itself.

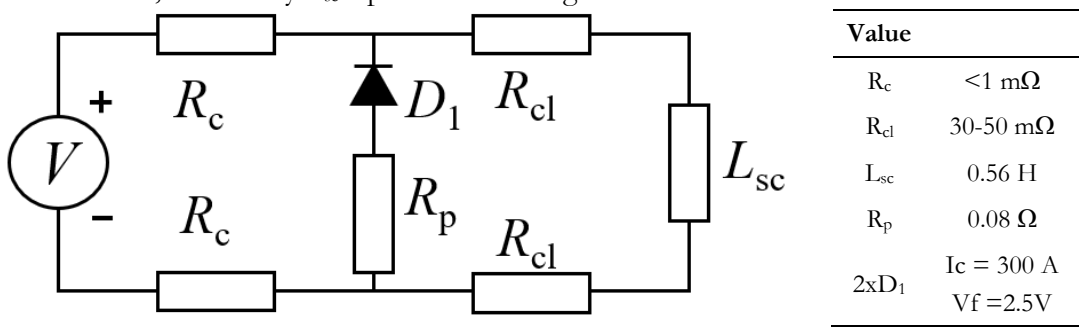


Figure 56. Schematic of the electric circuit of the superconducting magnet and main components value.

The magnet will be cycled following a trapezoidal function as shown in Figure 57, to be able to ramp the magnet, up and down, in 20 seconds we will need at least a voltage ±12.6V. An EA-PSB 10060 power source model will be used capable of providing up to 1000A, 60V and 30kW.

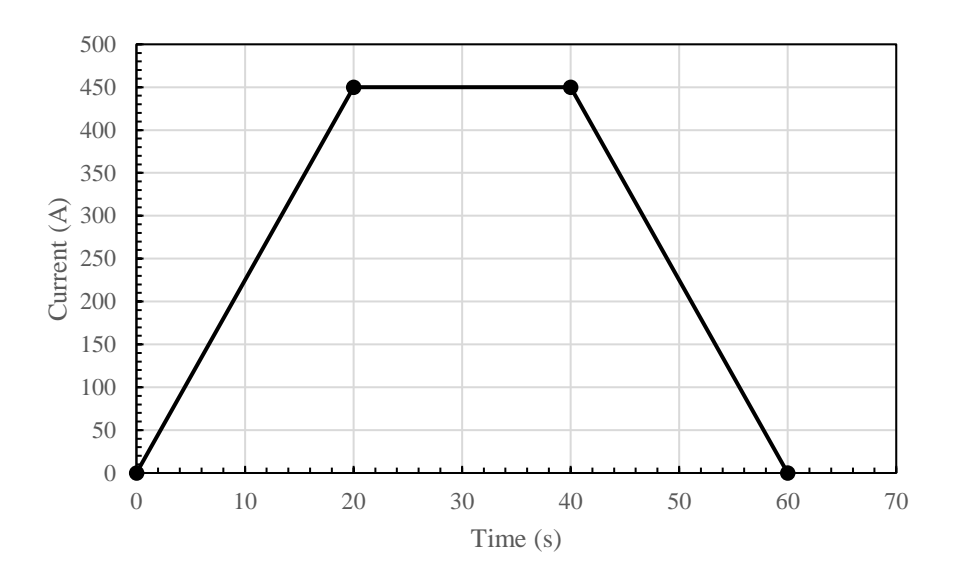


Figure 57. Target magnetic cycle during testing.

3.3.2.1 Critical current and magnet protection

The operation of a superconducting magnet requires a detection and protection system in case a quench happens. A quench occurs when a part of the superconducting material transitions from the superconducting state to a normal resistive state. This transition can be triggered by various factors such as exceeding the critical current, local heating, or external disturbances. When quenching happens, the affected region generates heat due to its resistance, which can propagate rapidly through the superconductor, causing a cascade effect that may lead to the entire magnet becoming resistive.

To compute the critical current in a superconducting magnet, it's crucial to account for the specific properties of the superconducting material, including its temperature, the surrounding magnetic field, and the wire's geometry. The critical current is the maximum current that the material can conduct while remaining in the superconducting state. Exceeding this limit initiates quenching.

Since there is no available data of the critical curve of the superconducting material, the current density of a known manufacturer has been used. Using this data, the critical current obtained is lower than the critical current reported in previous documentation. ($\sim 500 \text{ A}$ vs 600 A). Figure 58 shows the load line of the magnet.

The magnet will be operated at a maximum current of 450 A in this test stand, which is 75% of the initially reported critical current, providing a conservative safety margin. However, it is worth noting that the coil has previously reached a maximum current of 433 A. Therefore, while aiming for 450 A, we should be prepared for the possibility of a quench. Additionally, there is a non-zero probability that the magnet may require retraining at lower current values.

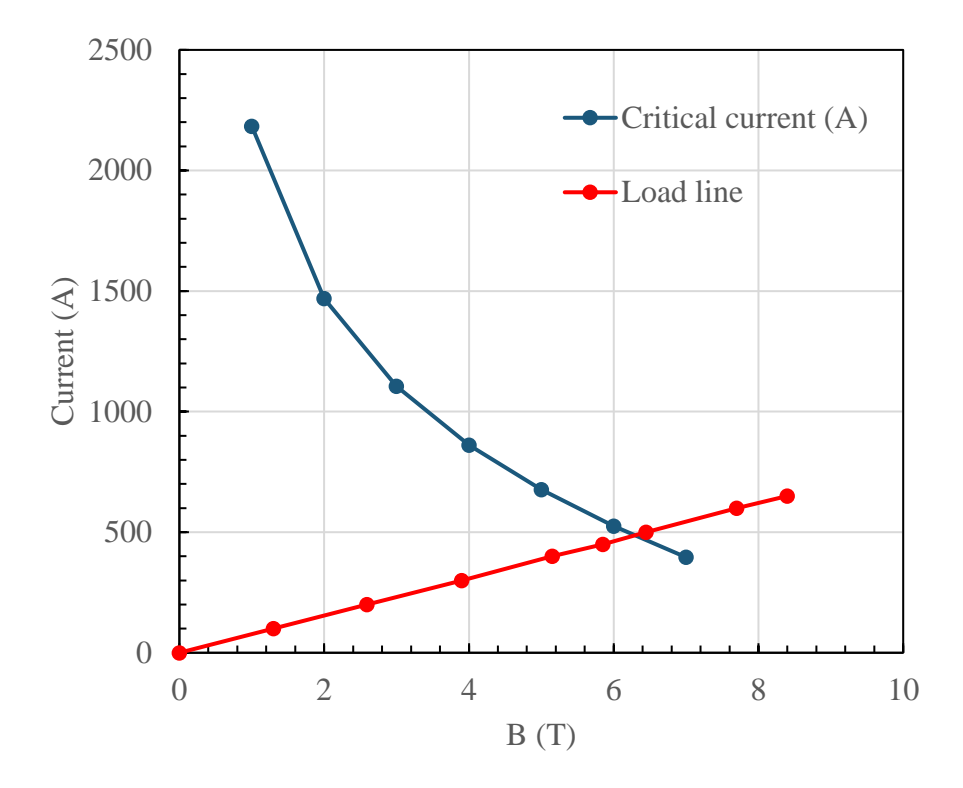


Figure 58. Expected load line of the CRISA magnet.

The potential impact of a quench is closely related to the energy stored in the coil, which during maximum current operation is 56 kJ. Although the coil could technically be operated without protection, a dump resistor will be used to extract some energy and reduce helium consumption.

Two different programs have been used to simulate the quench, one developed specifically for this test by the author, and the other program is the standard quench simulation program used in CIEMAT [117]. The most relevant results of the coil's behavior with a $0.5~\Omega$ dump resistor are shown in Figure 59.

The peak temperature remains within the safe range (< 200 K), although the voltage nearly reaches 1500 V when using the second simulation program. Previous experimental tests have indicated that this voltage may be overestimated, as the observed current decay was slower than the simulated decay, with stabilization times of 600 ms versus 300 ms. The energy extracted using the dump resistor is only 5 kJ, resulting in a reduction of helium consumption by approximately 10%.

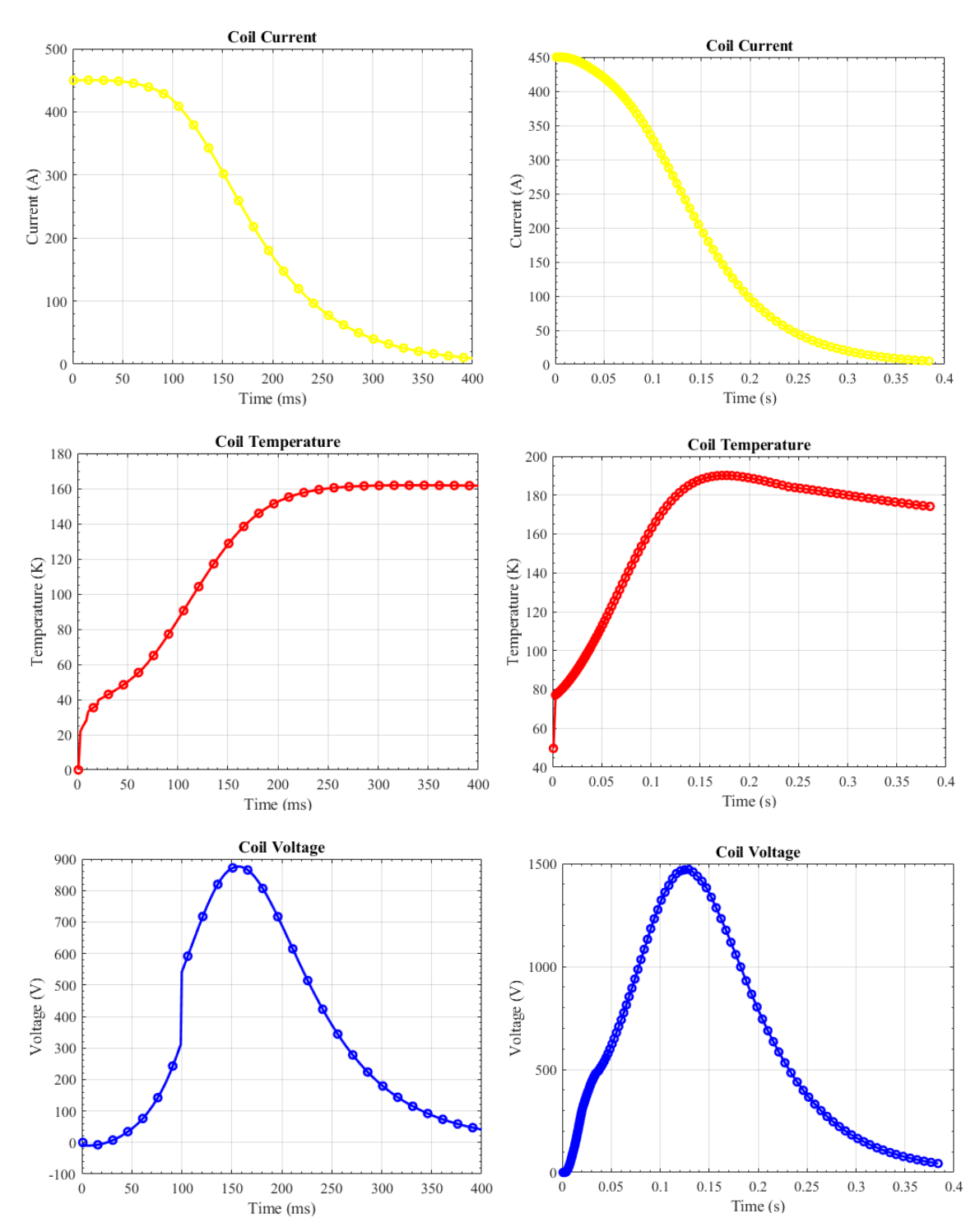


Figure 59. Quench simulation results using a 0.5 Ohm resistance showing a) Current decay b) Temperature evolution c) Voltage evolution. The simulations were done with two codes, on the left the results from the inhouse developed code and on the right the results using CIEMAT developed code.

3.3.3 Superconducting Magnet Testing

The CRISA magnet was tested in stand-alone mode before commissioning the entire setup to mitigate potential risks. During this test, the magnet will be cooled with liquid helium. The objectives shown in Table 21 are set for the CRISA magnet tests:

Table 21. Objectives for the CRISA magnet tests

Objective		Description	Target value (if applicable)
Electromagnetic	Magnet status	Check magnet status, analyze if it is possible to reach nominal current (450 A.)	I > 250 A
	Magnetic Field measurement	Measure the magnetic field in the center of the magnet. Optional: Ambient temperature measurements for full magnetic field mapping	B > 2 T
	Ramping rates	Check operation of power source and test the developed control programs. Test different ramp times.	Ramp times: 20 s
	Protection system	Check existing equipment for quench detection and protection. Ensure proper working during ramping.	
Cryogenics		Validate procedure for LHe handling during testing. Establish leak rates of the cryostat.	

3.3.3.1 Test results

The magnet cooling was successful. The first test done was the measurement of the coil inductance from the terminals of the current leads outside the cryostat. The values were found to be within the expected range.

Afterwards the magnet was powered up to nominal current. Figure 60 shows retraining from the magnet before achieving its nominal current, as it quenched during the first test at 312 A, probably due to the long time out of operation. The detection and protection system behaved as expected.

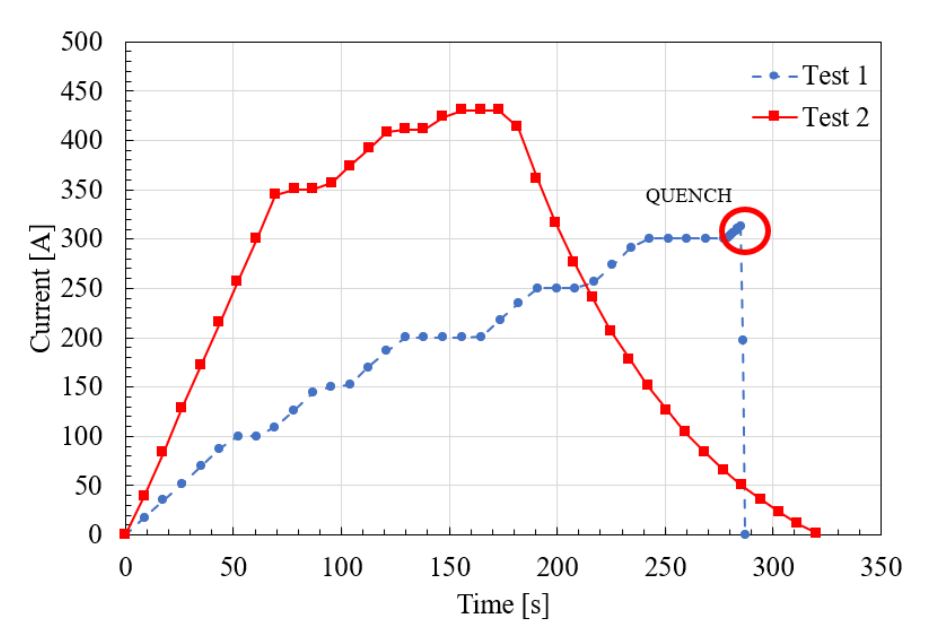


Figure 60. Measured current ramp-up during training of CRISA superconducting magnet.

During the magnet power-up the magnetic field was measured with a teslameter. Figure 61 shows magnetic field measurements versus the expected values, there was a small relative error in the measurement probably due to the placement of the teslameter inside the magnet bore.

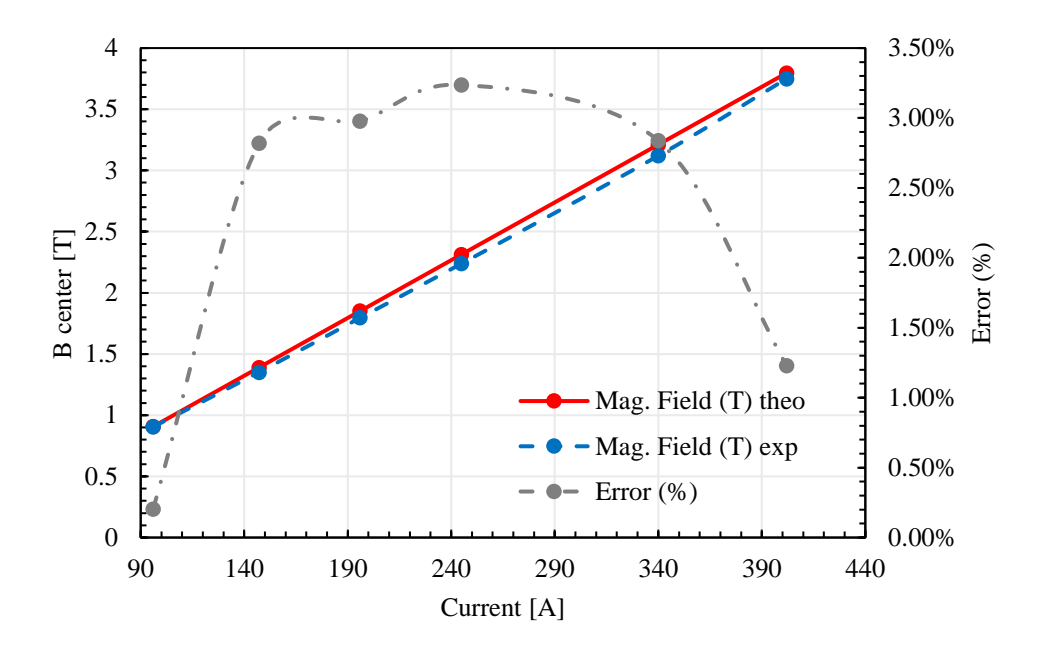


Figure 61. Magnetic field measurement of the CRISA magnet during ramping.

Finally, the magnet was ramped up to 250 A at varying ramping rates, ranging from 5 A/s to the target rate of 20 A/s. Figure 62 (left) illustrates the successful ramping of the magnet. However, a complete magnetic cycle could not be achieved because the power source was unable to absorb the magnet's energy at the required rate during the rampdown phase. This limitation is expected, as the power source used was unipolar, and the high inductance of the magnet significantly slows the response of the RL circuit. Figure 62 (right) shows the ideal versus the actual cycle obtained with the set-up.

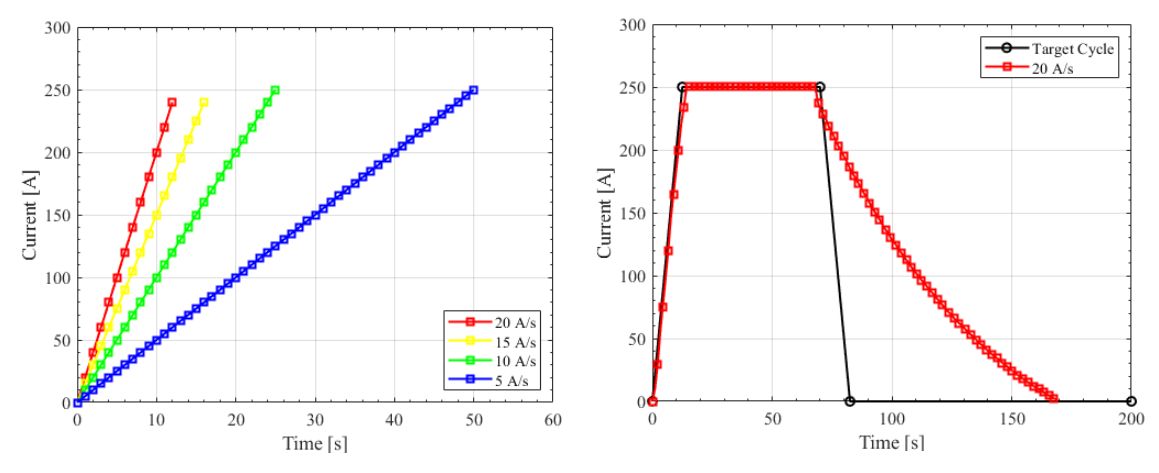


Figure 62. Ramping of the magnet to 250 A at different ramping rates, from 5 to 20 A/s (left), target cycle versus real cycle during testing (right).

Table 22 summarizes the results from the magnet experimental campaign.

Table 22. Summary of CRISA magnet testing results

		Notes
Electromagnetic	Magnet status	Reached more than 410A
	Magnetic Field measurement	Reasonable for the level of precision available in the measurement configuration. Reached 3.9 T.
	Ramping rates	Ramps up achieved successfully. Consider changes to increase the speed of the ramps down.
	Protection system	The protection system acted correctly when it was required.
Cryogenics		Positive results in handling LHe, from injection to extraction. The vessel appears to maintain its seal.

3.3.4 Final Assembly

The magnet commissioning tests were satisfactory but to be able to fulfill the test expectations the electrical circuit should be modified in order to allow ramping down the magnet at higher velocities.

Figure 63 shows the updated electrical circuit, the main change was that the location and value of the protection resistance was changed. The resistance was put in series to the superconducting magnet, to increase the time constant value of the equivalent RL circuit. The value of the resistance was slightly increased from $0.08~\Omega$, to $0.1~\Omega$.

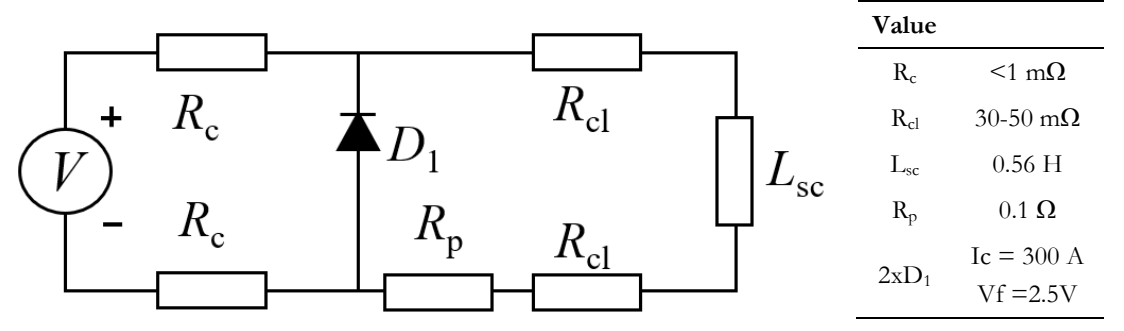


Figure 63. Updated schematic of the experimental test with protection resistance placed in series.

This configuration is not highly efficient, and rarely adopted in the operation of a superconducting magnet, since there is significant heat waste, $Q = I^2R > 20 \text{ kW}$ at maximum current (450 A). The resistors must be capable of rejecting that amount of heat to the environment. Figure 64 shows the resistors protection set-up.



Figure 64. Protection resistance set-up. Equivalent resistance of 0.1 Ω .

3.4 Heat Transfer Circuit

The heat transfer system employs a closed helium gas circuit, which is divided into two primary sections: the ambient side, housing the pumping circuit, and the cryostat side, where the magnetocaloric packed beds are located.

Figure 65 provides a schematic representation of the experimental setup. The system incorporates a mechanical pump, while pressure and mass flow are regulated using two mass flow controllers (MFCs), designated as MFC1 and MFC2 in Figure 65. Within the cryostat, helium gas is cooled in a specialized three-fluid heat exchanger. This device is termed a "three-fluid heat exchanger" because the incoming fluid stream passing through the packed bed transfers heat to two separate fluid streams: the returning stream of the closed-loop circuit and the evaporated helium originating from the liquid helium bath that submerges the magnet.

This section is structured into two parts. The first part briefly describes the key components of the pumping circuit, while the second part provides a detailed discussion on the design, manufacturing, and testing of the three-fluid heat exchanger.

3.4.1 Pumping circuit

The pumping circuit is located at ambient temperature, the main components of the pumping circuit are summarized in Table 23.

Table 23. Summary of main components of pumping circuit

Equipment	Model
Mechanical Pump	KNF Diaphragm Gas Pump
	N 630.1.2
Mass flow controllers	Voegtlin mass flow controllers
Fluid circuitry	Swagelok tubes and fittings

A mechanical pump from KNF which is helium compatible was used. The pump is oil free, with low leakage and low vibration. The pressure and mass flow of the system are controlled with two mass flow controllers (MFC), MFC1 and MFC2 in Figure 65.

Before entering the cryostat side there are three manual valves (MV) which control the flow direction inside the cryostat, allowing the testing of two different materials during the same set of experiments.

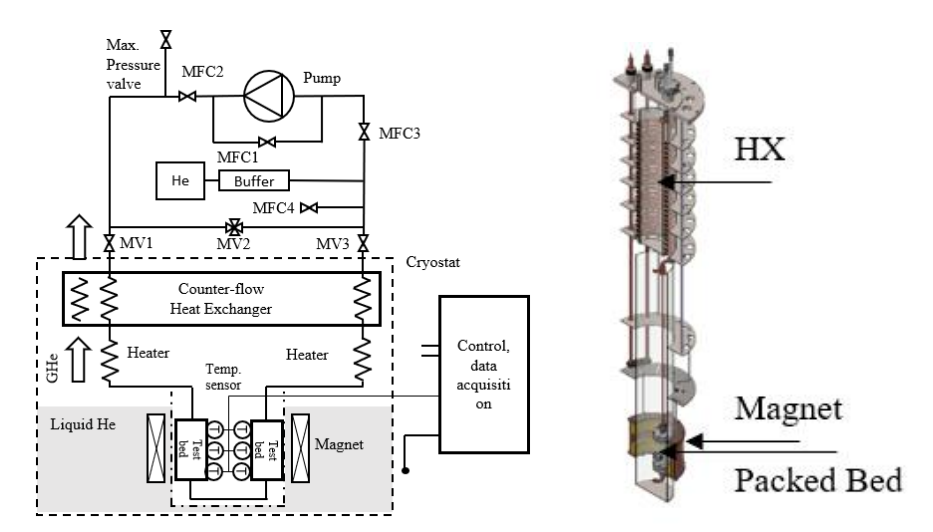


Figure 65. Schematic of apparatus and data acquisition system (left), the portion enclosed by dashed lines is inside a cryostat. Cryostat side of the test stand (center). Schematic of the heat exchanger (right).

3.4.2 Three-Fluid Heat Exchanger

The primary purpose of the three-fluid heat exchanger is to cool the helium mass flow as it passes through the packed bed. This is achieved by recovering the enthalpy of the evaporated helium within the heat exchanger. To enable simultaneous testing of both packed beds, a coaxial-type heat exchanger has been proposed.

This component is critical to the test stand, as its performance directly determines the ability to achieve the desired temperature conditions in the packed bed. The complexity of the heat exchanger arises not only from the significant temperature gradient between its inlet and outlet but also from the mechanical and industrial challenges inherent in its design and fabrication. This section outlines the procedures for designing, manufacturing, and validating this essential component.

3.4.2.1 Definition and Boundary Conditions

The helium gas enters the cryostat and is cooled within a three-fluid heat exchanger (HX), which features a coaxial tubular design. This design incorporates a shell specifically engineered to direct and concentrate the flow of evaporated liquid helium, optimizing heat transfer efficiency. The configuration and operation of this heat exchanger are illustrated schematically in Figure 66.

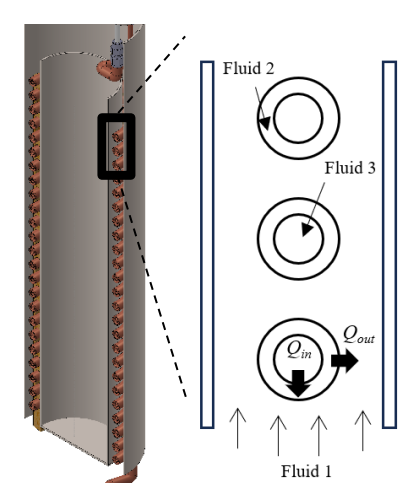


Figure 66. Detailed view of the cross section of the heat exchanger, showing the heat transfer (Q_{out}) from fluid 2 (Annular fluid) to fluid 1 (Evaporated fluid), and the heat transfer (Q_{in}) from fluid 3 (Interior fluid) to fluid 2.

This cryogenic heat exchanger resembles a Giauque-Hampson heat exchanger [1], but it incorporates an additional heat recovery stage between the two coaxial tubes.

The nomenclature for the helium streams is defined as follows:

- Fluid 1 refers to the evaporated helium gas originating from the liquid helium bath.
- Fluid 2 corresponds to the helium gas flowing through the annular region of the heat exchanger.
- Fluid 3 represents the helium gas traversing the inner tube.

The high-pressure (HP) fluid can be either fluid 2 or fluid 3, depending on the configuration of manual valves shown in Figure 65:

- Configuration 1: fluid 2 as HP fluid.
- Configuration 2: fluid 3 as HP fluid.

Figure 67 and Table 24 presents a simplified schematic of the heat exchanger along with boundary conditions for configuration 2, where fluid 3 functions as the HP fluid. This configuration is identified as less effective, as the thermal resistance from the cold to hot source is larger.

The coordinate system depicted in Figure 67 is consistent across all configurations, with x = 0 always denoting the outlet of the HP fluid (the cold side of the HX).

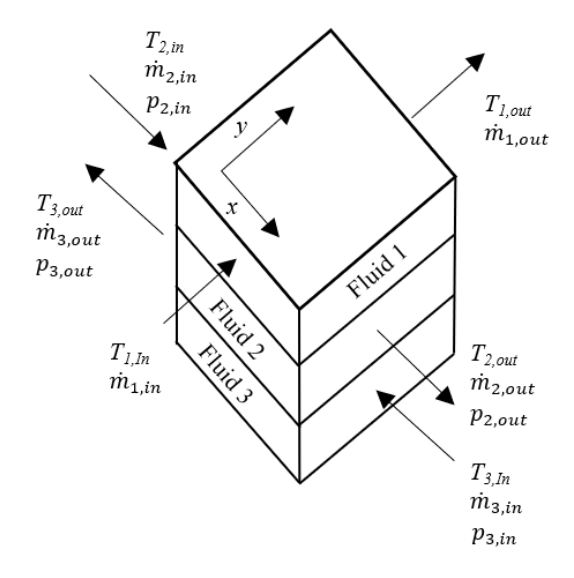


Table 24. BCs and Fluid 3 thermal targets

Boundary conditions	Values
Fluid 1 (Evaporated LHe)	$T_{1,in} = 6 K$ $\dot{m}_{1,in} = 40 g/min$
Fluid 2 (LP GHe)	$T_{2,in} = T_{3,out} + 2 K$ $\dot{m}_{2,in} = \dot{m}_{3,in}$ $p_{2,in} = p_{3,out}$
Fluid 3 (HP GHe)	$T_{3,in}=293K$
Thermal target	
Fluid 3 (HP GHe)	$T_{3,out} = 10K$ $\dot{m}_{3,in} = 10 \ g/min$ $p_{3,in} = 1.5 \ bar$

Figure 67. Boundary conditions of the 3-fluid heat exchanger.

The primary objective is to achieve a temperature of 10 K at the outlet of fluid 3 while maintaining a mass flow rate of 10 g/min. The boundary conditions for fluid 1 are determined based on cryostat heat losses and prior experimental data. In contrast, the boundary conditions for fluids 2 and 3 are governed by other components in the circuit, particularly by the pressure-mass flow characteristics of the mechanical pump. To enhance the design's safety margin, a temperature gradient of 2 K is added to the inlet temperature of fluid 2 relative to the outlet temperature of fluid 3.

3.4.2.2 Thermohydraulic Modelling

For the thermal design of the heat exchanger the methodology and nomenclature presented in [118] will be adopted. Table 25 shows the definition of the main dimensionless variables used in the thermal modeling.

Table 25. Dimensionless groups for three-fluid parallel. Stream heat exchangers with two thermal communications

Dimensionless independent parameters				
Symbol	Definition	Title	Meaning	
NTU ₁	$\frac{(UA)_{1,2}}{\left(\dot{m}c_p\right)_1}$	Number of transfer units	Thermal size measure	
$C_{1.2}^{*}$	$\frac{\left(\dot{m}c_{p}\right)_{1}}{\left(\dot{m}c_{p}\right)_{2}}$	Heat capacity rate ratio	Thermal balance measure	
$C_{3,2}^*$	$\frac{\left(\dot{m}c_{p}\right)_{3}}{\left(\dot{m}c_{p}\right)_{2}}$	Heat capacity rate ratio	Thermal balance measure	
R^*	$\frac{(UA)_{3,2}}{(UA)_{1,2}}$	Conductance ratio	Heat conductance balance	
$\Theta_{i, ext{in}}$	$\frac{T_{i,in} - T_{1,in}}{T_{2,in} - T_{1,in}}$	Inlet temperature ratio	Inlet relative temperature levels	
Dimensionless dependent variables (effectiveness)				
\hat{v}_1	$\frac{T_{1, \text{ out }} - T_{1, \text{ in}}}{T_{2, \text{ in }} - T_{1, \text{ in}}}$	Temperature effectiveness of fluid 1	The degree to which the temperatures of outer	
\hat{v}_3	$\frac{T_{3, \text{ out }} - T_{3, \text{ in}}}{T_{2, \text{ in }} - T_{3, \text{ in}}}$	Temperature effectiveness of fluid 3	fluids have approached the inlet temperature of the central fluid	
ε	$rac{\dot{Q}}{\dot{Q}_{ ext{max}}}$	Three-fluid heat exchanger effectiveness	Measure of the exchanger performance	

In this analysis, the following idealizations and approximations are adopted:

- 1. The three-fluid heat exchanger operates under steady-state conditions. Mass flow rates are constant, and fluid temperatures at the inlet and within the exchanger are also independent of time.
- 2. The heat exchanger is adiabatic; that is, heat losses to the surroundings are negligible.

- 3. The specific heats and other fluid and material properties are temperature dependent. The properties have been obtained from [119].
- 4. Non-linear pressure drop, and friction losses have been considered for fluid 2 and 3. No friction losses have been considered for fluid 1.
- 5. Zero heat conduction is assumed in fluids or in walls parallel to the fluid flow direction.
- 6. The fluid flow rate is uniformly distributed through the exchanger on each fluid side. The velocity and temperature at the entrance of the heat exchanger on each fluid side are uniform.

The heat balance and momentum equations of the 3-fluid heat exchanger are:

$$\frac{\partial T_1}{\partial y} - \frac{(UA)_{1,2}}{Y_0(\dot{m}c_p)_1} (T_1 - T_2) = 0 \tag{3.5}$$

$$t\frac{\partial T_2}{\partial x} - \frac{(UA)_{1,2}}{X_0(\dot{m}c_p)_2} (T_2 - T_1) + \frac{(UA)_{3,2}}{X_0(\dot{m}c_p)_2} (T_3 - T_2) + \mu_{JT,2} \frac{\partial P_2}{\partial x} = 0$$
 (3.6)

$$-t\frac{\partial T_3}{\partial x} - \frac{(UA)_{3,2}}{X_0(\dot{m}c_p)_3}(T_3 - T_2) + \mu_{JT,3}\frac{\partial P_3}{\partial x} = 0$$
(3.7)

$$t\frac{\partial P_3}{\partial x} = f_2 \frac{\dot{m}_2^2 X_0}{2\rho_2 A_2^2 D_{2,h}} \tag{3.8}$$

$$-t\frac{\partial P_3}{\partial x} = f_3 \frac{\dot{m}_3^2 X_0}{2\rho_3 A_3^2 D_{3,h}} \tag{3.9}$$

Where P_k is the pressure of fluid k (k = 2,3), $\mu_{JT,k}$ is the Joule-Thomson coefficient, f_k is the friction factor coefficient, ρ_k , is the fluid density, and A_k is tube cross section. The variable t indicates the direction of the closed helium circuit inside the cryostat, a value of 1 indicates that fluid 2 is the HP fluid, and a value of -1 that fluid 3 is the HP fluid.

The variable T_i is the temperature of each fluid (i = 1,2,3), $(UA)_{I,j}$ is the heat transfer coefficient, $U_{i,j}$, multiplied by the heat transfer area, $A_{i,j}$, between two fluids, $(\dot{m}c_p)_I$ is the heat capacity rate for each fluid, and X_0 is the heat exchanger flow length in the x direction. Since the heat exchanger has the form of a spiral, the y direction has been eliminated by a change of variable to reduce the problem dimension: $\partial y = \frac{\partial x * p}{\sqrt{c^2 + p^2}}$, where p and C are the pitch and circumference of the heat exchanger.

The dimensionless equations of the 3-fluid heat exchanger are:

$$\frac{\partial \Theta_1}{\partial \xi} = NTU_1(\Theta_2 - \Theta_1) \tag{3.10}$$

$$t\frac{\partial \Theta_2}{\partial \xi} = NTU_1 C_{12}^* (\Theta_2 - \Theta_1) - NTU_1 C_{12}^* R^* (\Theta_3 - \Theta_2) - \frac{\mu_{JT,2}}{T_{2,in} - T_{1,in}} \frac{\partial P_2}{\partial \xi}$$
(3.11)

$$-t\frac{\partial \Theta_3}{\partial \xi} = NTU_1 R^* \frac{C_{12}^*}{C_{23}^*} (\Theta_3 - \Theta_2) - \frac{\mu_{JT,3}}{T_{2,in} - T_{1,in}} \frac{\partial P_3}{\partial \xi}$$
(3.12)

$$t\frac{\partial P_2}{\partial \xi} = f_2 \frac{\dot{m}_2^2}{2\rho_2 A_2^2 D_{2h}} \tag{3.13}$$

$$-t\frac{\partial P_3}{\partial \xi} = f_3 \frac{\dot{m}_3^2}{2\rho_3 A_3^2 D_{3,h}} \tag{3.14}$$

The nondimensional parameters are defined as follows:

$$\Theta_i = \frac{T_i - T_{1,in}}{T_{2,in} - T_{1,in}}, \qquad \xi = \frac{x}{X_0}$$
(3.15)

$$NTU1 = \frac{(UA)_{1,2}}{\left(\dot{m}c_p\right)_1}, \qquad C_{12}^* = \frac{\left(\dot{m}c_p\right)_1}{\left(\dot{m}c_p\right)_2}, \qquad C_{23}^* = \frac{\left(\dot{m}c_p\right)_3}{\left(\dot{m}c_p\right)_2}, \qquad R^* = \frac{(UA)_{3,2}}{(UA)_{1,2}}$$
(3.16)

3.4.2.2.1 Heat transfer and pressure correlations

The determination of heat transfer coefficients involves a systematic evaluation of fluid dynamics in both external (fluid 1) and internal flows (fluids 2 and 3). The computation integrates Reynolds numbers for flow regime characterization, incorporating necessary geometric modifications for inline tube arrangements [120]. The Nusselt number correlations, defined distinctly for internal and external flows, are expressed as:

$$Nu = \frac{h_c D_e}{k_t} \text{ (internal flow)} \tag{3.17}$$

$$Nu = \frac{h_c L}{k_t} \text{ (external flow)}$$
 (3.18)

The overall heat transfer coefficient calculation employs an equivalent thermal circuit approach, accounting for convective and conductive resistances:

$$\frac{1}{U_i} = \frac{1}{R_{conv,i}} + R_{cond} + \frac{1}{R_{conv,i+1}}$$
(3.19)

In the appendix the applied heat transfer correlations for each type of flow can be found. The pressure gradient analysis follows the Darcy-Weisbach formulation:

$$\frac{\partial P}{\partial x} = f \frac{\dot{m}^2 L}{2\rho A^2 D_h} \tag{3.20}$$

where the friction factor f is determined through established correlations for both laminar and turbulent regimes, with appropriate consideration of the Reynolds number in the annular passage.

3.4.2.3 Mechanical Design

The design challenge of the heat exchanger goes beyond achieving optimal thermohydraulic performance; it also needs to fit within the spatial limitations of the cryostat and account for the fabrication and manufacturing constraints specific to this type of heat exchanger. Evaluating these factors shows that some of them are at odds with each other, necessitating a compromise. For instance, there is a trade-off between effectiveness and cost, as achieving very high thermal performance typically demands complex technical solutions, which in turn lead to expensive manufacturing processes and efforts.

Table 26 summarizes the key mechanical variables considered in the heat exchanger design, along with the preliminary constraints imposed by the cryostat enclosure. These constraints influence critical design parameters: first, the shell diameter, as well as the dimensions of internal components such as the coil and mandrel, and second, they affect the overall length of both the shell and mandrel, which, in combination with the coil pitch, determines the final length of the coil.

Table 26 Main design parameters of heat exchanger components

Parameter	Outer Pipe	Inner Pipe
Pipe Diameter	Φ_{out}	Φ_{in}
Pipe Width	t_{out}	t_{in}
Pipe length	Ι	_
Pipe Material	Mate	erial
Coil Diameter	$\Phi_{coil} < \Phi_{shell}$	
Coil Height	$H_{coil} = 267 \ mm$	
Pitch	P	
	Shell & Mandrel	
Shell Diameter	$\Phi_{shell} <$	155 mm
Mandrel Diameter	$\Phi_{mandrel} < \Phi_{coil}$	
Length	$H_{coil} = H_{shell} = H_{mandrel} = 267 mm$	

The adopted procedure for mechanical optimization is outlined as follows:

The shell and mandrel were designed to focus the flow and enhance the turbulence of the evaporated helium gas passing through the heat exchanger. The shell's diameter was maximized to its practical limit of 155 mm to simplify the manufacturing process of the heat exchanger coil. A larger winding diameter for the coil offers several advantages, including easier winding without deformation, the possibility of using thinner tube walls, and an increased heat exchanger length relative to its height.

The mandrel diameter was selected as a compromise between optimizing heat exchange performance, facilitating assembly, minimizing the risk of undesired thermal contacts, and ensuring material availability. Ultimately, the spacing between the mandrel and coil was matched to the spacing between the coil and shell, resulting in a mandrel diameter of approximately 125 mm. The heights of both the shell and mandrel were also maximized to extend the flow path of the evaporated gas within the heat exchanger, thereby improving thermal performance.

Stainless steel 316L was chosen as the material for both components due to its availability in the required dimensions, its favorable mechanical properties—particularly its low thermal conductivity—and its cost-effectiveness. The final values for the shell and mandrel are defined in Table 27.

Table 27 Shell and mandrel dimensions

Parameter	Shell	Mandrel
Diameter	155 mm	125 mm
Height	267 mm	267 mm
Thickness	1 n	nm
Material	31	6L

The heat exchanger coil employs a coaxial tubular configuration, with the defining variables summarized in Table 26. Similar to the shell and mandrel design, determining these variables required balancing multiple factors, including thermal performance, mechanical integrity, feasibility, material availability, and cost. Some decisions were guided by qualitative considerations.

To minimize thermal resistance among all configurations, copper was selected as the material for the tubing due to its excellent thermal conductivity and ease of fabrication. Extensive testing was conducted on copper tubes of varying diameters and thicknesses to

evaluate their minimum bending radii and ensure compatibility with the manufacturing process. During these tests the following was acknowledged:

a) Small thicknesses: below 1 mm. are prone to dent if the bending radius is too small (<100 mm.). Figure 68 shows a sample heat exchanger with a dented tube. Since the coil radius was estimated to be around 130-150 mm. a tube thickness of 1 mm. was preferred. For this thickness tubes of 12 and 6 mm. offered a reasonable choice when evaluating their availability and thermal performance.



Figure 68. Sample coil dented at the exit angle.

b) Stainless steel wire: the presence of an inner wire of stainless steel soldered to the inner tube helps during the winding process as it increases the rigidity of the assembly. It also increases the heat exchange surface area of the annular flow. Figure 69 shows the result of soldering the stainless steel wire to the inner copper tube.

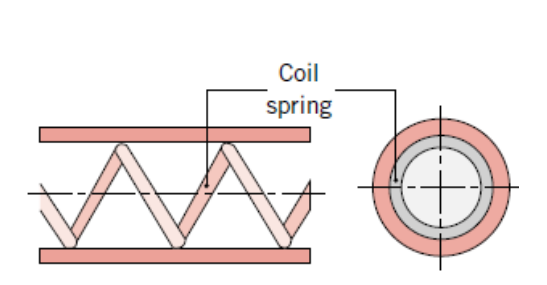




Figure 69. Addition of an inner wire soldered to the inner tube.

c) Pitch: the winded coil has certain spring-back, tendency to return to its original position, so to ensure a constant pitch it is necessary to incorporate spacers.

With the additional knowledge obtained from these tests the variables to be optimized were reduced to one, the length of the heat exchanger, as the pitch is related to the length, the height and the diameter of the coil. Table 28 summarizes the heat exchanger dimensions prior to the numerical optimization.

Parameter	Shell	Mandrel
Pipe Diameter	$\Phi_{out} = 12 mm$	$\Phi_{in} = 6 mm$
Pipe Width	$t_{out} = t_{in}$	= 1 mm
Pipe length	L	
Pipe Material	Copper DHP C12200	
Coil Diameter	$\Phi_{coil} = 14$	40 mm
Coil Height	$H_{coil}=2$	50 mm
Pitch	p	

3.4.2.4 Methodology and Numerical Scheme

Having reduced the number of variables the objective of the problem is reduced to the determination of the minimum length of the heat exchanger subjected to the established boundary conditions, i.e. that the outlet temperature of fluid is smaller than 10 K in steady-state conditions.

This type of optimization problem is typically categorized as a sizing problem, which is a traditional inverse problem in heat transfer systems. However, since there is no explicit closed form formula for NTU in this case, an iterative approach is adopted.

The ODE system, Eqs. (3.10-3.14), is solved in Matlab using the bvp5c solver. A fixed mesh of n cells is generated to divide the length of the heat exchanger into smaller segments. Within each cell, the non-dimensional parameters of the ODE (NTU, thermal capacity rates, and thermal capacity ratio) are evaluated iteratively to account for the temperature-dependent properties of the materials and fluids used. The mesh is refined adequately to ensure a converged solution is obtained. Figure 70 shows the process used by the numerical model scheme to find the adequate heat exchanger length to reach the target temperature.

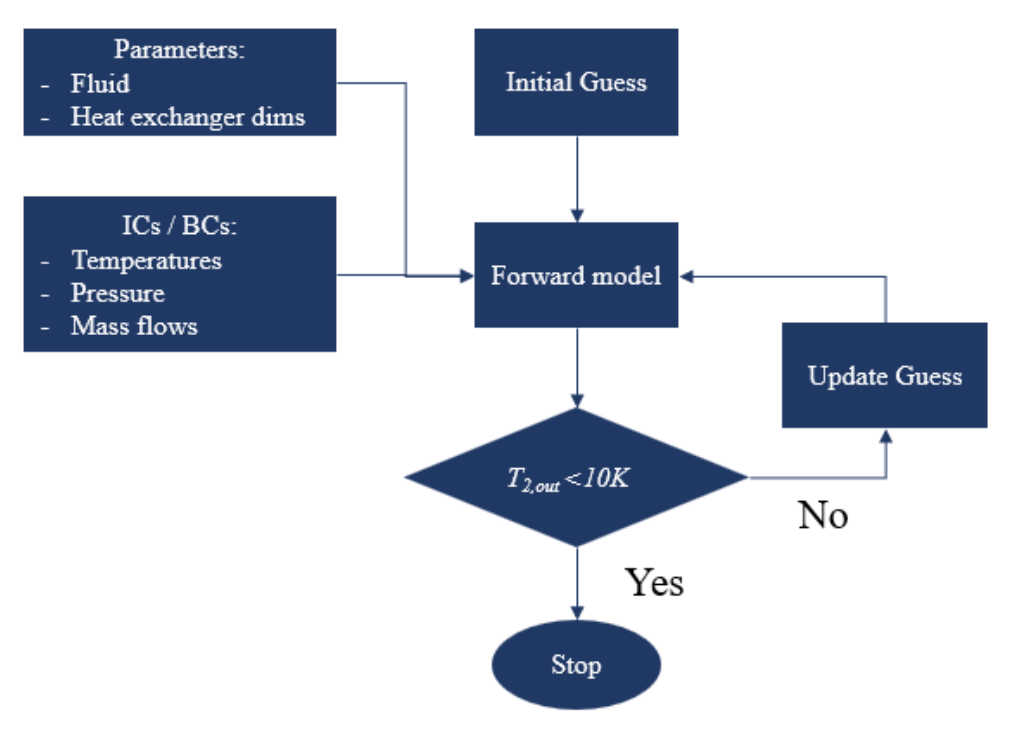


Figure 70. Flowchart illustrating the iterative numerical scheme for optimizing the heat exchanger length.

3.4.2.5 Pretesting

The boundary conditions outlined at the beginning of this section, as summarized in Table 24, were estimated based on prior experiments conducted within the same cryostat. However, there remains considerable uncertainty regarding the boundary conditions of fluid 1, particularly concerning whether the estimated mass flow rate and temperature achieve the required accuracy.

Deviations from the expected boundary conditions can significantly affect the overall performance of the heat exchanger. This sensitivity is illustrated in Figure 71. The left panel demonstrates how variations in the temperature boundary condition of fluid 1 influence its outlet temperature, while the right panel highlights the impact of changes in the mass flow rate.

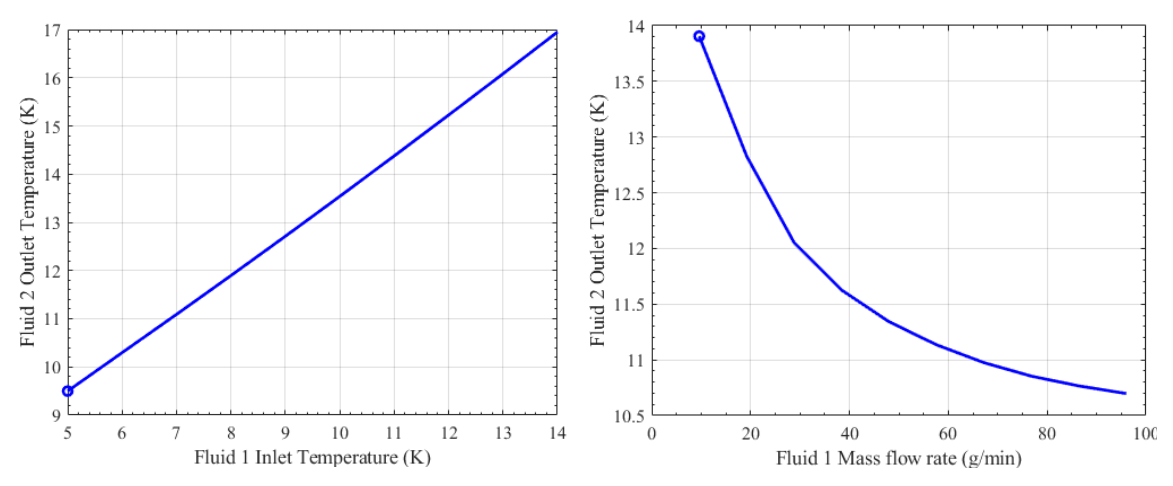


Figure 71. Influence of fluid 1 inlet temperature in fluid 2 outlet with fixed values of length (8 m.) and a fluid 1 mass flow (0.1 g/s) (left), and influence of mass flow with fixed values of length (8 m.) and a fluid 1 inlet temperature (7 K) (right).

Due to the uncertainties associated with the boundary conditions of fluid 1, a series of additional measurements were conducted during the testing of the superconducting magnet. The primary objectives of these measurements were: (i) precise determination of the mass flow rate of fluid 1, (ii) accurate measurement of its inlet temperature, and (iii) estimation of the confidence interval for the heat transfer coefficient.

To measure the mass flow rate, a flow counter already installed in the laboratory was employed. For determining the inlet temperature, a diode temperature sensor was positioned slightly above the intended placement of the heat exchanger.

To analyze the convective heat transfer coefficient of evaporated gaseous helium (GHe), a copper cylinder equipped with a heater was specifically designed and installed above the inlet temperature sensor. Figure 72 shows the placement of the copper cylinder in the cryostat. This setup enabled the calculation of the convection coefficient through an energy balance approach:

$$Q_{heat} - Q_{cool} = mc_p \frac{dT}{dt} (3.21)$$

$$Q_{cool} = hA(T_f - T_s) (3.22)$$

By varying Q_{heat} with the resistance inside the copper cylinder, enough points could be obtained to be able to solve for the heat transfer coefficient with a high level of security.



Figure 72. Placement of copper cylinder with heater for the evaluation of the heat transfer coefficient.

Figure 73 and Table 29 show the results of the test. For the temperature inlet a value of 6 K was selected while for the mass flow a value of 40 g/min was established. The validation of the heat transfer coefficient values was less straightforward, as the established method and the acquired data were not conclusive due to a divergence of the experimental heat transfer coefficient of 0.5-2 times the theoretical heat transfer coefficient. A margin of security was established by multiplying the heat transfer coefficient by 0.5.

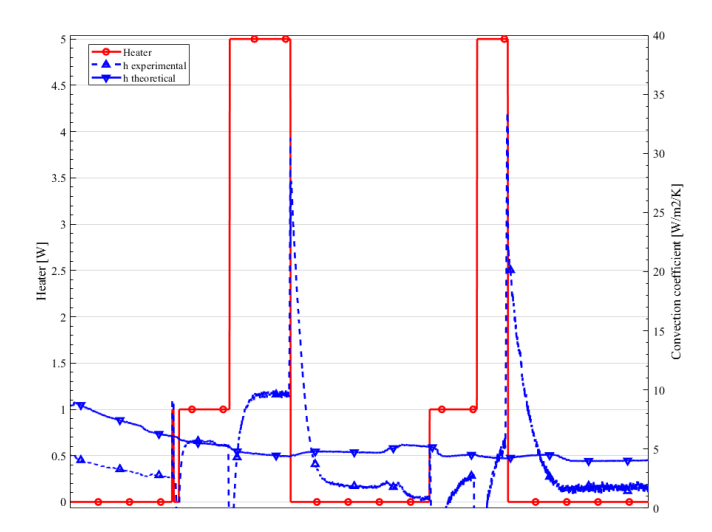


Table 29. Percentile distribution values for inlet temperature and mass flow rate

Percentile	T _{in}	Mass flow [g/min]
Minimum	3.98	42.42
25 %	4.21	43.8
-0 / 0		10.0
50 %	4.73	43.8
75 %	5.65	45.24
70 70	0.00	
Maximum	8.05	46.74

Figure 73. Experimental vs theoretical heat transfer coefficient during the superconducting magnet tests. Solid lines represent theoretical data, and discontinuous lines represent experimental data.

3.4.2.6 Design Analysis

Figure 74 illustrates the relationship between the outlet temperature of fluid 3 and the length of the heat exchanger under the previously defined boundary conditions. The figure reveals that the exchanger's length increases almost exponentially to achieve the final fractions of a Kelvin reduction in temperature. This challenge in lowering the outlet temperature arises primarily from the imposed boundary conditions, particularly the limited temperature gradient between fluids 2 and 3.

Table 30 presents the finalized dimensions of the heat exchanger, which has a total length of 10.25 meters. A substantial safety margin was incorporated into the length selection, reflecting the critical role of this component in the successful development of the test stand.

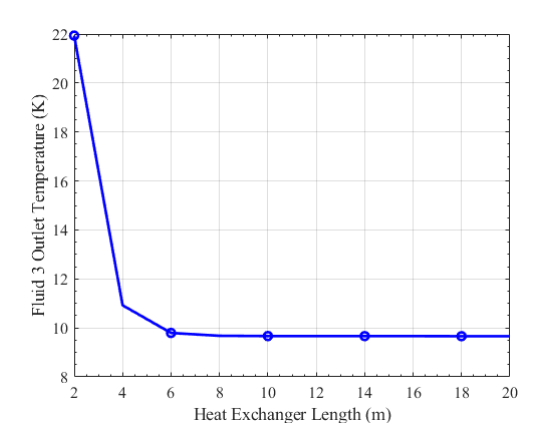


Table 30.	Thermal	design	values	for the	3-fluid HX

Parameter	Outer Pipe	Inner Pipe
Pipe Diameter	12 mm	6 mm
Pipe Width	1 mm	1 mm
Temperature range	293-12 K	10-125 K
Pressure Drop	1 mbar	1.5 mbar
Pipe length	10.2	5 m
Effectiveness	98.2	2%
Pipe Material	Cop	per
Diameter & Height	150 mm x	250 mm

Figure 74. Fluid 3 outlet temperature ($\xi = 0$) as function of heat exchanger length.

Figure 75 shows the temperature distribution along the heat exchanger for each fluid with the final dimensions. Notably, there is a temperature crossover between fluids 2 and 3 at $\xi = 0.05$, where the heat exchange between the two fluids changes sign. This crossover arises from the boundary conditions defined at the outset of the design process, which specified that the returning fluid—designated as fluid 2 in this case—maintains a positive temperature gradient of 2 Kelvin relative to fluid 3.

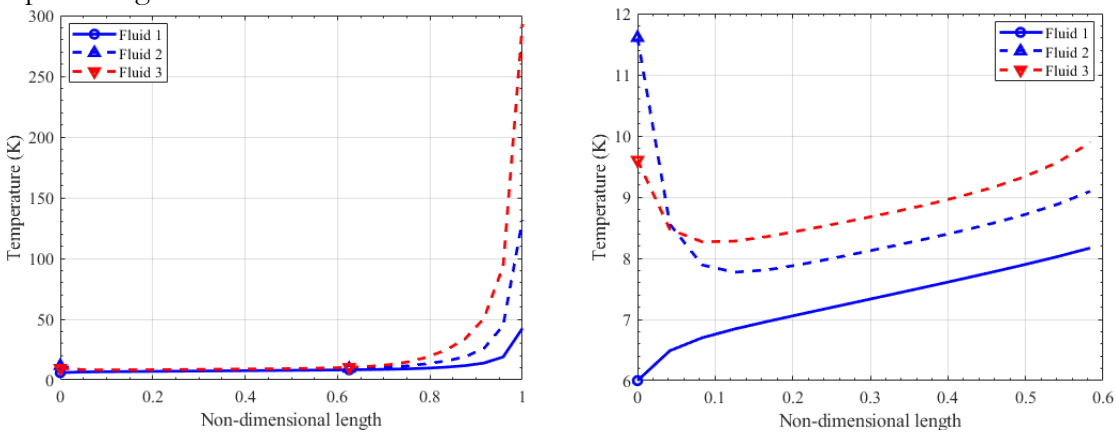


Figure 75. Temperature evolution along the heat exchanger (left), with a detailed view in the 0-0.6 non-dimensional length (right).

The effectiveness of the heat exchanger varies non-linearly along its length. A substantial portion of the NTU exchange between fluid 1 and the other fluids occurs predominantly near the hot end. The primary reason is the temperature dependence of the gas properties on the NTU.

Figure 76 (left) shows the evolution of NTU1 across the heat exchanger. The reduction of NTU and the temperature cross at the beginning of the heat exchanger explains the low marginal gain of effectiveness with length shown in Figure 74.

Figure 76 (right) shows the pressure loss of each fluid along the heat exchanger. The total pressure loss at nominal conditions is just 2.5mbar.

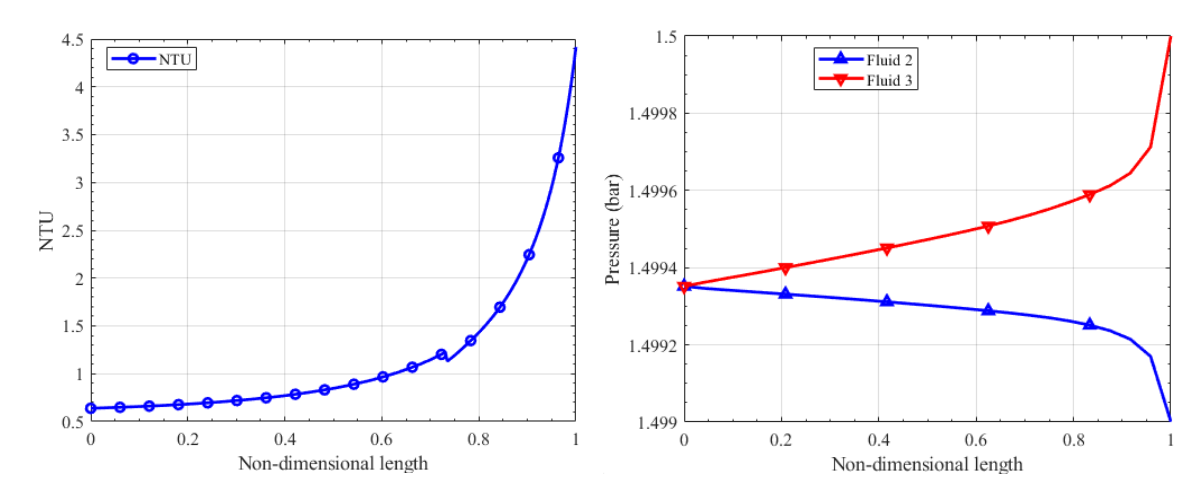


Figure 76. NTU between fluid 1 and fluid 2, denominated NTU₁ in the text, evolution along the heat exchanger (left), and pressure evolution along the heat exchanger length (right).

3.4.3 Commissioning of Three-Fluid Cryogenic Heat exchanger

3.4.3.1 Assembly

The manufacturing of the heat exchanger was done in collaboration with a private company called ANTEC. The manufacturing process was divided into two parts. First, the stainless-steel wire was soldered to the smaller tube, and then the 6 mm tube was inserted into the 12 mm tube. Second, the coil was wound into the desired shape.

Once the heat exchanger was received (shown in Figure 77), it was prepared for integration into the test stand. The initial steps included cleaning the heat exchanger, adapting components for better integration, and fabricating the outlet connectors.



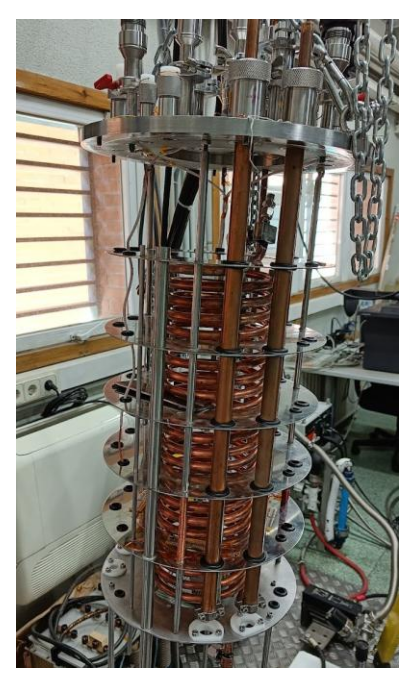


Figure 77. Heat exchanger as received with fiber glass separators (left), and heat exchanger assembled in cryostat (right)

Cleaning the heat exchanger proved challenging. The annular area containing the soldered stainless-steel wire was more contaminated than anticipated, with weld slag observed during visual inspection. This area was difficult to access, and traditional copper cleaning methods were not feasible, as manually scrubbing the area with a chemical agent was impossible.

After several iterations, the following cleaning process was established: (1) blow the heat exchanger with pressurized dry air, (2) place it in an ultrasound machine for 15 minutes using NGL 17.40 SP ALU III, (3) blow it again with pressurized dry air, and (4) circulate alcohol through the heat exchanger to remove any traces of the chemical agent. This process was repeated until no slag was detected in the alcohol residue.

The fiberglass components that maintain the required distance between the tubes (shown in Figure 77) needed modification to fit correctly within the heat exchanger. The inner diameter of the holes where each tube was allocated was initially defined as 13 mm (compared to the 12 mm tube diameter). However, due to the tubes becoming more elliptical during the winding process, they no longer fit into the separator slots, which themselves were outside the established tolerances and often smaller than specified. The slots were subsequently machined using a 13-14 mm drill bit.

The heat exchanger tube connectors were fabricated in-house from a copper bar. The assembly process was iterative: initially, one of the tubes was brazed to the connector, but due to excessive slag accumulation the process was modified. In the next iteration, the connection to the heat exchanger was secured using soldering and Stycast to ensure hermeticity.

However, during the assembly of other components, one of the connectors broke twice. The combination of soldering and Stycast proved insufficiently robust, necessitating the fabrication of a new connector. This time, the connector was made from a stainless-steel tube with a larger diameter. The part was brazed to the heat exchanger while argon gas was circulated through the heat exchanger to minimize the formation of weld slag inside. Figure 78 shows the two type of tested connectors.





Figure 78. Glued copper heat exchanger connector (left), and stainless-steel connector before brazing (right).

3.4.3.2 Validation: Liquid Nitrogen Testing

3.4.3.2.1 Test Set-Up

To evaluate the performance of the heat exchanger prior to using liquid helium, it was tested with liquid nitrogen as the evaporating fluid. This approach not only reduces costs but also mitigates risks associated with the final test stand configuration, as many components are shared between the two setups.

During these tests, the fluid circuit bypassed the heat exchanger, redirecting the flow to an instrumented container designed to measure the fluid temperature. Additionally, a heater was installed in the liquid nitrogen bath to regulate the evaporation rate. Figure 79 presents the circuit schematic and the final assembly used for these tests. Notably, the test

bed depicted in Figure 79 was not filled with particles during these trials but was instead equipped solely with temperature instrumentation.

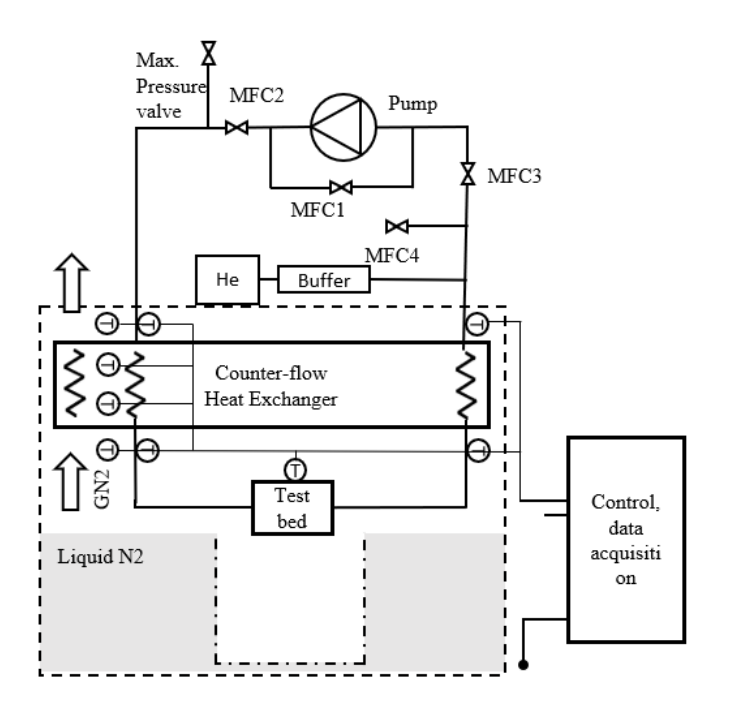




Figure 79. Schematic for the validation of the heat exchanger performance (left), and final testing assembly for liquid nitrogen characterization of the heat exchanger (right).

The most challenging aspect of this assembly was the connections of heat exchanger to the other parts of the fluid circuit. Figure 80 shows the upper and lower connections as finally assembled.





Figure 80. Upper (left) and lower (right) side of the heat exchanger.

Figure 81 and Table 31 shows the position and the type of temperature sensors used for the liquid nitrogen tests.

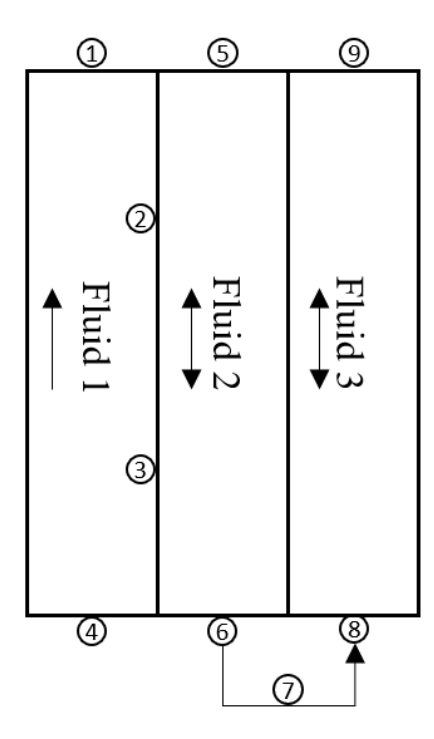


Table 31. Type of temperature sensor used in heat exchanger characterization

Туре		
PT100	2,3,5,9	All sensors were placed in the outer wall of the heat exchanger tube
Diode	1,4	
CERNOX	6,7,8	Sensor 6 and 8 were placed in the wall, while sensor 7 was placed inside the circuit

Figure 81. Temperature sensor position and type along the heat exchanger.

Temperature sensor 7, which is inside the bypass between fluid 2 and 3 was positioned inside the fluid circuit, to precisely acquired the temperature at the end of the heat exchanger. In order to place a temperature sensor inside the circuit, a hermetic feedthrough sealed with Stycast 2850 FT was developed and tested. Figure 82 (right) shows the sealed feedthrough.



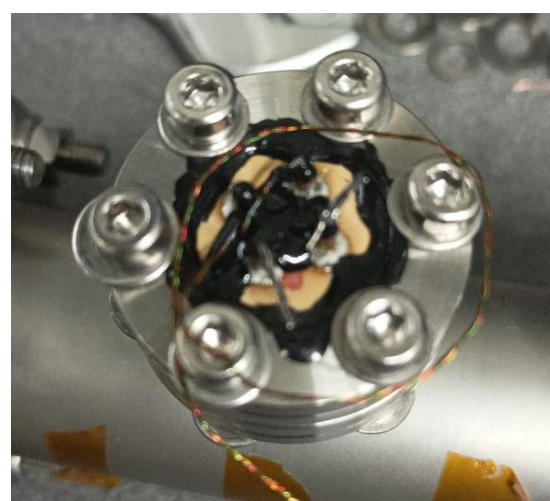


Figure 82. Position of temperature sensor 4, at the heat exchanger inlet (left), and instrumentation sensor sealed with Stycast (right).

3.4.3.2.2 Test Results

Before the liquid helium tests, the heat exchanger was tested in a liquid nitrogen bath to validate the design and compare the theoretical model against experimental data. The heat exchanger was bypassed at the outlet, connecting the fluid 2 inlet with the fluid 3 outlet, and instrumented with CERNOX temperature sensors at different locations to acquire the real operating data of the 3 fluids. Table 32 shows the measured conditions in each test, which are used as inputs for the numerical model.

Test – HP fluid	LN2 Test-Fluid 2	LN2 Test-Fluid 3
	$T_{1,in} = 77.8 K$	$T_{1,in} = 77.8 K$
Fluid 1 (Evaporated cryogen)	$\dot{m}_{1,in} = 0.55 \frac{g}{s}$	$\dot{m}_{1,in} = 0.55 \frac{g}{s}$
	$T_{2,in}=290\ K$	$T_{3,in}=290K$
Fluid 2/3	$T_{3,in} = T_{2,\text{out}}$	$T_{2,in} = T_{3,out}$
	$p_{2,in} = 1.5 \ bar$	$p_{3,in} = 1.5 \ bar$

Table 32. Measured boundary conditions during LN2 heat exchanger characterization

Figure 83 shows the temperature at the exit of the heat exchanger, against the model expected values. Each test was done in both configurations. Figure 83 (left) shows the configuration 1, fluid 2 as the high-pressure fluid, and in the right, Figure 83 shows the results from configuration 2, fluid 3 as the high-pressure fluid.

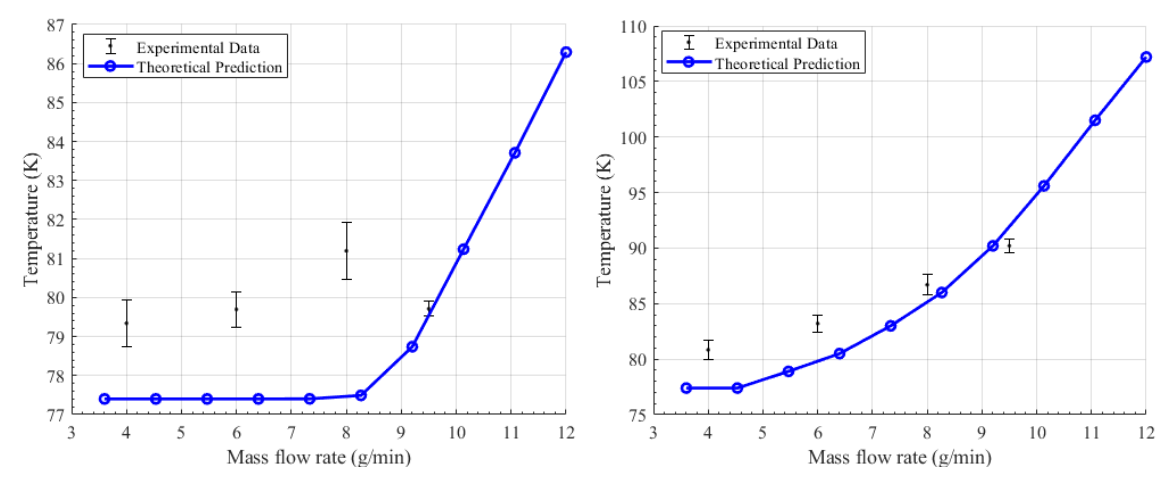


Figure 83. Fluid 2 (left) and Fluid 3 (right) outlet temperature ($\xi = 0$) as function of fluid 2/3 mass flow during liquid nitrogen testing

The discrepancies between the model and data are probably due to the model assumptions, specifically the neglection of heat conduction along the heat exchanger and the adiabatic hypothesis. However, the results were considered sufficiently accurate. After some final assembly optimizations to mitigate external heat leaks and increase the mass flow rate of fluid 1 through the heat exchanger, the last components of the magnetocaloric test stand were assembled for liquid helium testing.

3.4.4 Final Assembly and Liquid Helium testing

Following the completion of liquid nitrogen testing, the remaining components of the test stand were assembled. The packed bed, equipped with heaters as illustrated in Figure 52, was integrated downstream of the heat exchanger. Additionally, the superconducting magnet, along with the dry recipient designed to prevent contact between liquid helium (LHe) and the packed beds, was installed. Figure 84 provides an overview of the fully assembled system.

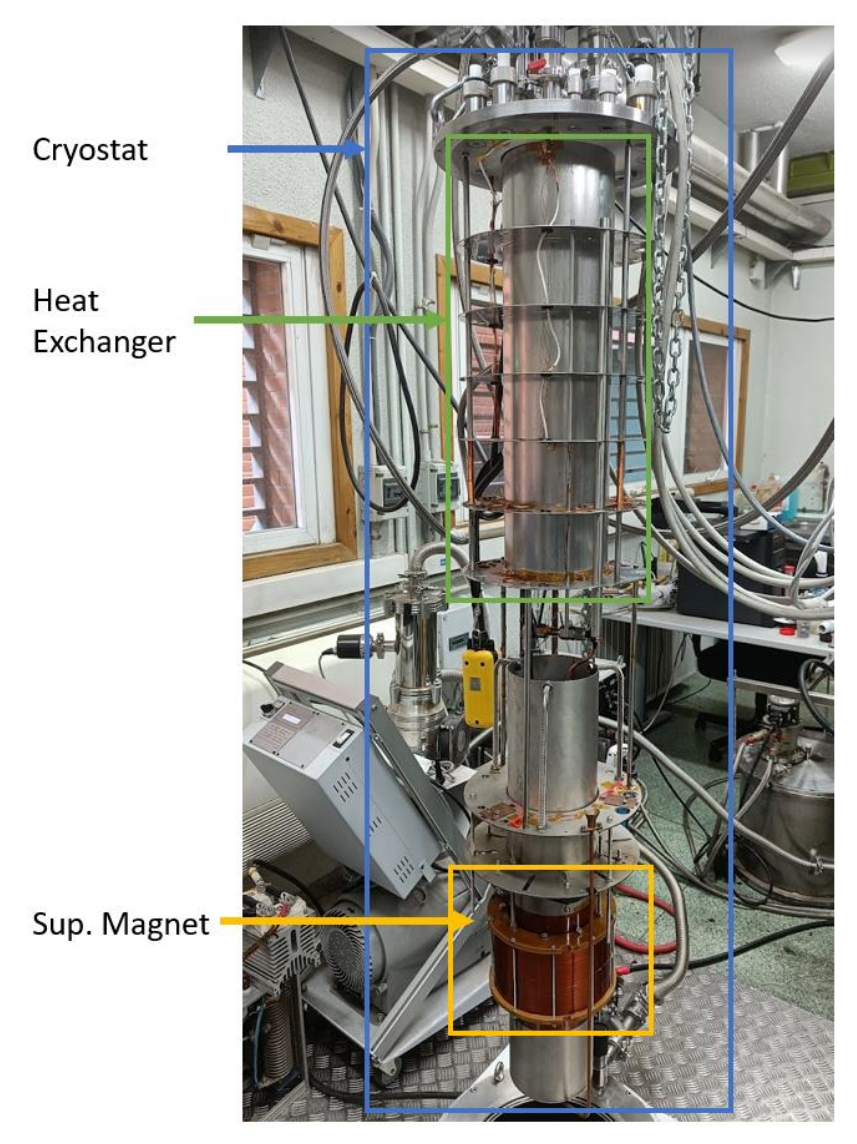


Figure 84. Final assembly of the MCE test stand. The superconducting magnet is placed at the base of the cryostat insert, with the dry recipient in its bore.

Table 33 shows the measured conditions in each test, used as inputs for the model.

Table 33. Measured boundary conditions during LHe heat exchanger characterization

Test – HP fluid	LHe Test-Fluid 2	LHe Test-Fluid 3
Fluid 1 (Evaporated cryogen)	$T_{1,in} = 4.8 K$	$T_{1,in} = 4.8 K$
Time T (Evaporated cryogen)	$\dot{m}_{1,in} = 0.7 \frac{\mathrm{g}}{\mathrm{s}}$	$\dot{m}_{1,in} = 0.7 \frac{g}{s}$
	$T_{2,in}=288K$	$T_{2,in}=288K$
Fluid 2/3	$T_{3,in} = T_{2,out}$	$T_{2,in} = T_{3,out}$
	$p_{2,in} = 1.9 bar$	$p_{3,in} = 1.9 bar$

Figure 85 presents the outlet temperatures for two configurations during liquid helium testing. The temperature reached far exceeded design target, reaching temperatures below 5 K. In this experiment, temperature measurements were taken 450 mm below the heat exchanger outlet, just before the fluid entered the test bed. The measured temperatures were found to be slightly lower than those predicted by the model, likely due to the additional heat transfer area provided by the connecting tube between the heat exchanger and the test bed. Despite this minor discrepancy, the objective—achieving an inlet temperature below 10 K for both test beds—was successfully met with a sufficient margin.

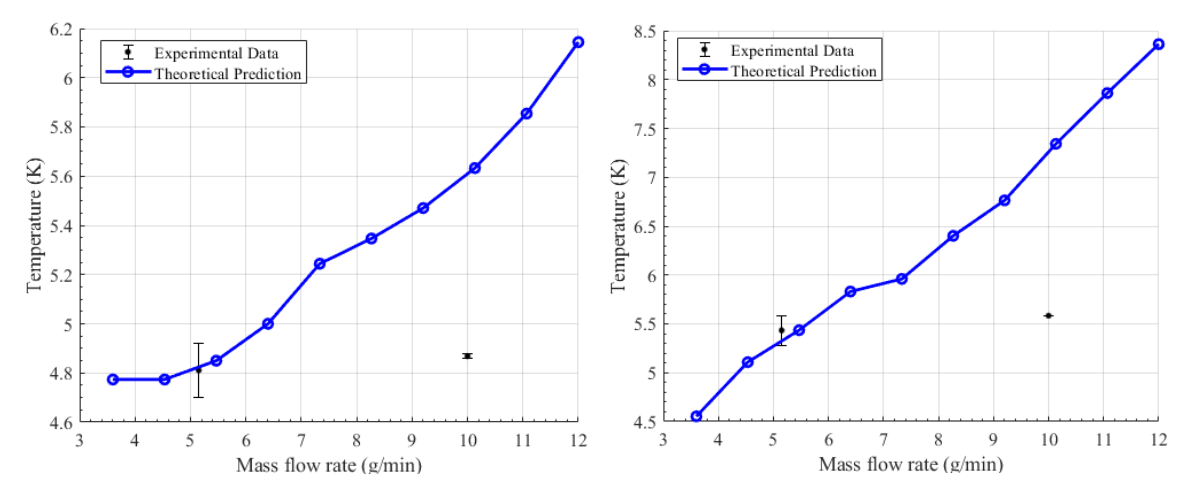


Figure 85. Fluid 2 (left) and Fluid 3 (right) at the entry of the magnetocaloric regenerator ($\xi = 0$) as function of fluid 2/3 mass flow during liquid helium testing.

3.5 Summary: Development of Test Stand

This chapter begins by emphasizing the importance of complementing analytical work with experimental investigations to achieve the outlined objectives. These objectives include acquiring expertise in magnetocaloric materials, developing a manufacturing process for the packed bed, validating the numerical model under ambient and cryogenic conditions, and demonstrating technological feasibility. Following the establishment of a conceptual design for the experimental test stand, the chapter is organized into three subsections.

The first subsection focuses on the production of magnetocaloric packed beds, specifically using gadolinium gallium garnet (GGG) and erbium aluminum (ErAl₂). These materials were crushed and sieved to particle sizes of approximately 0.3–0.5 mm before being housed in custom-designed CF fittings. The fittings were engineered to minimize porosity near 0.45 while avoiding flow blockages. Initial tests conducted under ambient conditions allowed for an evaluation of manufacturing tolerances and fluid-flow characteristics without prematurely subjecting the system to cryogenic environments.

The second subsection addresses the magnetic source, a NbTi superconducting magnet previously tested in quench studies. This magnet was selected for its ability to generate a magnetic field exceeding 2 T within a bore diameter of 180 mm, enabling simultaneous accommodation of two packed beds, for both magnetocaloric materials, GGG and ErAl₂. Electromagnetic simulations and experimental testing verified the magnet's operability within a safe current range of up to 450 A, ensuring reliable performance under experimental conditions.

The final subsection details the design and validation of a three-fluid coaxial heat exchanger, which was developed to cool helium flow to approximately 10 K before it interacts with the magnetocaloric beds. Initial validation was performed at liquid nitrogen temperatures to mitigate development risks, followed by successful operation with liquid helium. The system consistently achieved target temperatures below 10 K at a helium mass flow rate of 10 g/min. These efforts demonstrate that the experimental setup fulfills its primary objectives: enabling reliable studies of the magnetocaloric effect under cryogenic conditions, collecting experimental data on heat transfer and pressure drop, and facilitating comparisons with numerical models.

During this chapter, significant progress was achieved, including the establishment of manufacturing processes for magnetocaloric materials and the attainment of temperatures below 10 K at the magnetocaloric packed beds. These milestones represent critical steps toward validating the experimental setup and its capabilities. In the following chapters, the

test stand will undergo a series of experiments designed to evaluate its performance and address the established objectives.

Chapter 4: Experimental Procedure And Results

This chapter is organized into three sections to provide a comprehensive overview of the experimental process and outcomes.

The first section details the experimental procedures implemented for each test, including the operational aspects of the experimental apparatus and the specific objectives of each test. This section ensures clarity on the methodology and the intended outcomes of the experiments conducted.

The second section outlines the developments that occurred during the testing phase, including the procedures adopted for data acquisition. It also discusses any modifications and variations from the original plan, offering insights into the adaptability of the testing process in response to real-time challenges or observations.

The third section presents a selection of key data collected during the tests, while the remaining experimental data is provided in the appendix for reference. This section includes a qualitative analysis of individual test results, focusing on deviations from the initial targets and offering insights into these variations. By providing a transparent account of the data obtained, this section establishes a foundation for the more detailed analysis and discussion presented in the subsequent chapter.

4.1 Experimental Procedure

The experimental tests are targeted at validating the model presented in Chapter 2. The experimental tests are divided into two main parts:

- Heat transfer tests: the objective of these tests is the thermal characterization of the packed bed, providing validation to the heat transfer correlations between fluid and solid at cryogenic temperatures. The tests procedures were validated first at ambient temperature, and at liquid nitrogen temperatures. Although, the results that are presented here were made near liquid helium temperatures, in the range of 4.2-20 K.
- Magnetic tests: In these tests, the magnetic field was varied throughout the duration of the test. The objective was to measure the magnetocaloric effect and heat transfer properties by monitoring the temperature change in the fluid

The next subsections provide an overview of the test objectives and procedures undergone in the laboratory.

4.1.1 Heat Transfer Tests

The thermal performance of heat exchangers is typically assessed using various correlations available in the literature, many of which are derived from experimental measurements. However, as in the present case, these experimental studies are sometimes conducted under conditions that do not precisely match the specific operational boundaries of the intended application.

The purpose of these tests is to analyze the validity of the state-of-the-art correlations. With that objective, two transient measurement techniques will be used: the single-blow testing and periodic blow testing.

4.1.1.1 Single Blow testing

Single-blow testing technique is a transient method used to characterize heat exchangers, particularly regenerators like packed beds. It originated from early studies by Anzelius, Nusselt, Hausen, and Schumann [121] on transient heat transfer between a porous medium and a fluid, and it was first applied by Furnas (1932) for measuring heat transfer coefficients [122]. Comprehensive reviews of these developments are available in the literature.

The procedure followed during the experimental testing is as follows:

- 1. Steady-state: The packed bed is first brought to a steady-state condition, ensuring a uniform temperature distribution across both the magnetocaloric material and the fluid, typically within the range of 5 to 10 K. During testing, two types of temperature steps can be implemented: a hot step, which involves increasing the inlet temperature, and a cold step, which involves decreasing the inlet temperature. However, due to the considerations detailed in the following sections, only hot steps will be tested in this study.
- 2. Single Blow: A sudden change in temperature, in the form of a hot or cold step, is introduced into the fluid stream at the inlet of the heat exchanger with the activation of the heater placed at the packed entry.
- 3. Measurement: acquisition of the temperature with the sensors placed along the length of the packed bed as the thermal pulse moves through the system.

Figure 86 presents a simulation example of a single blow test conducted within the temperature range of 10 K to 20 K. In this simulation, $T_{\rm in}$ represents the inlet temperature, $T_{\rm Mid}$ corresponds to the temperature at the midpoint of the packed bed, and $T_{\rm Exit}$ denotes the temperature at the exit of the packed bed.

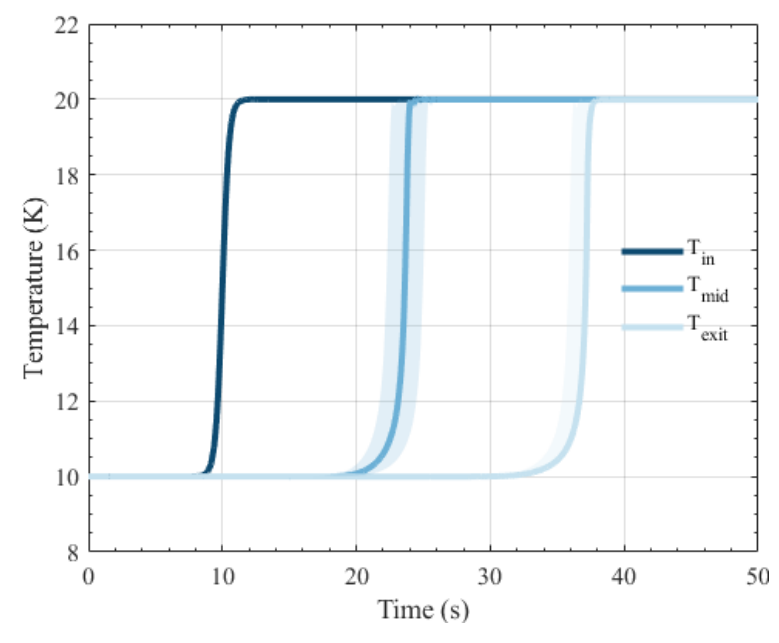


Figure 86. Simulated example of the temperature evolution during a single blow test.

4.1.1.2 Periodic Blow testing

The periodic blow testing technique represents an alternative approach for thermal characterization. In contrast to the single blow technique, this method involves imposing a periodic variation in either the inlet temperature or the flow rate of the working fluid. The

resulting oscillatory thermal response of the system is then analyzed to determine its heat transfer characteristics and dynamic thermal behavior.

The recorded temperature data are analyzed in the frequency domain, often employing Fourier transform techniques. This analysis yields the system's frequency response, from which key thermal parameters, such as the heat transfer coefficient and the thermal capacity, can be inferred. The dynamic thermal behavior over a range of frequencies is also elucidated.

The periodic blow testing technique is particularly advantageous for characterizing the dynamic thermal performance of systems subject to cyclic or oscillatory conditions. It provides a more detailed understanding of the frequency-dependent thermal behavior, which is critical for applications where the heat exchanger operates under varying thermal loads. The method's enhanced sensitivity to certain heat transfer characteristics, compared to the single blow technique, allows for a more nuanced analysis of the system's performance.

The procedure is as follows:

- 1. Steady-state: The packed bed is initially stabilized under steady-state conditions, ensuring a consistent thermal baseline.
- 2. Periodic Blow: A periodic fluctuation in temperature or flow rate is introduced at the inlet of the regenerator. In this set of experiments, the test stand is prepared to do temperature fluctuations controlling the heater voltage with a function generator.
- 3. Measurement: temperature oscillations are monitored using temperature sensors. Figure 87 shows an example of a periodic blow applied to the regenerator

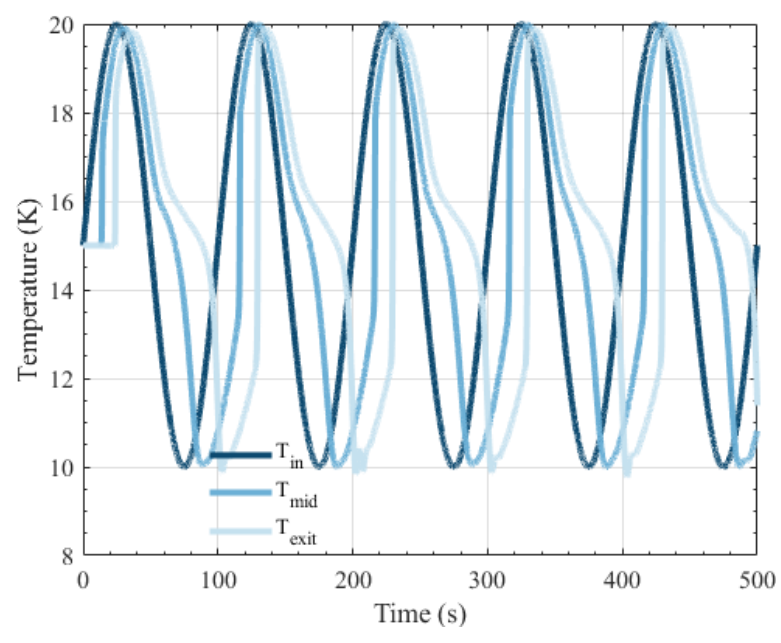


Figure 87. Simulated example of temperature evolution during a periodic blow test.

4.1.2 Magnetocaloric Tests

4.1.2.1 No-Load testing

The first set of tests done with a variable magnetic field are denominated "no-load" tests. The objective of these tests is to qualitatively evaluate the magnetocaloric effect on both materials. The procedure adopted for these tests is the following:

1. Remove helium gas in the regenerator by doing a vacuum in the gas helium circuit.

- 2. After some minutes, to ensure that the gas has been extracted apply a defined magnetic field profile.
- 3. Record data and temperature measurements in the regenerator.

Figure 88 shows a simulation of a no load test. In the case that adiabatic conditions are achieved the temperature in the regenerator will increase uniformly and proportional to the applied current (magnetic field). In this case a triangular magnetic field waveform is applied to the regenerator.

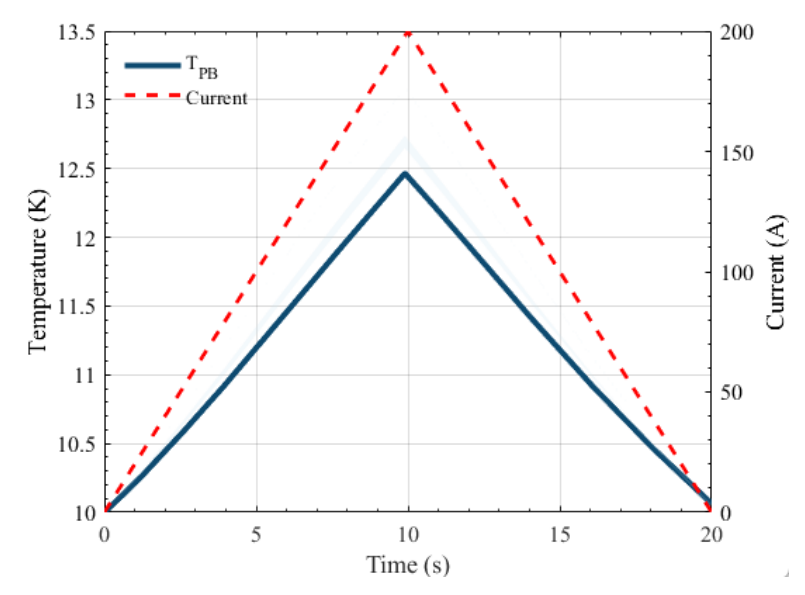


Figure 88. Simulated example of a no-load test applied to the ErAl₂ magnetocaloric regenerator. A triangular magnetic field waveform is applied, while measuring the temperature evolution along the packed bed.

4.1.2.2 Ramping Rate Testing

The next set of tests consist of applying a cycle of trapezoidal magnetic fields waveforms with different ramping rates, while maintaining constant conditions at the inlet of the packed bed. The procedure is the following:

- 1. Steady-state: The packed bed is stabilized under steady-state conditions, ensuring a constant mass flow and the target temperature along the bed.
- 2. Magnetic field profile: a series of trapezoidal field functions are applied to the packed bed. The ramping rate of the magnetic field is the iteration variable.
- 3. Measurement: temperature variations along the regenerator are monitored using the CERNOX sensors.

Figure 89 presents an example of an applied ramping rate test. As will be explained in the next section, the achievement of perfect waveforms proved to be challenging due to the high inductance of the magnet.

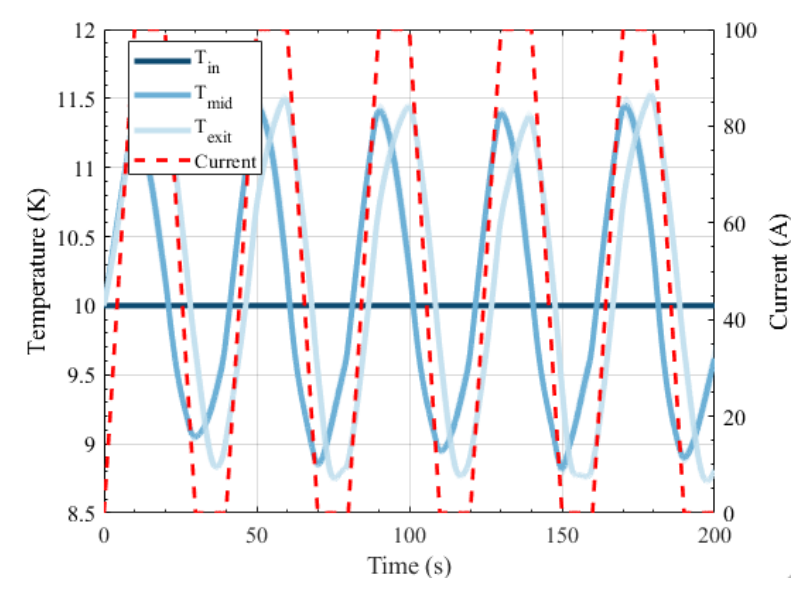


Figure 89. Simulated example of a ramping rate test. A series of 5 trapezoidal magnetic field waveforms is applied to the regenerator while maintaining a constant inlet temperature of 6.2 K and a constant mass flow.

4.1.2.3 Variable Temperature Testing

The final set of tests, known as variable temperature testing, follows a procedure similar to the previous experiments. In these tests, the ramp rate is kept constant, while the initial temperature of the packed bed and the mass flow through the regenerator are varied.

This approach aims to replicate magnetic field profiles similar to those described in Chapter 2. The procedure for these tests is as follows:

- 1. Steady-state: The packed bed is brought to steady-state conditions, ensuring a consistent mass flow and the target temperature along the bed.
- 2. Magnetic field profile: A series of trapezoidal magnetic field functions are applied to the packed bed.
- 3. Measurement: Variations in temperature along the regenerator are measured using CERNOX sensors.

Figure 90 illustrates one of the tests conducted. In this case, the inlet temperature was increased to 11 K, compared to the 6 K used in the previous example.

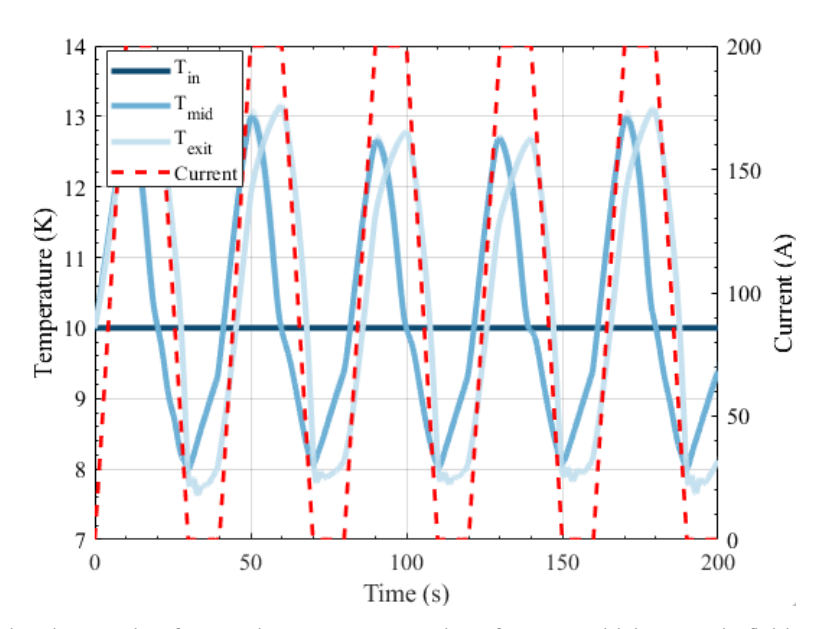


Figure 90. Simulated example of a ramping rate test. A series of 5 trapezoidal magnetic field waveforms is applied to the regenerator while maintaining a constant inlet temperature of 6.2 K and a constant mass flow.

4.2 Summary of experimental runs and modifications

This section describes the experimental procedure used in each of the experimental runs. The procedure changed and was updated during the operation of the test stand as the understanding of the operation of the test stand from the participants improve.

The main guidelines from the procedure are described below:

3-4 Days before testing

- 1. Preliminary Checks: a. Validate the positioning of the elements to be used in the test, paying special attention to the cryogenic transfer line and funnel and the LHe sensor level. Check that sensors are within range: temperature, vacuum pressure, insulation, and resistances in current leads.
- 2. Start insulation vacuum in the cryostat

2 Days before testing

- 1. Preliminary Checks: Check that all sensors are within range: temperature, vacuum pressure, insulation.
- 2. Fill cryostat with LN2 according to lab procedure. Perform at least 2 washes with GHe. In this test it was important to not fill the cryostat above the maximum level of the dry recipient.

Testing day

- 1) Preliminary Checks: Check that all sensors are sensors within range
- 2) Arrival of LHe and Filling: Follow lab procedure and fill LHe to an adequate level. Figure 91 shows the laboratory equipment during the experimental testing.



Figure 91. Illustration of testing day showing the liquid helium dewar feeding to the laboratory cryostat.

- 3) Start GHe Circuit: Start the compressor and run the GHe circuit. Initially, the low pressure will remain constant at 0.2 bar. Target parameters: Mass flow: 10 g/min and MC1 Temperature: 10-15 K -> If not reached, consider actions such as turning on resistances to increase LHe evaporation and/or reducing mass flow.
- 4) Thermal Tests: Follow Thermal Test Table. Below is a brief procedure description:
 - a) Single blow testing:
 - b) Periodic testing:
- 5) Magnetocaloric material tests: Control input resistances ensuring the regenerator is at a constant temperature. Perform established tests:
 - a) No load testing
 - b) Ramp
 - c) Variable temperature
- 6) Change GHe flow direction to test the other material: a. Close GHe passage valves to the cryostat. Ensure a good seal. b. Change the flow direction by switching hose positions. c. Perform 2-3 washes without opening the valves. d. Open valves and perform 2-3 washes. Figure 92 shows the cryostat instrumentation.



Figure 92. Upper view of the cryostat showing the cryogenic transfer lines and the manual valves used for changing the flow direction.

- 7) Repeat steps 4 and 5. Test the other magnetocaloric material.
- 8) LHe Recovery: transfer LHe from the cryostat to the Dewar.

This guide outlines the ideal scenario proposed for the testing day. However, adjustments may be necessary based on real-time conditions. Always prioritize the safety of personnel, and avoid prolonging the test if it can be easily rescheduled. Additionally, ensure the safety of the test components, as the magnet used is the only one available with the required characteristics to continue this line of research.

4.3 Raw Experimental Results

This section shows the type of acquired data during testing and qualitatively describes certain trends observed in the data. The section is divided in 5 subsections, one for each major group of tests done, and all subsections are structured in the same way: first a table summarizing the main variables of each test, and next a series of grouped figures showing the experimental results.

Given the extensive number of tests conducted, only the most significant results are presented in this section. Detailed characteristics of each test, along with the corresponding measured data, are provided in the Appendix.

The results presented in the following subsections all follow the same nomenclature (Table 34), the tests of the ErAl₂ starts with a 1, and the tests of the GGG starts with a 2.

Table 34. Nomenclature	for each	nacked bed	instrumentation
Table 34. Nomenciature	101 Caci	packed bed	mstrumentanon

	PB1: ErAl ₂	PB2: GGG
Inlet Temperature	BP1	BP2
Sensor 1	MC1	MC4
Sensor 2	MC2	MC5
Sensor 3	MC3	MC6
Wall Sensor	W1	W2

4.3.1 Thermal: Single Blow Testing

4.3.1.1 Ambient Temperature

Chapter 3 discusses the initial validation of the packed bed manufacturing process using glass beads. Furthermore, Section 3.2.3.2 describes how the glass packed bed was employed to determine the maximum packing pressure that can be applied to the regenerator without causing occlusion. To further validate the thermal testing procedure outlined earlier, single-blow tests were also conducted using the glass-filled packed bed.

Table 35 shows the test data, and Figure 93 shows the measurements.

Table 35. Ambient temperature single blow data test information table

Test Run	MCM	B (T)	P _{low} (bar)	Mass Flow (g/min)
SB00	Glass	0	0.4	13.5
SB01	Glass	0	0.4	13.5

A hot blow was initially performed in SB00, followed by a cold blow in SB01, both involving temperature steps exceeding 30 K. Each test type presents distinct advantages. In SB00, it was easier to maintain homogeneous initial conditions within the regenerator. Conversely, in SB01, heat losses to the ambient resulted in a linear temperature gradient, as evidenced in the graph by a slight divergence between the three measured temperatures at t=0. However, as the test progressed, ambient heat losses became more pronounced in SB00. This is reflected in the greater temperature difference between MC1 and MC3 observed toward the end of the test.

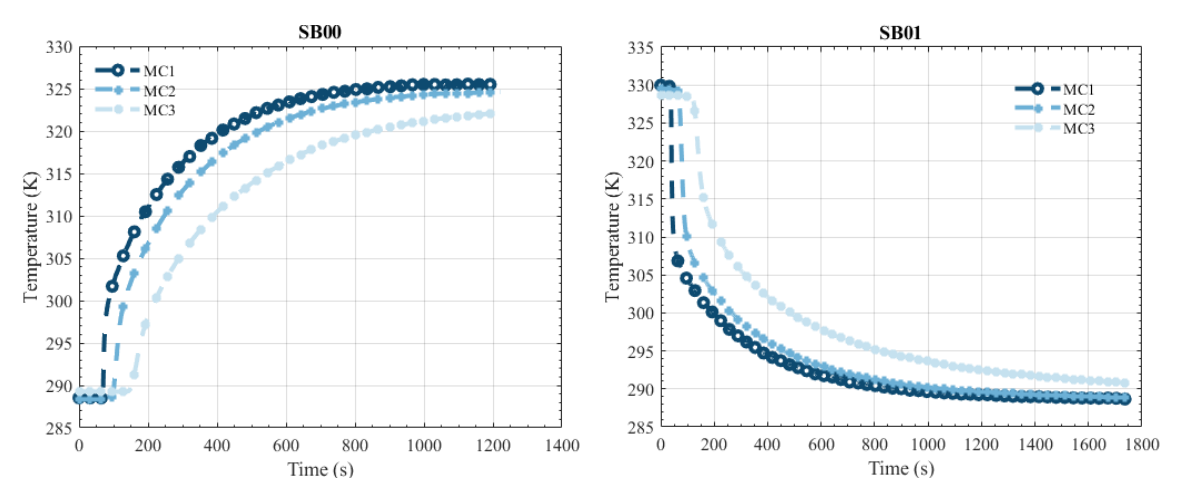


Figure 93. SB00-SB01 tests measured data: single blow test of glass packed bed with mass flow of 13.5 g/min.

4.3.1.2 Liquid Helium

The single-blow tests conducted at liquid helium temperatures were performed at the lowest achievable temperature for the test stand, approximately 5 to 6 K. In all instances, hot blows were executed, as generating cold blows proved challenging due to the difficulty in achieving a steady-state temperature across the entire packed bed, primarily because of heat losses to the ambient environment.

Table 36 provides the variable ranges for the single blow tests. Two key variables were adjusted: the magnetic field and the mass flow rate. The sensitivity of the heater made repetition of these tests challenging, although this did not significantly impact on the overall results.

Table 36. Single blow data test information table

Test	MCM	B (T)	P_{low} (bar)	Mass Flow (g/min)	Number of Tests
SB	ErAl ₂ /GGG	0-1-2-3	0.2	6-10	16

A selection of representative test results is presented in this section. Figure 94 illustrates the SB11 test, conducted on ErAl₂ without an applied magnetic field and with a mass flow rate of 10 g/min. During the hot blow, the temperature step ranged from approximately 5–6 K to 9–10 K. Minor oscillations in the data are observed, likely caused by small fluctuations in pressure and mass flow within the helium circuit.

In comparison, Figure 95 presents the results for SB12, performed under identical conditions to SB11 but with a 1 T magnetic field. The data clearly demonstrate the effect of the magnetic field on the specific heat of the packed bed. Specifically, the temperature at the packed bed outlet changes more rapidly under higher magnetic field, indicating a direct correlation between the magnetic field and the thermal response of the material.

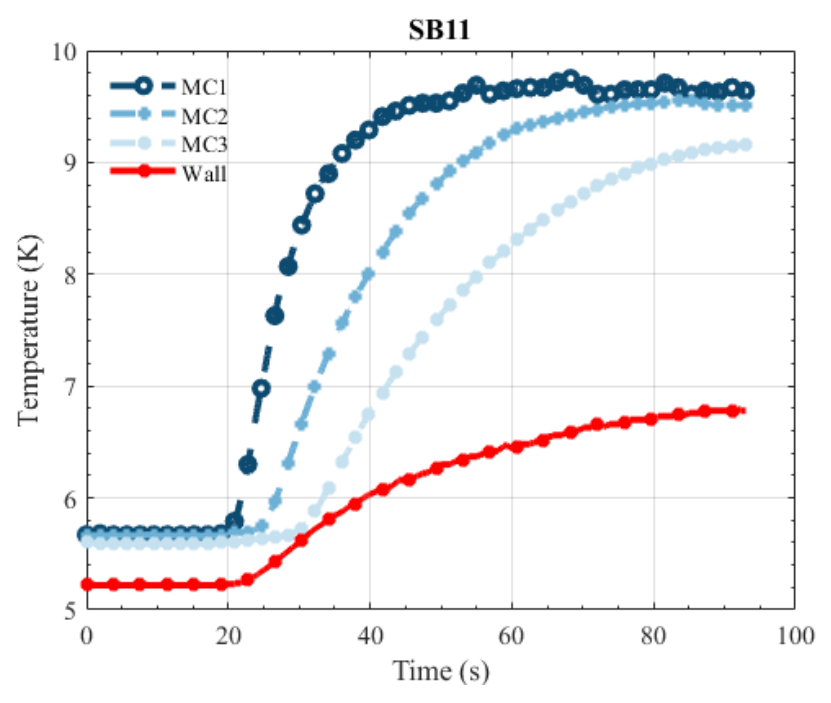


Figure 94. SB11 test measured data: single blow test of $ErAl_2$ with $\dot{m} = 10$ g/min and B = 0 T.

In SB12, as illustrated in Figure 95, a decrease in the specific heat of the packed bed is observed, which results in increased sensitivity to external disturbances.

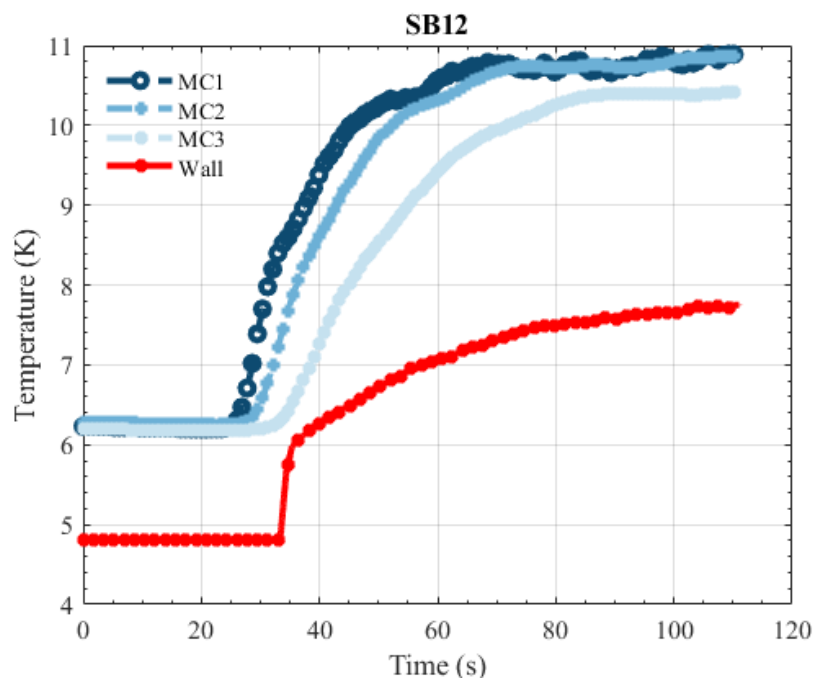


Figure 95. SB12 test measured data: single blow test of ErAl₂ with $\dot{m} = 10$ g/min and B = 1 T.

Figure 96 and Figure 97 present the results of the SB16 and SB18 tests, respectively, in which the mass flow rate was reduced to 6 g/min. As anticipated, the transient response is slower, as evidenced by the extended time scale compared to the previous tests, where steady-state conditions were achieved at approximately 100 s. Notably, in both tests, the wall temperature measurements were unavailable.

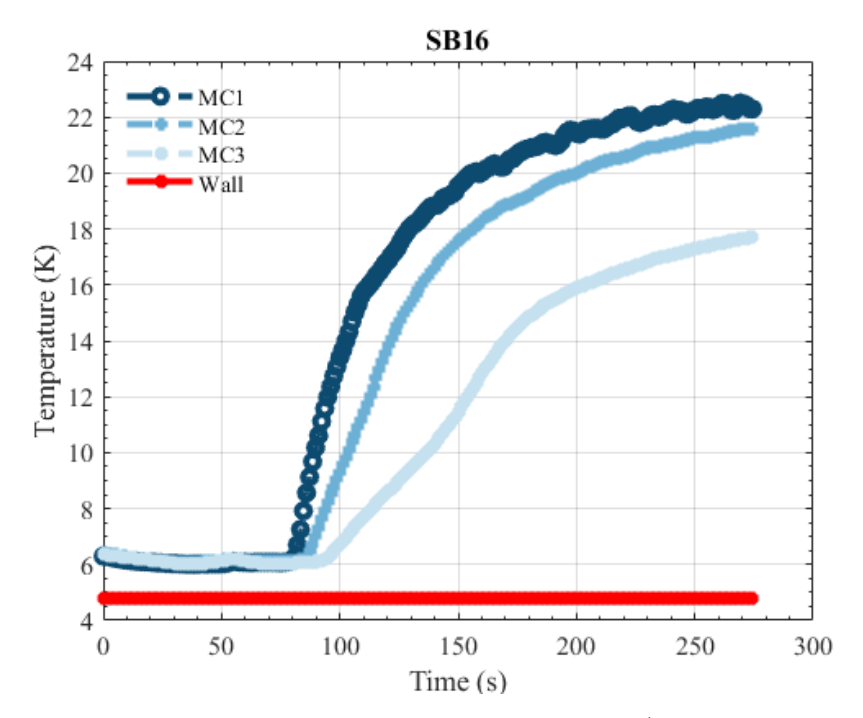


Figure 96. SB16 test measured data: single blow test of ErAl₂ with $\dot{m} = 6$ g/min and B = 0 T.

Similar to the SB11-12 tests, the thermal response in the higher magnetic field test (SB18) was slightly faster compared to SB16. Another significant observation is the increased temperature difference between MC1 and MC3 upon reaching steady-state conditions. This suggests that the wall and external heat losses are influencing the results.

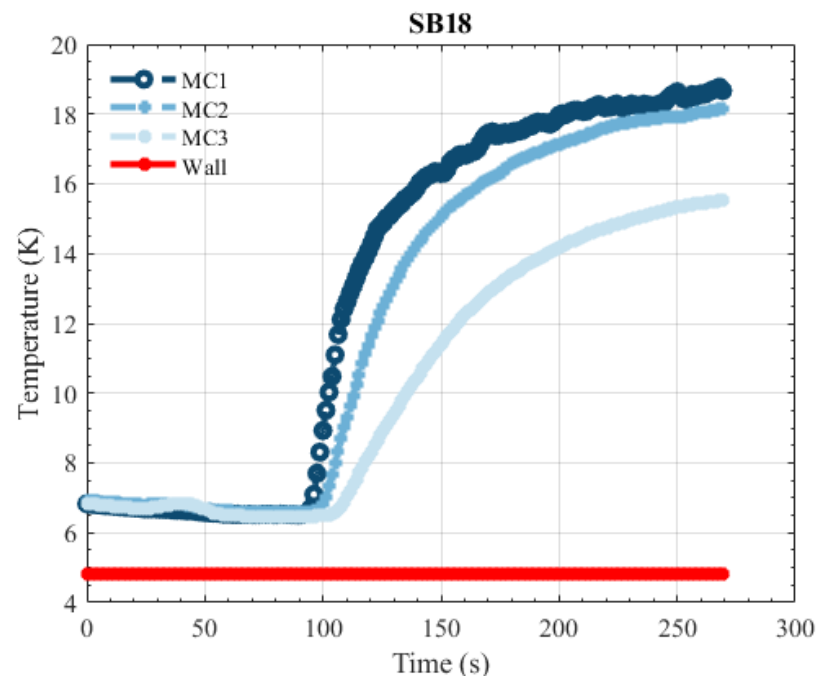


Figure 97. SB18 test measured data: single blow test of $ErAl_2$ with $\dot{m} = 6$ g/min and B = 2 T.

Figure 98 and Figure 99 shows the results for two GGG tests. In this case it is observed how the transient response is slower with increasing magnetic fields. This is because GGG specific heat, unlike ErAl₂, increases with higher magnetic fields.

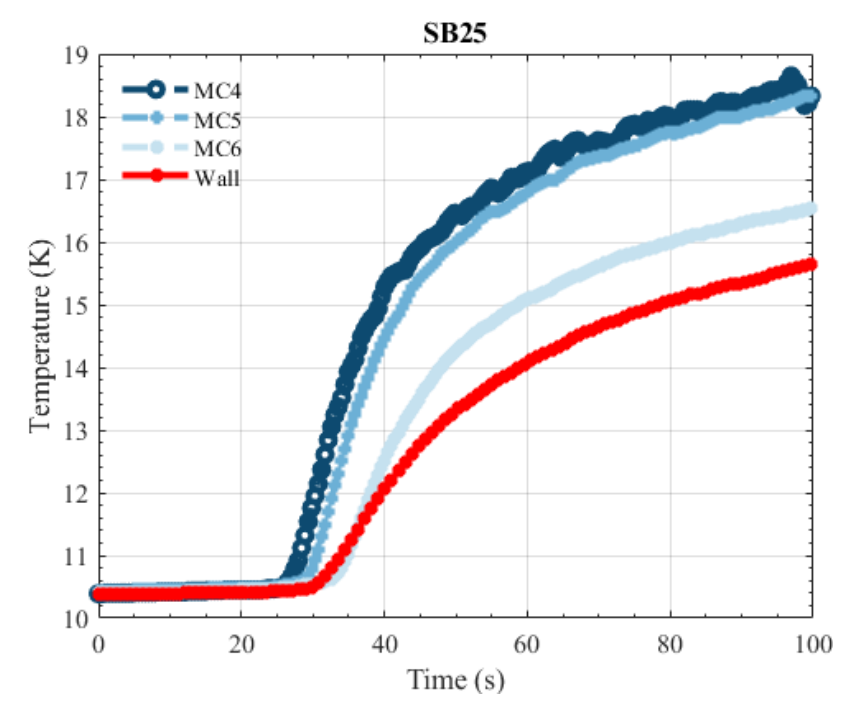


Figure 98. SB25 test measured data: single blow test of GGG with $\dot{m} = 6$ g/min and B = 0 T.

In certain tests with the GGG packed bed there were errors with the wall temperature sensor. Test SB27 in Figure 99, was one of the cases.

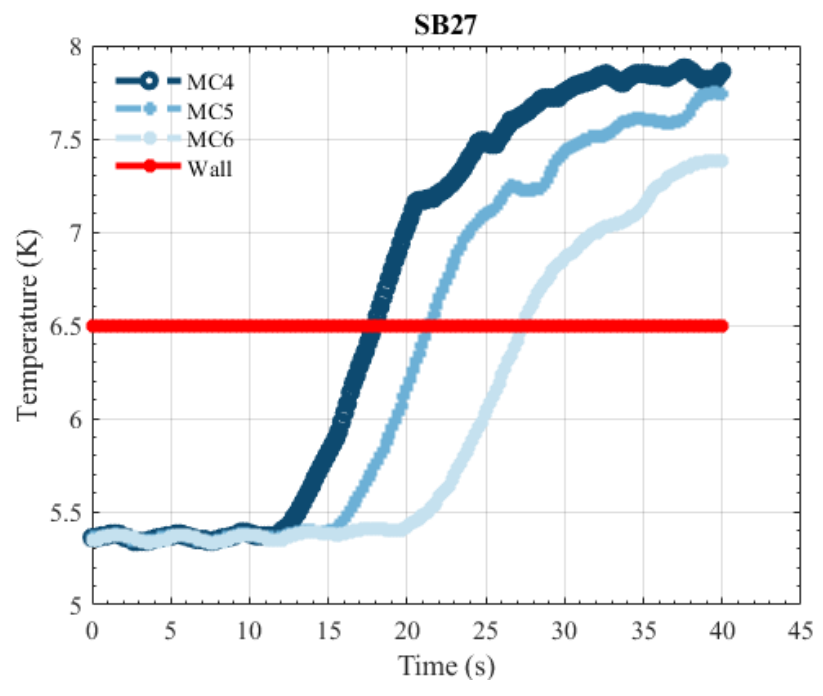


Figure 99. SB25 test measured data: single blow test of GGG with $\dot{m} = 6$ g/min and B = 2 T.

4.3.2 Thermal: Periodic Blow Testing

4.3.2.1 Liquid Helium

The periodic blow tests were conducted at temperatures ranging from 5 to 15 K. Similar to the single blow tests, each series began with a hot blow. Table 37 summarizes the range of variables used in these experiments. Consistent with previous tests, the two parameters varied during the experiments were the magnetic field and the mass flow rate. However, it should be noted that three of the tests could not be completed due to time constraints.

Table 37. Periodic blow data test information table

Title	MCM	B (T)	P _{low} (bar)	Mass Flow (g/min)	Number Of Tests
PB	ErAl ₂ /GGG	0-1-2	0.2	6-10	12

Figure 100 and Figure 101 presents the results of the first set of periodic blow tests, PB11 and PB13. Similar to the single blow test, it can be qualitatively observed that the specific heat decreases as the magnetic field increases. This is evidenced by the faster temperature response in PB13.

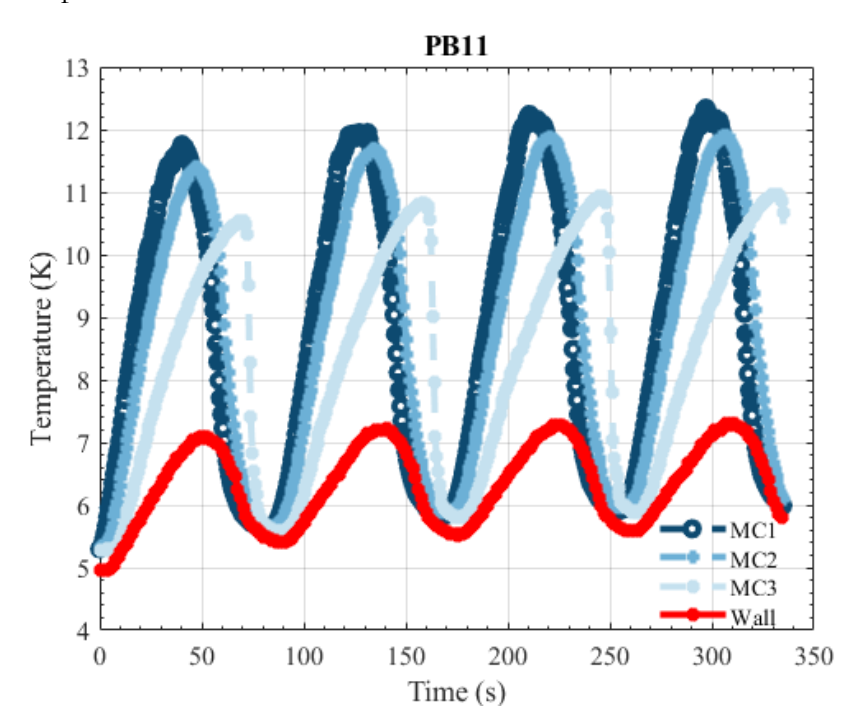


Figure 100. PB11 test measured data: periodic blow test of ErAl₂ with $\dot{m} = 10$ g/min and B = 0 T.

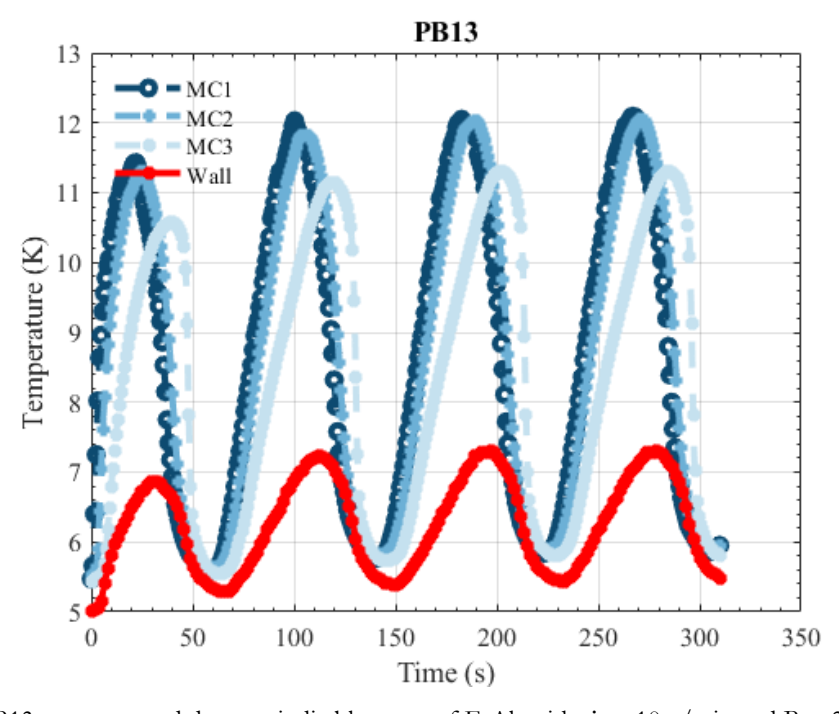


Figure 101. PB13 test measured data: periodic blow test of $ErAl_2$ with $\dot{m} = 10$ g/min and B = 2 T.

Figure 102 and Figure 103 display the results for the GGG packed bed. In this case, the specific heat of GGG increases with the magnetic field within the studied region. This trend is evident in tests PB24 and PB26.

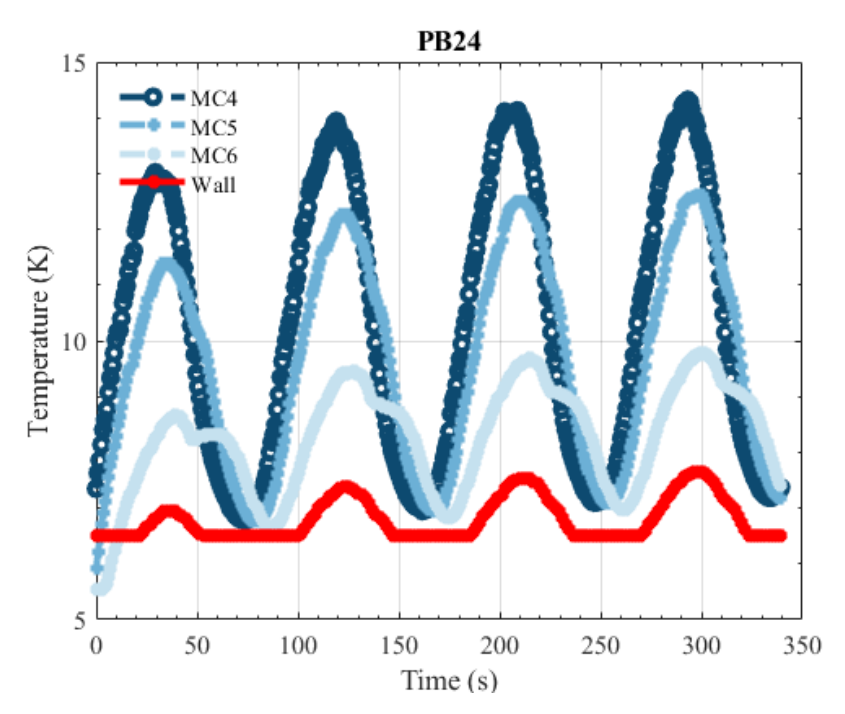


Figure 102. PB24 test measured data: periodic blow test of GGG with $\dot{m} = 6$ g/min and B = 0 T.

The thermal response observed in tests PB24 and PB26 appears somewhat unexpected, particularly regarding the temperature evolution at the packed bed exit, as measured by MC6. Notably, the temperature profile exhibits a double peak, and the temperatures recorded for both the wall and MC6 are closely aligned. This behavior may suggest that the tests were conducted under low Reynolds number conditions, where laminar flow effects dominate, and become more pronounced. A more comprehensive analysis, which is presented in the subsequent chapter, is required to validate this interpretation.

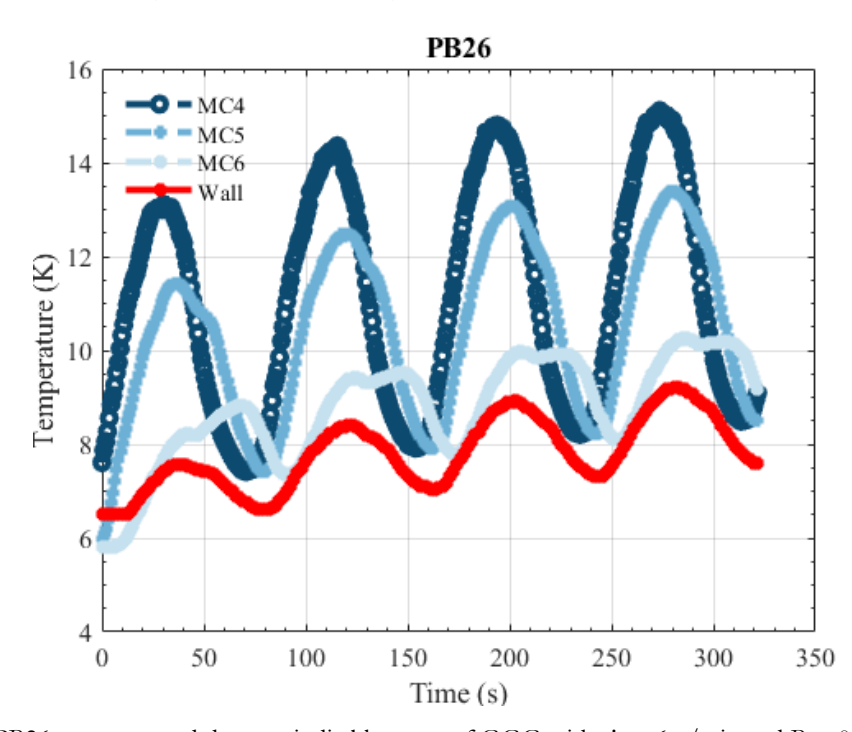


Figure 103. PB26 test measured data: periodic blow test of GGG with $\dot{m} = 6$ g/min and B = 0 T.

4.3.3 Magnetic: No-Load Testing

The first set of tests that evaluated the thermal response of the magnetocaloric properties of ErAl₂ and GGG are denominated no-load tests.

Table 38 summarizes the range of values during these tests. In these experiments, the two variables adjusted were the initial temperature of the packed beds and the magnetic field profile.

The figures presenting the results will include the current profile, as the magnetic field varies along the length of the packed bed. As discussed in previous chapters, the current and magnetic field at the magnet's center are related by a 100 A to 1 T ratio.

Table 38. No-load data test information table

Title	MCM	$T_{start}\left(K\right)$	Waveform	B_{max} (T)	Number of Tests
NL	ErAl ₂ /GGG	4-15	Triangular/Trapezoidal	3	10

Figure 104 illustrates two tests conducted on both materials. A key observation is the limited magnetocaloric response of ErAl₂ across all tests, particularly during the ramp-up phases. In test NL12, where the initial temperature ranges between 10 and 12 K, the magnetocaloric effect of ErAl₂ is negligible. However, during demagnetization, a noticeable change in the temperature trend is observed.

Several factors related to the experimental setup may account for these results. First, significant thermal losses are likely due to an incomplete vacuum, which results in entrained helium within the packed bed and heat dissipation through the walls. Second, the slow temperature response of the CERNOX sensors, attributed to their specialized packaging designed to address insulation issues, may also contribute to these findings. These aspects will be examined in greater detail in subsequent chapters.

In contrast, the results obtained for GGG align more closely with expectations.

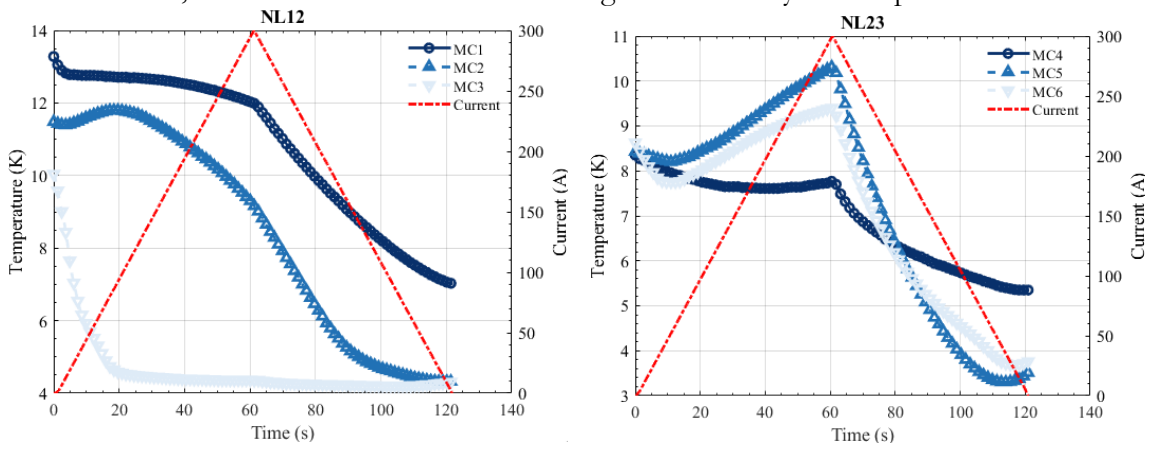


Figure 104. NL12 and NL23 tests measured data. A triangular magnetic field profile is applied to the packed beds.

Tests NL14 and NL25 utilized trapezoidal magnetic waveforms applied to the packed bed, allowing for cooling intervals between ramps. The results of these tests are presented in Figure 105. As expected, the ErAl₂ response remained limited, which can be attributed to the low initial temperature of approximately 4.2 K.

In contrast, the GGG exhibited a more pronounced magnetocaloric effect, though the experimental setup faced challenges similar to those observed with the other packed bed, albeit to a lesser extent. In test NL24, the packed bed temperature increased from 4 K to nearly 9 K, falling short of the ideal final temperature of approximately 12–13 K. This deviation highlights the diminishing magnetocaloric effect at higher temperatures. A minimum temperature of 2.9 K was achieved; however, analysis of the graph suggests that this lower limit was likely constrained by helium entrapped within the packed bed, which was not evacuated, as it reached helium's liquefaction temperature.

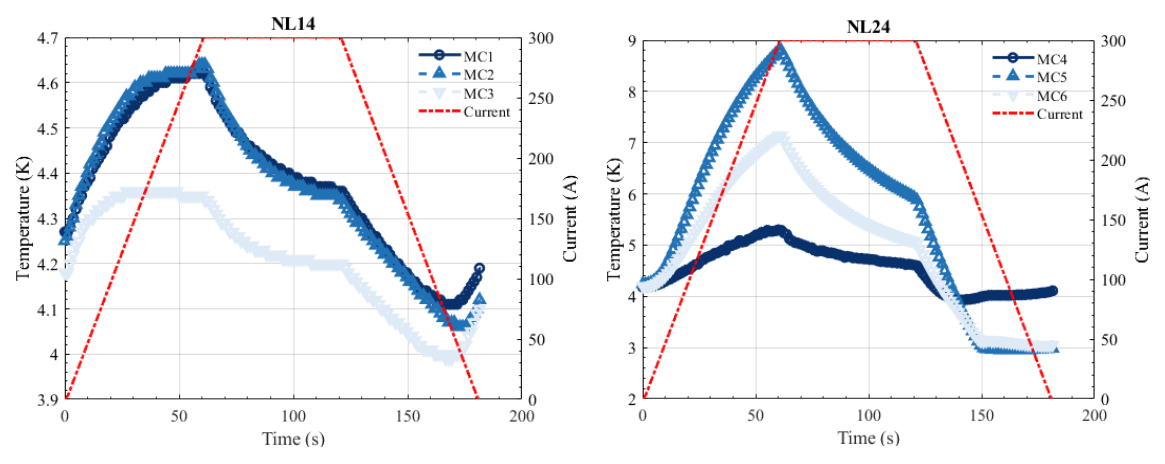


Figure 105. NL14 and NL24 tests measured data. A trapezoidal magnetic field profile is applied to the packed beds.

4.3.4 Magnetic: Ramping Rate Testing

The next set of tests, referred to as the ramping rate tests, aimed to evaluate two aspects: the maximum ramping rates the magnet can withstand and the temperature transients in the packed bed.

In these tests, the mass flow was kept constant at 10 g/min, while two variables were adjusted: the initial packed bed temperature (either 5–6 K or 9–11 K) and the magnetic field ramping rates (5, 10, or 20 A/s). Table 39 summarizes the variable range of the different test runs.

To reach the desired starting temperature, the heater was turned on, and once the system has reached steady state the test was performed.

Table 39. Ramping rate data test information table

Title	MCM	$T_{start}\left(K\right)$	dI/dt (A/s)	Number of tests
RR	ErAl ₂ /GGG	5-10	5-10-20	12

Figure 106 illustrates the results of the RR15 tests conducted with a ramp rate of 10 A/s and an initial temperature of 10.5 K in the magnetocaloric material. The data reveal that the inlet temperature at MC1 is not consistently maintained due to significant thermal losses, which adversely impact the transient response. Furthermore, the magnetic field deviates from an ideal trapezoidal waveform, a discrepancy caused by the high inductance of the magnet, as previously discussed. Although a series resistance was implemented to mitigate this issue, its value was constrained by both the power supply's capacity and safety considerations; increasing the resistance further would have resulted in excessive heat dissipation.

Despite these challenges, the magnetocaloric effect was clearly observed, with the outlet temperature at MC3 exhibiting a variation exceeding 2 K.

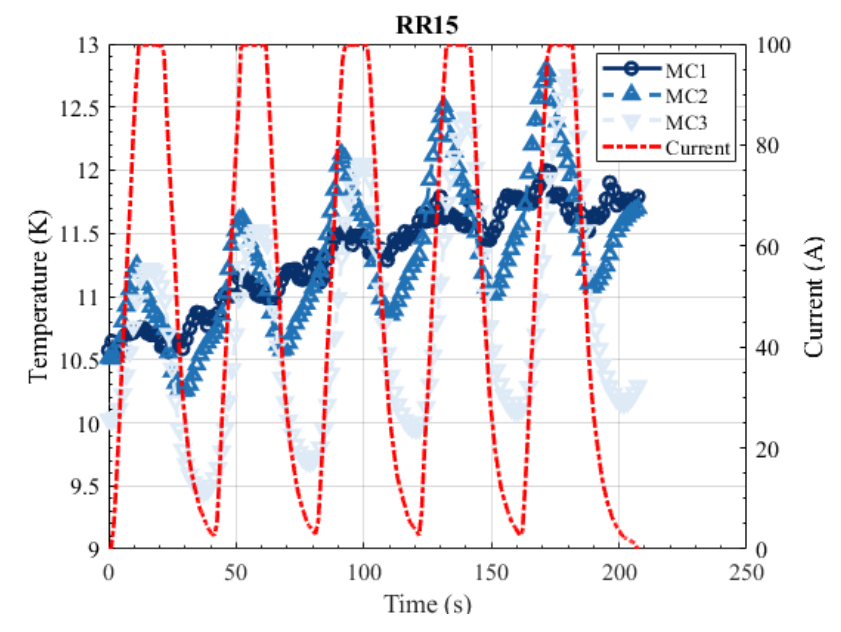


Figure 106. RR15 test measured data (ErAl₂): A trapezoidal magnetic field profile is applied with ramping rates of 10 A/s. Starting temperature is between 10-12 K.

Figure 107 displays the results from the RR16 tests, conducted with a ramping rate of 20 A/s and an initial temperature of 12 K. In this case, the inlet temperature remains more stable compared to previous tests. Interestingly, the graph reveals that the measured temperature difference is greater at MC2 than at MC3, which is unexpected given typical thermal behavior. This surprising observation will be analyzed in greater detail in the next chapter to better understand the underlying causes.

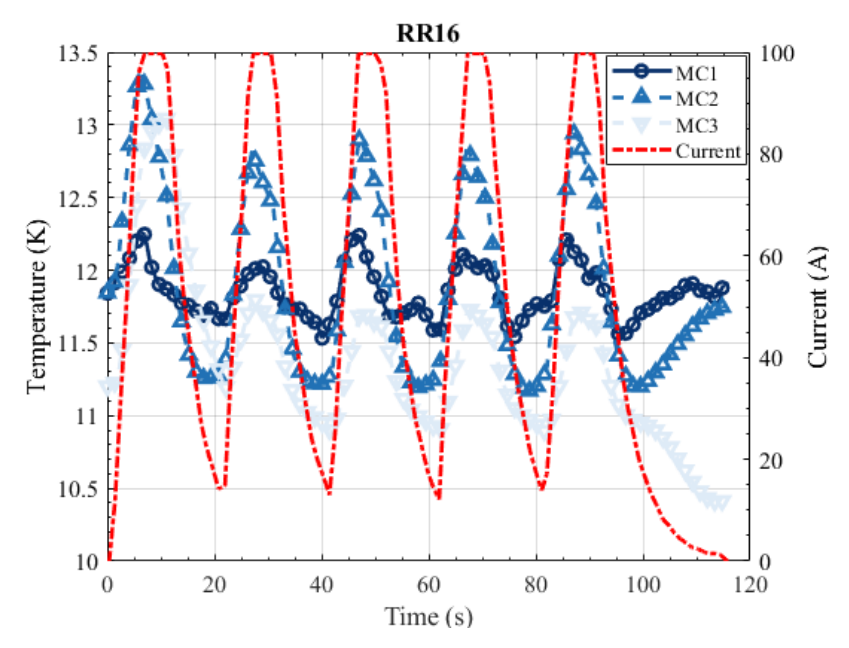


Figure 107. RR16 test measured data (ErAl₂): A trapezoidal magnetic field profile is applied with ramping rates of 20 A/s. Starting temperature is between 10-12 K.

The initial tests with GGG, RR22 and RR23, were conducted under stable conditions. Figure 108 and Figure 109 presents the results, showing that the temperature range in both cases was slightly below 1 K.

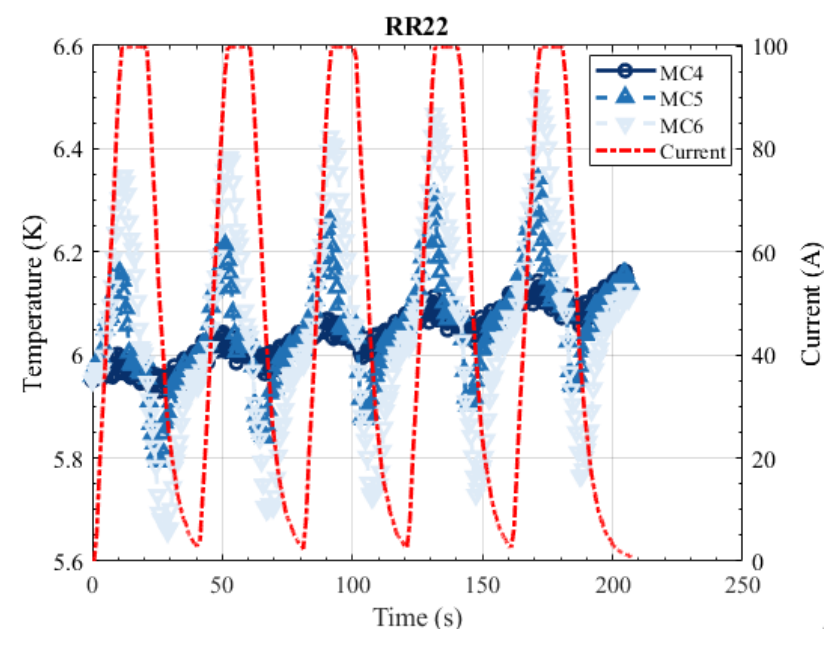


Figure 108. RR22 test measured data (GGG):. A trapezoidal magnetic field profile is applied with ramping rates of 10 A/s. Starting temperature is between 5-6 K.

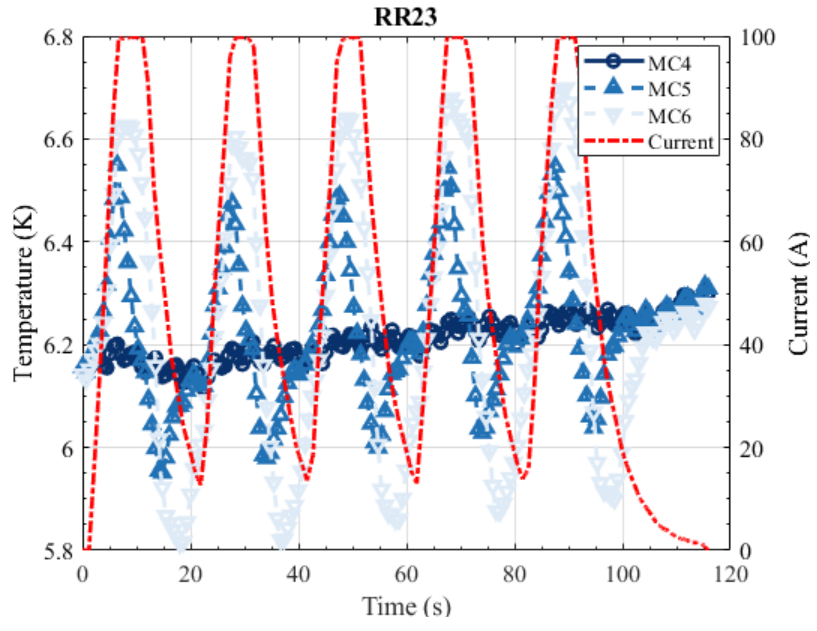


Figure 109. RR23 test measured data (GGG): A trapezoidal magnetic field profile is applied with ramping rates of 20 aA/s. Starting temperature is between 5-6 K.

4.3.5 Magnetic: Variable Temperature Testing

The final set of tests, referred to as variable temperature tests, follows a procedure similar to the previous ones. In these tests, the mass flow and inlet temperature are held constant, while a series of trapezoidal magnetic field waveforms are applied to the magnetocaloric material.

Table 40 summarizes the conditions of the test runs. For all tests, the ramping rate was fixed at 20 A/s. The dependent variables were the maximum magnetic field, the initial temperature, and the mass flow

Table 40. Variable temperature data test information table

Title	MCM	B (T)	T _{start} (K)	Mass Flow (g/min)	Test done
VT11	ErAl ₂ /GGG	1-2-3	6-10-15	6-10	36+2

Some tests conducted at a mass flow rate of 6 g/min were either incomplete or excluded due to lower data quality. In contrast, the majority of tests performed at a mass flow rate of 10 g/min were successfully completed.

The results from the ErAl₂ testing are presented first. Figure 110 highlights the outcomes for the low-temperature range, specifically below 6 K, as observed in test VT111, where a 2 T magnetic field was applied with an inlet temperature below 6 K. While the magnetocaloric effect is evident, it is relatively modest, with outlet temperature variations limited to approximately 1 K.

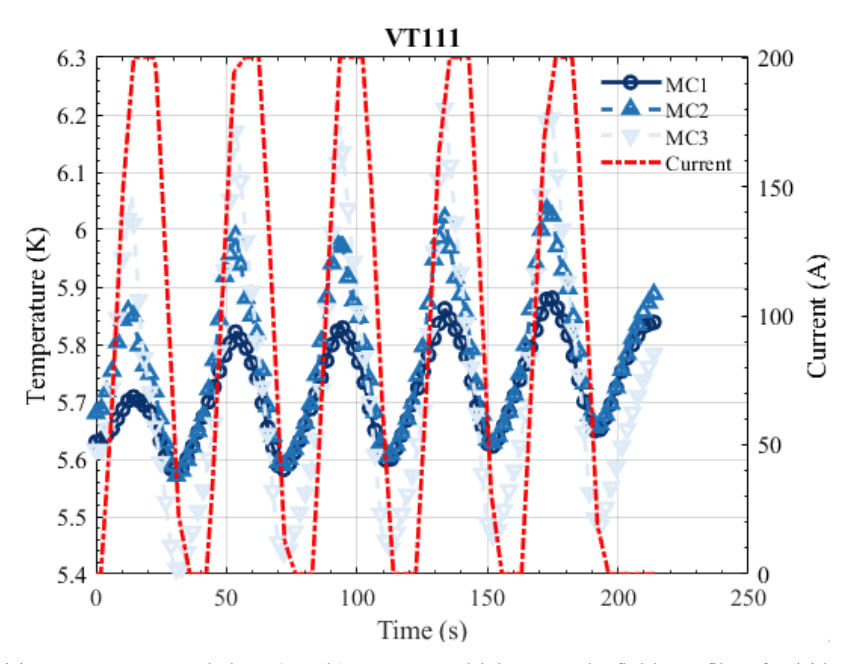


Figure 110. VT111 test measured data (ErAl₂): A trapezoidal magnetic field profile of 2 T is applied to the magnetocaloric material with a constant inlet temperature around 5-7 K, and a constant mass flow of 10 g/min.

Figure 111 shows the results for the VT115 tests. In this case, the thermal response of the magnetocaloric material to the applied field is more pronounced, with the exit temperature varying by almost 7 K between the maximum and minimum for VT115. This behavior is expected, as the material is approaching its Curie temperature.

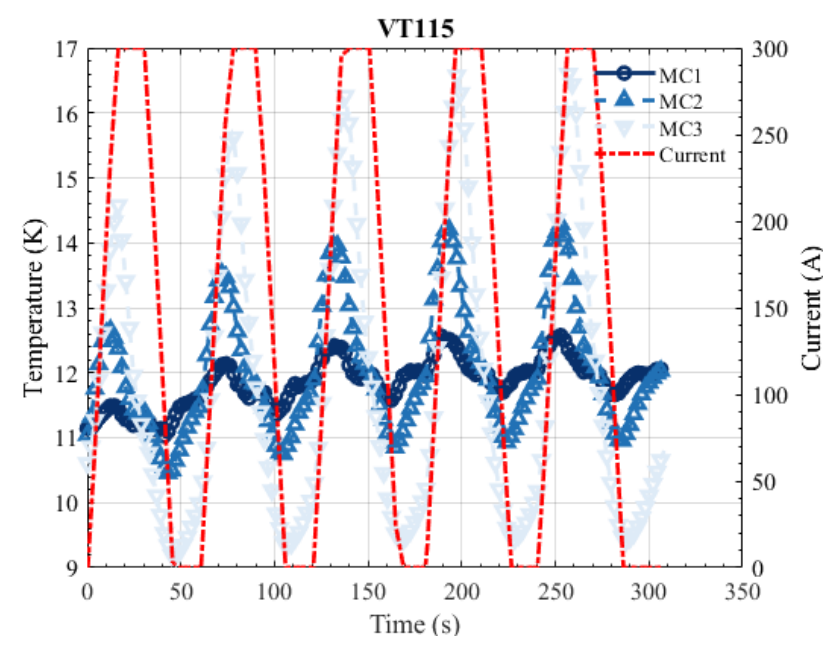


Figure 111. VT115 test measured data (ErAl₂): A trapezoidal magnetic field profile of 3 T is applied to the magnetocaloric material with a constant inlet temperature around 10-12 K, and a constant mass flow of 10 g/min.

Finally, Figure 112 presents the results of the higher-temperature tests for ErAl₂, conducted at temperatures exceeding 15 K. Similar to the previous tests, the magnetocaloric effect is clearly evident in this temperature range.

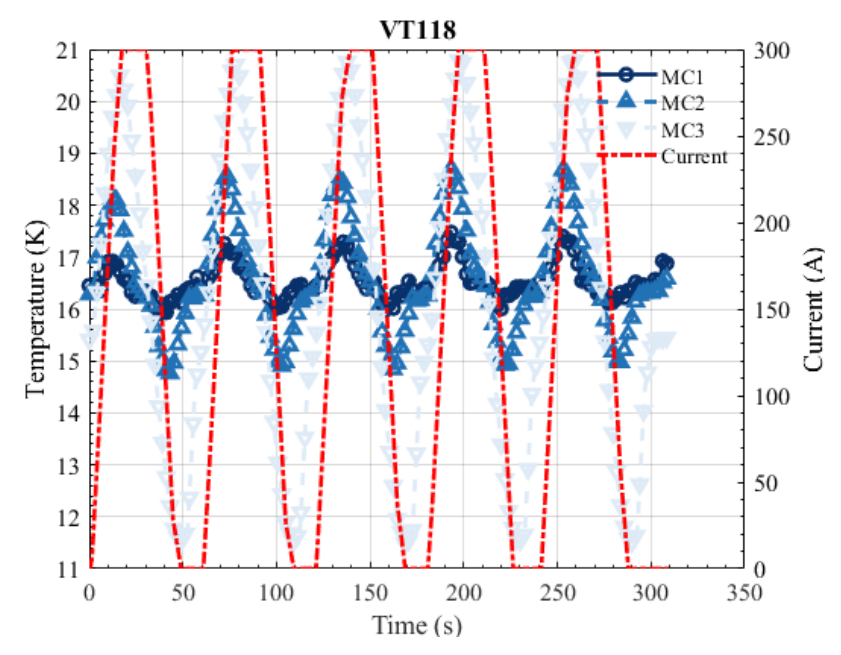


Figure 112. VT118 test measured data (ErAl₂): A trapezoidal magnetic field profile of 3 T is applied to the magnetocaloric material with a constant inlet temperature around 16-17 K, and a constant mass flow of 10 g/min.

The next figures present the results for the GGG testing. Figure 113 shows the first set of tests, with a mass flow of 6 g/min and an inlet temperature of around 5 K. The results show a clear heating during magnetization, moreover, during demagnetization helium appears to liquefy as the temperature did not pass the 4.8 K limit.

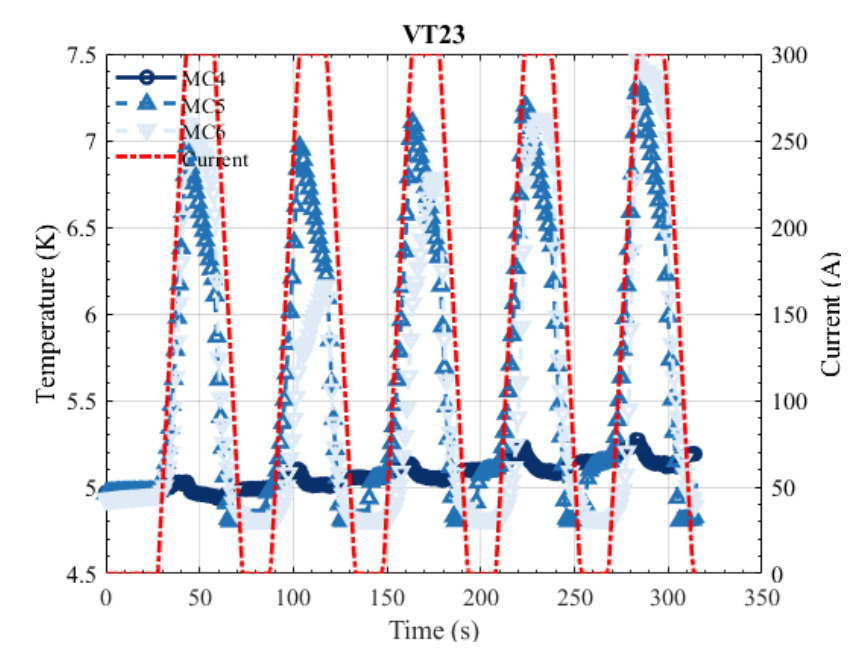


Figure 113. VT23 test measured data (GGG): A trapezoidal magnetic field profile of 3 T is applied to the magnetocaloric material with a constant inlet temperature around 5 K, and a constant mass flow of 6 g/min.

Figure 114 shows the results for the VT212 tests. Similar to the VT22 test, helium gas began to liquefy during the demagnetization phase. It is interesting to see this effect in VT212, where the outlet temperature was lower for each cycle, as there was a net cooling effect applied to the helium gas.

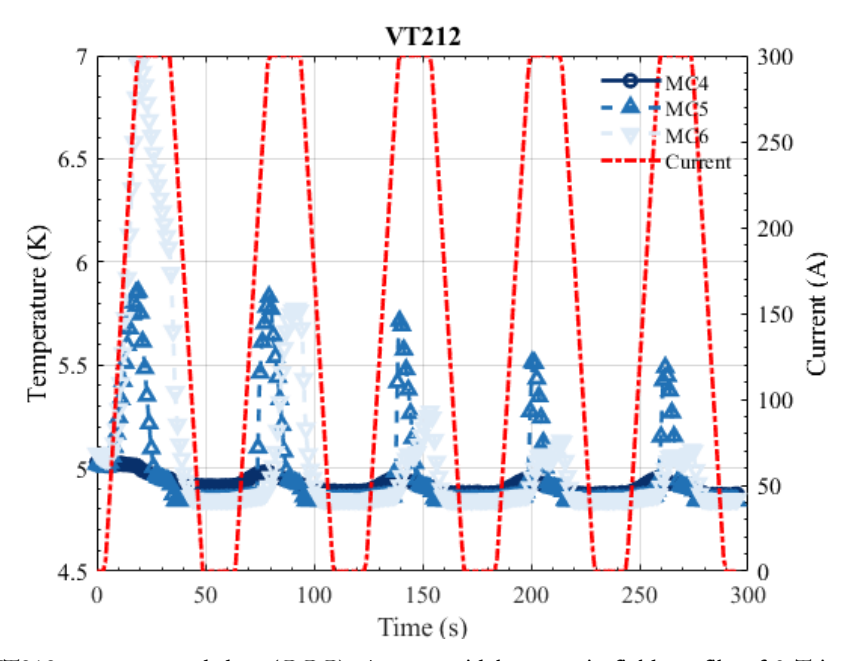


Figure 114. VT212 test measured data (GGG): A trapezoidal magnetic field profile of 3 T is applied to the magnetocaloric material with a constant inlet temperature around 5 K, and a constant mass flow of 10 g/min.

Figure 115 presents the results of the VT215 test. The input temperature remained highly stable, and despite being well above the Néel temperature of GGG, the material exhibited a significant magnetocaloric response.

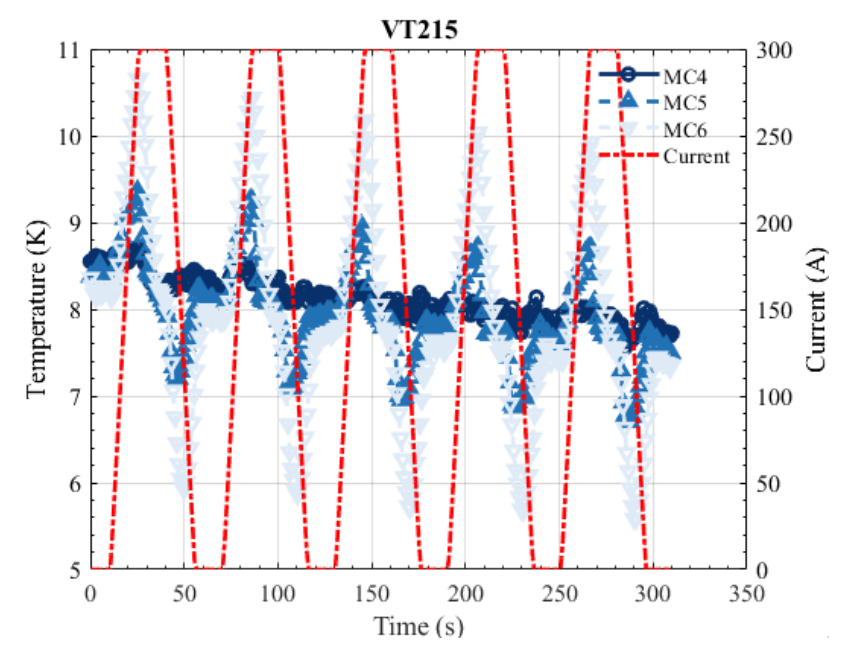


Figure 115. VT215 test measured data (GGG): A trapezoidal magnetic field profile of 3 T is applied to the magnetocaloric material with a constant inlet temperature around 9 K, and a constant mass flow of 10 g/min.

The final two tests deviated from the original plan. In VT220, shown in Figure 116, the magnetic field was increased to 4 T while maintaining an inlet temperature of 10 K and a mass flow rate of 10 g/min. In VT221, detailed in the appendix, the mass flow rate was increased to 15 g/min.

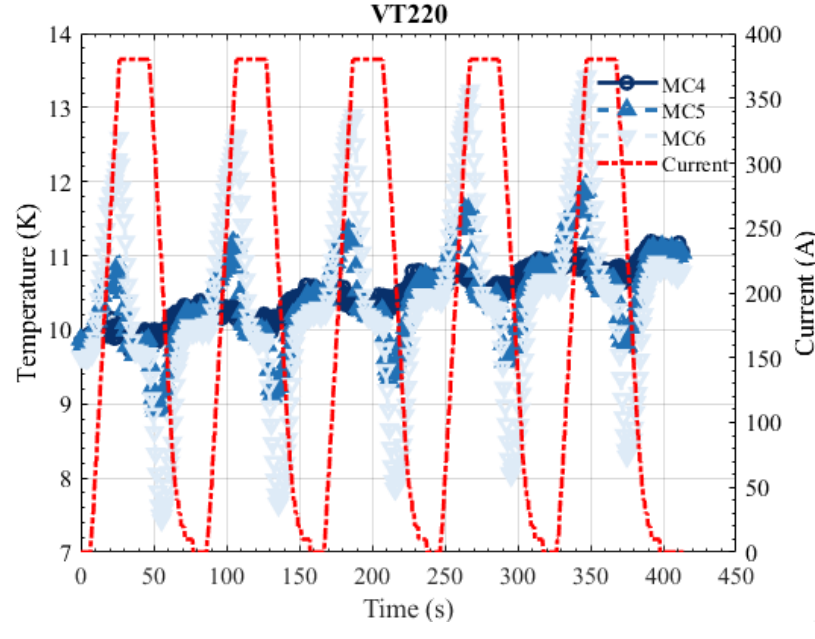


Figure 116. VT220 test measured data (GGG): A trapezoidal magnetic field profile of 4 T is applied to the magnetocaloric material with a constant inlet temperature around 10 K, and a constant mass flow of 10 g/min.

4.4 Summary: Experimental Procedure and Results

This chapter provides a detailed explanation of the experimental testing procedures and the corresponding results. The key points and conclusions are summarized as follows:

The experimental procedure was divided into two main blocks: thermal tests and
magnetic tests. Thermal Tests: These included single-blow and periodic-blow testing,
both standard methods for evaluating heat transfer in packed beds. Magnetic Tests:

These were further subdivided into three groups—no-load tests, ramping rate tests, and variable temperature tests. In the no-load tests, the goal was to achieve adiabatic magnetization and demagnetization of the material. In the ramping rate and variable temperature tests, a trapezoidal magnetic field profile was applied to the magnetocaloric packed bed while maintaining constant inlet temperature and mass flow.

- The tests were conducted in separate instances for different materials. ErAl₂ was
 tested first, followed by GGG in a later phase. All testing conditions were
 successfully maintained within the required ranges, ensuring appropriate
 temperatures in the packed bed and reasonable control of variables. However,
 some heat leaks to the ambient environment were observed, which influenced the
 results.
- The thermal tests qualitatively met expectations but were visibly affected by heat leaks. This impact was particularly noticeable in tests with lower mass flow rates. The thermal tests qualitatively met the expectations. However, the heat leaks had a visible effect on the results.
- The magnetic tests were successfully conducted overall. However, no-load tests proved challenging due to entrained helium and heat leaks, which complicated achieving true adiabatic magnetization and demagnetization. Conversely, ramping rate and variable temperature tests were performed satisfactorily.

The raw experimental data obtained in this section is evaluated against the model prediction in the next chapter.

Chapter 5: ANALYSIS OF EXPERIMENTAL DATA AND TECHNOLOGY ASSESSMENT

This chapter is organized into two sections. The first section focuses on analyzing the experimental tests. It begins by refining the model developed in Chapter 2, incorporating insights gained from the experimental observations. Following this, the section outlines the data reduction techniques applied to both thermal and magnetic tests. Using this methodology, the results are systematically analyzed, and conclusions are drawn. The section concludes by proposing alternative tests and improvements to the experimental methodology and test setup, which could facilitate the validation of future developments.

The second part of this chapter evaluates magnetic refrigeration technology by comparing the parameters established in the first chapter: CAPEX and OPEX per Watt of cooling power, and exergy efficiency. Two distinct cases are presented. The first case builds on the analysis from Chapter 2, where an active magnetic regenerator (AMR) stage is integrated into a traditional cryocooler. The second case introduces a conceptual alternative: a hybrid cryocooler that combines gas and magnetic refrigeration cycles.

5.1 Experimental Results Analysis

5.1.1 Numerical model update

This chapter aims to validate the numerical model developed in Chapter 2 by comparing it with the results and data measured in Chapter 4. A qualitative observation from the previous chapter was the presence of substantial heat loss to the surroundings, which notably influenced the measurements. As described in Chapter 3, while the heat loss was intended to be minimized, it proved to be significant, nevertheless.

To account for this heat loss, the equations describing the model (Eqs. 2.19-2.23) have been revised. Specifically, Eq. 2.23 has been modified to incorporate a heat loss term. The updated equation now reads:

$$m_w c_w \frac{\partial T_w}{\partial t} = \frac{A_w k_w^{eff}}{L} \frac{d^2 T_w}{d\bar{x}^2} + h_w A_w (T_f - T_w) + Q_{loss}$$

$$(5.1)$$

The heat loss term, Q_{loss} , is modeled as:

$$Q_{loss} = h_{ext} A_{ext} (T_w - T_c) (5.2)$$

Where $T_c = 4.2 \, K$, A_{ext} is the external heat transfer area of the wall, and h_{ext} is the external heat transfer coefficient. The cold source of the system was liquid helium (LHe) in which the superconducting magnet was submerged, providing a constant temperature T_c of 4.2 K. The external heat transfer coefficient, h_{ext} , remains the primary unknown in the system of equations. The subsequent section will elucidate how the proposed data reduction techniques enable either the computation or circumvention of this variable.

While the model incorporates heat loss to the surroundings, it is acknowledged that this alone is insufficient for achieving a perfect fit, as the boundary conditions established for the walls are not entirely accurate. The current model employs Neumann boundary conditions, specifically assuming adiabatic walls (excluding the added term). However, this assumption overlooks the presence of axial conduction along the wall to other parts of the circuit, as well as radial effects non included in the 1D model.

The following boundary conditions are applied for the resolution of the numerical model, and its comparison against the measured data:

$$T_f(x=0,t) = T_{MC1}(t)$$
 (5.3)

$$\frac{\partial T_f}{\partial x}(x=L) = \frac{\partial T_s}{\partial x}(x=0) = \frac{\partial T_s}{\partial x}(x=L) = 0$$
 (5.4)

$$\dot{m}_f(x=0,t) = \dot{m}_{MC1}(t); p_f(x=0,t) = p_{MC1}(t);$$
 (5.5)

$$\frac{\partial \dot{m}_f}{\partial x}(x=L) = \frac{\partial p_f}{\partial x}(x=L) = 0 \tag{5.6}$$

$$B(t,x) = B_{nom}(x) * \frac{I(t)}{I_{nom}}$$
(5.7)

The inlet temperature $T_{MC1}(t)$, the mass flow $\dot{m}_{MC1}(t)$, pressure $p_{MC1}(t)$, and current I(t), are all obtained through real-time data acquisition from the instrumentation

Finally, Table 63 compiles the main parameters of the regenerator and its housing used in the experimental test stand. These parameters form the basis for the results analysis presented in the following sections. Table 41 includes the data from the glass packed bed which was used in the ambient temperature tests.

Table 41. Main parameters of each test bed

	ErAl ₂	GGG	Glass		
Ro	egenerator				
Length	125 mm	125 mm	125 mm		
Diameter	35 mm	35 mm	35 mm		
Volume	120.26 cm ³	120.26 cm ³	120.26 cm ³		
MC mass	346.51 g	409.87 g	160.2 g		
Density	6200 kg/m^3	7090 kg/m^3	2520 kg/m ³		
Porosity	0.45 0.45		0.42		
Particle Diameter	0.45 mm	0.48 mm	0.75 mm		
Shape Factor	0.95	0.95	0.95		
	Wall (Stainles	ss Steel)			
Length		125 mm			
Int. Diameter	35 mm				
Thickness	1 mm				
Mass	750 g	g (Includes fla	nges)		

5.1.2 Thermal tests

This section analyses the thermal tests aimed to validate the numerical model presented in Chapter 2. The section begins by introducing the data reduction techniques employed to evaluate these objectives.

5.1.2.1 Data reduction techniques

Data reduction techniques play a pivotal role in the analysis of experimental data obtained from the tests. It is important to consider the significant non-linearity and stiffness inherent in the system of equations governing the developed test stand. These challenges arise primarily from the complex physical phenomena involved and the non-linear properties of the refrigerants, such as helium, as well as the magnetocaloric materials. The application of suitable data reduction methods enables the extraction of meaningful insights into heat transfer and flow characteristics from the experimental data, facilitating an accurate interpretation of the system's behavior.

We identify two primary approaches to data reduction: the curve-matching method and the variable-reduction method.

The curve-matching method involves adjusting a single free variable to minimize the residuals between experimental and theoretical curves. Once optimized, this variable is compared with other experimental results or existing correlations for validation.

The variable-reduction method, on the other hand, establishes a unique relationship between two variables and evaluates the agreement between experimental and theoretical relationships. A notable example of this approach, discussed subsequently, is the single-blow method, which leverages the unique relationship between the maximum slope of the regenerator's exit temperature profile and the NTU value. While the variable-reduction method is generally preferred due to its ability to provide higher certainty, it is highly sensitive to experimental conditions, which can limit its robustness.

In the following subsections, we provide a detailed examination of these methods as applied to both single-blow and periodic-blow analyses. Additionally, we assess the feasibility of employing the variable-reduction method through a sensitivity analysis.

5.1.2.1.1 Single blow

The maximum slope method and the curve matching method are two essential data reduction techniques employed in single blow testing. Widely utilized in previous studies [123]–[125], these methods aim to determine the heat transfer characteristics, specifically the number of transfer units (NTU), by comparing predicted and experimental temperature responses at the regenerator's exit. In this analysis, an average NTU value, denoted as (\overline{NTU}) is used and is defined as:

$$\overline{NTU} = \frac{\overline{h}A}{\overline{C}_r} \tag{5.8}$$

here, \bar{h} represents the average heat transfer coefficient, A is the heat transfer area, and $\overline{C_r}$ is the average thermal capacity rate of the fluid, calculated as the product of the average mass flow rate and the average specific heat. The choice of an average \overline{NTU} aligns with the nature of the developed numerical model, which incorporates variable properties as functions of temperature, pressure, magnetic fields, and other factors. This approach inherently limits the use of non-dimensional variables in the analysis due to the complexity introduced by these varying properties.

The maximum slope method focuses on the maximum rate of change in the exit fluid temperature. This method is based on Locke findings [126], which established that a unique relationship exists between the maximum slope and the NTU. By comparing the experimentally measured maximum slope with this relationship, the NTU can be deduced.

This method offers a significant advantage by isolating a single feature—the maximum slope—of the temperature response curve, thereby reducing sensitivity to experimental noise or deviations in other curve segments. However, its accuracy is dependent on precise modeling of heat transfer effects, including non-adiabatic wall conditions.

To assess the maximum slope method's accuracy and precision, a sensitivity analysis is conducted using the developed numerical model. A step function serves as the boundary condition for the inlet temperature, which is approximated by a logistic function:

$$T_{inlet}(t) = T_{inlet}(0) + \Delta T_{inlet} \frac{\tanh\left(k(t - t_{step})\right)}{2}$$
(5.9)

where $T_{inlet}(0)$ is the initial temperature before the step, ΔT_{inlet} is the temperature difference between the start and ending of the test, t_{step} defines the instant where the step is done, and k controls the steepness of the function.

The sensitivity of the maximum derivative (S_{max}) is analyzed with respect to three parameters: step velocity, wall influence, and external losses. Step velocity is defined as the time interval between reaching 20% and 80% of the total temperature change.

Two cases were analyzed to evaluate the relationship between the exit temperature slope and the NTU, as well as their sensitivity to the three key parameters. In the first case, no influence from wall effects or external heat losses was considered. In the second case, both wall effects and external heat losses were included, with the latter modelled as described in the previous section. Table 42 summarizes the initial conditions for both analyses. The external heat transfer coefficient (h_{ext}) was estimated to be 25 W/m²K, consistent with measured values obtained during testing, as discussed in subsequent sections.

Table 42. Maximum slope analysis information table

	Case 1: No losses	Case 2: External Losses			
Wall (hwall)	No	Yes (Correlations from 2.3.3)			
External Loss (h _{ext})	No Yes $(h_{ext}=25 \text{ W/m}^2\text{H})$				
T_{in}		5.5 K			
$\Delta \mathrm{T}$		10 K			
Mass Flow		10.5 g/min			
Pressure	1.5 bar				
t_{step}		0.5-30 s			

Figure 117 (left) illustrates the results of the first analysis, which yielded the following observations: a step time of less than five seconds is required to achieve adequate sensitivity using this method, and sensitivity decreases as NTU increases in every case.

Figure 117 (right) presents the results of the second analysis, showing that external heat losses and wall effects significantly reduce the sensitivity of the maximum slope method. For NTU values exceeding 200, the sensitivity becomes negligible across all cases, regardless of step velocity.

The second technique is the curve matching method. It takes a broader approach by comparing the entire predicted and measured exit fluid temperature response curves. This technique typically minimizes the residuals between the predicted and experimental exit temperatures by adjusting a target variable, such as the heat transfer coefficient between the fluid and the magnetocaloric material or the external heat loss. While this method provides a more comprehensive evaluation, it requires significantly greater computational effort and is highly sensitive to inaccuracies in modeling inlet conditions or heat transfer effects.

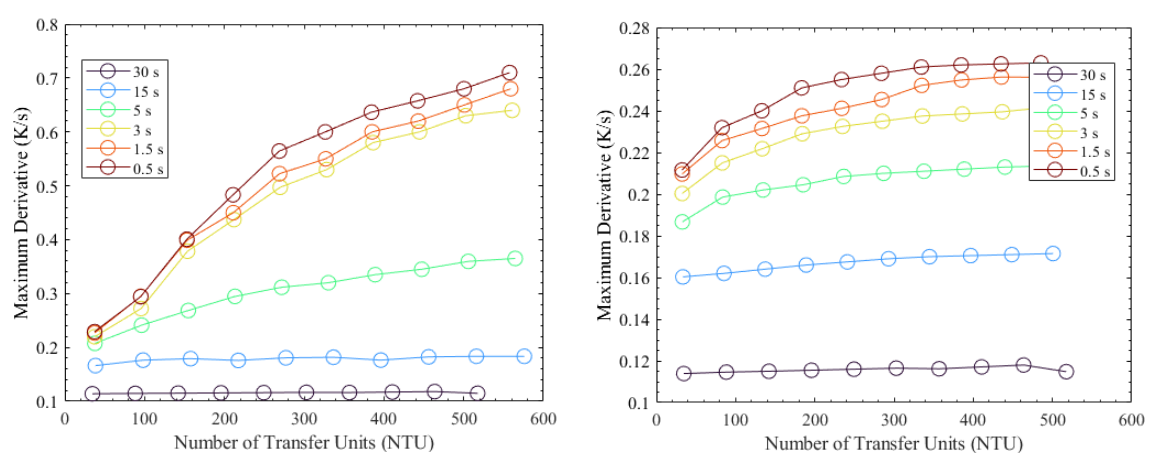


Figure 117. Maximum slope of exit temperature for different NTU values assuming no influence from the wall and no external leaks (left) and including wall and external leaks effects (right).

For example, if the objective is to compute the external heat loss, the optimization process can be expressed as:

$$\min_{h_{amh}} R \tag{5.10}$$

where R is defined as:

$$R = \sum_{i=2}^{t=3} \left[\sum_{t=0}^{t=t_{end}} \left(T_{f_i,t,th} - T_{f_i,t,exp} \right)^2 \right]^{\frac{1}{2}} + \left[\sum_{t=0}^{t=t_{end}} \left(T_{w,t,th} - T_{w,t,exp} \right)^2 \right]^{\frac{1}{2}}$$
 (5.11)

where $T_{f_i,t,th}$ and $T_{f_i,t,exp}$ represent the theoretical and experimental fluid temperatures, $T_{w,t,th}$ and $T_{w,t,exp}$ denote the theoretical and experimental wall temperatures. Measurements are taken at positions $x = \frac{L}{2}$ (i=2) and x = L (i=3). The time domain extends from t = 0 to $t = t_{end}$.

Furthermore, to evaluate the goodness of the fitting, in addition to the residuals, the combined Normalized Root Mean Square Error (NMRMSE) is computed as follows:

Combined NRMSE =
$$\frac{\sqrt{\sum_{i=1}^{N} \sum_{j=1}^{n_i} (T_{ij} - \hat{T}_{ij})^2}}{\frac{1}{N} \sum_{i=1}^{N} (T_{max,i} - T_{min,i})}$$
(5.12)

where N is the number of temperature datasets (e.g., MC1, MC2, MC3, wall temperature), n_i is the number of data points in the i-th dataset, T_{ij} is experimental value at the j-th time point in the i-th dataset, \hat{T}_{ij} is the theoretical value at the j-th time point in the i-th dataset, and $T_{max,i}$ and $T_{min,i}$ are the maximum and minimum values of the experimental data in the i-th dataset.

Based on the results of the sensitivity analysis, it was determined that the applicability of the maximum slope method is constrained by the experimental conditions. Specifically, the rapidity required for the blow process and the influence of external leaks significantly limit its practical use. Consequently, the curve-matching method has been selected as the primary data reduction technique for this analysis.

5.1.2.2 Periodic blow

In periodic blow testing, the variable reduction method is implemented through amplitude attenuation analysis, while the curve-matching method can also be applied in a similar manner [127]. In both approaches, the governing energy equations for the fluid and matrix are solved under periodic boundary conditions, and experimental data are compared with theoretical predictions.

The amplitude attenuation method evaluates the heat transfer performance of a regenerator by examining how an imposed periodic temperature wave is attenuated and phase-shifted as it propagates through the regenerator matrix. Specifically, this method focuses on the reduction in the amplitude of the sinusoidal temperature wave as it travels through the regenerator. Similar to the maximum slope method, a sensitivity analysis is performed using a developed numerical model to assess its applicability and reliability. In this case a sinusoidal function is used as the boundary condition for the inlet temperature:

$$T_{inlet}(t) = A * sin(wt + \phi_0) + D$$
(5.13)

where A is the amplitude of the function, W is the angular frequency, ϕ_0 is the phase shift which indicates the initial position, and D is the offset.

Two cases were conducted to analyze the influence of the angular frequency, the wall and the external losses. The first case neglects the influence of the last 2, while the second case includes both. Table 43 summarizes the main parameters of the analysis.

Table 43. Amplitude attenuation analysis information table

	Case 1: No losses	Case 2: External Losses				
$T_{in} = D$		10 K				
A		5 K				
Mass Flow	8 g/min					
Pressure	1.5 bar					
W	0.05-2 rad/s (Periods 3-125 s)					
Wall (hwall)	No	Yes (Correlations from 2.3.3)				
External Loss (h _{ext})	No	Yes (h _{ext} =1)				

Figure 118 (left) shows the results of the results of the sensitivity analysis while considering no external losses and no influence from the wall. On the other hand, Figure 118 (right), shows the same analysis having considered external losses and the wall influence. It is apparent that there is an optimum angular frequency where the sensitivity of this method is higher, which in this case is around 0.2-0.5 rad/s.

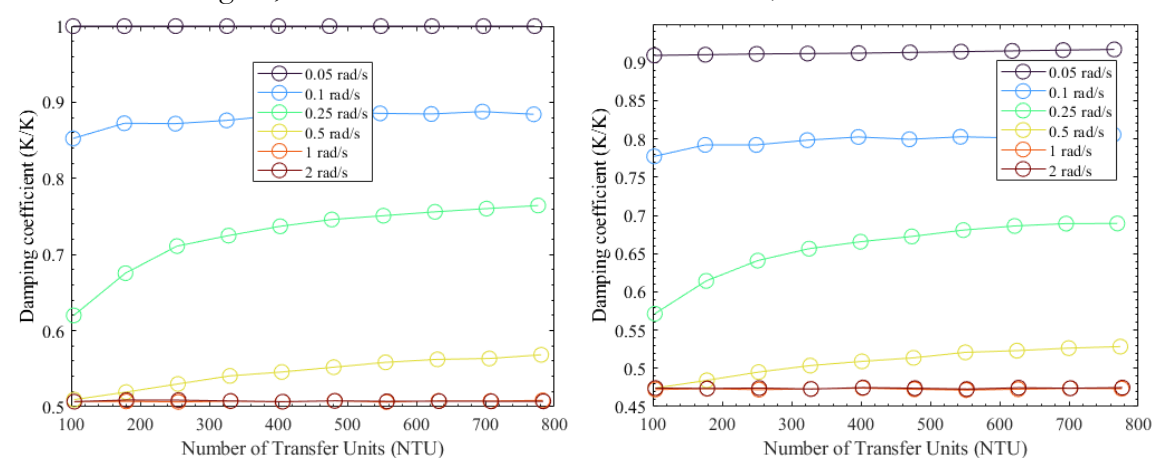


Figure 118. Exit temperature attenuation for different NTU values assuming no influence from the wall and no external losses (left) Exit temperature attenuation for different NTU values accounting for the influence from the wall and external losses (right).

More importantly, it is evident that the wall and the external losses have less influence in the sensitivity than the maximum slope method for single blow testing. Figure 119 shows the sensitivity for both cases. This has been previously reported by Stang and Bush [127].

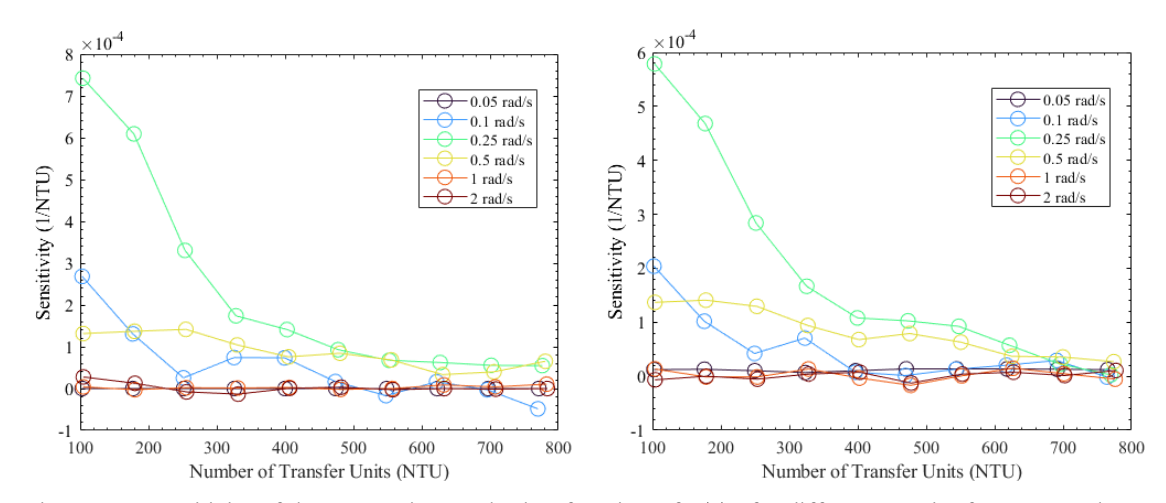


Figure 119. Sensitivity of the attenuation method as function of NTU for different angular frequency, where no influence from the wall nor external losses are considered (left), and when considering wall effects and external losses (right).

The amplitude attenuation method can be effectively combined with phase shift analysis, which assesses the time delay (or phase lag) between the sinusoidal temperature waves at the inlet and outlet. However, in the present study, phase shift analysis has not been included, as no additional information has been observed to be gained by including this factor.

Additionally, the curve matching method proves valuable for analyzing periodic blow tests. Similar to its application in single blow testing, this method aims to estimate a target parameter by minimizing the residuals between the measured and predicted temperature profiles.

5.1.2.3 Results Analysis

This section applies the previously described data reduction techniques to the results obtained from the thermal tests. The analysis begins with the assessment of ambient temperature tests, followed by an evaluation of the cryogenic tests.

5.1.2.3.1 Ambient Temperature

The first set of experiments involved ambient temperature tests using the glass packed bed to validate both the test stand and the experimental procedure. Table 44 shows the results from the curve matching method.

Table 44. Ambient temperature ErAl₂ single blow results summary table

Test Run	B (T)	Mass Flow (g/min)	R	NRMSE
SB00	0	10	45	0.0335
SB01	1	10	83	0. 0456

The fitting results are highly encouraging, as evidenced by the graphical comparison between the model and the measured data presented in Figure 120. The agreement is particularly robust at MC2, situated at the midpoint of the regenerator. However, a minor discrepancy is observed at MC3, which can be attributed to entrance and exit effects causing turbulence at the outlet of the packed bed. Notably, these experiments were performed without the inclusion of conical reducers in the regenerator, which were subsequently introduced to mitigate this issue. Despite this slight inconsistency, the results are considered satisfactory, justifying the advancement to cryogenic temperature testing.

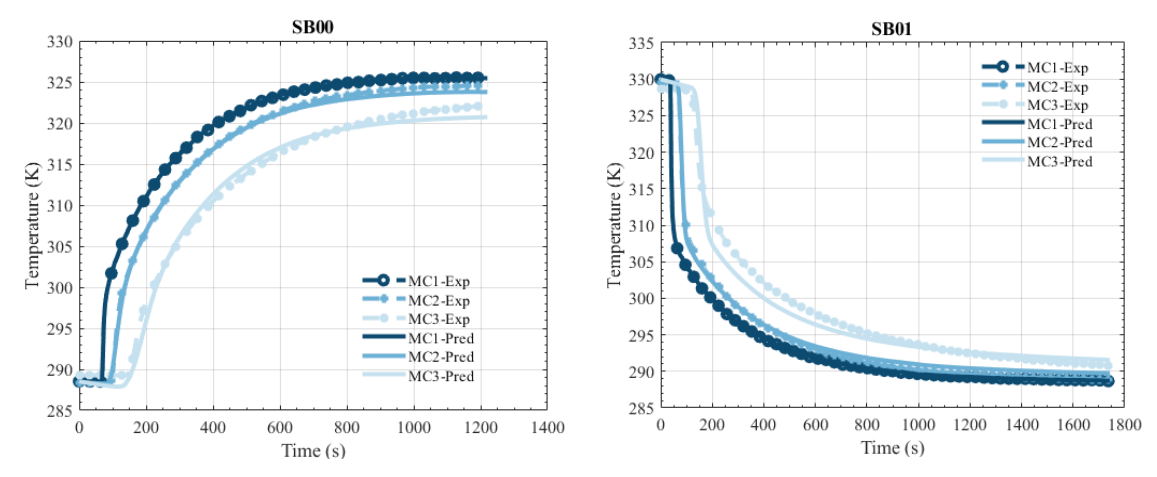


Figure 120. Comparison of experimental and theoretical values from single-blow tests conducted at ambient temperature using a glass packed bed.

5.1.2.3.2 Liquid Helium

The analysis of the ErAl₂ single-blow tests is presented first. The following approach will be employed: the curve-matching method will be used to estimate the external heat transfer coefficient by accounting for ambient heat losses. Based on the figures comparing predicted and experimental results, key conclusions will be drawn.

It should be noted that the maximum slope method is unsuitable for evaluating the heat transfer coefficient in this case. This limitation arises because the temperature step is insufficiently rapid, and significant ambient heat losses reduce the method sensitivity.

Table 45 summarizes the results of the ErAl₂ tests, presenting the residuals and the external heat transfer coefficient obtained from the curve fitting. To aid in comparison, the table also includes the number of transfer units (NTU) between the wall and fluid, as well as between the wall and ambient. These variables are defined as follows:

$$\overline{NTU}_{w} = \frac{\overline{h}_{w}A_{w}}{\overline{C}_{r}} \tag{5.14}$$

where \bar{h}_w represents the average wall-fluid heat transfer coefficient, A is the wall-fluid heat transfer area. The NTU between wall and ambient is computed as follows:

$$\overline{NTU}_{amb} = \frac{\overline{h}_{ext} A_{ext}}{\overline{C_w}} \tag{5.15}$$

where $\overline{C_w}$ is the wall thermal capacity.

Table 45. ErAl₂ single blow results summary table

Test Run	B (T)	Mass Flow (g/min)	R	NRMSE	\overline{NTU}	\overline{NTU}_w	\overline{NTU}_{amb}	h_{ext} (W/m ² K)
SB11	0	10	45	0.1385	327	0.31	2.2e-3	43
SB12	1	10	83	0.1219	344	0.32	3.9e-4	8.6
SB13	2	10	36	0.0413	342	0.32	4.4e-4	8.1
SB14	3	10	28	0.0369	356	0.32	4.4e-2	8.3
SB15	0	6	16	0.1434	404	0.32	5.4e-4	21.5
SB16	1	6	170	0.0756	700	0.35	1.93e-4	6.45
SB17	2	6	84	0.0585	612	0.35	4e-4	6
SB18	3	6	98	0.0592	626	0.35	3.2e-4	2

The results presented in Table 45 allow for the following observations: Tests SB11 and SB15, which were the first conducted, exhibit higher ambient heat losses. This is likely

because the test stand had not yet reached steady-state conditions at the start of testing, and helium evaporation was still significant. The NRMSE indicates reasonably low error across all cases. Furthermore, a comparison of the NTU values suggests that heat transfer to both the wall and the ambient remained relatively low throughout the tests.

Based on the data the model appears to work reasonably well; however, the graphical comparison shows certain discrepancies. Figure 121 compares the results presented in the previous section with the model predictions.

The comparison of SB11 reveals a noticeable discrepancy between the experimental and theoretical results, particularly regarding the wall temperature. This suggests the presence of additional heat loss mechanisms in the test bed, most likely due to heat conduction through the walls and two-dimensional effects, such as radial conduction, which are not accounted for in the developed model. However, these factors alone cannot fully explain the divergence observed in the evolution of the packed bed temperature, as heat losses generally slow down the thermal response of the packed bed. By contrast, in SB13 and SB17, the measured temperature (MC2-Exp) exhibits a faster response than predicted.

Several factors could account for this divergence:

First, inaccuracies in the thermophysical properties of ErAl₂ may play a role. As discussed in Chapter 2, discrepancies exist in the literature regarding material properties. Variations in the actual entropy values could partially explain the observed differences. Additionally, the entropy has a significant dependence on the magnetization direction. For instance, it has been reported that the magnetocaloric effect is more pronounced along the easy magnetization direction (<1,1,1>) compared to other directions (<1,1,0> or <1,0,0>). In this study, an average set of material properties was used under the assumption that particles were randomly oriented. However, this assumption may not hold if particles distribution was not sufficiently arbitrary. Another potential source of divergence lies in property changes during the preparation of the packed bed. A similar phenomenon was reported by Yamamoto et al. [128], who observed alterations in ErCo2's magnetocaloric properties during atomization (100-500 µm particle size). They attributed these changes to their specific atomization process—electrode induction melting gas atomization (EIGA) which involves substantial heating of the material. Two studies have shown a similar effect in ErAl₂: Yamamoto et al. [129] shows slight differences in MCE properties of PIT ErAl₂ wires due to the magnetic anisotropy produced by the PIT process, and in Prusty et al. [130] reports that the melt-spun process introduced variations into the material MCE properties. In the present study, such effects are unlikely to have significantly influenced ErAl₂, as no substantial temperature changes occurred during its atomization process. Nevertheless, it remains unclear how the original material was processed prior to its use in the present study, and specific measurements are needed to confirm this possibility.

A second potential source of error arises from the lack of local measurements for mass flow and pressure. Although all sensors were placed near the packed bed for ambient temperature measurements, the cryogenic assembly recorded mass flow and pressure in the ambient temperature circuit. Local fluid properties may therefore differ substantially, and the assumed boundary conditions may not fully capture actual system behavior.

A third option is the inaccurate positioning of the temperature sensors along the packed bed, which can also contribute to discrepancies. For instance, a larger distance between MC2 and MC3 might explain the larger temperature differences. This possibility was evaluated, and the predicted temperatures in the figures include a shaded region representing a $\pm 5\%$ positioning error. This effect is more evident in the MC2 temperature prediction for SB15, yet it does not entirely account for the observed deviations.

Additional unmodeled effects may further undermine accuracy. Examples include radial conduction within the packed bed and surrounding wall, nonuniform flow profiles with pronounced entrance and exit influences, and variations in porosity throughout the bed.

The results obtained from the single blow tests will be complemented later with the results of the periodic blow testing.

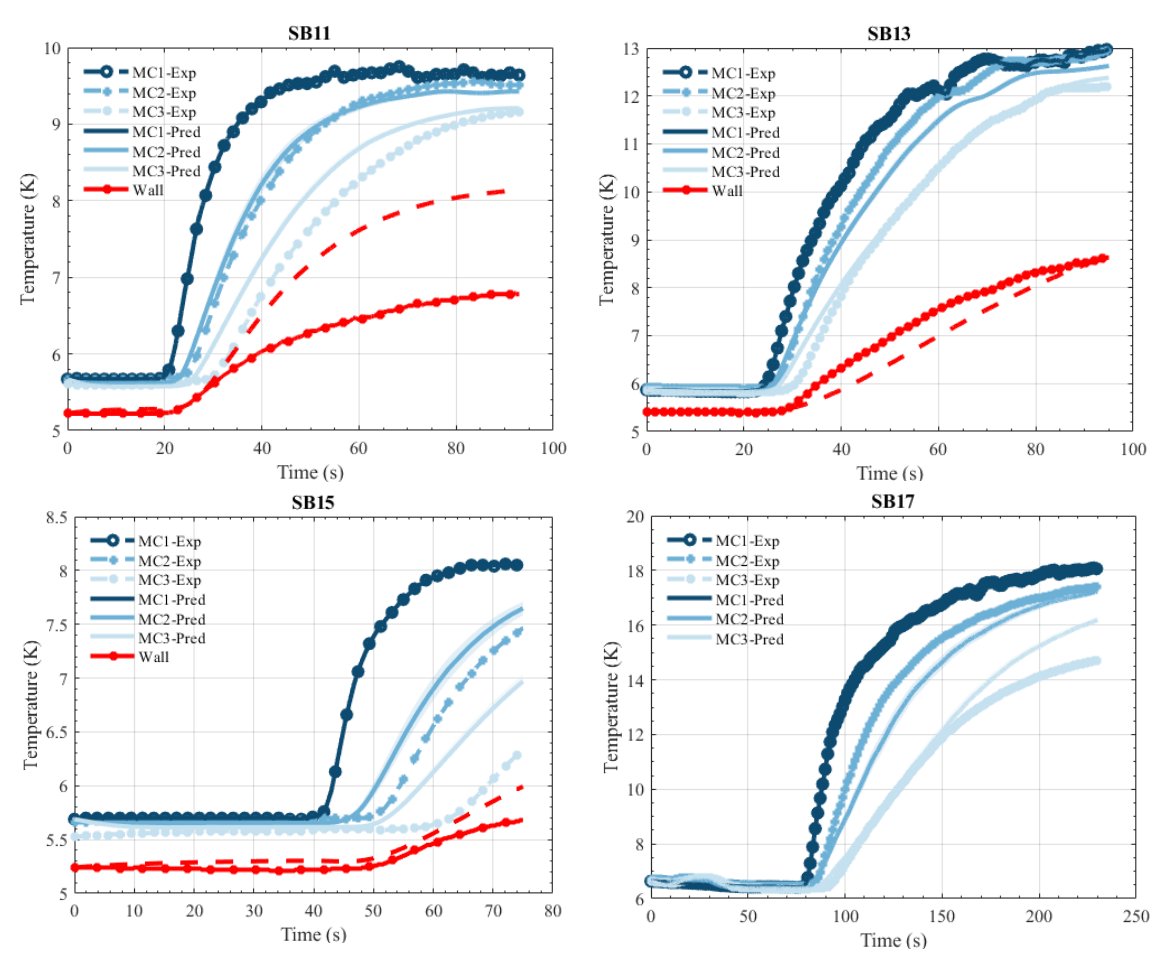


Figure 121. Comparison of experimental (discontinuous lines with data points) and theoretical (continuous lines) values from ErAl₂ single-blow tests.

Next is the analysis of the GGG single blow test results. Similarly, Table 46 shows the results of the tests and the fitting process.

Table 46. GGG single blow data test information table

Test Run	B (T)	Mass Flow (g/min)	R	NRMSE	\overline{NTU}	\overline{NTU}_w	\overline{NTU}_{amb}	h_{ext} (W/m 2 K)
SB21	0	10	25	0.1651	329	0.31	5e-3	100
SB23	2	10	137	0.2782	279	0.28	5.2e-3	100
SB25	0	6	195	0.2281	626	0.32	5.6e-3	100
SB27	2	6	226	0.1747	690	0.33	5.3e-3	100

A less accurate fit is observed in the GGG results compared with those for ErAl₂. Because the wall temperature sensor failed during testing, the fitting for GGG proceeded without that measurement, reducing the accuracy of the curve matching method. The external heat transfer coefficient was capped at 100 W/m²K since higher values identified in the optimization were considered implausible, given that the test conditions closely resembled those of the ErAl₂ experiments.

Figure 122 assists in interpreting the data. The low specific heat capacity of GGG in the target temperature range, which is below 3 J/kg K at 0 T (see Figure 20), suggests a faster temperature response during the single-blow tests than that observed with ErAl₂. Contrarily, the measured temperatures rose significantly more slowly than expected.

These results may be attributed to unaccounted external losses that influence the overall dynamics of the system. Similar factors raised in the ErAl₂ tests could also apply here. The periodic blow tests presented next will further clarify these findings.

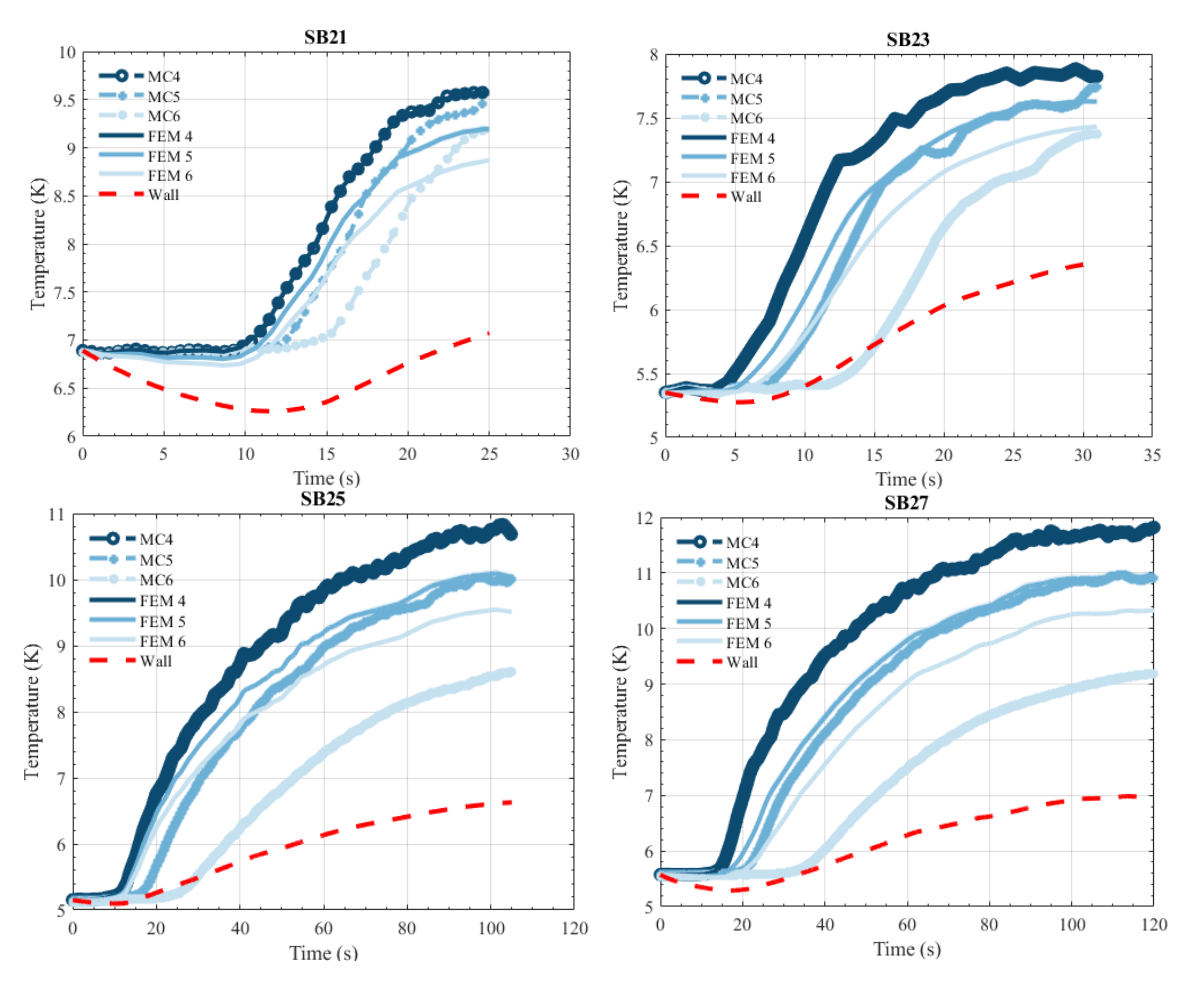


Figure 122. Comparison of experimental (discontinuous lines with data points) and theoretical (continuous lines) from GGG single-blow tests.

In the next paragraphs the results from the periodic blow tests are analyzed.

Table 47 shows the results for the $ErAl_2$ tests, presenting the test information, the residuals and the goodness of the fitting with the NRMSE value, and the \overline{NTU} value with the theoretical damping coefficient (Z) and the experimental damping coefficient (Z_{exp}).

Table 47. ErAl ₂ periodic blow data	a test information table
------------------------------------------------	--------------------------

Title	B (T)	Mass Flow (g/min)	F (rad/s)	R	NRMSE	\overline{NTU}	\overline{NTU}_w	\overline{NTU}_{amb}	Z	Z_{exp}
PB11	0	10	0.08	198	0.1141	333	0.31	4.8e-3	0.88	0.81
PB13	2	10	0.1	157	0.1068	333	0.31	4.8e-3	0.88	0.89
PB14	0	6	0.1	261	0.1972	619	0.33	5.3e-3	0.71	0.51
PB16	2	6	0.1	312	0.1779	618	0.33	4.5e-3	0.66	0.59

The values of NRMSE are reasonable; however, a clear distinction is evident between the results for high and low NTU values. Specifically, while PB11 and PB13 exhibit NRMSE values of approximately 0.1, the values for PB14 and PB16 are nearly double. Additionally, the difference between the damping coefficients (Z and Z_{exp}) is notable.

Figure 123 provides a comparison between theoretical predictions and experimental results, visually reinforcing these observations. For the low NTU tests, the experimental data align reasonably well with the theoretical predictions, though some discrepancies remain. These deviations may be attributed to factors previously discussed in relation to the single-blow test. Notably, the MC2 curve appears closer to the MC1 curve than to the MC3 curve, which could suggest inaccuracies in the positioning of temperature sensors.

The discrepancies are more pronounced in the high NTU region. Significant differences are observed between the temperature measurements and theoretical predictions within the packed bed. While MC2 shows some resemblance to the predicted behavior, MC3 deviates substantially. This discrepancy suggests that the flow may not have fully developed. This phenomenon is particularly evident in PB16, where temperature evolution at the end of the cycle aligns more closely with predictions compared to the beginning of the cycle.

A plausible explanation for these observations is that the flow transitions toward a laminar regime as the Reynolds number decreases below 50. In such conditions, axial and radial dispersion effects may become more significant than predicted, and may exert a greater influence on flow dynamics.

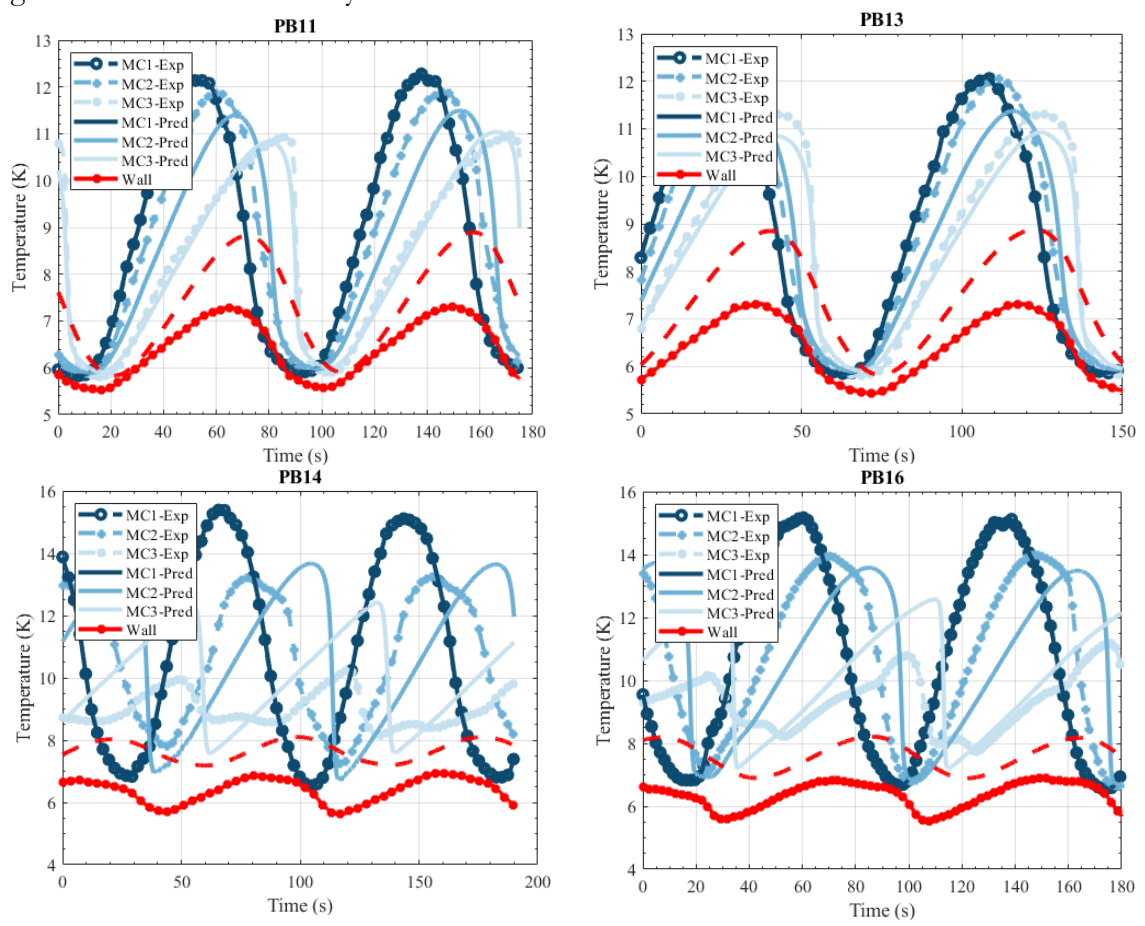


Figure 123. Comparison of experimental (discontinuous lines with data points) and theoretical (continuous lines) values from ErAl₂ periodic-blow tests.

Next, Table 48 shows the results for the GGG periodic blow tests.

Table 48. GGG periodic blow data test information table

Title	В (Т)	Mass Flow (g/min)	F (rad/s)	R	NRMSE	\overline{NTU}	\overline{NTU}_w	\overline{NTU}_{amb}	Z	Z_{exp}
PB21	0	10	0.07	171	0.1413	296	0.29	4.9e-3	0.92	0.88
PB22	1	10	0.1	115	0.0774	396	0.32	3.2e-3	0.81	0.92
PB23	2	10	0.08	144	0.1018	340	0.31	4.6e-3	0.84	0.86
PB24	0	6	0.07	272	0.1997	725	0.35	4.4e-3	0.72	0.56
PB25	1	6	0.07	146	0.0693	537	0.34	3.6e-3	0.79	0.83
PB26	2	6	0.09	318	0.2116	827	0.37	3.8e-3	0.67	0.58

The results of the GGG tests exhibit similarities to those of the ErAl₂ tests, particularly in that the low NTU tests demonstrate a better fit to the model compared to the high NTU

tests. Notably, the actual NRMSE for PB21 is lower than the value reported in the table, as the wall temperature sensor was unable to accurately measure temperatures below 6.5 K. Additionally, PB25 appears to be an exception, as it shows a very low NRMSE. However, this can be attributed to its unexpectedly low NTU value—537 compared to the 700–800 range observed in the other tests within the same group. This reduced NTU value is explained by a mass flow rate exceeding the target of 6 g/min.

The disparity in model fitting between high and low NTU values can be attributed to the same factors discussed previously. At high NTU values, laminar flow conditions dominate, leading to increased dispersion and more pronounced wall effects, which negatively impact the agreement between experimental results and theoretical predictions.

The periodic blow tests yielded results that differed notably from those of the single-blow tests. While the temperature responses in the single-blow tests were slower than anticipated, the periodic blow tests generally exhibited quicker responses. This trend is evident as shown in Figure 124 and further supported by the damping coefficients presented in Table 48, where $Z_{exp} > Z$ is typically observed. However, an exception to this pattern occurs in the high NTU tests (PB24 and PB26).

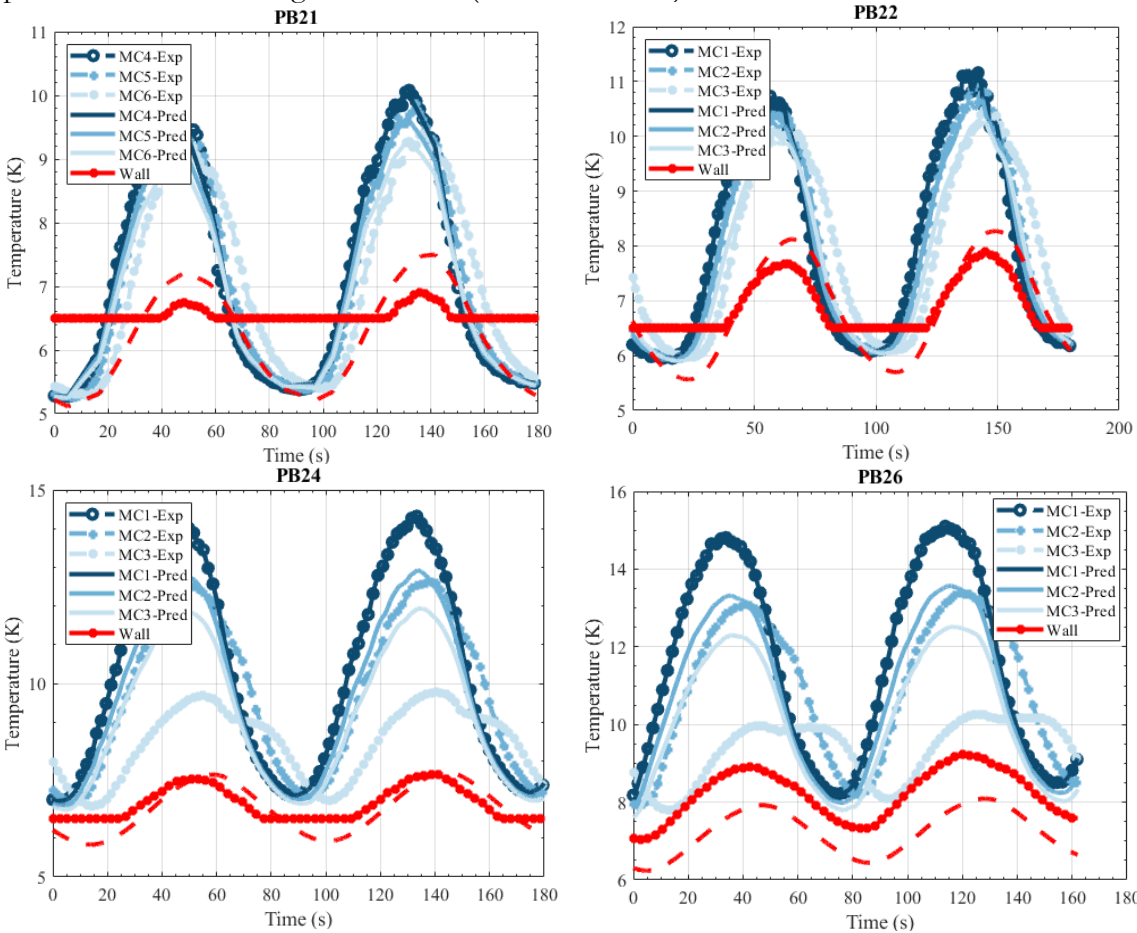


Figure 124. Comparison of experimental (discontinuous lines with data points) and theoretical (continuous lines) values from GGG periodic-blow tests.

This chapter demonstrates that the numerical model successfully captures the fundamental thermal behavior at ambient conditions, providing an initial validation of its predictive capabilities. However, the transition to cryogenic operations introduces significant complexities, most notably from external heat losses, nonuniform flow profiles, and the intrinsic material characteristics of ErAl₂ and GGG. The single and periodic blow tests exhibit distinct responses, with the former tending to show slower temperature evolution than predicted and the latter often presenting faster dynamics. These discrepancies arise partly from incomplete knowledge of local fluid properties, uncertain

sensor positioning, and the non-ideal flow regimes that emerge at low temperatures and low Reynolds numbers.

Although external losses complicate direct comparisons between experimental data and theoretical predictions, the partial agreement observed across multiple experimental configurations indicates that the model retains a reasonable degree of reliability. Nevertheless, the clear impact of wall effects, radial conduction, and uncharacterized magnetocaloric properties exposes gaps that should be addressed. More accurate characterizations of material properties through independent measurements, improvements to the test stand to reduce extraneous heat losses, and an emphasis on optimized testing conditions at higher mass flow rates are logical steps toward refining the correlation between model outcomes and experimental evidence. Future work may prioritize periodic blow tests, which appear less sensitive to certain external losses, and incorporate more precise sensor placement to enhance confidence in local boundary conditions. Overall, these findings underscore both the promise of the numerical model and the need for continued refinements in experimental methods and system design to achieve reliable correlations in cryogenic heat transfer studies.

5.1.3 Magnetic tests

This section provides an analysis of the magnetic tests conducted. As in the preceding section, it begins with a description of the data reduction techniques applied to the measurements. Furthermore, it introduces potential additional testing methodologies that could enhance the characterization of magnetocaloric packed beds.

5.1.3.1 Data reduction techniques

The data analysis described next will be applied to the ramping rate, and variable temperature test. Due to the limited knowledge of the boundary conditions under which the no-load tests were conducted, only the qualitative analysis detailed in Chapter 4 will be presented.

Unlike the thermal tests, no standardized techniques currently exist for evaluating the magnetic properties of magnetocaloric packed beds. To address this, a methodology similar to that outlined in the previous section will be employed. The curve-matching method will serve as the primary approach for assessing the accuracy of the numerical model. Additionally, the relation between the experimental and theoretical maximum temperature differences will be analyzed and compared to provide further insights. For that purpose, the variable θ is defined as follows:

$$\theta = \frac{\Delta T_{exp}}{\Delta T_{pred}} \tag{5.16}$$

Figure 125 illustrates the maximum temperature difference at the end of the packed bed (MC3) obtained from a simulated case. The simulation corresponds to Case 1 in Table 49, where standard heat transfer correlations were applied.

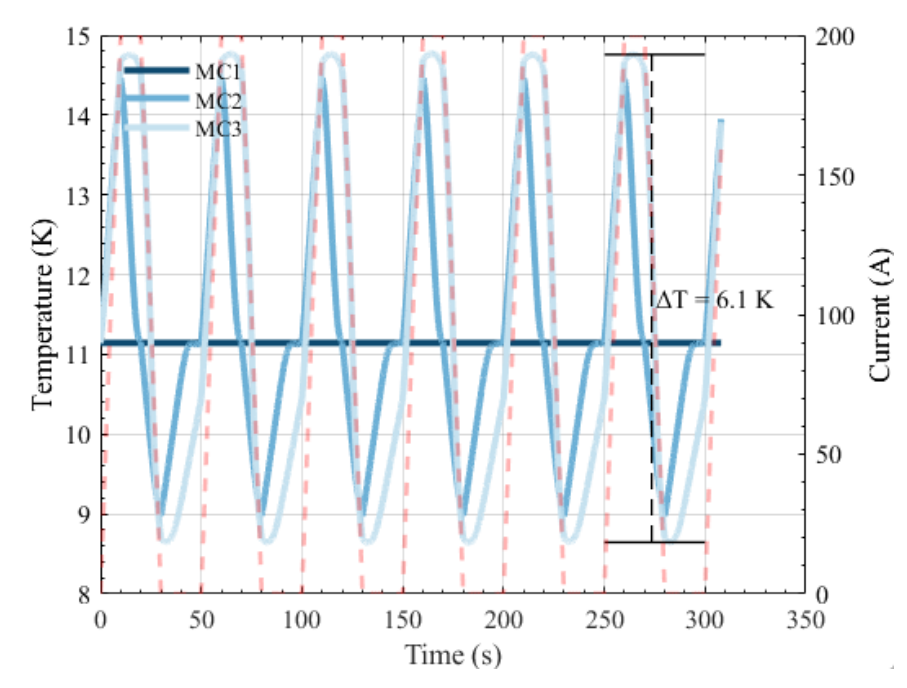


Figure 125. Simulation of magnetic cycle tests, indicating the magnetic field evolution (discontinuos red), and the temperature evolution in 3 positions of the packed bed: MC1, MC2, and MC3. The outlet (MC3) total temperature difference is indicated in the figure.

Since the use of standard heat transfer correlations was not validated during the thermal tests, their associated uncertainty is, by default, incorporated into the analysis of the magnetic tests. Before evaluating the results, an assessment of the impact of heat transfer dynamics is conducted. A similar analysis to the developed in the previous section is done. To examine the influence of heat transfer, wall effects, and external losses, two cases were analyzed. In the first case, the effects of wall heat transfer and external losses were neglected, while in the second case, both factors were included. Table 49 summarizes the key parameters used in this analysis.

Table 49. Magnetic tests analysis information table

	Case 1: No losses	Case 2: External Losses
T_{in}		11 K
Mass Flow		10 g/min
Pressure		1.5 bar
Magnetic Field	Trapez	oidal profile: 0-2 T
Wall (h _{wall})	No	Yes (Correlations from 2.3.3)
External Loss (h _{ext})	No	Yes (h _{ext} =1-50)

The results of the analysis are presented in Figure 126. It can be observed that, after accounting for the wall and the heat loss term, the influence of the external heat transfer coefficient decreases as its value increases. Additionally, the value of NTU, heat transfer between fluid and magnetocaloric, has not a significant influenced in the NTU range of study (200-500).

Consequently, to simplify the analysis of the measured data, an external heat transfer coefficient of 25 W/m²K was assumed. This value lies within the upper range based on the thermal test measurements.

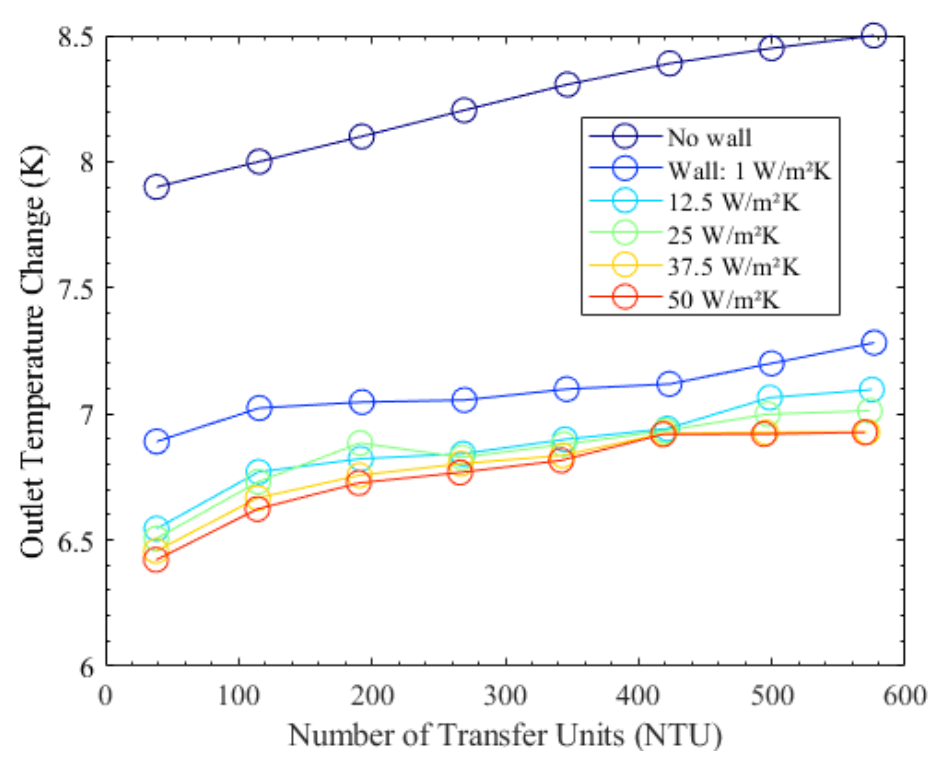


Figure 126. Sensitivity of the maximum outlet temperature difference as function of NTU for different external heat transfer coefficients.

5.1.3.2 Results Analysis

The results analysis section follows a structure similar to that of the previous sections. Initially, a table is presented containing the fitting results and data reduction variables. This is accompanied by a graphical comparison between the model predictions and the measured data, which serves as the foundation for the subsequent discussion. The analysis begins with the ErAl₂ data, followed by an examination of the GGG test results.

Table 50 summarizes the outcomes of the ErAl₂ tests. In addition to metrics such as the normalized root mean square error (NRMSE) and NTU, as reported in the thermal tests, additional variables are included: the mass ratio U, θ_2 (MC2), θ_3 (MC3), and θ_{max} which is introduced later.

Table 50. ErAl₂ magnetic test results information table

Title	B (T)	dI/dt (A/s)	T _{start} (K)	Mass Flow (g/min)	NRMSE	NTU	U	θ_2	θ_3	θ_{max}
RR12	1	10	5-6	10	0.2367	241	0.2354	0.54	0.63	0.63
RR13	1	20	5-6	10	0.2273	235	0.2627	0.52	0.48	0.52
RR15	1	10	10-12	10	0.1483	393	0.0376	0.68	1.12	0.96
RR16	1	20	10-12	10	0.1932	411	0.0357	0.81	0.91	0.70
VT18	2	20	15	6	-	-	-	-	-	-
VT19	3	20	15	6	-	-	-	-	-	-
VT110	1	20	6	10	0.4486	207	0.3170	0.43	0.45	0.45
VT111	2	20	6	10	0.2667	249	0.1839	0.64	0.71	0.71
VT112	3	20	6	10	0.1410	274	0.1157	0.51	0.71	0.71
VT113	1	20	10	10	0.2139	407	0.0366	0.68	0.97	0.97
VT114	2	20	10	10	0.2113	411	0.0363	0.59	1.14	0.95
VT115	3	20	10	10	0.1665	401	0.0367	0.61	1	0.98
VT116	1	20	15	10	0.5346	472	0.0424	0.70	1.11	0.74
VT117	2	20	15	10	0.4905	475	0.0513	0.39	0.78	0.78
VT118	3	20	15	10	0.4341	474	0.0568	0.42	0.77	0.77

Prior to discussing the results, it is important to note that tests VT18 and VT19 could not be compared with the numerical model due to a malfunction in the temperature sensor MC1 during testing.

The data presented in Table 50 provide several key observations. First, the normalized root mean square error (NRMSE) for most tests, with the exception of those conducted at 15 K, falls within the range of 0.15 to 0.25. In contrast, tests performed at 15 K exhibit poorer agreement, with NRMSE values ranging from approximately 0.4 to 0.55. Figure 127 illustrates a comparison between the model predictions and experimental measurements for selected tests.

A reasonable agreement is evident in the first three images, corresponding to RR15, VT112, and VT115. However, the final panel image, representing VT116, shows a clear discrepancy between the model and the experimental data. Upon closer examination of this image, it becomes apparent that most of the mismatch originates from MC2. Specifically, while the model predicts a significant temperature difference in MC2, this is not observed in the measurements. In contrast, the model captures the temperature evolution of MC3 reasonably well. Additionally, the measured temperature difference in MC3 exceeds expectations, as reflected by its larger θ_3 value.

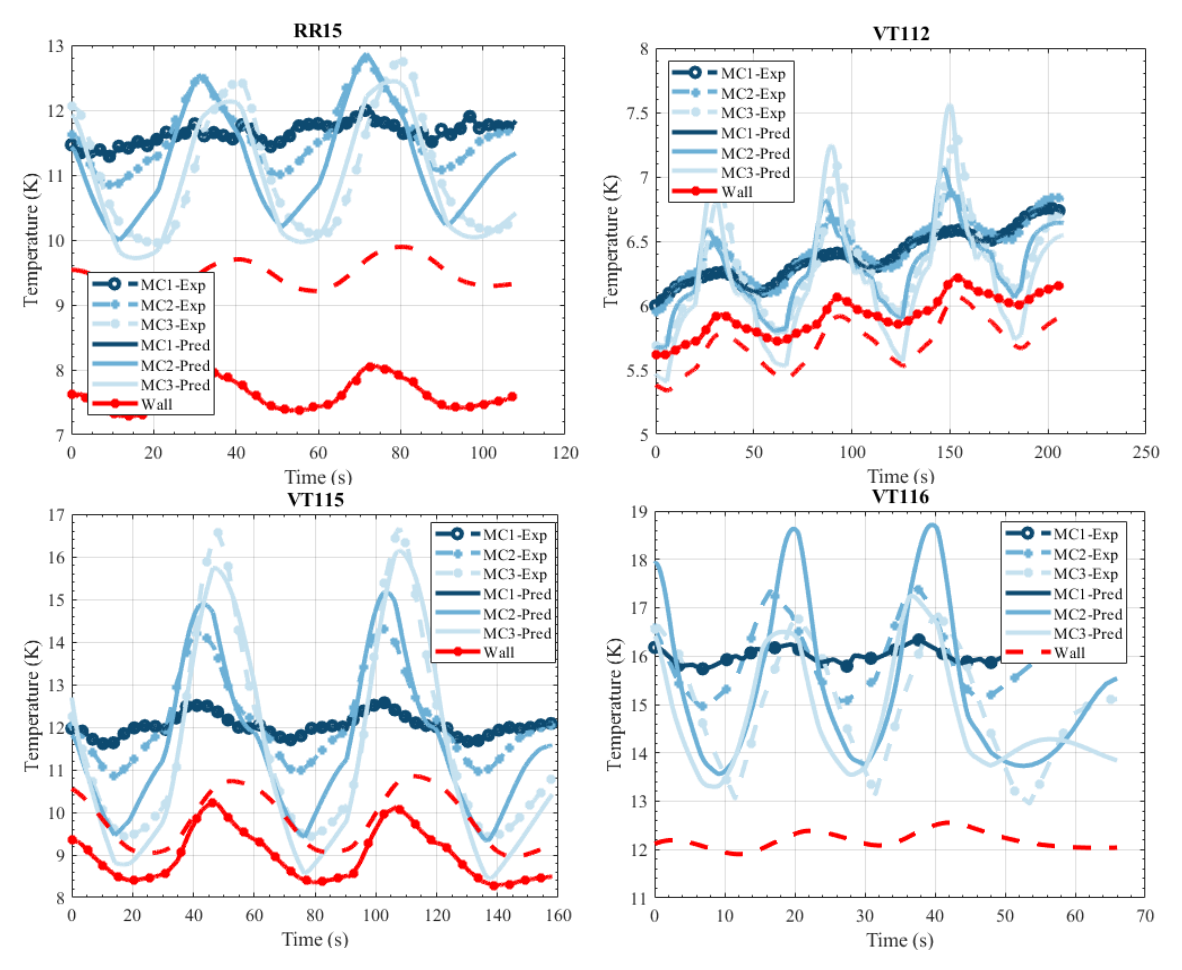


Figure 127. Comparison of experimental (discontinuous lines with data points) and theoretical (continuous lines) values from ErAl₂ magnetic tests.

At first glance, it may seem unexpected that θ_3 could exceed a value of 1. However, this phenomenon is not unique to VT116; similar behavior is observed in tests RR15 and VT114, where θ_3 also surpasses 1. Moreover, an analysis of the θ_2 and θ_3 data reveals a consistent trend: the values of θ_2 are generally much smaller than those of θ_3 , which more frequently approach or exceed 1. This pattern suggests distinct underlying dynamics influencing these two variables.

A 3D plot depicting the evolution of temperature over time and space provides critical insights into the system's behavior. Figure 128 presents the numerical model's prediction of the temperature distribution for test VT114.

The results indicate that the peak temperature does not occur at the end of the packed bed, as might initially be expected, but rather at an intermediate position along its length. This observation motivates the introduction of the variable θ_{max} , defined as the ratio between the maximum measured temperature difference and the maximum predicted temperature difference at any position within the packed bed.

$$\theta_{max} = \frac{max(\Delta T_{exp})}{max(\Delta T_{pred})}$$
 (5.17)

The inclusion of θ_{max} facilitates determining whether the observed differences between θ_2 and θ_3 arise from an unexpectedly high magnetocaloric effect or are attributable to other factors.

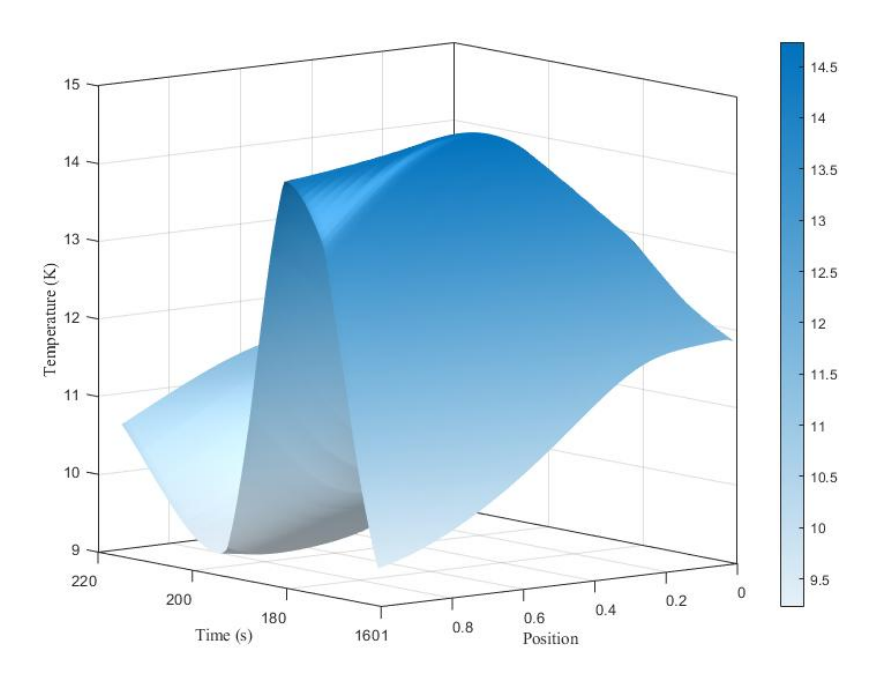


Figure 128. 3D visualization of temperature evolution during the last cycle of VT114.

Figure 129 provides a contour plot of the same test, offering improved visualization of the observed phenomena. In the absence of mass flow through the packed bed, the temperature evolution would be expected to follow a pattern proportional to the applied magnetic field. However, when a mass flow rate is present, the temperature increase of the inlet particles is constrained by heat exchange with the fluid. The heat generated (or removed) is subsequently transferred downstream from one particle to the next. This process continues until either the magnetic field ceases to increase or the magnetocaloric effect significantly diminishes due to elevated temperatures or reduced entropy change at higher magnetic fields. This progression creates the effect seen in the plots: initially, the magnetocaloric contributions from successive particles are additive, leading to a cumulative increase in temperature. However, once saturation is reached, the magnetocaloric effect begins to diminish, resulting in a decrease in the temperature change.

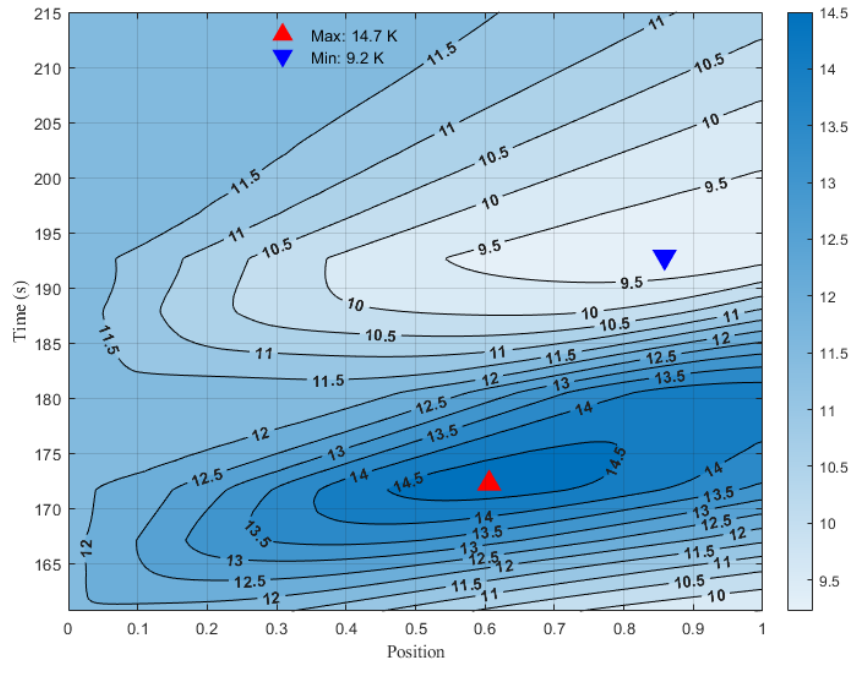


Figure 129. Contour plot of temperature evolution during the last cycle of VT114.

Moreover, the interplay of constructive and destructive superposition can result in a periodic response within the packed bed. This phenomenon is evident in the analysis of the results from test VT116, as shown in Figure 130. Specifically, during the time interval between approximately 85 and 95 seconds, at a position corresponding to 0.4 of the total regenerator length, a notable behavior is observed. At this point, when the temperature reaches its maximum, it initially decreases but subsequently begins to rise again, highlighting the dynamic nature of the thermal response.

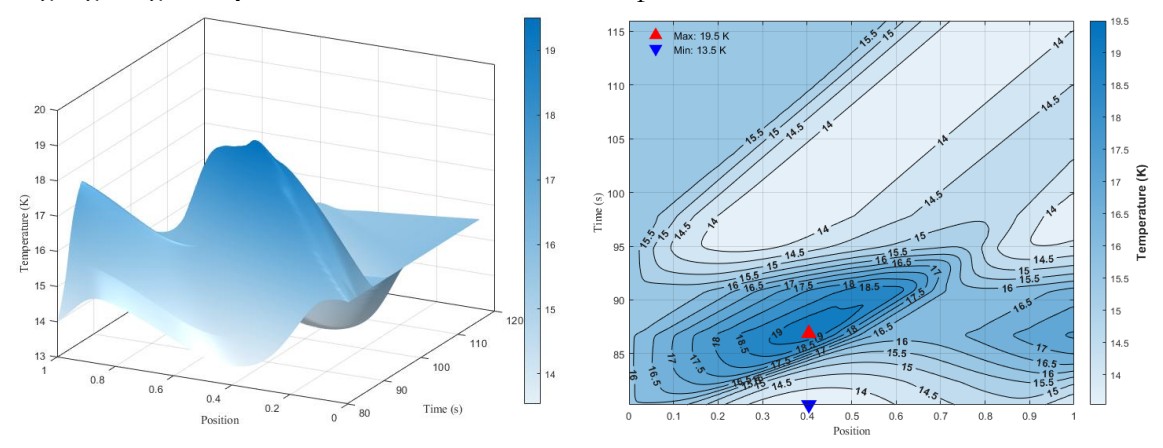


Figure 130. 3D visualization of temperature evolution during the last cycle of VT116.

This observed phenomenon partially accounts for the results, particularly the tendency of θ_3 to exceed θ_2 . During the testing scenarios, the packed bed reached saturation at a later position than predicted by the model, indicating a positional shift in the temperature response. This discrepancy could suggest factors such as flow maldistributions, deviations in material properties compared to expectations (as highlighted in the thermal tests), or potential setup errors. Notably, measurements from the 15 K tests (VT116–118) suggest that material property variations may be more pronounced near this temperature range.

Table 51 presents the results of the GGG magnetic tests. It should be noted that not all tests could be analyzed using the proposed methodology. Specifically, tests VT22-23 and VT211-212 exhibit indications of helium liquefaction during the demagnetization phases. In the absence of precise information on the actual conditions, such as pressure and initial vapor quality, accurately replicating these testing conditions within the numerical model proves challenging.

The results of the GGG testing are mixed. The variable temperature (VT) tests yield reasonable outcomes, particularly when considering that VT25 and VT26 exhibit a very high NTU. As noted in the thermal tests section, this range is dominated by laminar flow effects. The first panel of Figure 131 illustrates the comparison for the VT25 tests, clearly showing a temperature gradient between MC1 and MC3, which is consistent with observations from PB24 and PB26. The remaining VT tests demonstrate better alignment between the model predictions and experimental data.

The initial ramping rate (RR) tests yielded poorer results, particularly for RR22 and RR23. This can be partially attributed to the low temperatures at which these tests were conducted, where helium, as in tests VT22-23, was near its critical temperature. Inaccuracies in pressure and mass flow measurements had a significant impact on the reliability of the results.

A similar trend to the ErAl₂ tests is observed, where θ_3 is typically larger than θ_2 . This could similarly indicate set up errors or flow maldistribution and the presence of void volumes.

Table 51. GGG magnetic test results information table

Title	B (T)	dI/dt (A/s)	T _{start} (K)	Mass Flow (g/min)	NRMSE	NTU	U	θ_2	θ_3	θ_{max}
RR22	1	10	5-6	10	0.3347	276	3.3481	0.70	0.68	0.68
RR23	1	20	5-6	10	0.6856	284	3.4601	0.47	0.42	0.42
RR25	1	10	10-12	10	0.1256	419	3.5638	1.09	1.32	1.09
RR26	1	20	10-12	10	0.3421	436	3.2380	0.69	0.58	0.58
VT22	2	20	6	6	-	-	-	-	-	-
VT23	3	20	6	6	-	-	-	-	-	-
VT25	2	20	10	6	0.5572	910	0.8442	0.62	0.55	0.55
VT26	3	20	10	6	0.3428	846	1.0367	0.75	0.67	0.67
VT211	2	20	6	10	-	-	-	-	-	-
VT212	3	20	6	10	-	-	-	-	-	-
VT214	2	20	10	10	0.0890	408	4.3	0.82	0.92	0.92
VT215	3	20	10	10	0.1222	355	4.23	0.81	1	1
VT220	4	20	10	10	0.1826	405	3.61	1.23	1.90	
VT221	2	20	10	15	0.1880	356	4.87	0.75	0.87	0.87

The magnetic tests, broadly confirmed the findings of the earlier thermal tests highlighting the persistent influence of wall effects, radial conduction, and uncharacterized magnetocaloric properties in the packed beds. Although external heat losses complicated direct comparisons between measured data and the numerical predictions, partial convergence across multiple configurations demonstrated that the model retained an appreciable degree of fidelity.

ErAl₂ demonstrated reasonable agreement with the measured behavior below 15 K, indicating that the assumed property data may not fully capture its actual magnetocaloric response. Experimental observations revealed a resonance-like phenomenon, characterized by the emergence of a maximum thermal difference in specific axial segments of the packed bed, which exhibited a phase shift relative to the modeled predictions. These discrepancies are likely attributable to previously identified setup errors, flow maldistribution, or the presence of void volumes within the bed.

GGG exhibited qualitatively similar behavior during testing, although particular runs near helium's critical region could not be definitively analyzed with the chosen methodology.

Overall, the results underscore a need for refined experiments and improved characterization of external losses, as well as more accurate material property data, to strengthen the correlation between simulated predictions and observed magnetocaloric performance.

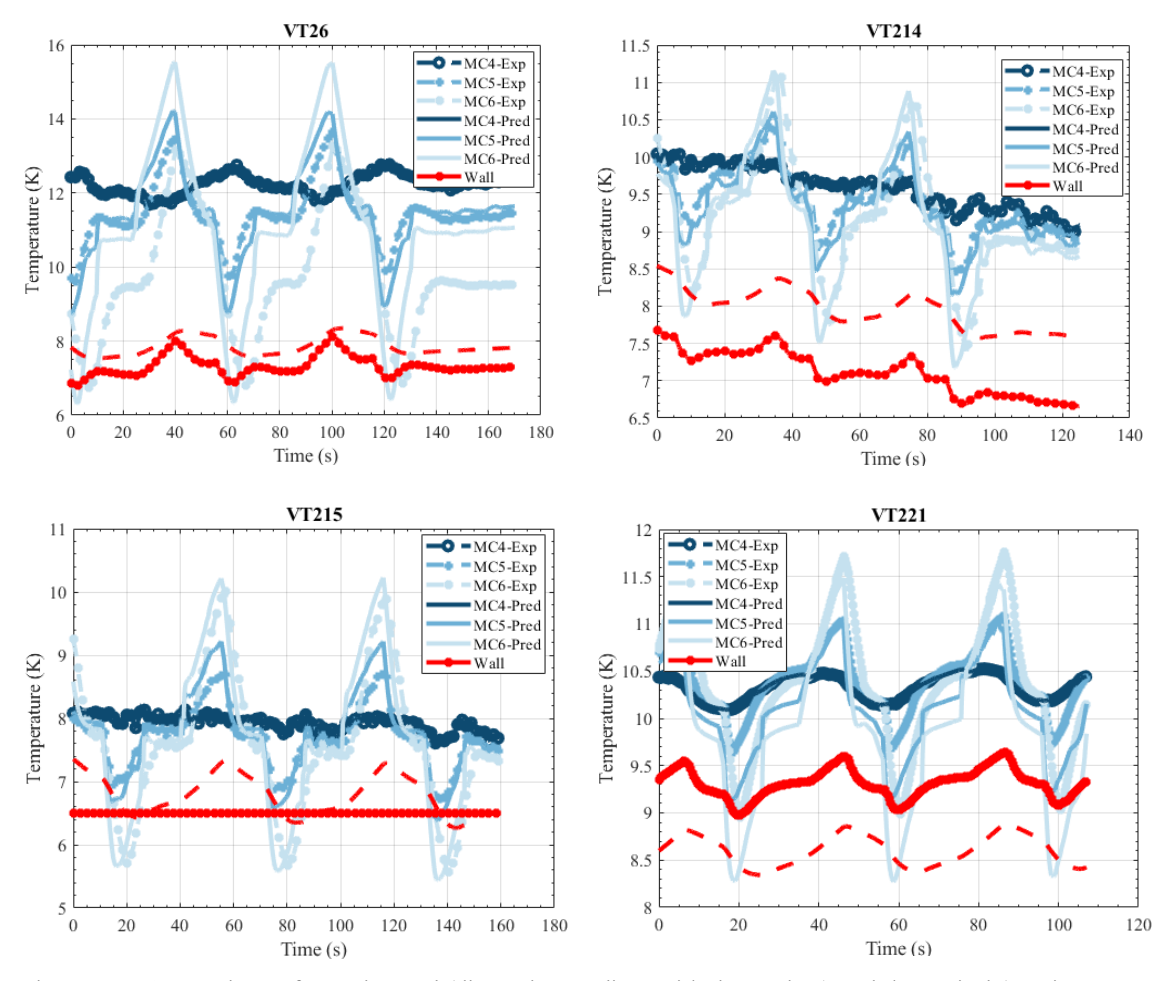


Figure 131. Comparison of experimental (discontinuous lines with data points) and theoretical (continuous lines) values from GGG magnetic tests.

5.1.3.3 Alternative magnetic tests

Based on the insights gained from these tests and the subsequent analysis of the results, this section proposes the inclusion of additional tests for the characterization of a magnetocaloric regenerator.

The first proposed test is the magnetic single-blow test, which serves as an adaptation of the conventional single-blow test. A significant limitation of the standard SB test lies in its heating mechanism, particularly at cryogenic temperatures. Ideally, the heating mechanism should be rapid and minimally intrusive to avoid interference with other aspects of the test. However, achieving such conditions presents considerable challenges. The magnetic single-blow test addresses this issue by utilizing the magnetocaloric material itself as the heating mechanism. This is achieved by applying a quasi-step change in the magnetic field to the regenerator, thereby inducing a thermal response. Figure 132 shows an example of the temperature response of the packed bed during a magnetic single blow test.

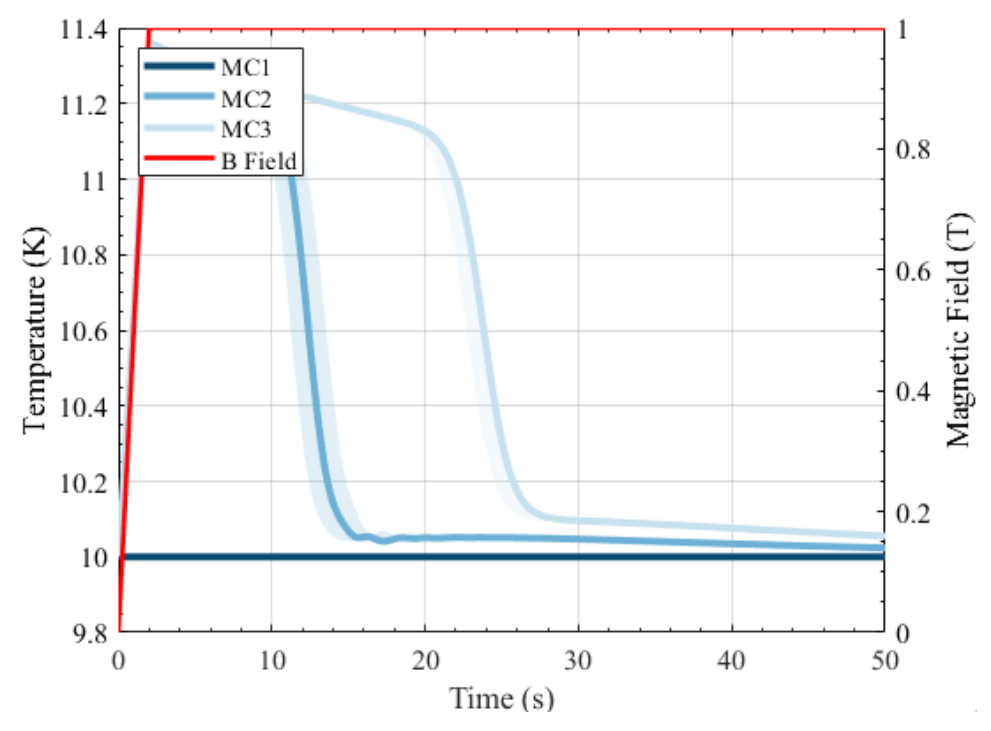


Figure 132. Thermal response of the packed bed in a simulated magnetic single blow test.

The numerical model developed in this study demonstrates a unique relationship between the number of transfer units (NTU) and the maximum derivative observed during the relaxation phase, as the packed bed returns to its initial temperature. This relationship is illustrated in Figure 133, which compares two cases: one with a magnetic field ramp rate of 0.1 T/s (left) and another with a ramp rate of 0.5 T/s (right). The figure also highlights the effects of wall and external thermal losses on this relationship. Notably, similar to the single-blow test, the sensitivity of the system is greater at lower NTU values, emphasizing the influence of these parameters on the thermal behavior of the regenerator.

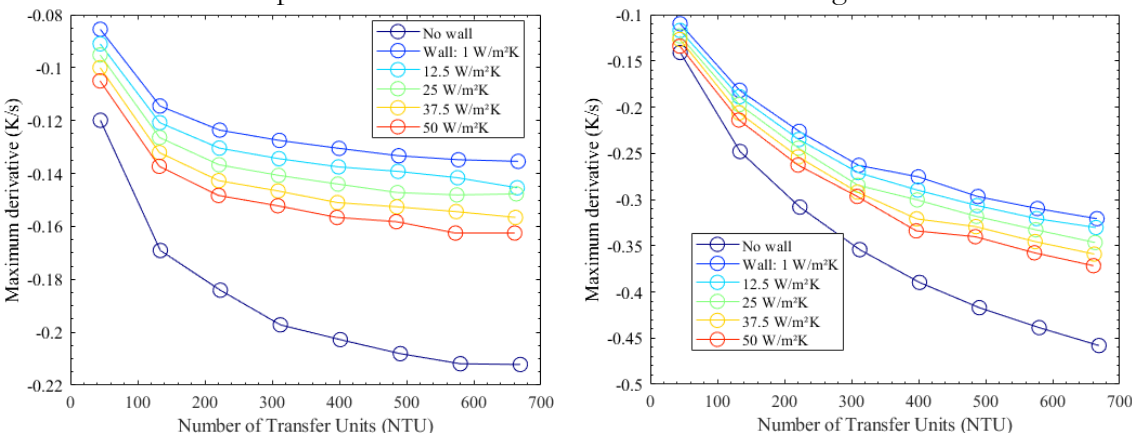


Figure 133. Maximum slope of the exit temperature as a function of NTU for various external heat transfer values (0 W/m·K to 50 W/m·K), shown for magnetic ramp rates of 0.1 T/s (left) and 0.5 T/s (right).

The second proposed test, referred to as the magnetic periodic blow test, is analogous to the conventional periodic blow test. In this method, a sinusoidal magnetic field is applied to the regenerator, and the resulting thermal response is analyzed. Figure 134 provides an example of the temperature response of the regenerator during such a test.

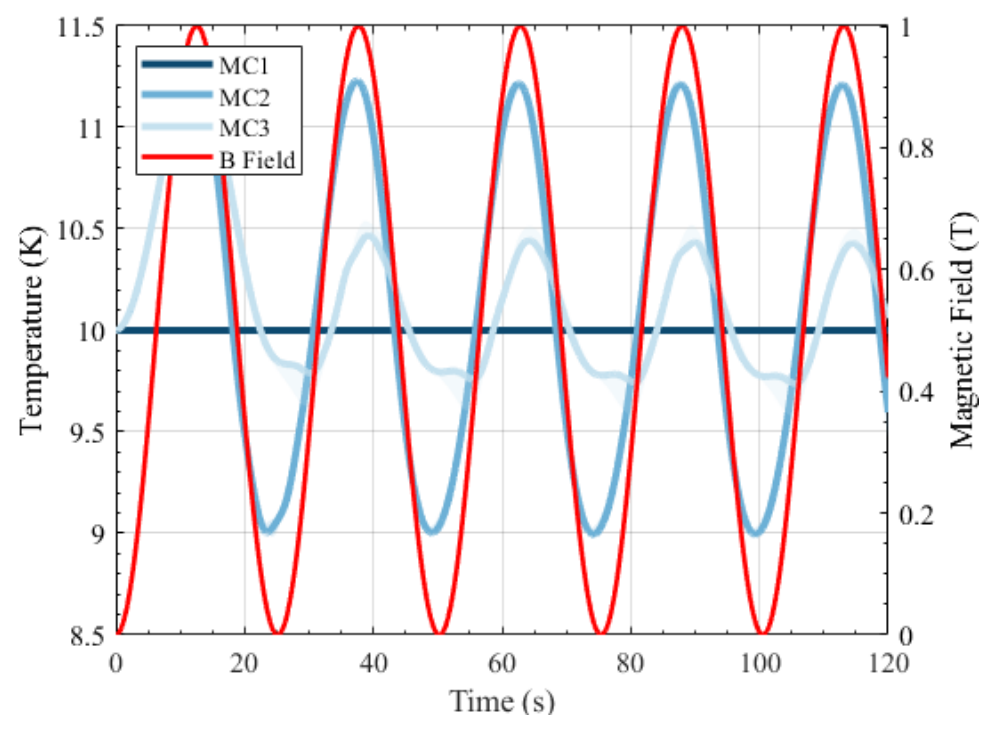


Figure 134. Thermal response of the packed bed in a simulated magnetic periodic blow test.

In this case, the reduction variable is the phase difference between the magnetic field profile and the outlet fluid temperature. Figure 135 (left) illustrates the relationship between the number of transfer units (NTU) and the phase difference for various external heat transfer coefficients. Notably, this method demonstrates exceptionally high sensitivity for measuring the heat transfer coefficient, particularly when compared to a "thermal" periodic blow test, with an increase in sensitivity by four orders of magnitude. Figure 119 depicts the sensitivity of the attenuation method in a thermal periodic blow test, while Figure 135 (right) highlights the sensitivity of the magnetic periodic blow test.

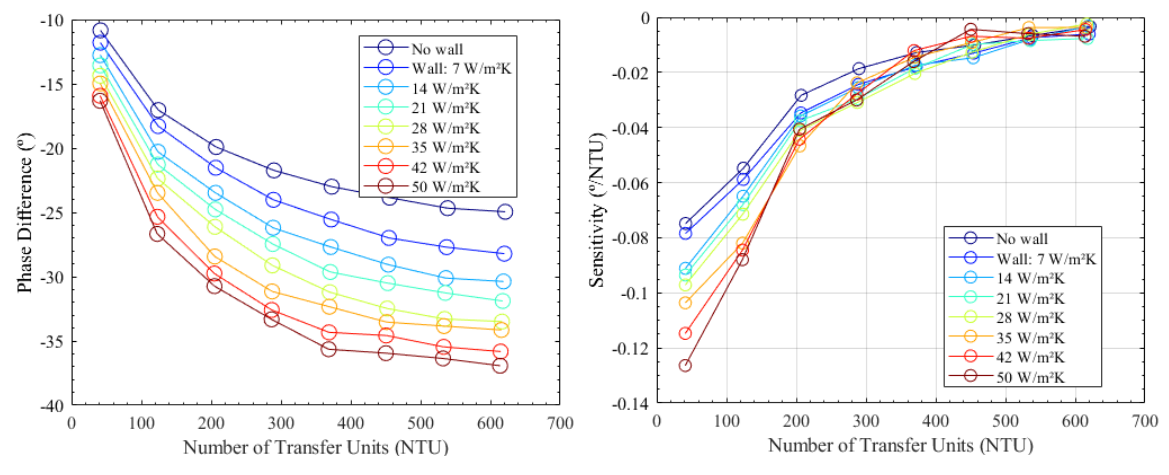


Figure 135. Phase difference of the outlet fluid temperature relative to the magnetic field as a function of NTU for varying external heat transfer coefficients (0 W/m·K to 50 W/m·K) (left). Sensitivity of the magnetic periodic blow method as a function of NTU for different external heat transfer coefficients (right).

Furthermore, investigating the impact of varying the frequency of the magnetic field on the thermal response of the regenerator could yield valuable insights. As previously noted, the regenerator appears to exhibit resonant-like behavior under specific conditions. This phenomenon is similarly observed in magnetic periodic blow tests. Figure 136 (left) presents a contour plot of the temperature response to a high-frequency magnetic field input, while Figure 136 (right) illustrates the axial temperature evolution at the point where

the maximum temperature is reached. The temperature profile exhibits a clearly damped oscillatory behavior, characterized by an initial peak where the temperature reaches its maximum value, followed by a gradual attenuation as the system approaches thermal equilibrium.

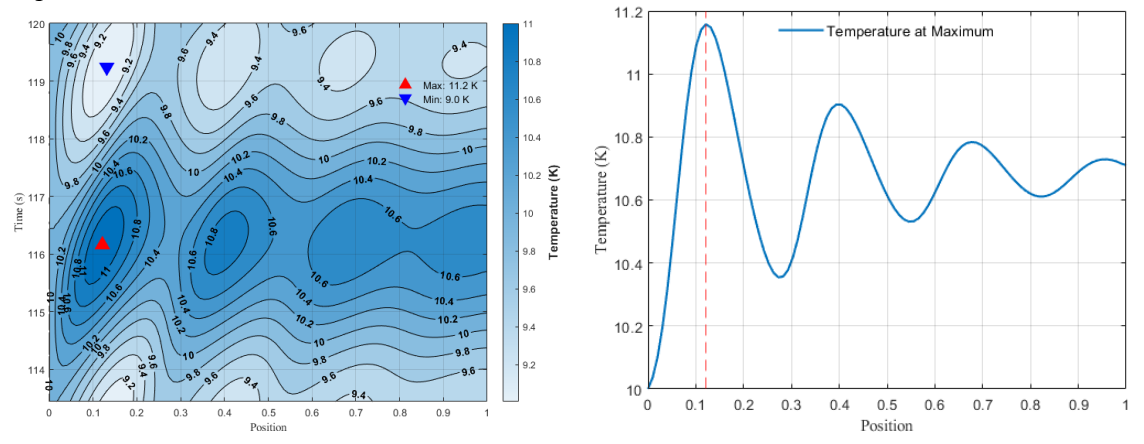


Figure 136. Contour plot of temperature evolution during a simulated magnetic periodic blow test.

Figure 137 (left) illustrates the position at which the maximum temperature is reached as a function of NTU for various frequencies. The data reveal that the peak position remains unaffected by the NTU value and instead depends solely on the frequency. This relationship is further emphasized in Figure 137 (right), which directly correlates frequency with the peak temperature position.

This behavior is particularly noteworthy, as experimentally determining this relationship can provide valuable insights into flow distribution and regenerator utilization. Specifically, a rightward shift in the frequency-position curve may indicate the presence of unutilized regions within the regenerator. Such regions could result from factors such as occlusion, flow maldistribution, or other inefficiencies, thereby offering a diagnostic tool for system optimization.

However, determining the frequency-position curve poses significant experimental challenges, primarily due to the requirement for a greater number of sensors compared to previously employed techniques. This increased demand for instrumentation complicates data acquisition and may limit the practicality of this approach in certain experimental setups.

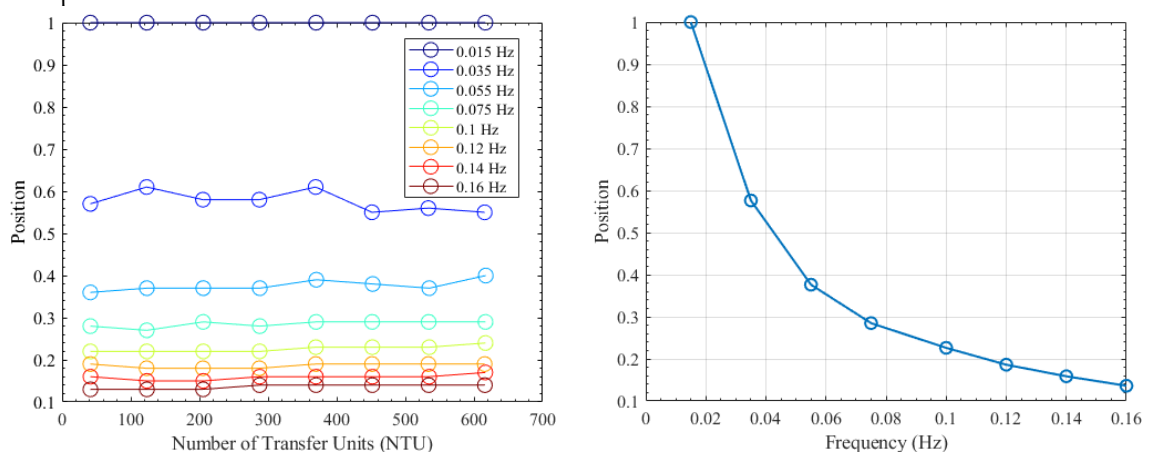


Figure 137. Peak temperature position as function of NTU for different magnetic field frequencies (left), and peak temperature position as function of frequency (right).

The analysis presented here, along with its implications, is confined to the experimental evaluation and characterization of the regenerator. However, it holds potential for broader applications, such as assessing the performance of magnetic refrigerators. Notably, phasor analysis—a technique previously employed in cryogenics, particularly for pulse tube

cryocoolers [131] where mass flow and pressure oscillations are sinusoidal—could be adapted for this purpose.

One limitation of the current approach lies in its reliance on the complete non-linear model, which only permits indirect parameter evaluation. This constraint may obscure fundamental relationships critical for guiding the design process.

To address this, future work should prioritize first the development of a simplified system model analogous to an RLC circuit. Such a model would facilitate phasor analysis and enable the derivation of explicit relationships between key variables and inputs. This approach could not only enhance testing procedures and regenerator characterization but also provide valuable insights into optimizing design parameters—such as regenerator geometry and operational variables—for cryogenic magnetic refrigerators.

5.1.4 Conclusions and recommendations for future testing

The results confirm the utility of the test stand in achieving the proposed objectives, particularly in validating the numerical model and demonstrating the potential of the technology. However, experimental findings reveal that while the numerical model is conceptually robust, limitations of the test stand constrained a more comprehensive validation at cryogenic temperatures. Specifically, under the given testing conditions, the heat transfer coefficient could not be accurately measured, preventing the full achievement of objective 3.2.

Future work should prioritize minimizing uncertainties in material characterization before testing. Observations indicate that slight deviations in magnetocaloric properties can lead to significant discrepancies in predicted temperature profiles. Variations arising from processing steps, may alter entropy changes in ways not adequately captured by standard property datasets or theoretical models. Maintaining detailed records of material manufacturing histories and measuring properties across appropriate temperature ranges would enhance the accuracy of predictive models.

Another critical goal is reducing external heat leakage. While the current setup incorporates insulating elements and mitigates conduction along the stainless-steel housing, further improvements—such as employing conduction-cooled magnets within a vacuum environment—could significantly reduce unwanted heat flux to and from the regenerator.

Advancing data acquisition methods and employing more precise sensors are also essential for improving alignment between experimental observations and model predictions. Additionally, advanced testing procedures should be developed to isolate specific phenomena. Magnetic single-blow tests, for instance, can generate steep thermal gradients with minimal interference at cryogenic temperatures by leveraging the magnetocaloric effect rather than conventional heaters. Periodic-blow tests, which exhibit reduced sensitivity to external heat leakage, offer a promising approach for determining heat transfer coefficients under challenging conditions. Moreover, the proposed magnetic blow tests, shows significant sensitivity at determining NTU. Additionally, aligning cycle frequencies or ramp rates with the regenerator's dominant time scales could further enhance diagnostic insights, especially at low temperatures. Evidence also suggests that moderate to higher mass-flow operations can mitigate issues related to laminar dispersion and wall effects, improving experimental reliability.

5.2 Technology assessment: Economic analysis

In the first chapter of the thesis three parameters were established to evaluate the performance of a cryogenic refrigerator including economic terms. These three parameters were: capital cost per Watt, operational cost per W and exergy efficiency.

To facilitate the evaluation of the proposed technology, the comparison of parameters is conducted using an exergoeconomic analysis [132]. This term refers to the integration of

economic and exergy analyses. For this purpose, we will define a Levelized Cost of Exergy (LCOEx), which comprises the levelized cost of capital (C_{capex}) and the operational levelized cost (C_{opex}) incurred over the device's lifetime:

$$LCOEx = \frac{C_{capex} + C_{opex}}{E\dot{x}_c} = c_{capex} + c_{opex}$$
 (5.18)

Here, C represents a levelized cost, measured as cost per unit time, and c a levelized cost per unit of exergetic cooling. In this work the LCOEx, and equivalent parameters will be based in dollars per kilowatt-hour (\$/kW·h).

To obtain the CAPEX contribution to the LCOEx, the capital costs, Z, are amortized them over the expected life of the refrigerator:

$$c_{capex} = \frac{CRF \cdot Z}{E\dot{x}_c \cdot H} \tag{5.19}$$

where CRF denotes the Capital Recovery Factor, calculated as:

$$CRF = \frac{i(1+i)^n}{(1+i)^n - 1} \tag{5.20}$$

where i is the interest rate and n, is the number of periods over which the recovery, or expected life of the refrigerator, is calculated. The values for both parameters will be constant across all the different alternatives, Table 62 shows the adopted values. A capacity factor of a 100% has been assumed in the analysis.

In a detailed analysis, operational costs should include maintenance and variable costs. However, for simplicity, maintenance costs are neglected here. Instead, operational costs are defined as the product of exergy consumption, or work input (W) and the electricity cost (c_e) :

$$c_{opex} = \frac{c_e \dot{w}}{E \dot{x}_c} \cdot CELF = \frac{c_e}{ECOP} \cdot CELF \tag{5.21}$$

where *ECOP* is the Exergetic Coefficient of Performance (ECOP) defined in Chapter 2, and *CELF* is the Constant Escalation Levelization Factor, that is used to account for changes in costs over time, such as inflation. The CELF is defined as:

$$CELF = k \cdot \frac{1 - k^n}{1 - k} \cdot CRF \tag{5.22}$$

$$k = \frac{1+r}{1+i} \tag{5.23}$$

where r is the nominal escalation rate, which has been assumed to be equal to zero, therefore the CELF is considered to be one in the present study.

Based on Eqs. 5.19-5.20, Eq. 5.18 can be rewritten as:

$$LCOEx = \frac{CRF \cdot Z}{E\dot{x}_C \cdot H} + \frac{c_e \dot{W}}{E\dot{x}_C} = \frac{CRF \cdot Z}{E\dot{x}_C \cdot H} + \frac{c_e}{ECOP}$$
(5.24)

This approach consolidates the three parameters introduced in Chapter 1 into a single variable for straightforward comparison.

Table 52 presents the common parameters utilized in the economic analysis. These include the CRF parameters, the electricity cost (c_e) , set at 0.07 €/kWh, and the ambient temperature of the refrigeration system, fixed at 290 K.

The subsequent sections apply this methodology to traditional cryogenic gas cycles based on costs outlined in Table 2, serving as a baseline for comparison. The methodology is then extended to assess the magnetic refrigerator established in Chapter 2. This analysis qualitatively incorporates experimental findings. Finally, an alternative application of magnetic refrigeration for cryogenics applications will be discussed, and recommendations for future developments will be given.

Table 52. Common parameters for economic analysis

Parameter	Value
Interest Rate: i	5%
Number of periods: n	20 years
Hours per year: H	8760 hours
Cost of electricity: c _e	0.07 €/kWh
Ambient Temperature: T ₀	290 K

5.2.1 Base comparison

The initial parameters established in Chapter 1 are analyzed and derived following the methodology proposed in the preceding section. To compute the LCOEx, as defined by Eq. 5.24, it is essential to determine the cooling exergy, capital costs, and power consumption of the equipment. This analysis focuses on Gifford-McMahon cryocoolers designed for applications below 20 K.

Table 53 summarizes the primary characteristics of a selection of state-of-the-art commercial cryocoolers. The capital costs were estimated through private communications with manufacturers (year 2021), while the remaining data were obtained from publicly available information on their respective websites [49], [133]. It is noteworthy to mention that the capital costs only include cryocooler cold head and compressor, other costs which are usually necessary in the installation, like the compressor chiller, if it is water cooled, have not been included. Additionally, the compressor power is the only work considered.

Table 53. Main characteristics of commercial GM-Cryocoolers

Name	Туре	Capital Cost (ex VAT)	Power input	Reference Cooling power
Sumitomo RDE-418	2-Stage GM	43.000 \$	8 kW	1.8/2.0 W @ 4.2 K (50/60 Hz).
Sumitomo CH-210	2-Stage GM	25.000 \$	8 kW	6.0/7.0 W @ 20 K (50/60 Hz)
BlueFors AL630	1-Stage GM	69.000 \$	12.7 kW	100 W

The cooling power of each cryocooler is determined using the heat capacity maps provided by the suppliers, which are accessible on their websites. For double-stage cryocoolers, the second stage is utilized for the levelized cost calculations, assuming a first-stage temperature fixed at 77 K. Figure 138 illustrates the cooling capacity of the Sumitomo RDE-418 cryocooler (at 60 Hz) as a function of first and second-stage temperatures. The heat capacity of the cryocooler is shown to be relatively independent of the first-stage temperature, supporting this assumption.

Table 54 shows an updated version Table 2 including the LCOEx for 3 different temperatures. To distinguish the CAPEX and OPEX cost per watt of cooling power they will be defined as follows:

$$Z_u = \frac{Z}{\dot{O}_c} \tag{5.25}$$

$$OPEX_{u} = \frac{C_{op}}{\dot{Q}_{c}} \tag{5.26}$$

Additionally, in Table 54 the breakdown between CAPEX and OPEX contribution to the LCOEx is given.

Table 54. GM-Cryocooler cost comparison for below 20 K applications

Temperature (K)	Z _u (\$/W)	OPEX_u (\$/W·h)	ECOP	LCOEx (\$/kW·h)	CAPEX %
4.2 K	20,400 \$/W	0.25 \$/W·h	1.88%	6.48 \$/kW·h	42%
10 K	5,062 \$/W	0.063 \$/W·h	3.1%	3.9 \$/kW·h	42%
20 K	688 \$/W	0.01 \$/ W·h	10.6%	1.1 \$/kW·h	41%

Figure 139 illustrates the LCOEx for the selected cryocoolers within the temperature range of 4.2–20 K. The analysis reveals that, based on the proposed methodology, the Sumitomo RDK-418 emerges as the most exergoeconomically favorable option for temperatures below 18 K. Conversely, for temperatures exceeding 18 K, the BlueFors AL630 cryocooler demonstrates superior performance.

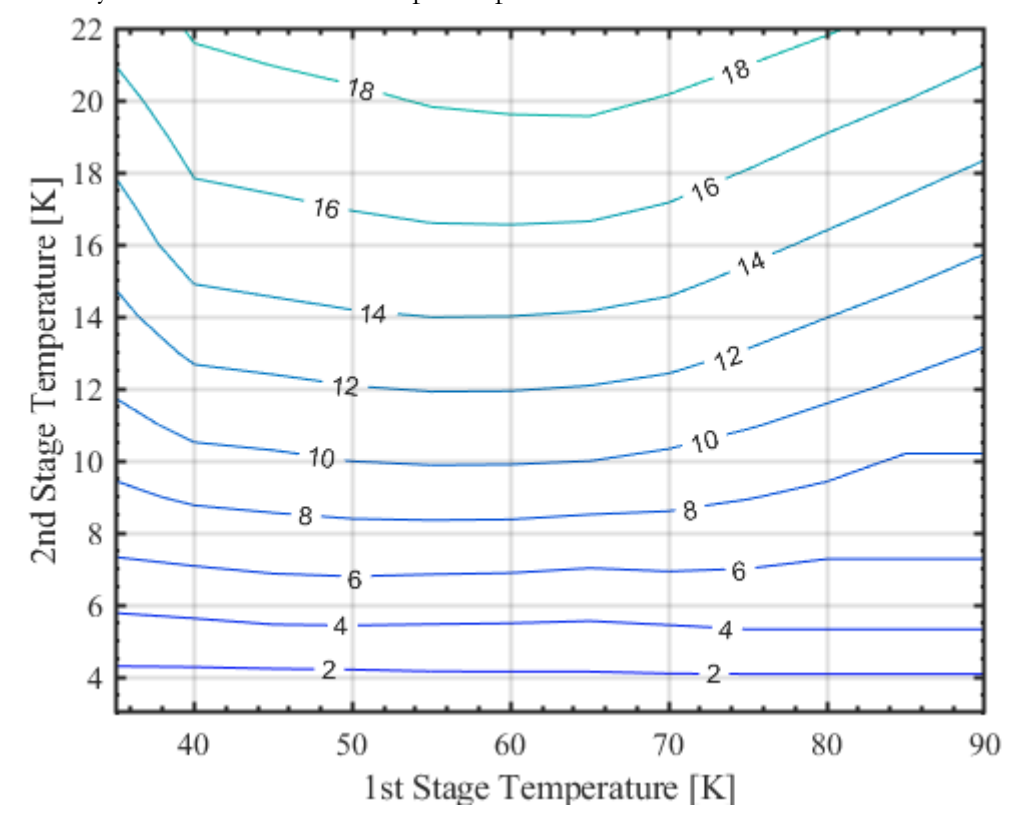


Figure 138. Heat load capacity curve of the 2nd stage of Sumitomo RDE-418 cryocooler

It is important to emphasize the minor positive derivative observed for the "Sumitomo RDK-418" in the temperature range of 10 to 18 K. Several factors could contribute to this counterintuitive behavior: First, the power consumption of the compressor may not remain constant. Although it is assumed that the cryocooler compressor consumes its nominal power at every operating point, this assumption might not hold true in practice. Second, variations in regenerator properties could play a role. As illustrated in Figure 5, some regenerator materials exhibit peaks in their volumetric heat capacity curves at specific temperatures. These variations can influence the ratio between the volumetric heat capacities of the regenerator and the fluid, potentially causing the derivative with respect to temperature to change sign.

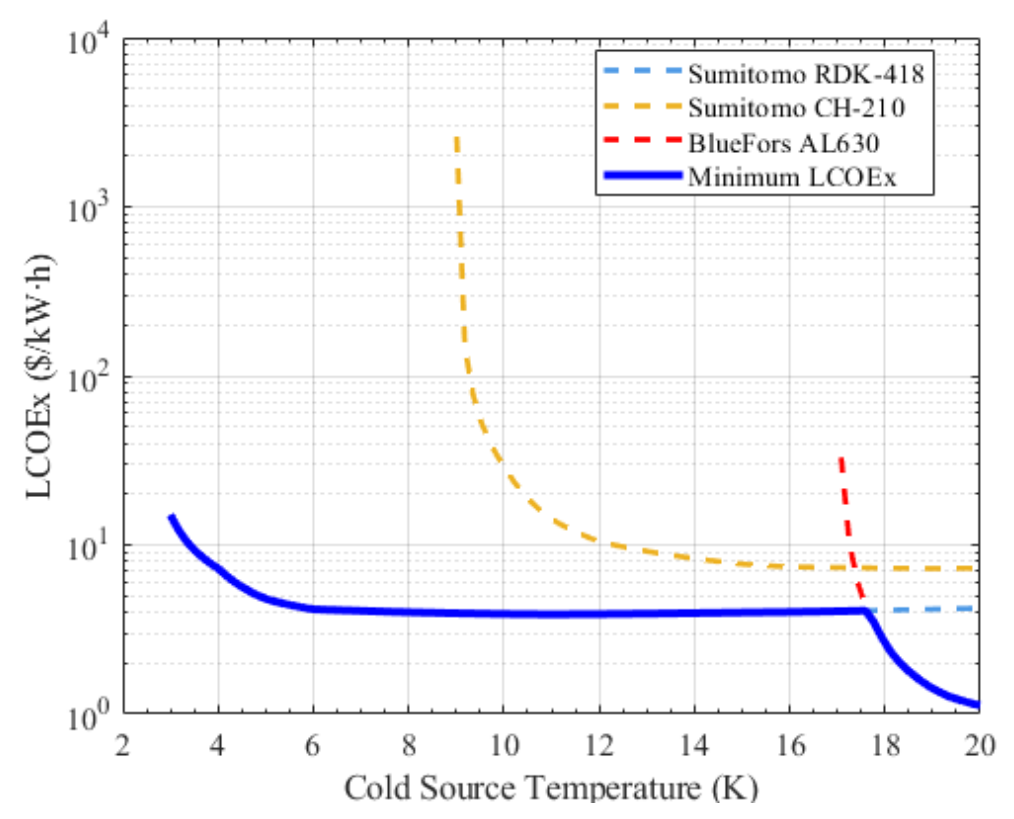


Figure 139. LCOEx (\$/kW·h) as function of cold source temperature for commercial GM cryocoolers.

5.2.2 Cost of components: Magnetic Refrigerator

This section outlines the primary cost components of a magnetic refrigerator and the methodology employed to calculate them. The total capital cost of a magnetic refrigerator is composed of three main components: the cost of the magnetocaloric material, Z_{MCM} , the cost of the magnet, Z_{mag} , and all other components, Z_{O} :

$$Z_{MR} = Z_{MCM} + Z_{mag} + Z_o (5.27)$$

The cost of the refrigerant can be readily determined based on its cost per unit mass and the quantity of magnetocaloric material used (in kilograms). To simplify the subsequent calculations, the cost of the magnetocaloric material is expressed as a function of the regenerator or packed bed (PB) volume:

$$Z_{MCM} = c_{MCM} \cdot m_{MCM} = c_{MCM} \cdot \rho_{MCM} \cdot V_{PB} \cdot (1 - \varepsilon)$$
(5.28)

The cost of the magnet can be similarly computed:

$$Z_{mag} = c_{mag} \cdot \rho_{mag} \cdot V_{mag} \tag{5.29}$$

In this case the volume of the magnet cannot be easily derived, but a relation can be established between the volume of the regenerator, V_{PB} , and the applied magnetic field (B_a) :

$$V_{mag} = f(V_{PB}, B_a) \tag{5.30}$$

This relationship depends on both the type and configuration of the magnet. The subsequent subsections will derive this relationship for two types of magnets: a Halbach array of permanent magnets and a superconducting solenoid.

The costs associated with other components (Z_O), primarily comprising housing and pumping elements, will be excluded from consideration in this analysis.

5.2.2.1 Permanent magnets: Halbach array

Permanents magnets were first introduced in chapter 2. A permanent magnet is a magnetic material which remains magnetized after the withdrawal of an external magnetic field. They are usually divided into: ceramics materials, rare-earth materials, Al-Ni-Co materials and polymer bonded materials. A review regarding their composition and critical properties can be found in [134]. The most basic permanent magnet for magnetic refrigeration are cylindrical Halbach arrays. To create the variable magnetic field there are two options, to employ a reciprocating magnetocaloric regenerator or to use nested Halbach arrays, similar to the shown in Figure 140, depicted from [135].

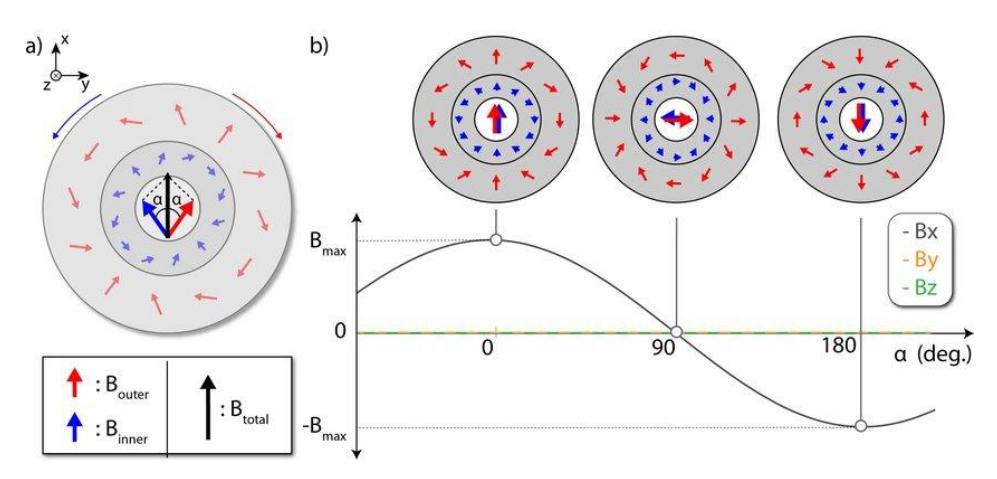


Figure 140. Representation of the magnetic field distribution generated by nested cylindrical Halbach dipoles, with the mutual angle between the inner (blue arrows) and outer (red arrows) dipoles determining the resulting field and orientation.

For this analysis a single Halbach cylindrical array will be considered.

A way to classify a permanent magnet array is to consider the figure of merit, M^* , which according to [136] is equal to:

$$M^* = \frac{\int_{V_{field}} ||\mu_0 H||^2 dV}{\int_{V_{mad}} ||B_{rem}||^2 dV}$$
 (5.31)

Where V_{field} is the volume where the magnetic field $(\mu_0 H)$ is created, V_{mag} is the volume of the permanent magnets and B_{rem} the remanence field, the magnetization left after the removal of the external magnetic field. If it is assumed that the magnetic field is constant in all the volume, as well as the remanence, Eq. (5.31) gives:

$$M^* = \frac{\left(\frac{B_a}{B_{rem}}\right)^2 V_{field}}{V_{mag}} \tag{5.32}$$

Which in the case of our magnetic refrigerator, V_{field} should be equal to the volume of the packed bed, V_{PB} . Therefore, the following expression can be derived:

$$V_{mag} = \left(\frac{B_a}{B_{mom}}\right)^2 \frac{V_{PB}}{M^*} \tag{5.33}$$

To completely establish the relation between magnet volume, packed bed volume and the applied field, the figure of merit, M^* , needs to be defined. Following Coey analysis [137] the following assumption will be made: the Halbach cylinder will be assumed of infinite length yielding the following relation $B_a = B_{rem} \ln \left(\frac{r_o}{r_i}\right)$, therefore:

$$M^* = \frac{\left(\frac{B_a}{B_{rem}}\right)^2}{e^{2\frac{B_a}{B_{rem}}} - 1} \tag{5.34}$$

The rest of the parameters are specific to the type of permanents magnet chosen. In this analysis, NdFeB magnets will be considered. Table 55 shows the assumed material properties and cost based on literature findings [134].

Table 55. Permanent magnet common parameters for economic analysis

Parameter	Value
Remanence Field: B _{rem}	1.2 T
Magnet density: $ ho_{mag}$	$7000~\rm kg/m^3$
Cost per unit mass: c _{mag}	100 €/kg

5.2.2.2 Electromagnets: Superconducting magnets

The other alternative is the use of superconducting magnets. As outlined in Chapter 2, superconducting magnets have been widely employed in magnetic refrigeration systems, particularly for low-temperature applications. Historically, most advancements relied on low-temperature superconductors (LTS), such as niobium-titanium (NbTi). These materials require cooling to liquid helium temperatures, which significantly increases the complexity and energy demands of the cooling system.

In recent years, new types of superconductors have been industrialized and commercialized, including Nb₃Sn, MgB₂, and high-temperature superconductors (HTS). The latter group comprises REBCO (rare-earth barium copper oxide), YBCO (yttrium barium copper oxide), and BSCCO (bismuth strontium calcium copper oxide). These materials exhibit higher critical current densities, elevated critical temperatures, and greater irreversibility fields compared to LTS. Figure 141 illustrates the progression of superconducting materials from NbTi to REBCO, highlighting their respective operating temperature ranges and critical magnetic fields.

HTS are particularly appealing for magnetic refrigeration technologies due to their higher critical temperatures, which exceed 77 K. This characteristic could simplify the system design and reduce operational costs.

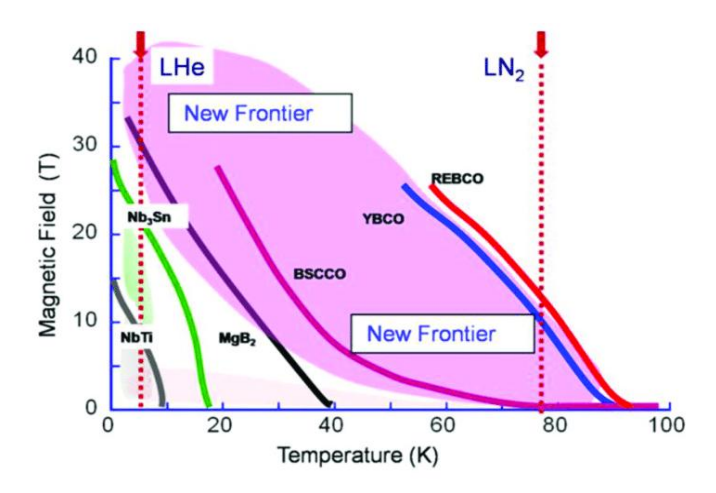


Figure 141. Variation of irreversibility field with temperature for different superconductors including HTS, MgB₂, metallic compounds, and alloys. The coated conductor technology including APC methodology has opened new frontiers of superconductivity applications in the temperature range of 5-77 K. Reproduced from Matsumoto and Mele [138].

Regarding magnet topology in magnetic refrigerators, the typical configuration is a solenoid. Figure 142 provides a cross-section view of superconducting solenoid magnet, indicating its main geometric parameters.

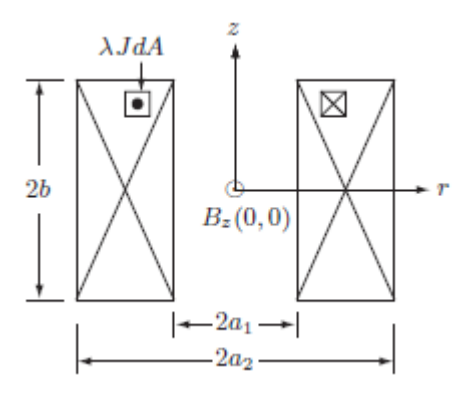


Figure 142. Cross section view of a superconducting solenoid.

The aperture of the solenoid provides a cylindrical space where the magnetocaloric material is placed. Extensive literature exists on the design and optimization of superconducting solenoids [139]. To facilitate the analysis, the following assumptions will be made:

- The proposed magnetic system will employ an HTS material. The engineering current density (J_e) HTS tape exhibits significant field and temperature dependence, as illustrated in Figure 143. This graph is constructed from critical current density data, obtained from the Robinson Research open database for Shanghai superconducting tape. A 75% margin load has been applied to compute the engineering current from the critical current dataset.

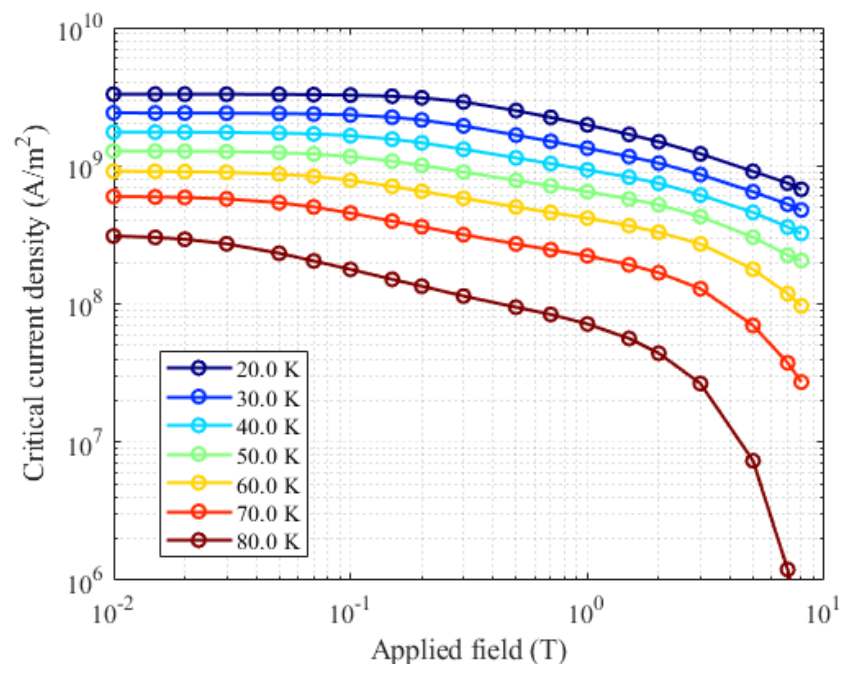


Figure 143. Engineering current density of Shanghai Superconductors tape as function of field and temperature.

- The magnet will operate at 20 K, which will be the hot source of the magnetic refrigerator. More detail is given in the next section. The thermal loads from static losses (conduction, radiation or convection), and from electrical losses (joule heating, AC losses) will not be taken into account when computing the performance of the refrigerator. The engineering current density exceeds 10⁹ A/m²

- when operating at 20K in magnetic fields below 5T. A constant value of 10° A/m² for the engineering current density will be assumed independent of magnetic field.
- The next assumption is that the length of the magnet is significantly larger than the internal radius (i.e. from Figure 142 that $2b \gg 2a_1$). This condition will be strongly enforced by considering a minimum aspect ratio of 10 ($\beta = 2b/2a_1 \ge 10$). The first consequence of this assumption is that the magnetic field at the center could be approximately as follows [139]:

$$B_a = B_z(0,0) = \frac{\mu_0 NI}{2a_1 \beta} \tag{5.35}$$

where μ_0 is the magnetic permeability in the vacuum, NI the amperes-turn of the magnet, and $\alpha=2a_2/2a_1$ and $\beta=2b/2a_1$. The second consequence is that the magnetic field in all the regenerator volume can be reasonably approximated to the magnetic field at the center.

Based on these assumptions a relation can be established between the magnet volume, the packed bed volume, and the magnetic field.

Additionally, the following relations should be considered. First, the engineering current density should be equal to the total ampere-turns divided by the cross section of the magnet:

$$J_e = \frac{NI}{a_1^2 \beta(\alpha - 1)} \tag{5.36}$$

And second, the volume of the packed bed, and magnet can be expressed as function of the geometric terms from Figure 142:

$$V_{PB} = 2\pi a_1^3 \beta \tag{5.37}$$

$$V_{Magnet} = 2\pi a_1^3 (\alpha^2 - 1)\beta$$
 (5.38)

Considering Eqs. (5.35-5.38) the following expression can be derived:

$$V_{mag} = V_{PB} \sqrt[3]{\frac{V_{PB}}{2\pi\beta}} \frac{B_a}{(\alpha+1)\mu_0 J_e}$$
 (5.39)

Table 56 summarizes the assumed material properties and associated costs. The density of the magnet is reasonably approximated by the density of copper, which constitutes the primary component of HTS tapes. This approximation is further supported by the similarity in density between copper (8960 kg/m³) and Hastelloy, the second most abundant constituent of HTS tapes, with a density of 8890 kg/m³. The cost of the HTS tape has been estimated based on current market prices, approximately \$30 per meter of tape. This value can be converted into a specific cost (\$/kg) by dividing the price per meter by the cross-sectional area and density of the tape.

Table 56. Superconducting magnet common parameters for economic analysis

Parameter	Value
Engineering Current density: Je	$10^9\mathrm{A/m^2}$
Magnet density: $ ho_{mag}$	$8960~\rm kg/m^3$
Cost per unit mass: c _{mag}	8300 €/kg

5.2.3 Case 1: GM-Cryocooler with an AMR stage

The case presented in chapter 2 analyzed a 2-stage cascade system. The first stage consists of a GM cryocooler, operating between ambient temperature and 20K, where it is more

cost-efficient. The second stage consist of an AMR stage, which provides cooling from 20K to the target cooling temperature (between 4-15 K). Figure 144 provides a schematic representation of the proposed two-stage cascade system.

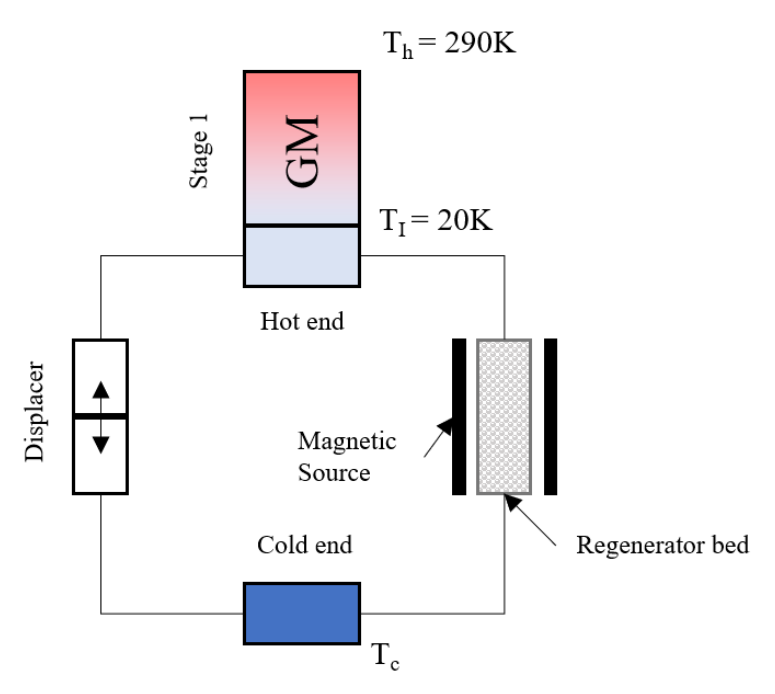


Figure 144. Schematic of the proposed 2-stage cascade system

The economic analysis of the system will follow the methodology outlined in this section. The following assumptions are adopted:

- Stage 1 operates at the minimum LCOEx established in the preceding section.
- Stage 2 will be independently analyzed using the model developed in Chapter 2.

The thermodynamic model determines key performance parameters, including the cooling power (Q_c) and ECOP, which are subsequently used to calculate the LCOEx for Stage 2.

The final step involves computing the equivalent performance variables for the entire system by integrating both stages. The integration of each variable will be done as follows: the CAPEX per Watt of cooling power is calculated as:

$$Z_{u,tot} = Z_{u,2} + Z_{u,1} \cdot \frac{\dot{Q}_{h_2}}{\dot{Q}_{c_2}}$$
 (5.40)

Where Q_{h_2} is the heat rejected by stage 2 in stage 1, and Q_{c_2} the cooling power of stage 2. Similarly, the OPEX per Watt of cooling power is determined using the following equation:

$$OPEX_{u,tot} = OPEX_{u,2} + OPEX_{u,2} \cdot \frac{\dot{Q}_{h_2}}{\dot{Q}_{c_2}}$$
 (5.41)

The COP of the cascade system is given by the following relation:

$$COP_{cascade} = \frac{COP_1COP_2}{COP_1 + COP_2 + 1} \tag{5.42}$$

Using Eqs. 5.42 and 2.59 the following relation can be established for the Exergetic Coefficient of Performance (ECOP) of the cascade system:

$$ECOP_{cascade} = ECOP_{1} \cdot ECOP_{2} \cdot \frac{COP_{1,CARNOT} + COP_{2,CARNOT} + 1}{ECOP_{1} \cdot COP_{1,CARNOT} + ECOP_{2} \cdot COP_{2,CARNOT}}$$
(5.43)

In this case, since the cascade cycle is operating with a hot source equal to the ambient temperature, the ECOP_{cascade} is equivalent to the exergy efficiency of the refrigerator.

Finally, the LCOEx for the entire system is expressed as:

$$LCOEx_{tot} = \frac{LCOEx_1 \cdot Ex_{c_1} + LCOEx_2 \cdot E\dot{x}_{c_2}}{E\dot{x}_c}$$
 (5.44)

Having established the procedure, the main parameters for the thermodynamic model of the AMR are presented in Table 57. The same cycle and regenerator geometry that was established in Figure 24 and Table 8 in Chapter 2 are used. The main difference is that in this case the mass ratio and frequency have been increased to 0.3, and 0.5 Hz respectively. These operating values provide a reasonable balance between cooling power and exergy efficiency based on the results obtained in Chapter 2.

Table 57. Operating parameters for the AMR stage, packed bed characteristics

Cycle	AMR Brayton	Characteristics	Characteristics	
T_{hot}	20 K	Magnetocaloric Material	ErAl ₂	
$T_{ m cold}$	4-15 K	Geometry (radius x length)	35 mm. x 305 mm.	
Nominal Pressure	15 bar	Mass	1 kg	
Utilization factor: U	0.3	Sphere diameter	0.1 mm	
Magnetic field: B	1 T	Shape factor	0.95	
Frequency: f	0.5 Hz	Porosity	0.45	

Figure 145 illustrates the cooling power and ECOP as functions of the cold source temperature for the analyzed case. A significant decline in both cooling power and exergy efficiency is observed below 6 K, which corresponds to the diminished magnetocaloric effect of ErAl₂ in this temperature range.

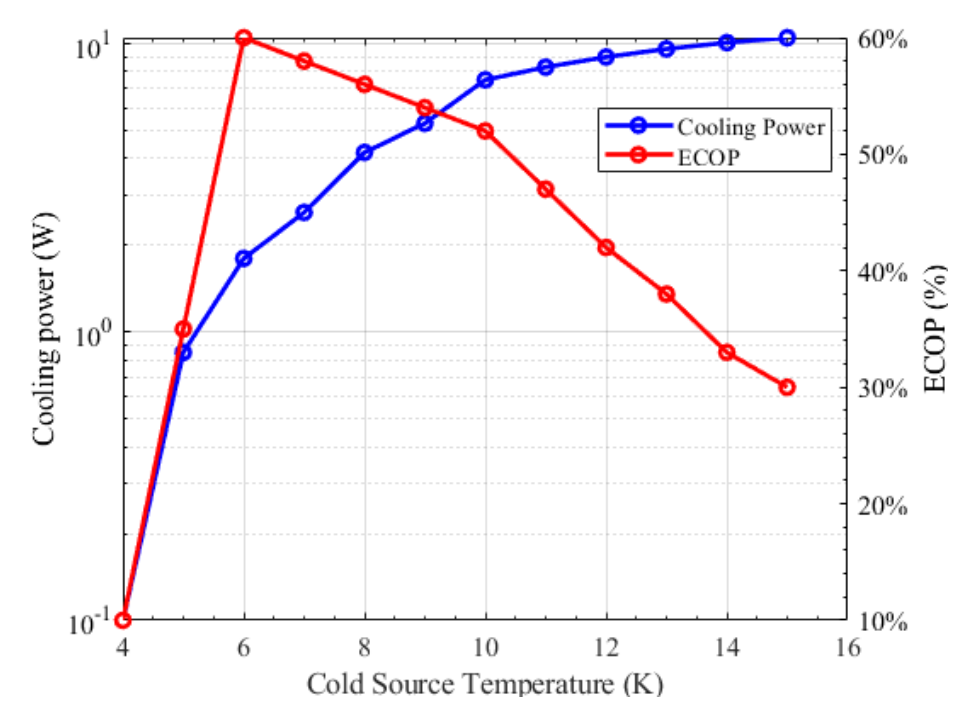


Figure 145. Cooling power and exergy efficiency as function of cold source temperatures in the economic analysis.

Based on the provided inputs, Stage 2, representing the AMR refrigerator, can be evaluated using the proposed methodology. Table 58 summarizes the stand-alone performance parameters for this stage. The results indicate that, under the established

assumptions, the use of a permanent magnet offers a slight cost advantage over a superconducting magnet. Superconducting magnets should not be entirely dismissed, especially considering that while PM technology is more established and mature, recent advancements in HTS superconductors have demonstrated significant improvements in both cost and performance. This positive trend may continue in the future. However, at equivalent cost-performance levels, permanent magnet systems may offer a more practical solution due to their lower system complexity.

Table 58. Second stage of the cascade AMR-GM cooling system cost comparison

Temperature (K)	$Z_{u,PM}$ (\$/W)	$Z_{u,SM}$ (\$/W)	$OPEX_{u,2}$ (\$/W·h)	$ECOP_2$
4.2 K	22,528 \$/W	24,588 \$/W	1.3·10 ⁻³ \$/W·h	17.8%
7 K	2,166 \$/W	2,364 \$/W	0.24·10 ⁻³ \$/W·h	58%
10 K	751 \$/W	819 \$/W	0.14·10 ⁻³ \$/W·h	52%
15 K	536 \$/W	585 \$/W	0.08·10 ⁻³ \$/ W·h	30%

After independently analyzing the performance of the second stage, the performance parameters of the combined cooling system were calculated using Eqs. (5.40-5.43). Table 59 shows the values of the performance targets for the combined cooling system.

The results are promising, as both the capital expenditure (CAPEX) and operational expenditure (OPEX) per watt improve in the 10 K and 15 K cases. However, the CAPEX per watt is higher for the 4.2 K case, primarily due to the diminished performance of the magnetocaloric effect at this temperature. In the 10 K and 15 K cases, the ECOP (or exergy efficiency) increases, which serves as a key factor driving the reduction in LCOEx. Consequently, the CAPEX accounts for a larger proportion of the total costs, as the enhanced efficiency significantly reduces the OPEX component.

Table 59. Cascade AMR-GM cooling system cost comparison for below 20 K applications

Temperature (K)	Z _u (\$/W)	$OPEX_u$ (\$/W·h)	ECOP (or η)	LCOEx (\$/kW·h)	CAPEX %
4.2 K	36,268 \$/W	0.198 \$/W	2.46%	13.33 \$/kW·h	40%
10 K	2,791 \$/W	0.03 \$/W·h	7.48%	1.80 \$/kW·h	50%
15 K	536 \$/W	0.02 \$/ W·h	6.79%	1.98 \$/kW·h	50%

Figure 146 illustrates a comparison between the LCOEx of commercial cryocoolers and that of the proposed two-stage cooling system. This comparison corroborates the findings presented in Table 59, demonstrating that the two-stage cooling system has the potential to reduce cryocooling costs by a factor of two or more in specific scenarios, particularly around 10 K, where the active magnetic regenerator (AMR) exhibits higher efficiency. Additionally, the figure highlights that at temperatures below 5 K, ErAl₂ may not serve as an effective refrigerant.

The analysis yields highly promising results. However, the performance of a real prototype may deviate significantly from the idealized performance predicted by the simulation. This discrepancy arises primarily from unmodeled effects, such as wall and external heat losses, which are clearly evident in the experimental data and can substantially impact system performance.

Additionally, common deficiencies in cryogenic regenerators, such as void volumes and flow maldistribution, can significantly affect performance and increase the LCOEx. Moreover, the assumptions made in the analysis may limit the applicability of the results to a real prototype. For instance, the assumption that heat can be deposited at the minimum rate at 20 K has inherent scaling limitations. Low cooling power systems may fail to achieve this due to the advantages of scale in gas cycle cryocoolers, as demonstrated by the performance differences between the Sumitomo CH210 and Bluefors AL630 systems.

Furthermore, CAPEX costs may be significantly underestimated, as critical factors such as associated pumping costs have been overlooked. Moreover, the development of a displacer or a regenerator/displacer system could pose substantial engineering challenges, further complicating implementation and increasing overall costs. Additionally, the inclusion of an extra stage could impact operational expenditure OPEX, particularly in terms of maintenance, as the incorporation of a magnetic system adds complexity to the refrigerator's design and operation. Certain authors [140] have reported that the characteristics of magnetocaloric materials degrade after undergoing numerous cycles. This aging effect, however, is not uniform across all magnetocaloric materials. Other studies [141] have found no evidence of degradation during cycling for specific materials. The properties of magnetocaloric materials are highly material-dependent, with the aging effect appearing more pronounced in first-order magnetic transition (FOMT) materials, which exhibit thermal hysteresis.

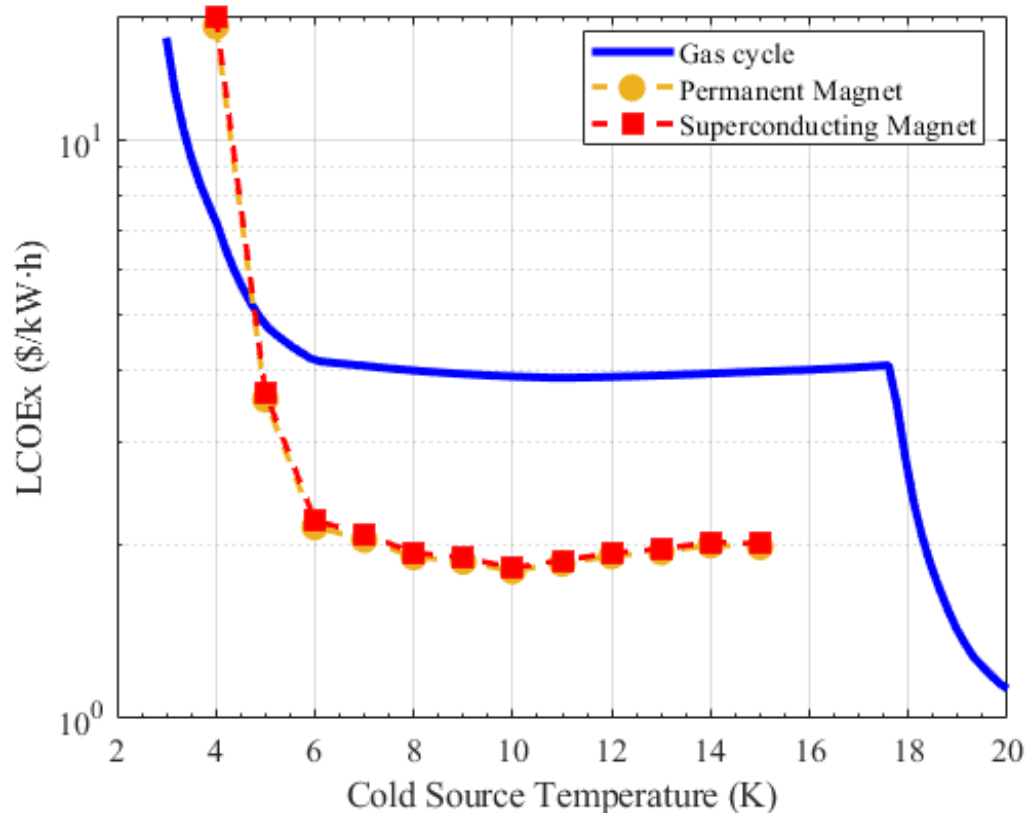


Figure 146. LCOEx (\$/kW·h) as function of cold source temperature for commercial GM cryocoolers.

It is important to note that these observations are not intended to diminish the potential of the technology. On the contrary, a realistic evaluation of its limitations and the identification of key risks are crucial for optimizing resource allocation and ensuring efficient development.

In the following section, another case will be qualitatively examined, which may offer strategies to effectively mitigate some of these risks.

5.2.4 Case 2: Magnetic Cryocooler

A second alternative that will be qualitatively studied involves combining the Gifford-MacMahon (GM) and Active Magnetic Regeneration (AMR) cycles into a single hybrid cycle, referred to as GM+AMR. This hybrid cycle would operate in six stages:

- 1. Magnetization: the regenerator is exposed to a magnetic field. This field induces a temperature increase in the MCM due to the magnetocaloric effect. The resulting heat is transferred to the heat transfer fluid.
- 2. Cold to hot blow: The heated fluid is then displaced toward the hot heat exchanger, where it releases the absorbed heat to a high temperature sink.
- 3. Compression: During this process, the working gas is compressed while the magnetic field remains high. This compression raises the gas temperature further, while the MCM (still magnetized) maintains its elevated temperature state.
- 4. Demagnetization: magnetic field is removed from the regenerator, causing the MCM to cool down. As the MCM's temperature decreases, it absorbs heat from the previously warmed fluid.
- 5. Hot to cold blow: The cooled fluid is directed toward the cold heat exchanger, where it absorbs heat, achieving the desired cooling effect.
- 6. Expansion: the pressurized fluid is allowed to expand, which causes the gas temperature to drop.

The phase relationships need not conform strictly to this process. Optimal phase timing constitutes a critical factor. Figure 147 illustrates the principal parameters of a generic GM+AMR configuration through the phasor methodology commonly employed in gas cryocooler analysis. This approach incorporates magnetic field as a fourth variable beyond the conventional parameters of pressure, hot and cold mass flow rates. The angular relationships between ϕ_h , ϕ_c and ϕ_B define the temporal coordination required between the refrigerator's operational stages.

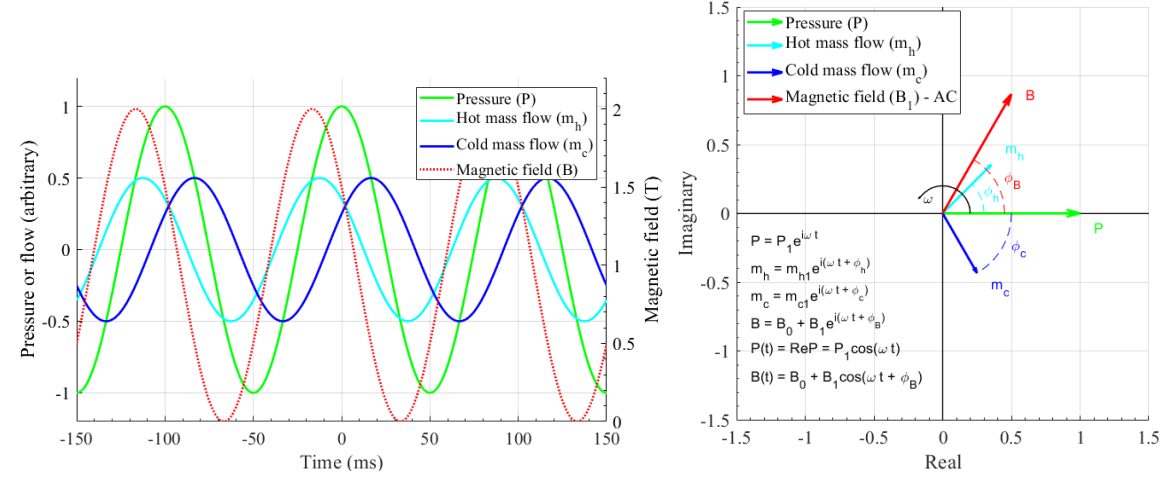


Figure 147. Generic parameters of a combined Gifford-McMahon and Active Magnetic Regeneration cycle in the time domain (left) and the frequency domain (right)

This hybrid cycle offers several advantages:

First, the regenerator can be shared between the two cycles. Since the structural and functional requirements of AMR and GM regenerators are inherently similar, sharing the mechanical and fluid framework reduces costs and simplifies the design.

The optimization of the regenerator must account for both cycles. From the AMR perspective, an optimal material should exhibit a significant Refrigerant Capacity (RCP) across the temperature span of the cycle. For the GM cycle, however, a key parameter is the volumetric heat capacity of the material, particularly at low temperatures where helium's volumetric heat capacity increases substantially.

Figure 148, is an update of Figure 5, which compares the volumetric fluid capacity of helium (in blue) with typical GM cycle regenerator materials (in black) and magnetocaloric materials analyzed in this study: ErAl₂ (in purple) and GGG (in green). The data reveal that GGG exhibits a low volumetric heat capacity, making it less effective in a GM+AMR cycle. Conversely, ErAl₂ demonstrates a high volumetric heat capacity within a temperature range of 10–16 K, making it a promising candidate for further analysis. To evaluate

materials for this hybrid cycle, we propose a new metric: Refrigerant Capacity Ratio (RCR). This metric combines two figures of merit by multiplying the volumetric heat capacity ratio between magnetocaloric material and fluid with the refrigerant capacity over a specified temperature range:

$$VRC = \frac{\rho_m \cdot \int_{T_{cold}}^{T_{hot}} T_m \frac{\partial s_m}{\partial T}}{\int_{T_{cold}}^{T_{hot}} \rho_f \cdot T_f \frac{\partial s_f}{\partial T}} \cdot \int_{T_{cold}}^{T_{hot}} \Delta S_{mag}(T, H) dT = \frac{\rho_m \cdot \widetilde{c_{p,m}}}{\widetilde{\rho_f} \cdot \widetilde{c_{p,f}}} \cdot RC$$
 (5.45)

Optimizing this variable enables combining different materials within the regenerator. This optimization is not limited to longitudinal variations, such as graded regenerators commonly used in GM refrigerators, but can also include spatial variations across regions of the regenerator. For instance, in a GM+AMR cycle, a weighted combination of materials like GOS and GGG may perform better in the 4-6K temperature ranges, that each separately. By tailoring material selection to specific regions, the regenerator can contribute effectively to overall performance.

From a CAPEX perspective, this solution offers notable advantages. First, there are no additional costs associated with the regenerator, as the regenerator material for the GM+AMR cycle replaces, rather than supplements, the existing GM regenerator. The unit cost per kilogram of regenerator material is also unlikely to increase significantly, given that the composition of most MCE materials used in sub-20 K applications is inherently similar to that of current GM regenerators (e.g., ErAl₂ versus HoCu₂). Second, no additional costs are incurred for pumping and compressor units, as these components are shared between the GM and GM+AMR cycles.

The primary CAPEX contribution arises from the magnet. However, as discussed in the previous section, this cost can be minimized by optimizing the cycle for operation in low-field regions. This optimization enables the use of permanent magnets or small HTS magnets, which are more cost-effective. Additionally, current GM cryocoolers integrate the regenerator and displacer into a single mechanism. This integration could allow for operation with static magnetic sources, significantly simplifying magnet design. However, careful consideration must be given to the phase difference optimization between the GM and AMR cycles, as its implementation may present challenges and may not be straightforward.

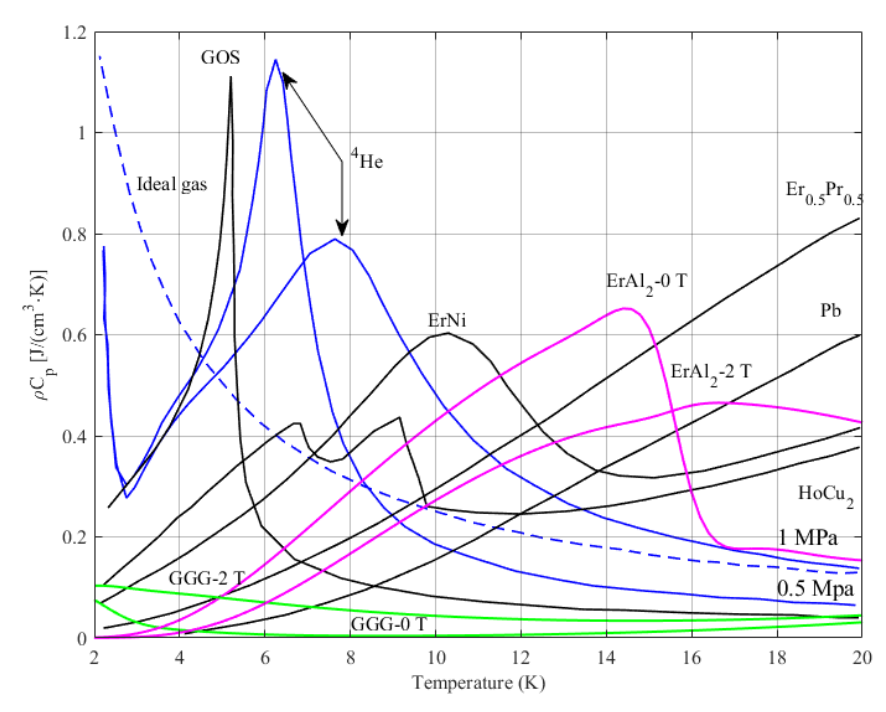


Figure 148. Volumetric heat capacity of various low temperature regenerator materials (in black), ErAl₂ (in purple), and GGG (in green) compared with that of Helium at various pressures-0.5MPa, 1.0MPa.

It is important to acknowledge that the limitations of each individual cycle also impose constraints on their combined operation. For instance, GM cycles typically operate at frequencies below 2 Hz due to the high volumetric heat capacity of helium at low temperatures. As a result, the operating frequency of a GM+AMR cycle may also be restricted to this range. However, this limitation is not absolute, as the relative contributions of the GM and AMR cycles could vary depending on the regenerator's position and the local temperature. Further investigation is required to fully understand and optimize these interactions.

The analysis of the GM+AMR cycle does not exclude the possibility of combining AMR with other gas-cycle cryocoolers, such as Stirling or Pulse-Tube cryocoolers. Each combination demands a dedicated evaluation because the dynamics of these integrated systems may differ significantly from those of the GM+AMR cycle. For example, the integration of Stirling and AMR cycles is expected to exhibit a more supplemental rather than complementary relationship. At lower temperatures, the regenerator in such a configuration may behave predominantly as an AMR cycle, while at higher temperatures, it may function more like a Stirling cycle. This dual behavior highlights the need for tailored optimization strategies to ensure efficient performance across varying temperature ranges.

5.3 Summary: Technology Assessment

This chapter evaluates magnetic refrigeration technology from multiple perspectives. The first section compares the developed simulation tools with experimental data, leading to the following key conclusions:

- Partial validation of the model has been achieved. While the model performs significantly well at ambient temperatures, its validation at cryogenic temperatures remains challenging. This difficulty arises from factors such as heat leaks, non-local mass flow and pressure measurements, and uncertainties in magnetocaloric material properties.
- Future test stands should focus on: 1) Testing magnetocaloric materials individually during their preparation process, 2) Reducing external heat leaks by operating the magnet under vacuum conditions with permanent or conduction-cooled

- superconducting magnets, 3) Employing more precise measurement and advanced data acquisition techniques.
- Two alternative tests have been proposed: the magnetic single blow and periodic blow tests. These are based on the principle that magnetocaloric materials can act as heating mechanisms. These tests demonstrate higher sensitivity for measuring heat transfer coefficients and serve as tools for diagnosing regenerator deficiencies.

The second section of the chapter assesses the technology from an exergoeconomic perspective, utilizing data from the model developed in Chapter 2. The main conclusions are as follows:

- A methodology has been proposed to integrate CAPEX, OPEX, and exergy efficiency into a single variable: LCOEx. This methodology has been applied to commercial GM cycles to establish a baseline for comparison.
- A cascade refrigerator was analyzed consisting of a first stage using a GM cycle (operating between ambient temperature and 20 K) and a second stage using an AMR cycle (operating between 20 K and the target cold temperature). Permanent or conduction-cooled superconducting magnets were considered as the magnetic source for the AMR stage.
- The results of the 2-stage cooling system demonstrate competitive performance compared to GM cycles, particularly above 5 K. However, significant development risks remain. To address these challenges, combining gas and magnetic cycles is proposed as an alternative approach that could mitigate development risks. This combination not only enhances cooling power but also allows shared components such as regenerators, housing, and pumping circuits, reducing complexity and costs.
- Adapting a commercial GM cryocooler by modifying its regenerator and adding a magnetic source is identified as a low-risk solution for advancing this technology further.

Chapter 6: CONCLUSIONS

This chapter provides a summary of the work completed during this project and is organized into two sections. The first section outlines the key accomplishments and highlights the major conclusions derived from this study. The second section offers recommendations for future research directions to build upon the findings presented here.

6.1 Summary and Conclusions

In this thesis, a detailed framework was established to explore novel cryogenic solutions in the 4.2–20 K range, motivated by the need to reduce both capital and operational costs of state-of-the-art cryogenic cooling systems. Magnetic refrigeration technology emerged as a promising candidate for achieving these goals, and a set of clearly defined objectives was established to guide the project. Table 60 summarizes the extent to which these objectives were accomplished.

Table 60. Thesis Objectives and level of accomplishment

Objectives	Level of accomplishment
Objective 1: Analysis of state-of-the- art cryocooling system. Investigate the potential of magnetic refrigeration for cryogenic purposes	Complete. A thorough review of prior developments in cryogenic magnetic refrigeration was conducted. Based on the findings from previous work in the field, magnetic refrigeration was validated as a promising technology for cryogenic applications, particularly within the targeted temperature range.
Objective 2: Numerical analysis of a magnetic refrigeration stage.	Complete. A 1D numerical model was developed. The model integrates the magnetocaloric effect and the real gas properties of helium. It offers significant flexibility, allowing for the simulation of various operational parameters, and is highly compatible with experimental data, enabling effective validation against real-world measurements
Objective 3: Design, fabricate, and test a technology demonstrator.	Complete. A test stand was designed, manufactured, and successfully tested, operating well within the established parameters. It provided valuable experimental data for validating the numerical model. The test stand has demonstrated itself to be an economical and versatile platform for evaluating magnetic refrigeration regenerators.
Objective 4: Experimental validation of the multiphysics involved in a cryogenic magnetic refrigerator.	Partially complete. The numerical model was validated at ambient temperatures with the test stand. The results obtained at cryogenic provided partial agreement, indicating areas for improvement. To enhance the characterization of regenerator performance at cryogenic temperatures, design updates and innovative testing methodologies have been proposed
Objective 5: Evaluate the technical performance and economic viability of magnetic refrigeration systems for cryogenic applications	Complete. The numerical model and test stand were utilized to technically evaluate the potential of magnetic refrigeration. Based on this insights, an economic analysis was conducted, yielding promising results. Additionally, recommendations for future work have been proposed to address remaining challenges and to further enhance the performance.

The thesis began with a comprehensive review of previous cryogenic magnetic refrigeration prototypes operating within the specified temperature range. The key findings from this analysis are as follows:

• One significant limitation of earlier prototypes was the choice of the magnetocaloric material, Gadolinium Gallium Garnet (GGG). Its drawbacks include constraints on the types of thermodynamic cycles that can be

implemented and the requirement for extremely high magnetic fields, necessitating the use of superconducting magnets. This requirement considerably increases system complexity and cost.

• Erbium Aluminum (ErAl₂) was identified as a more suitable magnetocaloric material, with the potential to deliver superior performance in an Active Magnetic Regenerator (AMR) cycle within the defined temperature range.

To validate this hypothesis, a one-dimensional numerical model of a magnetic refrigerator was developed using MATLAB. The development process involved:

- Addressing the primary challenge of constructing a robust framework that accurately incorporates both magnetocaloric effects and helium compressibility at low temperatures.
- Using this model to analyze a two-stage refrigerator incorporating a Brayton AMR stage. The results confirmed the suitability of ErAl₂ as a magnetocaloric material and demonstrated the feasibility of magnetic refrigeration for cryogenic applications.

Subsequently, a small-scale technology demonstrator was constructed for experimental validation. A modified single-blow test stand, commonly employed for regenerator analysis, was proposed. The objectives of this test stand included gaining expertise in magnetocaloric materials, developing a manufacturing process for packed beds, validating the numerical model under ambient and cryogenic conditions, and demonstrating technological feasibility. The main outcomes were:

- Packed Bed Fabrication: A glass packed bed was first used to validate the manufacturing process. Once validated, packed beds made from ErAl₂ and GGG were manufactured and characterized.
- Magnetic Source: A superconducting NbTi magnet was employed as the magnetic source. Independent testing confirmed its proper operation.
- Heat Exchanger Development: A three-fluid heat exchanger was designed to recover enthalpy from evaporated liquid helium, cool the superconducting magnet, and cool helium flowing through the magnetocaloric packed beds. This component was independently tested and validated.
- System Validation: All components were independently tested to ensure reliability. The test stand operated satisfactorily within target parameters, providing a practical and cost-effective platform for system performance validation and regenerator characterization.

An experimental methodology was subsequently proposed to achieve the outlined objectives:

- The experimental procedure was divided into two main categories: thermal tests and magnetic tests. *Thermal Tests:* These included single-blow and periodic-blow testing, both standard methods for evaluating heat transfer in packed beds. *Magnetic Tests:* These were further subdivided into three groups—no-load tests, ramping rate tests, and variable temperature tests.
- Testing was conducted separately for different materials, with ErAl₂ tested first, followed by GGG. All testing conditions were maintained within required ranges to ensure appropriate temperatures in the packed bed and controlled variables. However, some heat leaks to the ambient environment were observed, which influenced results.

The experimental data enabled a detailed results analysis, leading to the following conclusions:

 Model Validation: Partial validation of the numerical model was achieved. While robust performance was observed at ambient temperatures, results at cryogenic temperatures showed only partial agreement with predictions due to limitations in the test stand.

- Proposals for Future Improvements: Recommendations include reducing external heat leakage, integrating more precise sensors, and adopting advanced data acquisition techniques.
- Novel Experimental Methodology: Two new testing methods—magnetic singleblow and periodic-blow tests—were proposed using the magnetocaloric material as a heating mechanism. These methods demonstrated higher sensitivity for measuring heat transfer coefficients and could serve as diagnostic tools for regenerator deficiencies.

Building on operational insights from numerical modeling, test stand experience, and experimental results, an economic analysis of the technology was conducted. This analysis evaluated key parameters such as CAPEX, and OPEX per Watt of cooling power, exergy efficiency, and the Levelized Cost of Exergy (LCOEx). The main conclusions are:

- The two-stage cascade cooling system analyzed showed promising results when compared to state-of-the-art Gifford-McMahon cycles. It demonstrated potential LCOEx reductions by a factor of two within specific temperature ranges.
- Despite its potential advantages, implementing such a refrigerator may face challenges that could compromise its competitiveness. As an alternative approach, combining traditional gas cycles with AMR cycles is proposed as offering higher potential benefits with reduced risk.

This work provides advancements in cryogenic magnetic refrigeration technology while identifying areas for further development to enhance its feasibility and competitiveness.

6.2 Outlook

The current landscape of applied superconductivity is exceptionally dynamic, driven by the industrialization of high-temperature (and high current) superconductors. This progress is catalyzing the development of groundbreaking applications, including fusion reactors, advanced accelerators for medical and industrial purposes, and superconducting motors and generators, among others. The symbiotic relationship between cryogenics and superconductivity forms a virtuous cycle, where advancements in one field propel progress in the other. Consequently, the development of innovative cryogenic systems today has the potential to create a more profound impact than ever before, unlocking new possibilities for technological and industrial advancements.

This project has demonstrated the potential of magnetic refrigeration for cryogenic applications, opening pathways for future research that span multiple scientific disciplines and technologies.

First, the combination of gas and magnetic cycles presents a promising avenue, but further work is required to mitigate the associated technical risks. From a numerical analysis perspective, continued development of robust numerical methods is essential to accurately simulate the stiff systems of partial differential equations (PDEs) characteristic of cryogenic gas-magnetic cycles. Enhancing computational speed and flexibility is critical to enable meaningful comparisons with experimental results. Incorporating recent advancements in machine learning techniques and GPU-based computing could significantly improve the efficiency and accuracy of these simulations. Additionally, higher-complexity models that account for 2D/3D geometries, radial effects, and commonly observed phenomena in traditional gas cycles—such as void volumes—should be developed to better capture the intricacies of these systems.

Second, experimental validation remains a cornerstone for advancing this technology. The adapted single-blow test stand has proven to be a valuable tool, and with the updates

proposed in this thesis, it offers a controllable platform for optimizing magnetocaloric regenerators. Beyond this, the development of gas-magnetic prototypes is crucial. A practical approach would involve modifying an existing commercial cryocooler by replacing its regenerator with a magnetocaloric system and integrating a magnetic field source. This would allow for experimental assessment of the technology in real-world applications.

The exploration of magnetocaloric materials must continue, with an emphasis on identifying materials that exhibit both high volumetric heat capacity and a significant magnetocaloric effect over relevant temperature spans. Research into magnet design should also be prioritized, focusing on developing simple yet efficient magnetic systems that balance performance with practicality.

6.3 List of publications

Main contributions by the author from this thesis:

- [142] C. H. Lopez De Toledo *et al.*, "Cryogenic Test Stand for Characterization of Magnetocaloric Materials," *IEEE Trans. Appl. Supercond.*, vol. 34, no. 3, pp. 1–5, May 2024, doi: 10.1109/TASC.2024.3370126.
- [143] C. H. López de Toledo, J. M. López, and L. G. T. Rodriguez, "Exergoeconomic analysis of potential magnet configurations of a magnetic refrigerator operating at 4.2 K," *J. Instrum.*, vol. 17, no. 10, Oct. 2022, doi: 10.1088/1748-0221/17/10/C10019.
- [144] C. Hernando, J. Munilla, and L. García-Tabarés, "Performance evaluation of the magnetothermal properties of GGG and ErAl2 packed beds at cryogenic temperatures," *Cryogenics (Guildf).*, p. 104074, Apr. 2025, doi: 10.1016/J.CRYOGENICS.2025.104074

Peer reviewed, pending for publication:

C. Hernando, J. Munilla, L. Garcia-Tabares, and I. Castro, "Thermal characterization of a three-fluid cryogenic heat exchanger," *IOP Conference Series: Materials Science and Engineering, Advances in Cryogenic Engineering*

Additional contributions authored/coauthored related to this thesis:

- [145] J. Munilla *et al.*, "Commissioning of an Autonomous Cooling System for a Compact Superconducting Cyclotron Devoted to Radioisotope Production," *IEEE Trans. Appl. Supercond.*, vol. 31, no. 5, Aug. 2021, doi: 10.1109/TASC.2021.3070118.
- [146] L. Garcia-Tabares *et al.*, "Concept Design of a Novel Superconducting PTO Actuator for Wave Energy Extraction," *IEEE Trans. Appl. Supercond.*, vol. 32, no. 6, Sep. 2022, doi: 10.1109/TASC.2022.3148686.
- [147] C. Hernando, J. Munilla, L. Garcia-Tabares, and G. Pedrad, "Optimization of High Power SMES for Naval Applications," *IEEE Trans. Appl. Supercond.*, vol. 33, no. 5, Aug. 2023, doi: 10.1109/TASC.2023.3250169.
- [148] J. Munilla, I. Castro, L. Garcia-Tabares, C. Hernando, and F. Toral, "Analysis of the Limitations of the AMIT Magnet During Its Commissioning," *IEEE Trans. Appl. Supercond.*, vol. 34, no. 3, pp. 1–5, May 2024, doi: 10.1109/TASC.2024.3356487.

[149] C. Hernando *et al.*, "Design of superconducting magnetic energy storage (SMES) for waterborne applications," *IEEE Trans. Appl. Supercond.*, pp. 1–5, 2025, doi: 10.1109/TASC.2025.3529414.

REFERENCES

- [1] Randall F. Barron, Cryogenic Systems. Oxford University Press, 1985.
- [2] R. Radebaugh, "Refrigeration for Superconductors," in *Proceedings of the IEEE*, 2004, vol. 92, no. 10, pp. 1719–1734, doi: 10.1109/JPROC.2004.833678.
- [3] Y. Lvovsky, W. Stautner, and T. Zhang, "ChemInform Abstract: Novel Technologies and Configurations of Superconducting Magnets for MRI," *Supercond. Sci. Technol.*, vol. 26, p. 93001, 2013.
- [4] W. Yao, J. Bascunan, S. Hahn, and Y. Iwasa, "MgB2 coils for MRI applications," *Appl. Supercond. IEEE Trans.*, vol. 20, pp. 756–759, 2010.
- [5] H. Ueda, A. Ishiyama, S. Noguchi, S. Nagaya, J. Yoshida, and M. Fukuda, "Conceptual Design of Compact HTS Cyclotron for RI Production," *IEEE Trans. Appl. Supercond.*, vol. PP, p. 1, 2019.
- [6] R. Hirose *et al.*, "Development of 15 T cryogen-free superconducting magnets," in *IEEE Transactions on Applied Superconductivity*, Jun. 2006, vol. 16, no. 2, pp. 953–956, doi: 10.1109/TASC.2006.871282.
- [7] M. Linder, N. Rando, A. Peacock, and B. Collaudin, "Cryogenics in space A review of the missions and technologies," *ESA Bull. ASE.European Sp. Agency*, vol. 107, pp. 92–105, 2001.
- [8] G. Hechenblaikner *et al.*, "How cold can you get in space? Quantum Physics at cryogenic temperatures in space," *New J. Phys.*, vol. 16, 2013.
- [9] B. Wang and Z. H. Gan, "A critical review of liquid helium temperature high frequency pulse tube cryocoolers for space applications," *Prog. Aerosp. Sci.*, vol. 61, pp. 43–70, 2013.
- [10] A. Dubensky, K. Kovalev, A. Larionoff, K. Modestov, V. T. Penkin, and V. N. Poltavets, "An Outlook of the Use of Cryogenic Electric Machines On-board Aircraft," 2015, vol. 26.
- [11] S. Sahoo, X. Zhao, and K. Kyprianidis, "A Review of Concepts, Benefits, and Challenges for Future Electrical Propulsion-Based Aircraft," *Aerospace*, vol. 7, p. 44, 2020.
- [12] F. Berg, C. Palmer, P. Miller, M. Husband, and G. Dodds, "HTS Electrical System for a Distributed Propulsion Aircraft," *IEEE Trans. Appl. Supercond.*, vol. 25, pp. 1–5, 2015.
- [13] M. Filipenko *et al.*, "Concept design of a high power superconducting generator for future hybrid-electric aircraft," *Supercond. Sci. Technol.*, vol. 33, p. 54002, 2020.
- [14] E. Buchanan, D. Benford, J. Forgione, S. Moseley, and E. Wollack, "Cryogenic applications of commercial electronic components," *Cryogenics (Guildf)*., vol. 52, pp. 550–556, 2012.
- [15] K. Rajashekara and B. Akin, "A review of cryogenic power electronics status and applications," 2013, pp. 899–904.
- [16] A. Sosso, P. Durandetto, B. Trinchera, M. Fretto, E. Monticone, and V. Lacquaniti, "Cryogen-free Operation of SNIS for AC Quantum Voltage Standards," *IEEE Trans. Appl. Supercond.*, vol. 26, p. 1, 2016.
- [17] S. Tolpygo, "Superconductor Digital Electronics: Scalability and Energy Efficiency

- Issues," vol. 42, pp. 463–485, 2016.
- [18] A. Beckers, A. Tajalli, and J.-M. Sallese, "A Review on Quantum Computing: Qubits, Cryogenic Electronics and Cryogenic MOSFET Physics." 2019.
- [19] R. Das et al., "Cryogenic Qubit Integration for Quantum Computing," 2018, pp. 504–514.
- [20] D. Larbalestier, A. Gurevich, D. Feldmann, and A. Polyanskii, "High-Tcsuperconducting materials for electric power applications." pp. 311–320, 2010.
- [21] A. Abrahamsen, N. Magnusson, B. B. Jensen, and M. Runde, "Large Superconducting Wind Turbine Generators," *Energy Procedia*, vol. 24, pp. 60–67, 2012.
- [22] Y. BRUNET, P. TIXADOR, and H. NITHART, "Cryogenic conceptions for full superconducting generators: realization of superconducting armature cryostat," *Cryogenics (Guildf).*, vol. 28, pp. 751–755, 1988.
- [23] X. Song *et al.*, "Designing and Basic Experimental Validation of the World's First MW-Class Direct-Drive Superconducting Wind Turbine Generator," *IEEE Trans. Energy Convers.*, vol. PP, p. 1, 2019.
- [24] M. Parizh et al., "[Invited]: Superconducting Synchronous Motors for Electric Ship Propulsion," *IEEE Trans. Appl. Supercond.*, vol. PP, p. 1, 2020.
- [25] H. Yeom *et al.*, "Cooling performance test of the superconducting fault current limiter," *Prog. Supercond. Cryog.*, vol. 16, no. 4, pp. 66–70, Dec. 2014, doi: 10.9714/psac.2014.16.4.066.
- [26] A. Morandi, P. L. Ribani, A. Fiorillo, and S. Pullano, "Development of a Small Cryogen-Free MgB2 Test Coil for SMES Application," *IEEE Trans. Appl. Supercond.*, vol. PP, p. 1, 2017.
- [27] P. Chowdhuri, C. Pallem, J. Demko, and M. Gouge, "Feasibility of Electric Power Transmission by DC Superconducting Cables," *Appl. Supercond. IEEE Trans.*, vol. 15, pp. 3917–3926, 2006.
- [28] L. Trevisani, M. Fabbri, and F. Negrini, "Long distance renewable-energy-sources power transmission using hydrogen-cooled MgB 2 superconducting line," *Cryogenics* (Guildf)., vol. 47, pp. 113–120, 2007.
- [29] S. P. Ashworth and D. W. Reagor, "A novel cooling scheme for superconducting power cables," *Cryogenics (Guildf).*, vol. 51, pp. 161–167, 2011.
- [30] P. Cheetham, C. Kim, S. Pamidi, and L. Graber, "Optimization of a superconducting gas-insulated transmission line," *IEEE Trans. Dielectr. Electr. Insul.*, vol. 26, pp. 930–938, 2019.
- [31] P. Tixador, "Concepts for HTS and MgB2 in transformers," *Ind. Ceram.*, vol. 27, 2007.
- [32] F. Werfel, U. Floegel-Delor, R. Rothfeld, T. Riedel, P. Schirrmeister, and R. Koenig, "Experiments of Superconducting Maglev Ground Transportation," *IEEE Trans. Appl. Supercond.*, vol. 26, p. 1, 2016.
- [33] J. Mun, C. Lee, K. Kim, K. Sim, and S. Kim, "Operating Thermal Characteristics of REBCO Magnet for Maglev Train Using Detachable Cooling System," *IEEE Trans. Appl. Supercond.*, vol. PP, p. 1, 2019.
- [34] P. Lebrun, "Cryogenics for the Large Hadron Collider," *IEEE Trans. Appl. Supercond.*, vol. 10, no. 1, pp. 1500–1505, 2000, doi: 10.1109/77.828526.
- [35] P. Dauguet et al., "Cryogenics for fusion," in AIP Conference Proceedings, Mar. 2008, vol. 985, no. 1, pp. 1701–1707, doi: 10.1063/1.2908540.
- [36] M. Atrey, Cryocoolers Theory and Applications: Theory and Applications. 2020.
- [37] M. D. Atrey, "Cryocooler Technology: The Path to Invisible and Reliable Cryogenics," 2020, pp. 1–46.
- [38] V. S. Chakravarthy, R. K. Shah, and G. Venkatarathnam, "A review of refrigeration methods in the temperature range 4-300 K," *J. Therm. Sci. Eng. Appl.*, vol. 3, no. 2, Jul. 2011, doi: 10.1115/1.4003701.

- [39] W. E. Gifford, "The Gifford-McMahon Cycle," in *Advances in Cryogenic Engineering*, Springer US, 1966, pp. 152–159.
- [40] R. A. Ackermann, K. G. Herd, and W. E. Chen, "Advanced Cryocooler Cooling for MRI Systems," in *Cryocoolers 10*, Springer US, 2002, pp. 857–867.
- [41] K. D. Timmerhaus and T. M. Flynn, Cryogenic Process Engineering. Springer US, 1989.
- [42] R. Radebaugh, "Cryocoolers: the state of the art and recent developments," *J. Phys. Condens. Matter*, vol. 21, no. 16, p. 164219, 2009, [Online]. Available: https://doi.org/10.1088%2F0953-8984%2F21%2F16%2F164219.
- [43] I. Garaway, M. Lewis, P. E. Bradley, and R. Radebaugh, "Measured and Calculated Performance of a High Frequency, 4 K Stage, He-3 Regenerator," 2011, Accessed: Jan. 18, 2025. [Online]. Available: https://www.researchgate.net/publication/265990902_Measured_and_Calculated_Performance_of_a_High_Frequency_4_K_Stage_He-3_Regenerator.
- [44] G. Ventura and L. Risegari, *The art of cryogenics: low-temperature experimental techniques*. Elsevier, 2008.
- [45] D. S. Betts, "The Pomeranchuk refrigerator," in *An Introduction to Millikelvin Technology*, Cambridge University Press, 1989, pp. 46–59.
- [46] F. Pobell, "Low-Temperature Thermometry," in *Matter and Methods at Low Temperatures*, Berlin, Heidelberg: Springer Berlin Heidelberg, 1996, pp. 241–303.
- [47] J. Munilla López, "Development of a novel concept of efficient superconducting magnet for radioisotope production cyclotron," Universidad Pontificia Comillas, 2020.
- [48] "Cryocoolers SHI Cryogenics Group." https://shicryogenics.com/products/cryocoolers/ (accessed Jan. 03, 2025).
- [49] "Cryomech Cryocoolers Bluefors.com." https://bluefors.com/products/cryocoolers/ (accessed Jan. 03, 2025).
- [50] V. K. Pecharsky, V. K. Pecharsky, K. A. Gschneidner, K. A. Gschneidner, A. O. Pecharsky, and A. M. Tishin, "Thermodynamics of the magnetocaloric effect," *Phys. Rev. B Condens. Matter Mater. Phys.*, vol. 64, no. 14, pp. 1444061–14440613, Oct. 2001, doi: 10.1103/PHYSREVB.64.144406.
- [51] L. Li, "Review of magnetic properties and magnetocaloric effect in the intermetallic compounds of rare earth with low boiling point metal(s)," *Chinese Phys. B*, vol. 25, no. 3, Dec. 2015, doi: 10.1088/1674-1056/25/3/037502.
- [52] M. E. Wood and W. H. Potter, "General analysis of magnetic refrigeration and its optimization using a new concept: maximization of refrigerant capacity," *Cryogenics* (Guildf)., vol. 25, no. 12, pp. 667–683, Dec. 1985, doi: 10.1016/0011-2275(85)90187-0.
- [53] I. A. Abdel-Latif and M. R. Ahmed, "Use of Magnetocaloric Material for Magnetic Refrigeration System: A Review," *Mater. Sci. Res. India*, vol. 16, no. 3, pp. 209–224, Dec. 2019, doi: 10.13005/msri/160303.
- [54] J. A. Barclay, "The theory of an active magnetic regenerative refrigerator," NASA. Goddard Sp. Flight Cent. Refrig. Cryog. Sensors, 1983.
- [55] R. Bjørk, C. R. H. Bahl, A. Smith, and N. Pryds, "Review and comparison of magnet designs for magnetic refrigeration," *Int. J. Refrig.*, vol. 33, no. 3, pp. 437–448, May 2010, doi: 10.1016/J.IJREFRIG.2009.12.012.
- [56] A. Kitanovski, J. Tušek, U. Tomc, U. Plaznik, M. Ožbolt, and A. Poredoš, "Magnetocaloric Energy Conversion," *Green Energy Technol.*, vol. 179, no. Mcm, pp. 167–210, 2015, doi: 10.1007/978-3-319-08741-2.
- [57] V. Franco, J. S. Blázquez, J. J. Ipus, J. Y. Law, L. M. Moreno-Ramírez, and A. Conde, "Magnetocaloric effect: From materials research to refrigeration devices," *Progress in Materials Science*, vol. 93. Elsevier Ltd, pp. 112–232, Apr. 01, 2018, doi: 10.1016/j.pmatsci.2017.10.005.
- [58] L. Li et al., "Giant low field magnetocaloric effect and field-induced metamagnetic

- transition in TmZn," *Appl. Phys. Lett.*, vol. 107, no. 13, p. 132401, Sep. 2015, doi: 10.1063/1.4932058.
- [59] L. Li, O. Niehaus, M. Kersting, and R. Pöttgen, "Reversible table-like magnetocaloric effect in Eu4PdMg over a very large temperature span," *Appl. Phys. Lett.*, vol. 104, no. 9, p. 092416, Mar. 2014, doi: 10.1063/1.4867882.
- [60] L. Li, O. Niehaus, M. Kersting, and R. Pöttgen, "Magnetic properties and magnetocaloric effect in the rare earth-rich phases RE4PtMg (RE = Ho and Er)," *Intermetallics*, vol. 62, pp. 17–21, 2015, doi: 10.1016/j.intermet.2015.03.004.
- [61] W. Hermes, U. C. Rodewald, and R. Pöttgen, "Large reversible magnetocaloric effect due to a rather unstable antiferromagnetic ground state in Er4 NiCd," *J. Appl. Phys.*, vol. 108, no. 11, p. 113919, Dec. 2010, doi: 10.1063/1.3518556.
- [62] L. Li, B. Saensunon, W. D. Hutchison, D. Huo, and K. Nishimura, "Magnetic properties and large reversible magnetocaloric effect in TmMn 2Si2," *J. Alloys Compd.*, vol. 582, pp. 670–673, 2014, doi: 10.1016/j.jallcom.2013.08.117.
- [63] L. Li, M. Kadonaga, D. Huo, Z. Qian, T. Namiki, and K. Nishimura, "Low field giant magnetocaloric effect in RNiBC (R Er and Gd) and enhanced refrigerant capacity in its composite materials," *Appl. Phys. Lett.*, vol. 101, no. 12, p. 122401, Sep. 2012, doi: 10.1063/1.4752738.
- [64] L. Li, H. Igawa, K. Nishimura, and D. Huo, "Study of the magnetic transition and large magnetocaloric effect in DyCo3B2 compound," *J. Appl. Phys.*, vol. 109, no. 8, p. 083901, Apr. 2011, doi: 10.1063/1.3572060.
- [65] J. Huo *et al.*, "Magnetic properties and large magnetocaloric effects of GdPd intermetallic compound," *J. Rare Earths*, vol. 36, no. 10, pp. 1044–1049, Oct. 2018, doi: 10.1016/j.jre.2018.03.016.
- [66] P. Wikus, E. Canavan, S. T. Heine, K. Matsumoto, and T. Numazawa, "Magnetocaloric materials and the optimization of cooling power density," *Cryogenics (Guildf).*, vol. 62, pp. 150–162, Jul. 2014, doi: 10.1016/j.cryogenics.2014.04.005.
- [67] W. Dai, E. Gmelin, and R. Kremer, "Magnetothermal properties of sintered Gd3Ga5O12," J. Phys. D. Appl. Phys., vol. 21, no. 4, pp. 628–635, Apr. 1988, doi: 10.1088/0022-3727/21/4/014.
- [68] G. A. Slack and D. W. Oliver, "Thermal Conductivity of Garnets and Phonon Scattering by Rare-Earth Ions," *Phys. Rev. B*, vol. 4, no. 2, p. 592, Jul. 1971, doi: 10.1103/PhysRevB.4.592.
- [69] A. Bézaguet *et al.*, "Design and construction of a static magnetic refrigerator operatingbetween 1.8 K and 4.5 K," *Cryogenics (Guildf).*, vol. 34, no. SUPPL. 1, pp. 227–230, Jan. 1994, doi: 10.1016/S0011-2275(05)80049-9.
- [70] T. Hashimoto *et al.*, "Investigations on the Possibility of the RAl2 System as a Refrigerant in an Ericsson Type Magnetic Refrigerator," *Adv. Cryog. Eng.*, vol. 32, pp. 279–286, 1986, doi: 10.1007/978-1-4613-9871-4_33.
- [71] T. Lei, "Modeling of active magnetic regenerators and experimental investigation of passive regenerators with oscillating flow," 2016.
- [72] K. K. Nielsen, K. Engelbrecht, and C. R. H. Bahl, "The influence of flow maldistribution on the performance of inhomogeneous parallel plate heat exchangers," *Int. J. Heat Mass Transf.*, vol. 60, no. 1, pp. 432–439, 2013, doi: 10.1016/J.IJHEATMASSTRANSFER.2013.01.018.
- [73] T. Numazawa, K. Kamiya, T. Utaki, and K. Matsumoto, "Magnetic refrigerator for hydrogen liquefaction," *Cryogenics (Guildf).*, vol. 62, pp. 185–192, Jul. 2014, doi: 10.1016/J.CRYOGENICS.2014.03.016.
- [74] "What is Magnetic Refrigeration?" https://kiutra.com/what-is-magnetic-refrigeration/ (accessed Jan. 11, 2025).
- [75] A. Kitanovski, P. W. Egolf, and A. Poredos, "Rotary magnetic chillers with permanent magnets," *Int. J. Refrig.*, vol. 35, no. 4, pp. 1055–1066, Jun. 2012, doi: 10.1016/J.IJREFRIG.2012.02.005.

- [76] R. Bjørk, "Designing a magnet for magnetic refrigeration," Technical University of Denmark, 2010.
- [77] C. V. Heer, C. B. Barnes, and J. G. Daunt, "The Design and Operation of a Magnetic Refrigerator for Maintaining Temperatures below 1°K," Rev. Sci. Instrum., vol. 25, no. 11, pp. 1088–1098, Nov. 1954, doi: 10.1063/1.1770944.
- [78] J. Geuns, "STUDY OF A NEW MAGNETIC REFRIGERATING CYCLE.," 1966.
- [79] J. A. Barclay, W. F. Stewart, W. C. Overton, R. J. Candler, and O. D. Harkleroad, "Experimental Results on a Low-Temperature Magnetic Refrigerator," *Adv. Cryog. Eng.*, vol. 31, pp. 743–752, 1986, doi: 10.1007/978-1-4613-2213-9_84.
- [80] T. Numazawa, T. Hashimoto, H. Nakagome, N. Tanji, and O. Horigami, "The Helium Magnetic Refrigerator II: Liquefaction Process and Efficiency," *Adv. Cryog. Eng.*, vol. 29, pp. 589–596, 1984, doi: 10.1007/978-1-4613-9865-3_67.
- [81] T. NUMAZAWA, "Magnetic Refrigeration in Low Temperatures," J. Japan Soc. Appl. Electromagn. Mech., vol. 21, no. 1, pp. 34–39, Mar. 2013, doi: 10.14243/JSAEM.21.34.
- [82] K. Kamiya *et al.*, "Active magnetic regenerative refrigeration using superconducting solenoid for hydrogen liquefaction," *Appl. Phys. Express*, vol. 15, no. 5, p. 053001, Apr. 2022, doi: 10.35848/1882-0786/AC5723.
- [83] K. Kamiya *et al.*, "Active magnetic regenerative refrigeration using superconducting solenoid for hydrogen liquefaction," *Appl. Phys. Express*, vol. 15, no. 5, p. 053001, Apr. 2022, doi: 10.35848/1882-0786/AC5723.
- [84] C. P. (Carl P. Tausczik, "Magnetically active regeneration," Massachusetts Institute of Technology, 1986.
- [85] W. A. Steyert, "Final report on NRIP-funded magnetic refrigerator development project, July 1, 1975--October 1, 1977. [New Research Initiatives Program (NRIP)]," Los Alamos Scientific Laboratory, Los Alamos, NM, Feb. 1978. doi: 10.2172/5170870.
- [86] G. Nellis, "Stirling-magnetic cryocooler," Massachusetts Institute of Technology, 1997
- [87] A. M. Tishin, "Magnetic refrigeration in the low-temperature range," J. Appl. Phys., vol. 68, no. 12, pp. 6480–6484, 1990, doi: 10.1063/1.347186.
- [88] Gregory F. Nellis, "Magnetically aumented cryogenic refrigeration," University of Wisconsin (Doctoral thesis), 1992.
- [89] K. K. Nielsen *et al.*, "Review on numerical modeling of active magnetic regenerators for room temperature applications," *Int. J. Refrig.*, vol. 34, no. 3, pp. 603–616, 2011, doi: 10.1016/J.IJREFRIG.2010.12.026.
- [90] A. Smaïli, S. Aït-Ali, and R. Chahine, "Performance predictions of a first stage magnetic hydrogen liquefier," *Int. J. Hydrogen Energy*, vol. 36, no. 6, pp. 4169–4177, Mar. 2011, doi: 10.1016/J.IJHYDENE.2010.09.006.
- [91] T. Feng, R. Chen, and R. V. Ihnfeldt, "Modeling of hydrogen liquefaction using magnetocaloric cycles with permanent magnets," *Int. J. Refrig.*, vol. 119, pp. 238–246, Nov. 2020, doi: 10.1016/J.IJREFRIG.2020.06.032.
- [92] W. Zheng *et al.*, "Numerical simulation of a multistage magnetic refrigeration system in the temperature range of liquid hydrogen," *Int. J. Hydrogen Energy*, vol. 51, pp. 523–535, Jan. 2024, doi: 10.1016/J.IJHYDENE.2023.07.192.
- [93] T. Diamantopoulos, T. Matteuzzi, and R. Bjørk, "1D models of an active magnetic regeneration cycle for cryogenic applications," *Int. J. Refrig.*, vol. 167, pp. 246–256, Nov. 2024, doi: 10.1016/J.IJREFRIG.2024.08.011.
- [94] E. Achenbach, "Heat and flow characteristics of packed beds," *Exp. Therm. Fluid Sci.*, vol. 10, no. 1, pp. 17–27, Jan. 1995, doi: 10.1016/0894-1777(94)00077-L.
- [95] R. D. Skeel and M. Berzins, "A Method for the Spatial Discretization of Parabolic Equations in One Space Variable," *SIAM J. Sci. Stat. Comput.*, vol. 11, no. 1, pp. 1–

- 32, Jan. 1990, doi: 10.1137/0911001.
- [96] B. Greene, "GitHub wgreene310/pde1dm: 1D PDE Solver for MATLAB and Octave written in m-code." https://github.com/wgreene310/pde1dm (accessed Jan. 03, 2025).
- [97] S. Ergun, "Fluid Flow Through Packed Columns," *Chem. Eng. Prog.*, vol. 48, p. 89, 1952.
- [98] M. Kaviany, *Principles of Heat Transfer in Porous Media*. New York, NY: Springer New York, 1995.
- [99] "Thermophysical Properties of Fluid Systems." https://webbook.nist.gov/chemistry/fluid/ (accessed Jan. 04, 2025).
- [100] "Two-Phase Fluid Properties (2P)." https://es.mathworks.com/help/simscape/ref/twophasefluidproperties2p.html (accessed Jan. 04, 2025).
- [101] R. W. Murphy, "Thermodynamic property evaluation and magnetic refrigeration cycle analysis for gadolinium gallium garnet," Dec. 1994, doi: 10.2172/10114667.
- [102] F. N. Mastrup and K. D. Price, "Thermodynamic Performance Measurements of a 10K, Ga3Ga5O12 Paramagnetic Stage," *Proc. Interag. Meet. Cryocoolers*, pp. 149–159, 1988.
- [103] N. A. de Oliveira and P. J. von Ranke, "Theoretical aspects of the magnetocaloric effect," *Phys. Rep.*, vol. 489, no. 4–5, pp. 89–159, Apr. 2010, doi: 10.1016/J.PHYSREP.2009.12.006.
- [104] W. Schelp, W. Drewes, A. Leson, and H. G. Purwins, "Low temperature heat capacity of some heavy REA12 compounds (RE = Tb, Dy, Er and Tm) in a magnetic field," *J. Phys. Chem. Solids*, vol. 47, no. 9, pp. 855–861, Jan. 1986, doi: 10.1016/0022-3697(86)90056-9.
- [105] T. Inoue, S. G. Sankar, R. S. Craig, W. E. Wallace, and K. A. Gschneidner Jr., "Low temperature heat capacities and thermal properties of DyAl<inf>2</inf>, ErAl<inf>2</inf> and LuAl<inf>2</inf>," *J. Phys. Chem. Solids*, vol. 38, no. 5, pp. 487–497, 1977, doi: 10.1016/0022-3697(77)90182-2.
- [106] R. Michalski, "Simulated thermomagnetic properties of DyAl2, HoAl2 and ErAl2 compounds calculated by atomic matters MFA computation system," Res. Rev. J. Mater. Sci., vol. 06, 2018, doi: 10.4172/2321-6212-C6-029.
- [107] "Cryogenics Material Properties." https://trc.nist.gov/cryogenics/materials/materialproperties.htm (accessed Jan. 09, 2025).
- [108] K. L. Engelbrecht, G. F. Nellis, and S. A. Klein, "A Numerical Model of an Active Magnetic Regenerator Refrigeration System," *Cryocoolers* 13, pp. 471–480, 2005, doi: 10.1007/0-387-27533-9_60.
- [109] D. J. Magee and K. E. Niemeyer, "Accelerating solutions of one-dimensional unsteady PDEs with GPU-based swept time–space decomposition," *J. Comput. Phys.*, vol. 357, pp. 338–352, Mar. 2018, doi: 10.1016/J.JCP.2017.12.028.
- [110] M. M. Almajid and M. O. Abu-Al-Saud, "Prediction of porous media fluid flow using physics informed neural networks," J. Pet. Sci. Eng., vol. 208, p. 109205, Jan. 2022, doi: 10.1016/J.PETROL.2021.109205.
- [111] J. A. Barclay, W. C. Overton, W. F. Stewart, and Sunil Sarangi, "Experiment to determine properties of packed beds and regenerators at cryogenic temperatures," *Adv. Cryog. Eng.*, vol. 29, pp. 605–612, 1984, doi: 10.1007/978-1-4613-9865-3_69.
- [112] W. M. Rohsenow, J. P. Hartnett, and Y. I. Cho, Eds., *Handbook of Heat Transfer*, Third. MCGRAW-HILL, 1997.
- [113] P. G. Reedeker, A. Frydman, and J. A. Barclay, "A Laboratory Apparatus to Determine Fluid-Solid Heat Transfer Coefficient and Effective Thermal Conductivity of Solid Porous Media," Adv. Cryog. Eng., pp. 1723–1730, 2000, doi: 10.1007/978-1-4615-4215-5_98.

- [114] F. K. M. C. M. Gunderson, G. F. Nellis, "The Development of an Active Magnetic Regenerative Refrigerator (AMRR) for Sub-Kelvin Cooling of Space Science Instrumentation," *Cryogenics (Guildf).*, vol. 21.
- [115] T. Li, S. Li, J. Zhao, P. Lu, and L. Meng, "Sphericities of non-spherical objects," *Particuology*, vol. 10, no. 1, pp. 97–104, Feb. 2012, doi: 10.1016/J.PARTIC.2011.07.005.
- [116] R. Battiston, "The antimatter spectrometer (AMS-02): A particle physics detector in space," Nucl. Instruments Methods Phys. Res. Sect. A Accel. Spectrometers, Detect. Assoc. Equip., vol. 588, no. 1–2, pp. 227–234, Apr. 2008, doi: 10.1016/J.NIMA.2008.01.044.
- [117] F. Toral, "Design and calculation procedure for particle accelerator superconducting magnets: application to an LHC superconducting quadrupole," Universidad Pontificia de Comillas; Madrid, 2002.
- [118] D. P. Sekulić and R. K. Shah, "Thermal Design Theory of Three-Fluid Heat Exchangers," Adv. Heat Transf., vol. 26, no. C, pp. 219–328, Jan. 1995, doi: 10.1016/S0065-2717(08)70297-1.
- [119] "Cryogenics Material Properties." https://trc.nist.gov/cryogenics/materials/materialproperties.htm (accessed Jan. 18, 2022).
- [120] R. F. Barron, Cryogenic Heat Transfer, 1st ed. CRC Press, 1999.
- [121] T. E. W. Schumann, "Heat transfer: A liquid flowing through a porous prism," *J. Franklin Inst.*, vol. 208, no. 3, pp. 405–416, 1929, doi: 10.1016/S0016-0032(29)91186-8.
- [122] C. C. Furnas, "Heat Transfer from a gas Stream to bed of Broken Solids," *Ind. Eng. Chem.*, vol. 22, no. 1, pp. 26–31, Jan. 1930, doi: 10.1021/IE50241A007/ASSET/IE50241A007.FP.PNG_V03.
- [123] K. Krishnakumar, A. K. John, and G. Venkatarathnam, "A review on transient test techniques for obtaining heat transfer design data of compact heat exchanger surfaces," *Exp. Therm. Fluid Sci.*, vol. 35, no. 4, pp. 738–743, May 2011, doi: 10.1016/j.expthermflusci.2010.12.006.
- [124] Z. C. Chang, M. S. Hung, P. P. Ding, and P. H. Chen, "Experimental evaluation of thermal performance of Gifford-McMahon regenerator using an improved single-blow model with radial conduction," *Int. J. Heat Mass Transf.*, vol. 42, no. 3, pp. 405–413, Feb. 1998, doi: 10.1016/S0017-9310(98)00186-0.
- [125] P. F. Pucci, C. P. Howard, and C. H. Piersall, "The Single-Blow Transient Testing Technique for Compact Heat Exchanger Surfaces," *J. Eng. Power*, vol. 89, no. 1, pp. 29–38, Jan. 1967, doi: 10.1115/1.3616604.
- [126] G. L. Locke, "HEAT TRANSFER AND FLOW FRICTION CHARACTERISTICS OF POROUS SOLIDS. Technical Report No. 10," Jun. 1950.
- [127] J. H. Stang and J. E. Bush, "The Periodic Method for Testing Compact Heat Exchanger Surfaces," *J. Eng. Power*, vol. 96, no. 2, pp. 87–94, Apr. 1974, doi: 10.1115/1.3445767.
- [128] T. D. Yamamoto, A. T. Saito, H. Takeya, K. Terashima, T. Numazawa, and Y. Takano, "Tunable magnetic and magnetocaloric properties by thermal annealing in ErCo2 atomized particles," *J. Alloys Compd.*, vol. 935, p. 168040, Feb. 2023, doi: 10.1016/J.JALLCOM.2022.168040.
- [129] T. D. Yamamoto *et al.*, "Magnetic entropy change of ErAl2 magnetocaloric wires fabricated by a powder-in-tube method," *J. Phys. D. Appl. Phys.*, vol. 53, no. 9, Jan. 2020, doi: 10.1088/1361-6463/ab5c71.
- [130] M. M. Prusty *et al.*, "Magnetocaloric effect in melt-spun rare earth intermetallic compound ErAl2," *AIP Adv.*, vol. 12, no. 3, p. 35145, Mar. 2022, doi: 10.1063/9.0000358.

- [131] F. Kuriyama and R. Radebaugh, "Analysis of mass and energy flow rates in an orifice pulse-tube refrigerator," *Cryogenics (Guildf)*., vol. 39, no. 1, pp. 85–92, Jan. 1999, doi: 10.1016/S0011-2275(98)00129-5.
- [132] A. Bejan, G. Tsatsaronis, and M. Moran, "Thermal Design & Optimization," p. 542, 1996.
- [133] "Cryocoolers SHI Cryogenics Group." https://shicryogenics.com/products/cryocoolers/ (accessed Jan. 10, 2025).
- [134] R. W. McCallum, L. Lewis, R. Skomski, M. J. Kramer, and I. E. Anderson, "Practical Aspects of Modern and Future Permanent Magnets," *Annu. Rev. Mater. Res.*, vol. 44, pp. 451–477, Jul. 2014, doi: 10.1146/ANNUREV-MATSCI-070813-113457.
- [135] O. Tretiak, P. Blümler, and L. Bougas, "Variable single-axis magnetic-field generator using permanent magnets," *AIP Adv.*, vol. 9, no. 11, Nov. 2018, doi: 10.1063/1.5130896.
- [136] J. H. Jensen and M. G. Abele, "Maximally efficient permanent magnet structures," J. Appl. Phys., vol. 79, no. 2, p. 1157, Aug. 1998, doi: 10.1063/1.360914.
- [137] J. M. D. Coey, "Perspective and Prospects for Rare Earth Permanent Magnets," *Engineering*, vol. 6, no. 2, pp. 119–131, Feb. 2020, doi: 10.1016/J.ENG.2018.11.034.
- [138] K. Matsumoto and P. Mele, "Artificial pinning center technology to enhance vortex pinning in YBCO coatedconductors," *Supercond. Sci. Technol.*, vol. 23, no. 1, p. 014001, Dec. 2009, doi: 10.1088/0953-2048/23/1/014001.
- [139] Y. Iwasa, Case studies in superconducting magnets: design and operational issues; 2nd ed. Springer, 2009.
- [140] A. Chirkova, K. P. Skokov, L. Schultz, N. V. Baranov, O. Gutfleisch, and T. G. Woodcock, "Giant adiabatic temperature change in FeRh alloys evidenced by direct measurements under cyclic conditions," *Acta Mater.*, vol. 106, pp. 15–21, Mar. 2016, doi: 10.1016/J.ACTAMAT.2015.11.054.
- [141] N. Hirano, T. Watanabe, S. Nagaya, T. Okamura, K. Waki, and T. Kawanami, "Basic research on durability of Mn-based magneto-caloric material for magnetic heat pump.," *Int. Conf. Caloric Cool. (Thermag VIII). Proc. Darmstadt, Ger. Sept. 16-20, 2018.*), vol. 2018-January, pp. 102–107, 2018, doi: 10.18462/IIR.THERMAG.2018.0016.
- [142] C. H. Lopez De Toledo *et al.*, "Cryogenic Test Stand for Characterization of Magnetocaloric Materials," *IEEE Trans. Appl. Supercond.*, vol. 34, no. 3, pp. 1–5, May 2024, doi: 10.1109/TASC.2024.3370126.
- [143] C. H. López de Toledo, J. M. López, and L. G. T. Rodriguez, "Exergoeconomic analysis of potential magnet configurations of a magnetic refrigerator operating at 4.2 K," *J. Instrum.*, vol. 17, no. 10, Oct. 2022, doi: 10.1088/1748-0221/17/10/C10019.
- [144] C. Hernando, J. Munilla, and L. García-Tabarés, "Performance evaluation of the magnetothermal properties of GGG and ErAl2 packed beds at cryogenic temperatures," *Cryogenics (Guildf).*, p. 104074, Apr. 2025, doi: 10.1016/J.CRYOGENICS.2025.104074.
- [145] J. Munilla *et al.*, "Commissioning of an Autonomous Cooling System for a Compact Superconducting Cyclotron Devoted to Radioisotope Production," *IEEE Trans. Appl. Supercond.*, vol. 31, no. 5, Aug. 2021, doi: 10.1109/TASC.2021.3070118.
- [146] L. Garcia-Tabares *et al.*, "Concept Design of a Novel Superconducting PTO Actuator for Wave Energy Extraction," *IEEE Trans. Appl. Supercond.*, vol. 32, no. 6, Sep. 2022, doi: 10.1109/TASC.2022.3148686.
- [147] C. Hernando, J. Munilla, L. Garcia-Tabares, and G. Pedraz, "Optimization of High Power SMES for Naval Applications," *IEEE Trans. Appl. Supercond.*, vol. 33, no. 5, Aug. 2023, doi: 10.1109/TASC.2023.3250169.
- [148] J. Munilla, I. Castro, L. Garcia-Tabares, C. Hernando, and F. Toral, "Analysis of the

- Limitations of the AMIT Magnet During Its Commissioning," *IEEE Trans. Appl. Supercond.*, vol. 34, no. 3, pp. 1–5, May 2024, doi: 10.1109/TASC.2024.3356487.
- [149] C. Hernando *et al.*, "Design of superconducting magnetic energy storage (SMES) for waterborne applications," *IEEE Trans. Appl. Supercond.*, pp. 1–5, 2025, doi: 10.1109/TASC.2025.3529414.
- [150] W. M. Rohsenow, J. P. Hartnett, and Y. i. Cho, *Handbook of Heat Transfer*, no. 1. McGraw-Hill Education, 1998.
- [151] G. R. Hadley, "Thermal conductivity of packed metal powders," *Int. J. Heat Mass Transf.*, vol. 29, no. 6, pp. 909–920, Jun. 1986, doi: 10.1016/0017-9310(86)90186-9.
- [152] H. G. Purwins and A. Leson, "Magnetic properties of (rare earth)Al2 intermetallic compounds," *Adv. Phys.*, vol. 39, no. 4, pp. 309–403, Jan. 1990, doi: 10.1080/00018739000101511.

APPENDICES

APPENDIX 1: EXPERIMENTAL CORRELATIONS FOR A MAGNETIC REFRIGERATOR	173
APPENDIX 2: DERIVATION OF ERAL ₂ PROPERTIES	175
APPENDIX 3: HEAT TRANSFER AND PRESSURE CORRELATIONS FOR 3-FLUI	d Heat
Exchanger	178
APPENDIX 4: RAW EXPERIMENTAL RESULTS	180

APPENDIX 1: EXPERIMENTAL CORRELATIONS FOR A MAGNETIC REFRIGERATOR

Pressure Correlations

The parameter F_d in Eq. (2.27) is the drag force exerted by the magnetocaloric material in the fluid. For the purposes of this study F_d is computed under the Darcy-Forcheimer relation for a packed bed filled with spheres of uniform diameter:

$$F_d = \frac{\mu}{K}u + \frac{c_f \rho_f}{\sqrt{K}} |u|u \tag{A.1}$$

Where K and c_f are established in order to satisfy Ergun correlation [97]:

$$K = \frac{\varepsilon^3 d_p^2 \emptyset^2}{150(1 - \varepsilon)^2} \tag{A.2}$$

$$c_f = \frac{1.75\emptyset}{\sqrt{150}\varepsilon^{\frac{3}{2}}} \tag{A.3}$$

Where ε is the porosity and \emptyset the shape factor, defined as:

$$\varepsilon = \frac{Void\ Volume}{Total\ Volume} = \frac{V_v}{V_T} \tag{A.4}$$

$$\emptyset = \frac{Sphere\ Area}{Particle\ Area} = \frac{A_{sph}}{A_{part}} \tag{A.5}$$

Heat Transfer Correlations

Similarly for heat transfer there are numerous correlations for Nusselt numbers in a packed bed. Rohsenow [150] suggests:

$$Nu_{dp} = \frac{d_p \cdot h}{k_f} = 2 + 1.8 \cdot Pr^{\frac{1}{3}} \cdot Re_{dp}^{\frac{1}{2}}$$
(A.6)

where Pr is the Prandtl number.

However, this correlation is limited to $Re_{dp} > 50$, which maybe a limitation for AMR refrigerators. Achenbach [94] suggests a more general expression that is adopted in this thesis:

$$Nu_{dp} = (1 + 1.5(1 - \varepsilon))Nu_{sp}$$
 (A.7)

Where Nu_{sp} is defined as follows:

$$Nu_{sp} = 2 + (Nu_{lam}^2 + Nu_{turb}^2)^{1/2}$$
(A.8)

And the laminar and turbulent Nusselt are given by the following relations:

$$Nu_{lam} = 0.664 \cdot Pr^{1/3} \left(\frac{Re_{dp}}{\varepsilon}\right)^{1/3}$$
 (A.9)

$$Nu_{turb} = \frac{0.037 \cdot \left(\frac{Re_{dp}}{\varepsilon}\right)^{0.8} \cdot Pr}{1 + 2.443 \cdot \left(\frac{Re_{dp}}{\varepsilon}\right)^{-0.1} (Pr^{\frac{2}{3}} - 1)}$$
(A.10)

The heat transfer between the wall and the fluid is modeled as [150]:

$$Nu_{dn} = 0.17 \cdot Re_{dn}^{0.17} \tag{A.11}$$

Effective Thermal Conductivity

The fluid mixes along the direction of the flow due to the dispersion caused by the packed bed. This term can be treated as an axial conduction term. The total effective conductivity is a sum of the static thermal conductivity, and the axial conductivity caused by the dispersion. According to Kaviani [98], the total effective conductivity can be expressed as:

$$k_{eff} = k_{static} + k_f D^d (A.12)$$

Hadley [151] presents a correlation for the static fluid conductivity in a porous structure:

$$k_{static} = k_f \left[(1 - \alpha_0) \frac{\varepsilon f_0 + \frac{k_r}{k_f (1 - \varepsilon f_0)}}{1 - \varepsilon (1 - f_0) + \frac{k_r}{k_f \varepsilon (1 - f_0)}} + \alpha_0 \frac{2\left(\frac{k_r}{k_f}\right)^2 (1 - \varepsilon) + \frac{(1 + 2\varepsilon)k_r}{k_f}}{\frac{(2 + \varepsilon)k_r}{k_f} + 1 - \varepsilon} \right]$$

$$f_0 = 0.8 + 0.1\varepsilon$$

$$log \alpha_0 = -4.898\varepsilon, \ 0 \le \varepsilon \le 0.0827$$

$$log \alpha_0 = -0.405 - 3.154(\varepsilon - 0.0827), \ 0.0827 \le \varepsilon \le 0.298$$

$$log \alpha_0 = -1.084 - 6.778(\varepsilon - 0.298), \ 0.298 \le \varepsilon \le 0.580$$
(A.13)

For the dispersion coefficient the model presented by Kaviany is used:

$$D^d = \varepsilon \frac{3}{4} P e_f \tag{A.14}$$

Where Pe_f is the Peclet number defined as $Pe_f = Re_f Pr_f$.

APPENDIX 2: DERIVATION OF ERAL₂ Properties

The theoretical model for computing the magnetothermodynamic properties of ErAl₂ is adopted from Oliveira et al [103]. Since ErAl₂ has not been adopted in any prototype, a more thorough review of the procedure is explained. For a detailed derivation refer to the original source.

As described in Eq. (2.1) the total entropy of a magnetocaloric material is expressed as the sum of three contributions: S_m the magnetic entropy, S_l is the lattice entropy, and S_e is the electronic entropy from conduction electrons.

The magnetic contribution is derived from a Hamiltonian that includes: interaction between magnetic moments, the coupling between the applied magnetic field and the crystalline electrical field:

$$\mathcal{H}_{mag}^{4f} = -\sum_{i,j} \mathcal{G}_{ij}(r) \vec{J}_i \cdot \vec{J}_j - \sum_i g\mu_B \vec{B} \cdot \vec{J}_i + \sum_i \mathcal{H}_i^{CF}$$
(A.15)

The last term, the crystalline electrical field term per ion is given by the following expression:

$$\mathcal{H}^{CF} = \sum_{nm} B_n^m O_n^m \tag{A.16}$$

Where B_n^m are crystalline electrical field parameters, which are specific for each material and usually adjusted from experimental data.

Table 62 shows the $ErAl_2$ parameters adopted in this study. O_n^m are called Stevens operators an can be found in [152]. The number of parameters n and m depends on the points symmetry of the material. For $ErAl_2$ which has cubic symmetry, we have only two crystalline electrical field parameters, so that the crystalline electrical field Hamiltonian is given by:

$$\mathcal{H}_{cub}^{CF} = B_4(0_4^0 + 50_4^4) + B_6(0_6^0 - 210_6^4) \tag{A.17}$$

Eq. (A.15) can be simplified to the following expression:

$$\mathcal{H}_{mag}^{4f} = -\sum_{i} g\mu_{B} \vec{J}_{i} \vec{B}_{eff} + \sum_{i} \mathcal{H}_{i}^{CF}$$
(A.18)

Where \vec{B}_{eff} is the effective magnetic field, which can be written as:

$$\vec{B}_{eff} = \vec{B} + \widetilde{\lambda_0} M + \widetilde{\lambda_1} M^3 \tag{A.19}$$

Where $\widetilde{\lambda_0}$, $\widetilde{\lambda_1}$ are the exchange interaction parameter, and the magnetoelastic parameter respectively. Both are specific for each material. The exchange interaction parameter $\widetilde{\lambda_0}$, is shown in Table 61, while $\widetilde{\lambda_1}$ is assumed to be 0 as ErAl₂ undergoes a second order transition. \overrightarrow{M} is the magnetization vector and its components are calculated by:

$$\vec{M}_k = g\mu_B \langle J_k \rangle \tag{A.20}$$

Where the averages $\langle J_k \rangle$ are:

$$\langle J_k \rangle = \frac{\sum_m \langle \psi_m | J_k | \psi_m \rangle e^{-\beta \varepsilon_m}}{\sum_m e^{-\beta \varepsilon_m}}$$
(A.21)

Where $\beta = \frac{1}{k_b T}$, being k_b the Boltzmann constant. In Eq. (A.21), $\langle \psi_m |$ and ε_m are the eigenfunctions and eigenvalues of the Hamiltonian of Eq. (A.18). Therefore, a numerical approach is needed as the computation of the Hamiltonian needs the magnetization of the material and vice versa.

The magnetic partition function per ion is: $Z_{\text{mag}}^{4f} = \sum_{m} e^{-\beta \varepsilon_m}$. And the magnetic free energy per mol is given by:

$$F_{mag}^{4f}(T,B,P) = -N_A k_B T ln \left[\sum_m e^{-\beta \varepsilon_m} \right]$$
(A.22)

Where N_A is the Avogadro number. From the thermodynamic relation $S_{\rm mag}^{4f} = -\left(\frac{\partial F_{\rm mag}^{4f}}{\partial T}\right)_{\rm Beff}$, magnetic entropy can be computed:

$$F_{mag}^{4f}(T,B,P) = -N_m \Re \left[ln \left[\sum_m e^{-\beta \varepsilon_m} \right] + \frac{1}{k_B T} \frac{\sum_m \varepsilon_m e^{-\beta \varepsilon_m}}{\sum_m e^{-\beta \varepsilon_m}} \right]$$
(A.23)

Where \Re is the gas constant, and N_m is the magnetic ions per unit formula, one in the case of ErAl₂.

Table 61. Crystalline electrical field parameters, exchange interaction parameter $(\widetilde{\lambda_0})$ and the easy magnetization direction for ErAl₂.

Compound	x	W (meV)	B ₄ (meV)	B ₆ (meV)	$\widetilde{\lambda_0}\left(\frac{T^2}{meV}\right)$	Easy direction
$ErAl_2$	-0.26	-0.025	1.08*10-4	-1.33*10-6	$0.937*10^{23}$	(111)

The lattice entropy is computed with the assumption that it varies linearly in the rare earth series, from the non-magnetic La to the non-magnetic Lu. Therefore, the lattice entropy is computed by:

$$S_{lat}^{R}(T) = \frac{(14 - n)S_{lat}^{La}(T) + nS_{lat}^{Lu}(T)}{14}$$
(A.24)

Where n gives the relative position of the rare element in the series, n = 11 for ErAl₂. The lattice entropy of LaAl₂ and LuAl₂ are computed with the Debye approximation using the measured Debye temperature data in Figure 149 from [103].

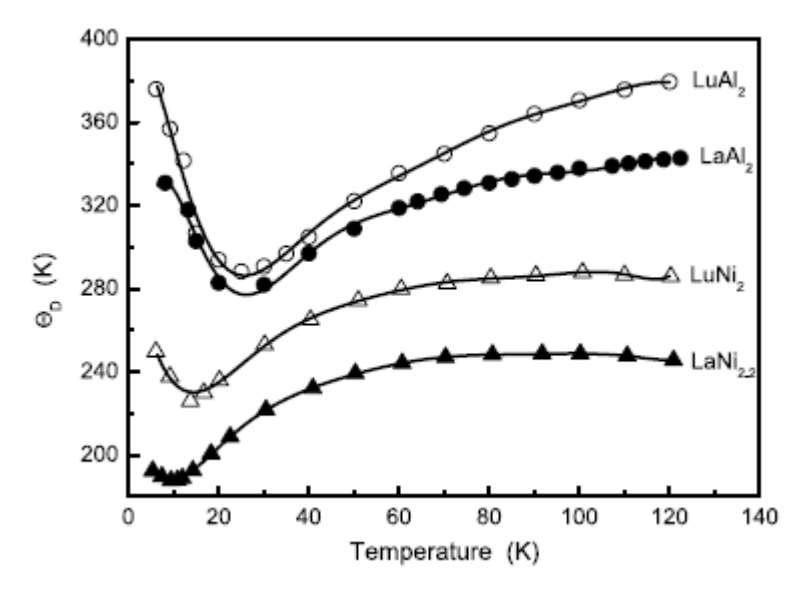


Figure 149. Temperature dependence of the Debye temperature in LaAl₂, LuAl₂, LaNi_{2:2} and LuNi₂

Finally, the electronic contribution to entropy is computed with:

$$S_l = \gamma T \tag{A.25}$$

Where γ is the electronic heat capacity coefficient. A value $\gamma = 5.4 \frac{mJ}{molK^2}$ is used in this study.

The main properties of ErAl₂ obtained with the model for the easy direction <1,1,1> are shown in Figure 153 and Figure 151.

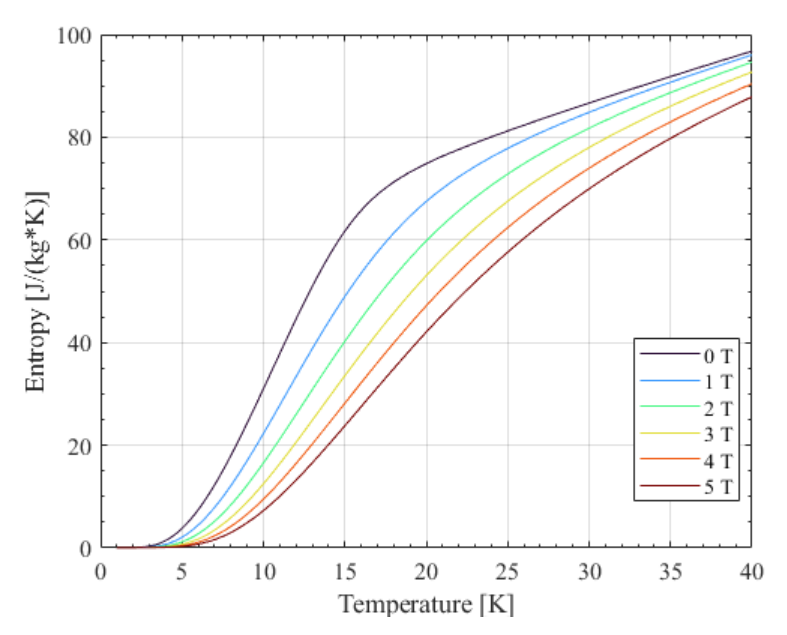


Figure 150. Entropy of ErAl₂ derived from the numerical model

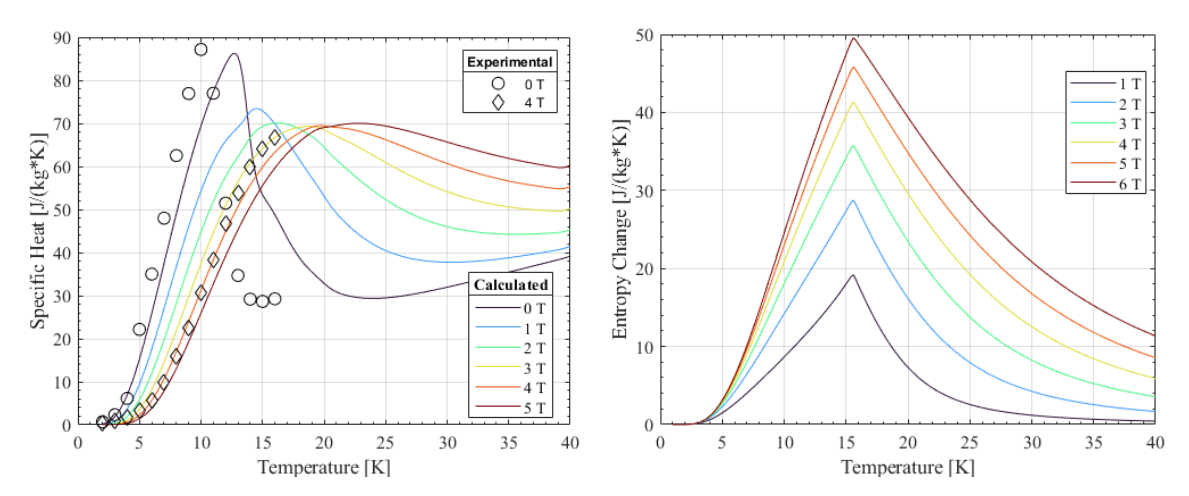


Figure 151. Specific heat of ErAl₂ as a function of temperature and magnetic field, solid lines represent model results, while markers represent data obtained from the literature [104] (left). Entropy change as function of temperature and magnetic field (right)

APPENDIX 3: HEAT TRANSFER AND PRESSURE CORRELATIONS FOR 3-FLUID HEAT EXCHANGER

Table 62. Heat transfer correlations for the different fluids and flows regimes of the 3-fluid heat exchanger

				Equation		
Fluid 1	Turbulent boundary layer separates	Laminar flow (Re < 2300)	All properties excep bulk Re Range 1-100 100-1000	C 0.9 0.9	ated at the mean e n 0.4 0.4	[120]
			1000-	0.52 $= CRe^{-n}$	0.5	
	(c) Wake region	Turbulent	Re Range	С	n	
	wake region	flow	0.1-4	0.989	0.670	
		(Re >	4-40	0.911	0.615	[120]
		10000)	40-4000	0.683	0.534	
			4000-40000	0.193	0.382	
			40000-400000	0.027	0.195	
				Equation		
			r	Nu_i	Nu_o	[112]
			0.01	54.0167	4.6923	
	a		0.02	32.7051	4.7342	
Fluid		Laminar	0.05	17.8113	4.7910	
2	a		0.1	11.9058	4.8342	
-			0.25 0.5	7.7535	4.9048	
	2		0.8	6.1810 5.5785	5.0365 5.2536	
			1	5.3846	5.3846	
	flow	Turbulent		[112] Table		-
	nne:			Equation		
	ow inner wal	Laminar		$a_{am} = 3.657$	7	[120]
	oute oute				$0.023Re^{0.8}Pr^{\frac{1}{3}}$	
Fluid	outer wall		(Sr	mooth pipe)		
3	- 3	Turbulent	$if\left(\frac{e}{D}\right)Re > 5 \qquad N$	$u_t = \frac{RePr^{\frac{1}{3}}}{8}$	$\frac{f}{1+1.27\left(\frac{f}{2}\right)^{\frac{1}{2}}\left(Pr^{\frac{2}{3}}-1\right)}$	[120]
				ough pipe)	(8/ ()	
			· ·			

Table 63. Friction factor correlations for the different fluids and flows regimes of the 3-fluid heat exchanger

		Equation	
	Laminar	$f_{lam} = \frac{64}{Re}$	
Fluid 2	Turbulent	$if\left(\frac{e}{D}\right)Re < 5 \qquad f_{turb} = \frac{1}{0.782*\log\left(\frac{1}{0.135*\frac{e}{2r_h} + \frac{6.5}{Re_h}}\right)} $ (Smooth pipe)	 [112]
		$if\left(\frac{e}{D}\right)Re > 5$ $f_{turb} = 0.316Re_{dh}^{-0.25}$ (Rough pipe)	
Fluid 3	Laminar	$f_{lam} = \frac{24r^*}{Re_{dh}}$	[120]

Turbulent
$$if\left(\frac{e}{D}\right)Re < 5 \qquad f_{turb} = \frac{1}{0.782*\log\left(\frac{1}{0.135*\frac{e}{2T_h} + \frac{6.5}{Re_h}}\right)}$$
 (Smooth pipe)
$$if\left(\frac{e}{D}\right)Re > 5 \qquad f_{turb} = 0.316Re_{dh}^{-0.25}$$
 (Rough pipe)

APPENDIX 4: RAW EXPERIMENTAL RESULTS

THERMAL TESTS

Single Blow - Ambient Temperature

Table 64. Ambient Temperature single blow data test information table

Test Run	MCM	B (T)	P_low (bar)	Mass Flow (g/min)	Annotations
SB00	Glass	0	0.4	13.5	
SB01	Glass	0	0.4	13.5	

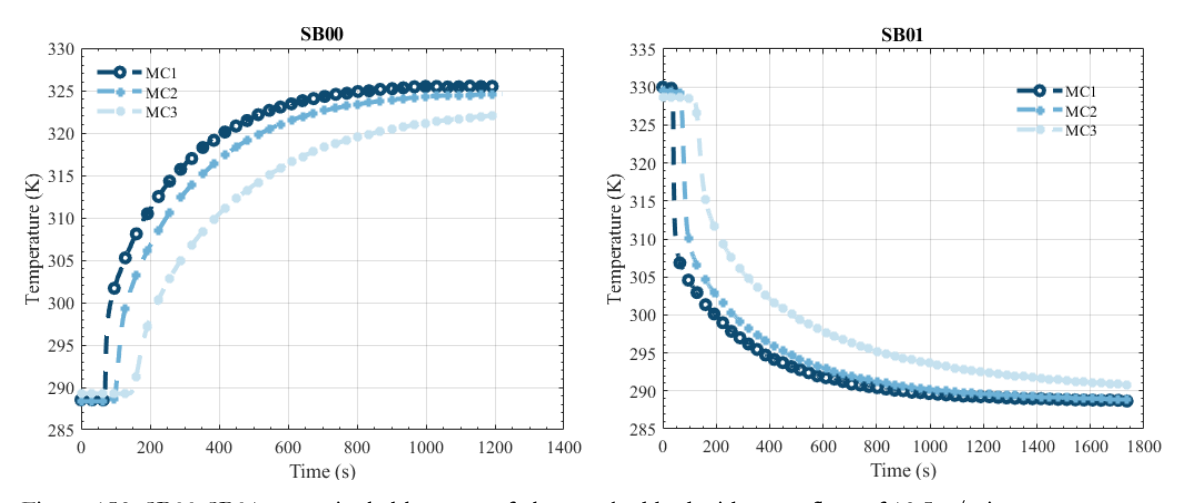


Figure 152. SB00-SB01 tests: single blow test of glass packed bed with mass flow of 13.5~g/min

<u>Single Blow – Liquid Helium</u>

Table 65. LHe temperature single blow data test information table

Test Run	MCM	B (T)	P_low (bar)	Mass Flow (g/min)	Annotations
SB11	ErAl_2	0	0.2	10	
SB12	ErAl_2	1	0.2	10	
SB13	ErAl_2	2	0.2	10	
SB14	ErAl_2	3	0.2	10	
SB15	ErAl_2	0	0.2	6	
SB16	ErAl_2	1	0.2	6	
SB17	ErAl_2	2	0.2	6	
SB18	ErAl_2	3	0.2	6	
SB21	GGG	0	0.2	10	
SB22	GGG	1	0.2	10	Not done
SB23	GGG	2	0.2	10	
SB24	GGG	3	0.2	10	Not done
SB25	GGG	0	0.2	6	
SB26	GGG	1	0.2	6	Not done
SB27	GGG	2	0.2	6	
SB28	GGG	3	0.2	6	Not done

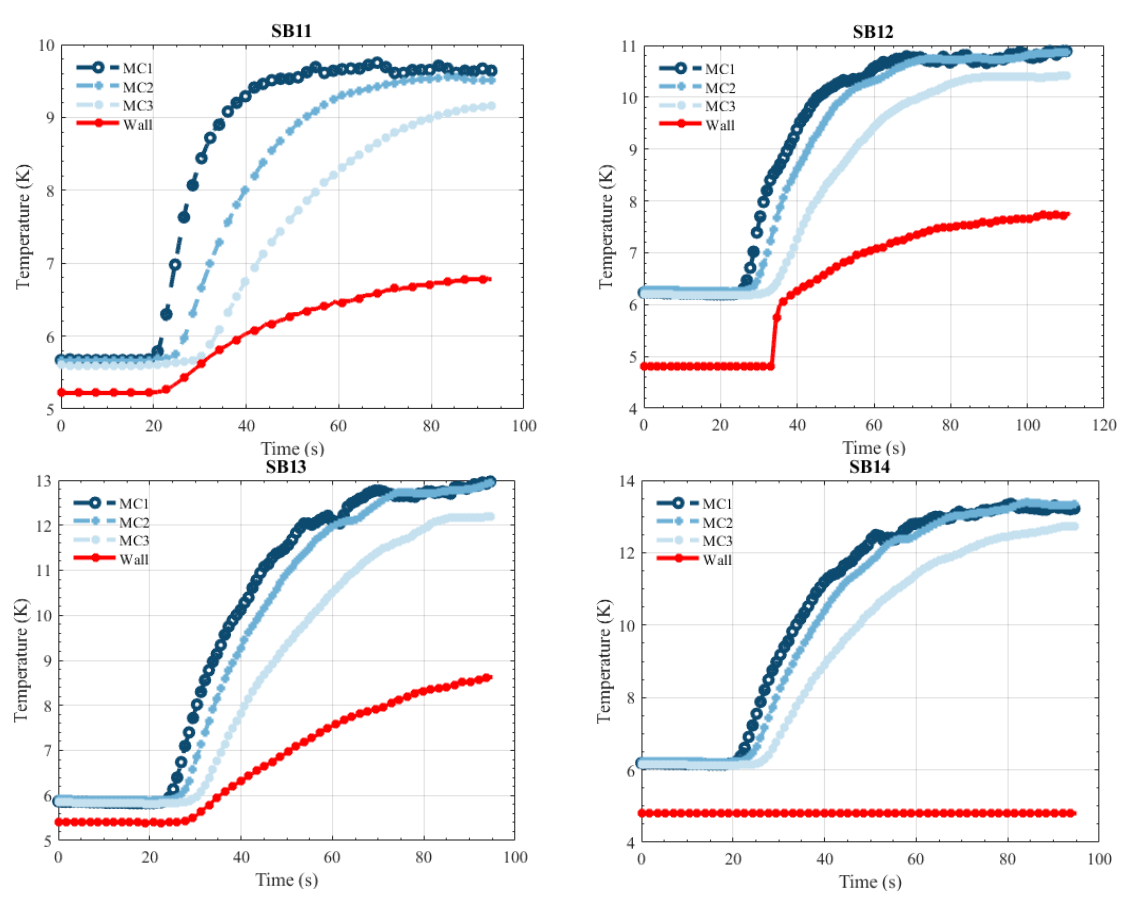


Figure 153. SB11-SB14 tests: single blow test of $ErAl_2$ with mass flow of 10 g/min for magnetic fields of 0-3 $^{\rm T}$

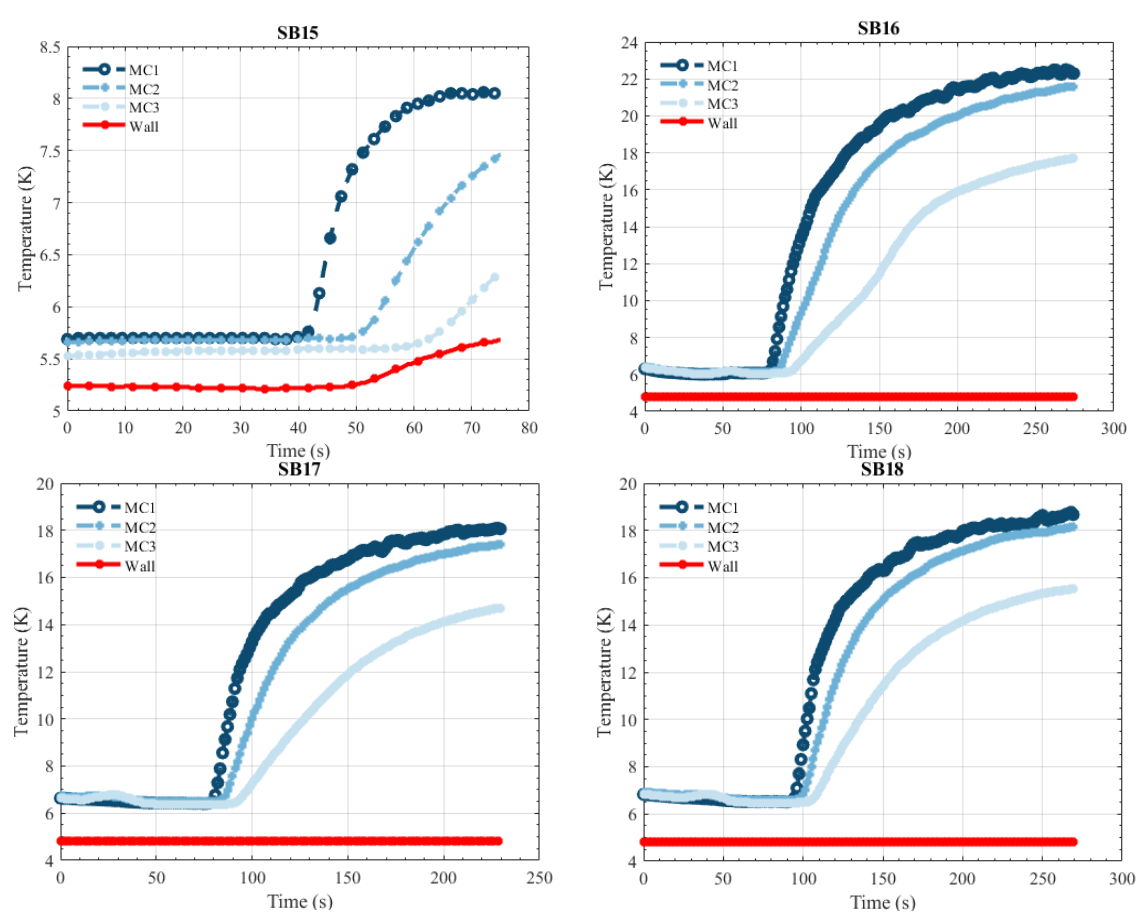


Figure 154. SB05-SB08 tests: single blow test of ErAl₂ with mass flow of 6 g/min for magnetic fields of 0-3 T

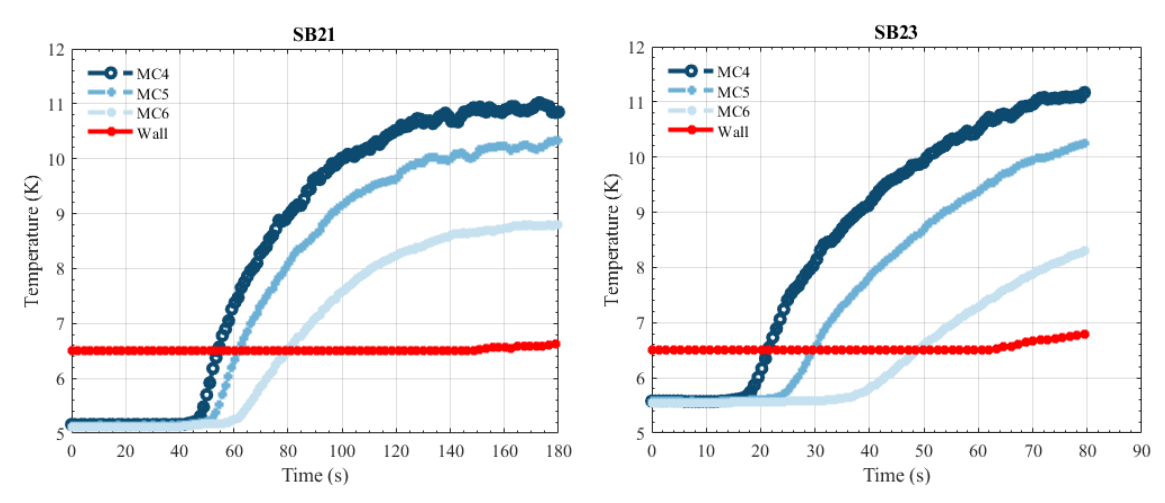


Figure 155. SB09-SB11 tests: single blow test of GGG with mass flow of 10 g/min for magnetic fields of 0-2

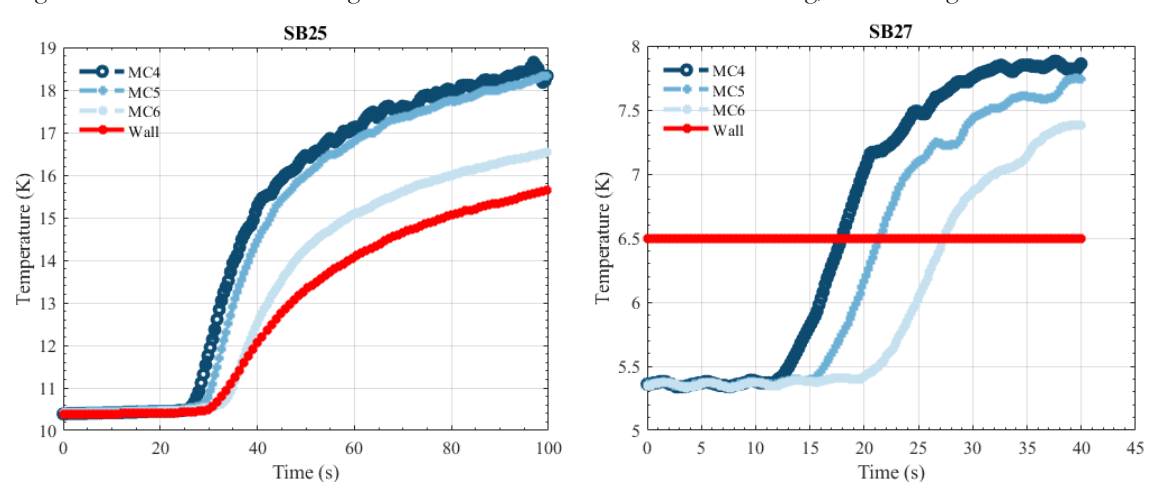


Figure 156. SB13-SB15 tests: single blow test of GGG with mass flow of 6 g/min for magnetic fields of 0-2 $^{\rm T}$

Periodic Blow

Table 66. LHe temperature periodic blow data test information table

Title	MCM	B (T)	P_low (bar)	Mass Flow (g/min)	Annotations
PB11	ErAl_2	0	0.2	10	
PB12	ErAl_2	1	0.2	10	Not done
PB13	ErAl_2	2	0.2	10	
PB14	ErAl_2	0	0.2	6	
PB15	ErAl_2	1	0.2	6	Not done
PB16	ErAl_2	2	0.2	6	
PB21	GGG	0	0.2	10	
PB22	GGG	1	0.2	10	
PB23	GGG	2	0.2	10	
PB24	GGG	0	0.2	6	
PB25	GGG	1	0.2	6	
PB26	GGG	2	0.2	6	

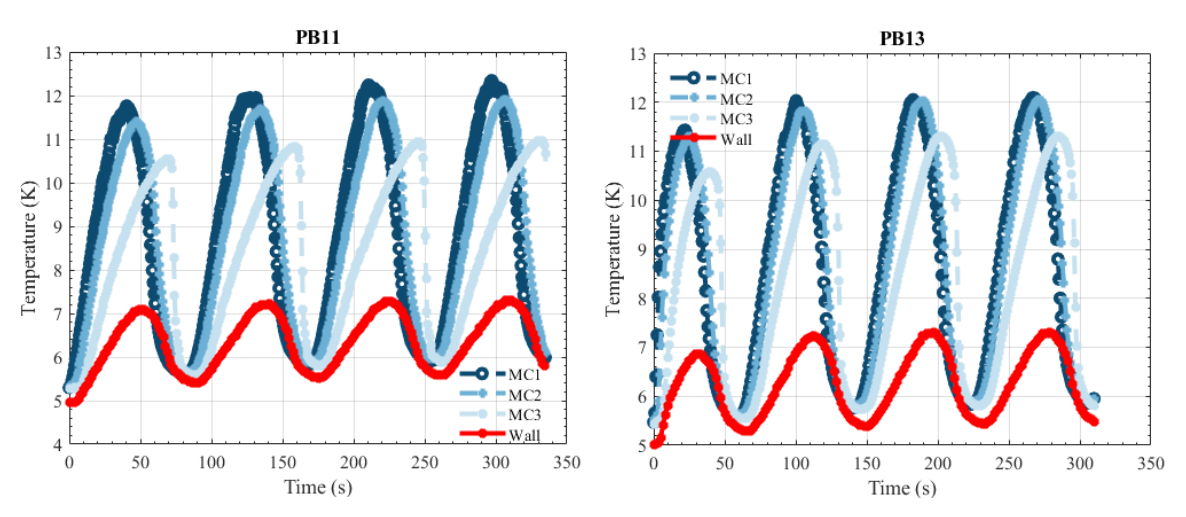


Figure 157. PB11 and PB13 tests: periodic blow tests of $ErAl_2$ with mass flow of 10 g/min with magnetic fields of 0-2 T

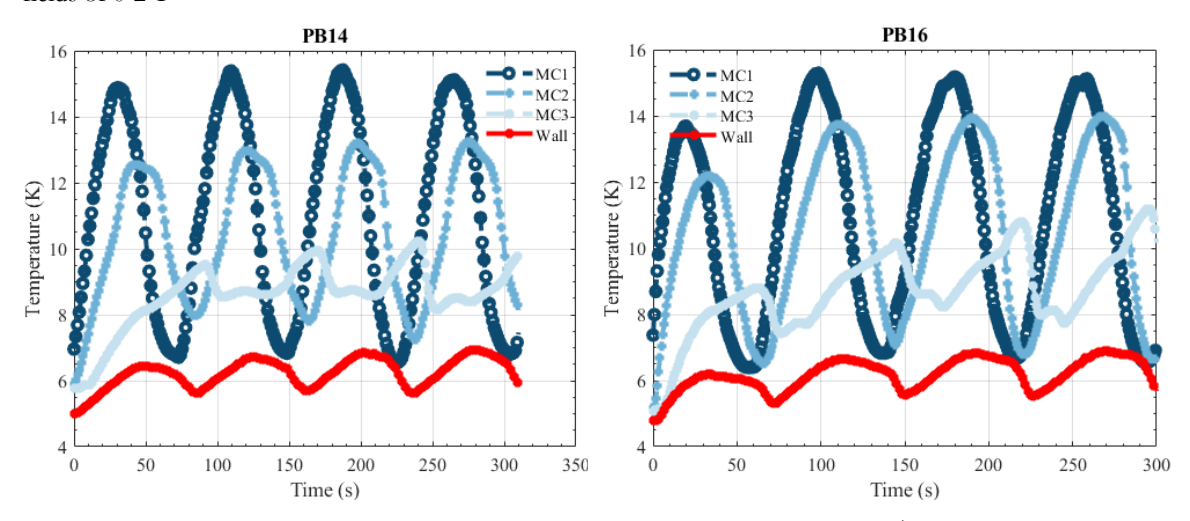
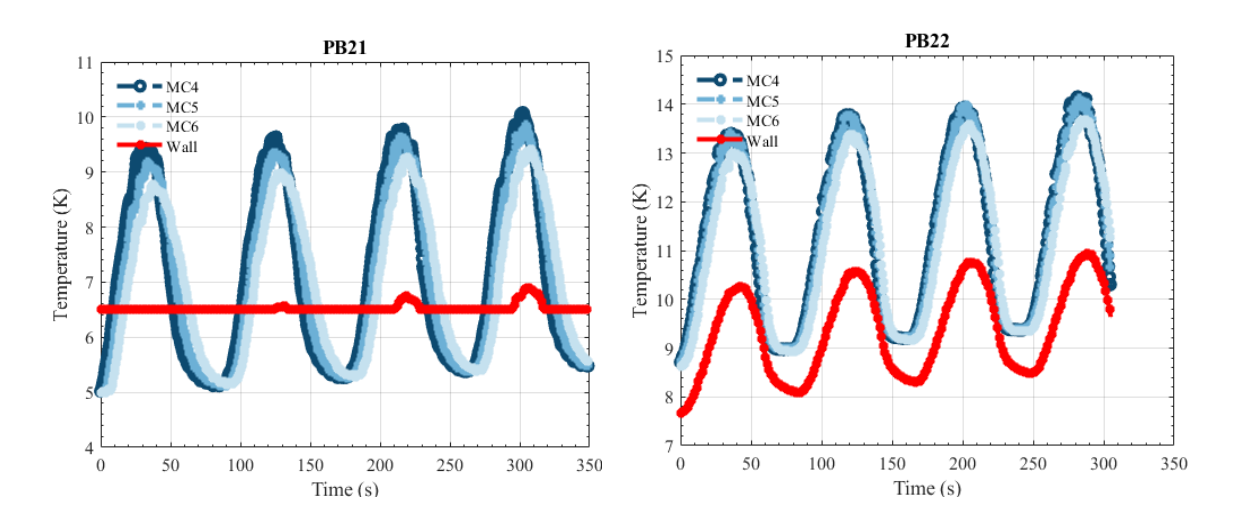


Figure 158. PB14 and PB16 tests: periodic blow tests of $ErAl_2$ with mass flow of 6 g/min with magnetic fields of 0-2 T



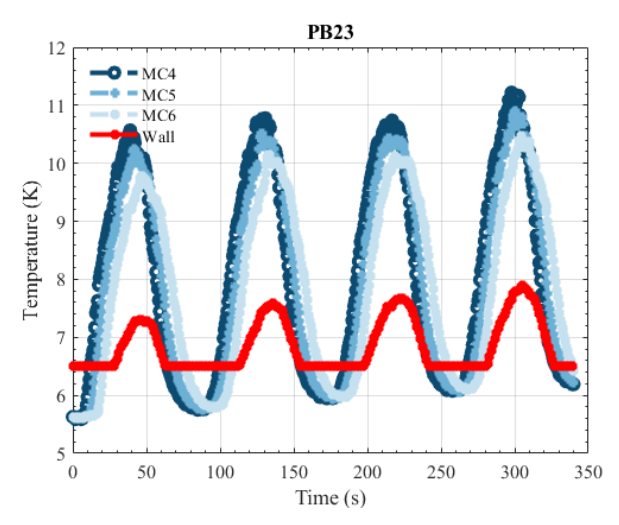


Figure 159. PB21-23 tests: periodic blow tests of GGG with mass flow of 10 g/min with magnetic fields of 0-1-2 $\rm T$

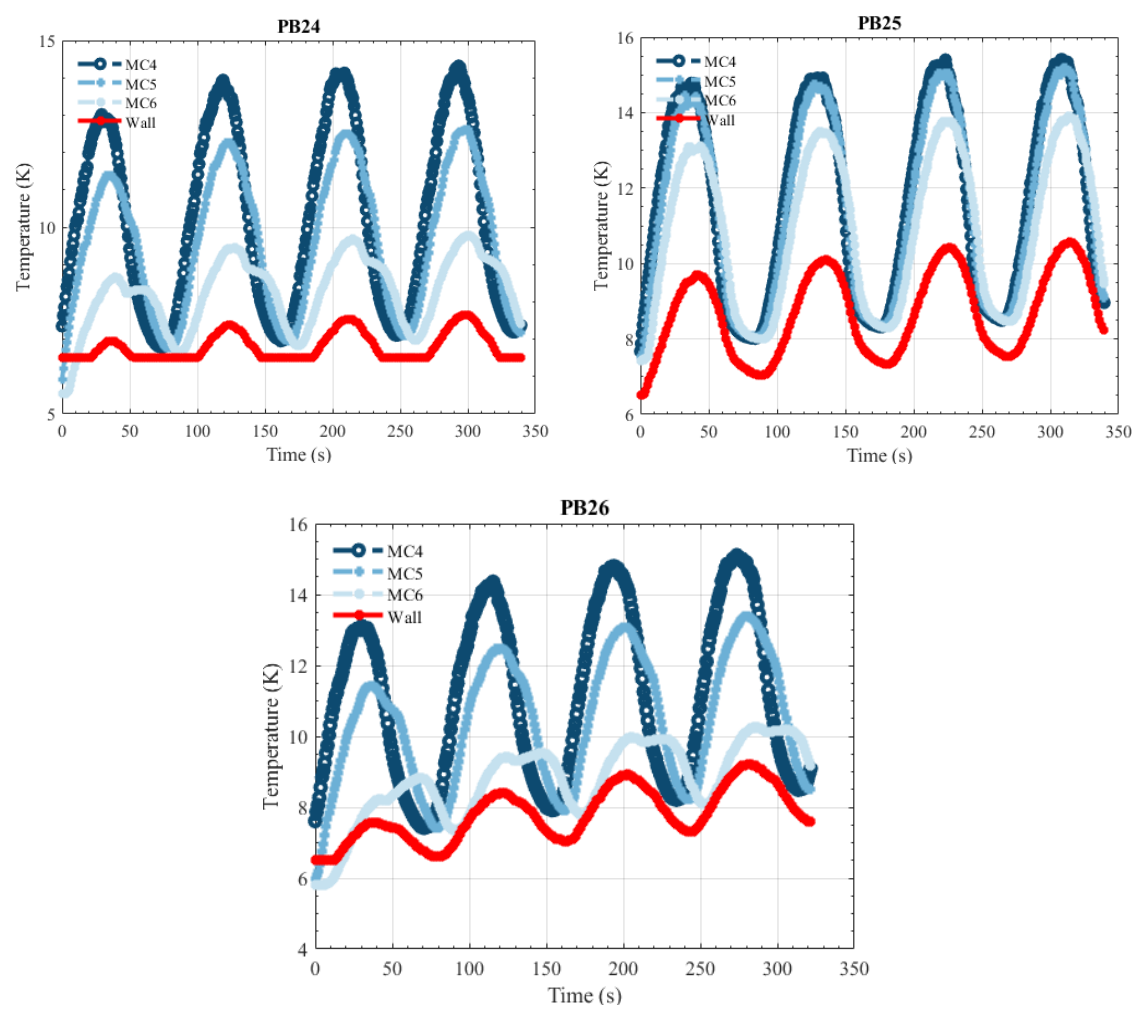


Figure 160. PB21-23 tests: periodic blow tests of GGG with mass flow of 6 g/min with magnetic fields of 0-1-2 $\rm T$

MAGNETIC TESTS

No-Load

Table 67. No-load data test information table

Title	MCM	T _{start} (K)	Waveform	B (T)	Annotations
NL11	ErAl ₂	4-5	Triangular	3	
NL12	ErAl_2	10-12	Triangular	3	
NL13	ErAl_2	14-16	Triangular	3	
NL14	ErAl_2	4-5	Trapezoidal	3	
NL15	ErAl_2	4-5	Trapezoidal	3	
NL21	GGG	4-5	Triangular	3	
NL22	GGG	5-6	Triangular	3	
NL23	GGG	8-9	Triangular	3	
NL24	GGG	4-5	Trapezoidal	3	
NL25	GGG	4-5	Trapezoidal	3	

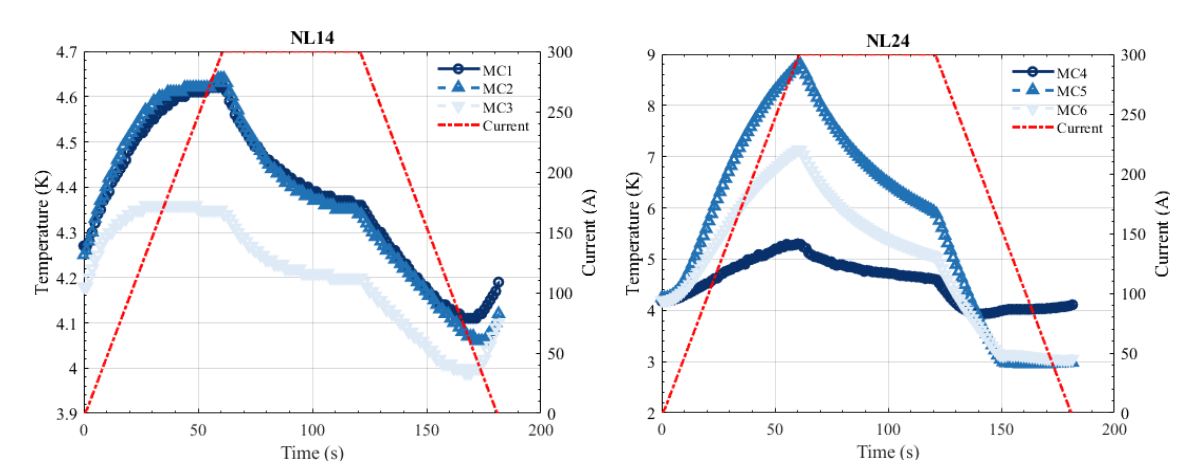


Figure 161. NL14 and NL24 tests. A trapezoidal magnetic field profile is applied to the packed beds.

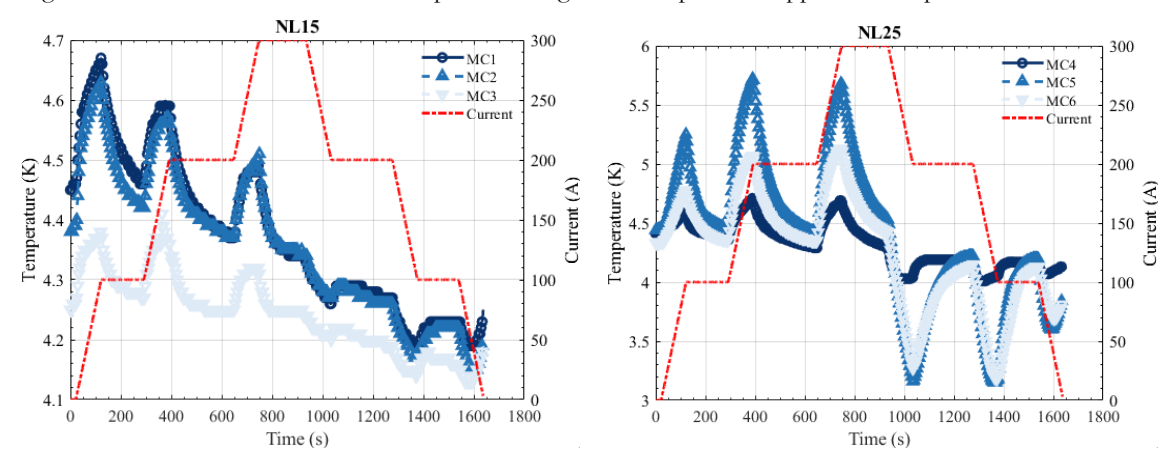


Figure 162. NL15 and NL25 tests. A trapezoidal magnetic field profile, with stops every 100A, is applied to the packed beds.

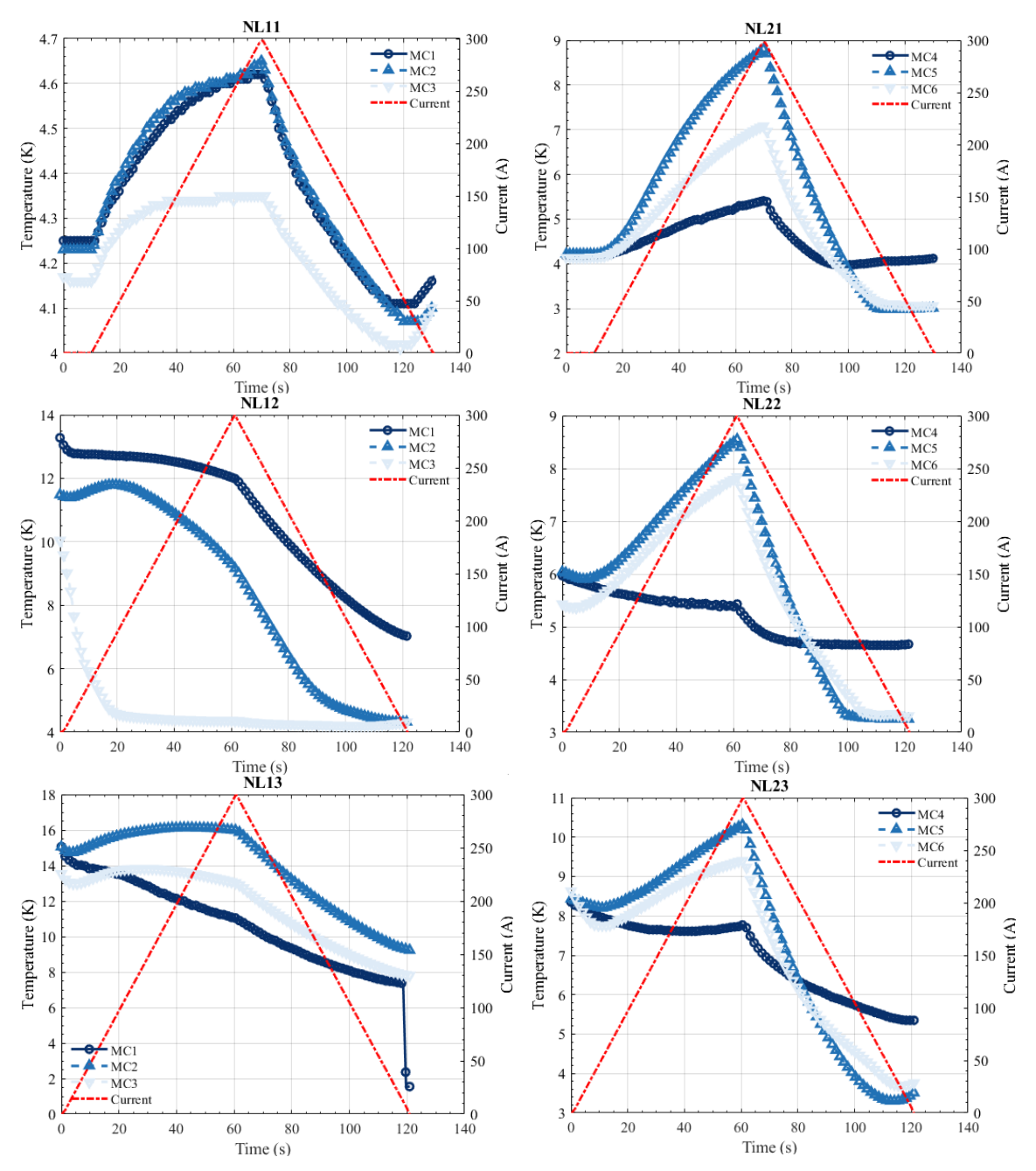


Figure 163. NL11-13 and NL21-23 tests. A triangular magnetic field profile is applied to the packed beds. The starting temperatures varies from 4 to 15 K.

Ramping Rate

Table 68. Ramping rate data test information table

Title	MCM	T _{start} (K)	dI/dt (A/s)	Annotations
RR11	ErAl ₂	5-6	5	Not done
RR12	ErAl_2	5-6	10	
RR13	ErAl_2	5-6	20	
RR14	ErAl_2	10-12	5	Not done
RR15	ErAl_2	10-12	10	
RR16	ErAl_2	10-12	20	
RR21	GGG	5-6	5	Not done
RR22	GGG	5-6	10	
RR23	GGG	5-6	20	
RR24	GGG	9-11	5	Not done
RR25	GGG	9-11	10	
RR26	GGG	9-11	20	

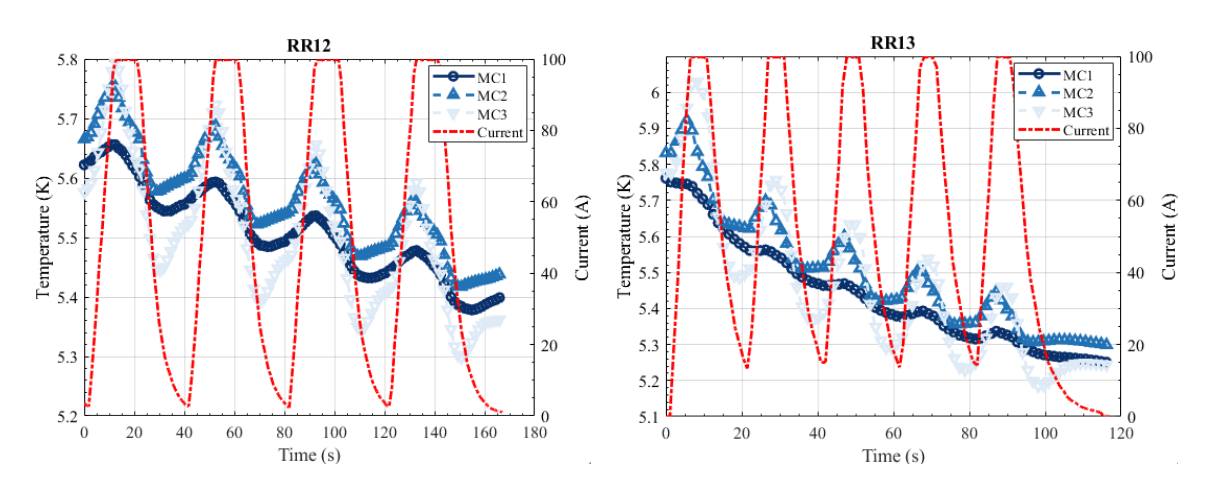


Figure 164. RR12 and RR12 tests. A trapezoidal magnetic field profile is applied with ramping rates of 10 and 20 A/s. Starting temperature is between 5-6K.

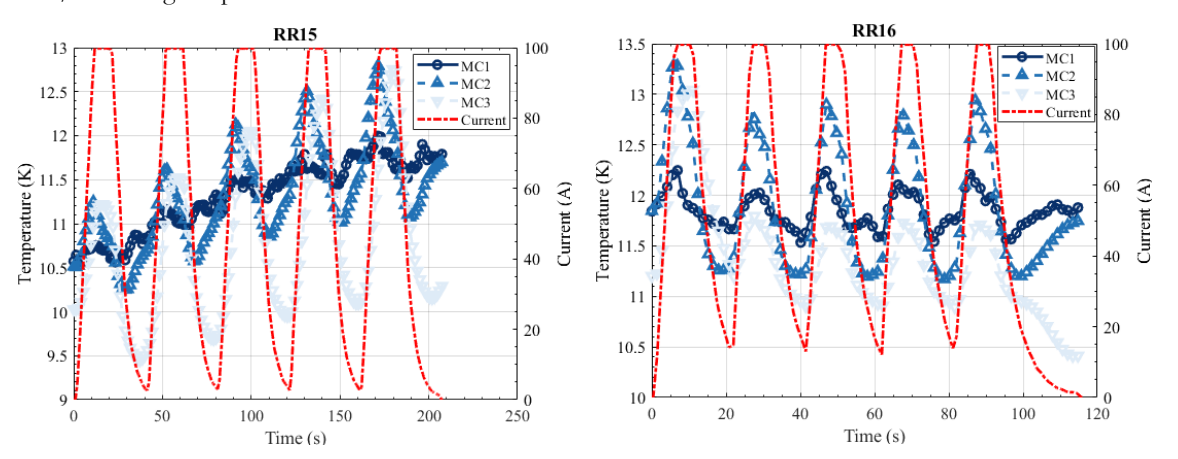


Figure 165. RR15 and RR16 tests. A trapezoidal magnetic field profile is applied with ramping rates of 10 and 20 A/s. Starting temperature is between 10-12 K.

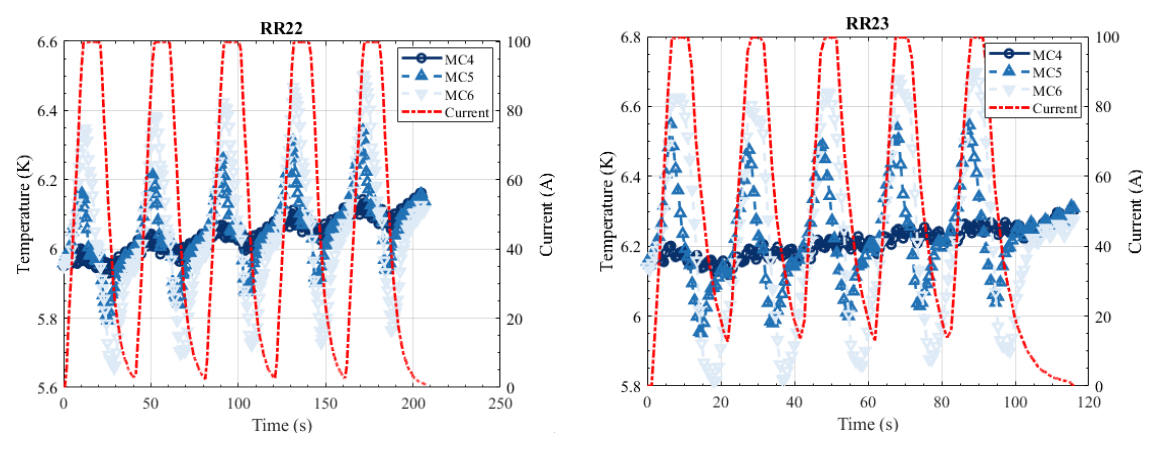


Figure 166. RR22 and RR23 tests. A trapezoidal magnetic field profile is applied with ramping rates of 10 and 20 A/s. Starting temperature is between 5-6 K.

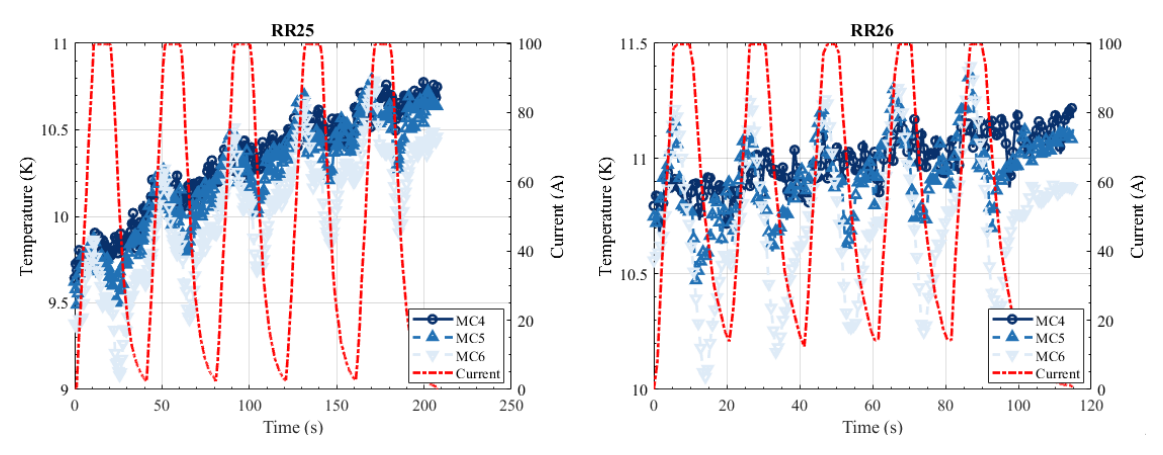


Figure 167. RR25 and RR26 tests. A trapezoidal magnetic field profile is applied with ramping rates of 10 and 20 A/s. Starting temperature is between 9-11 K.

Variable Temperature

Table 69. Variable temperature data test information table

Title	MCM	B (T)	T _{start} (K)	Mass Flow (g/min)	Annotations
VT11	ErAl ₂	1	6	6	Not done
VT12	ErAl_2	2	6	6	Not done
VT13	ErAl_2	3	6	6	Not done
VT14	ErAl_2	1	10	6	Not done
VT15	ErAl_2	2	10	6	Not done
VT16	ErAl_2	3	10	6	Not done
VT17	ErAl_2	1	15	6	Not done
VT18	ErAl_2	2	15	6	
VT19	ErAl_2	3	15	6	
VT110	ErAl_2	1	6	10	
VT111	ErAl_2	2	6	10	
VT112	ErAl_2	3	6	10	
VT113	ErAl_2	1	10	10	
VT114	ErAl_2	2	10	10	
VT115	$ErAl_2$	3	10	10	
VT116	ErAl_2	1	15	10	

VT117	ErAl ₂	2	15	10	
VT118	ErAl_2	3	15	10	
VT21	GGG	1	6	6	Not done
VT22	GGG	2	6	6	
VT23	GGG	3	6	6	
VT24	GGG	1	10	6	Not done
VT25	GGG	2	10	6	
VT26	GGG	3	10	6	
VT27	GGG	1	15	6	Not done
VT28	GGG	2	15	6	Not done
VT29	GGG	3	15	6	Not done
VT210	GGG	1	6	10	Equal to RR23
VT211	GGG	2	6	10	
VT212	GGG	3	6	10	
VT213	GGG	1	10	10	
VT214	GGG	2	10	10	
VT215	GGG	3	10	10	
VT216	GGG	1	15	10	Not done
VT217	GGG	2	15	10	Not done
VT218	GGG	3	15	10	Not done
VT220	GGG	4	10	10	
VT221	GGG	2	10	15	

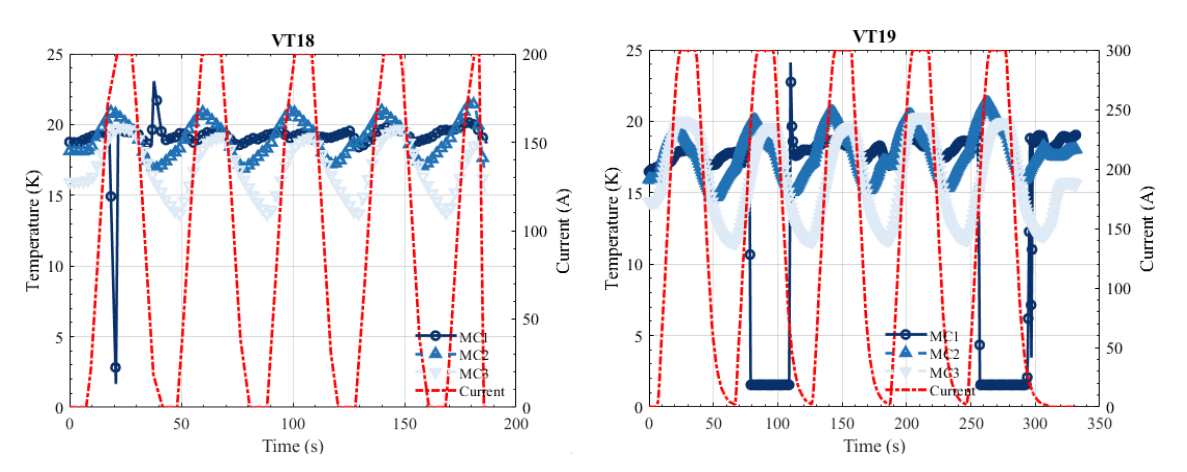


Figure 168. VT18 and VT19 tests. A trapezoidal magnetic field (2-3 T) profile is applied to the magnetocaloric material with a constant inlet temperature around 15-20 K, and a constant mass flow of 6 g/min.

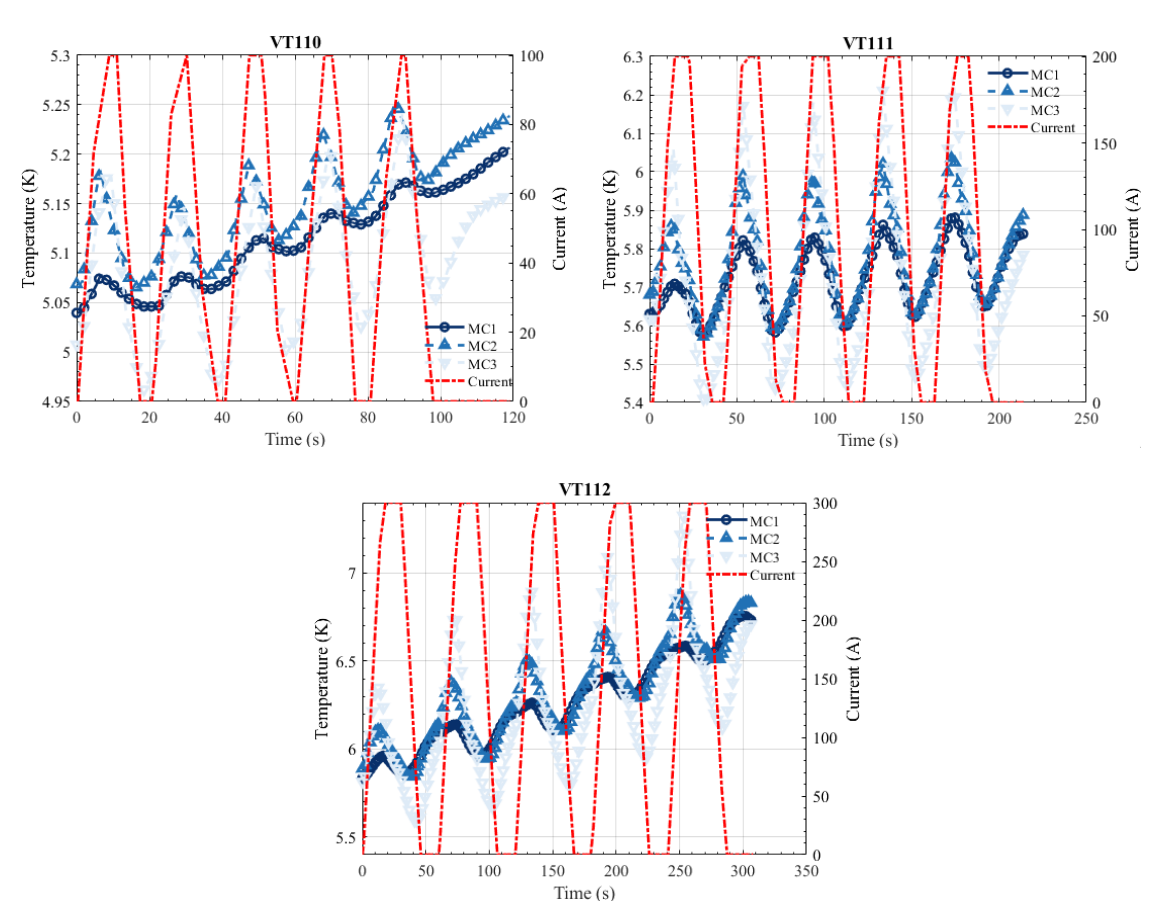
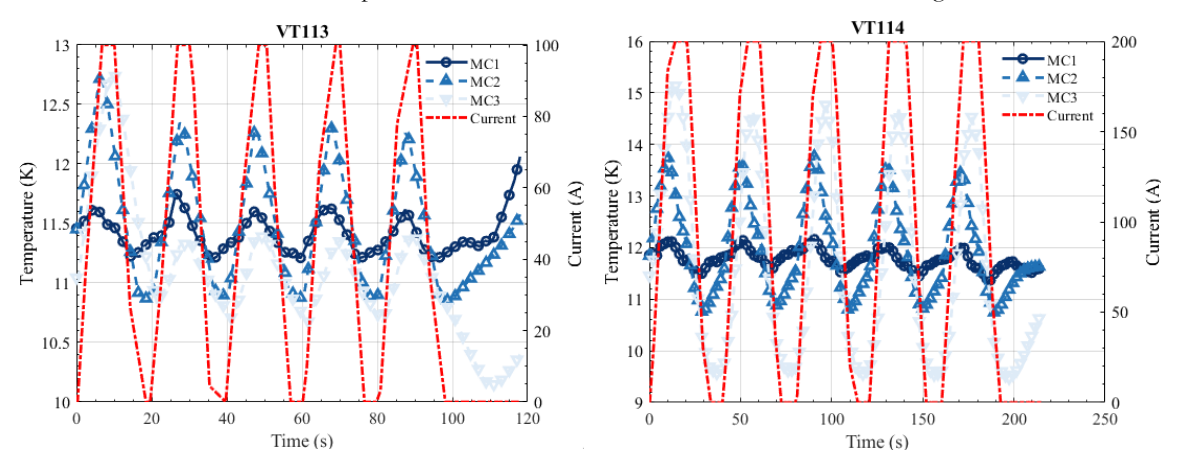


Figure 169. VT110-112 tests. A trapezoidal magnetic field (1-2-3 T) profile is applied to the magnetocaloric material with a constant inlet temperature around 5-7 K, and a constant mass flow of 10 g/min.



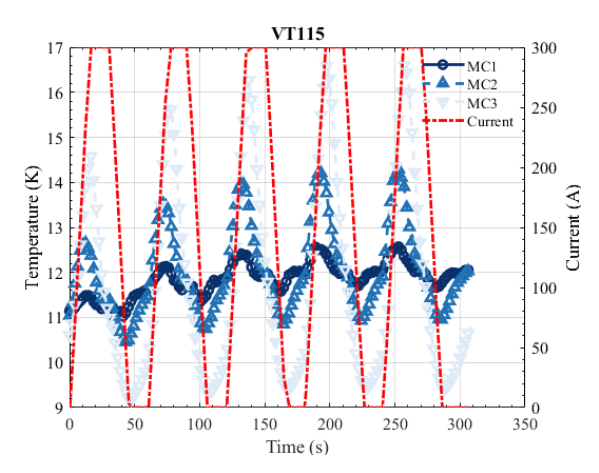


Figure 170. VT113-115 tests. A trapezoidal magnetic field (1-2-3 T) profile is applied to the magnetocaloric material with a constant inlet temperature around 10-12 K, and a constant mass flow of 10 g/min.

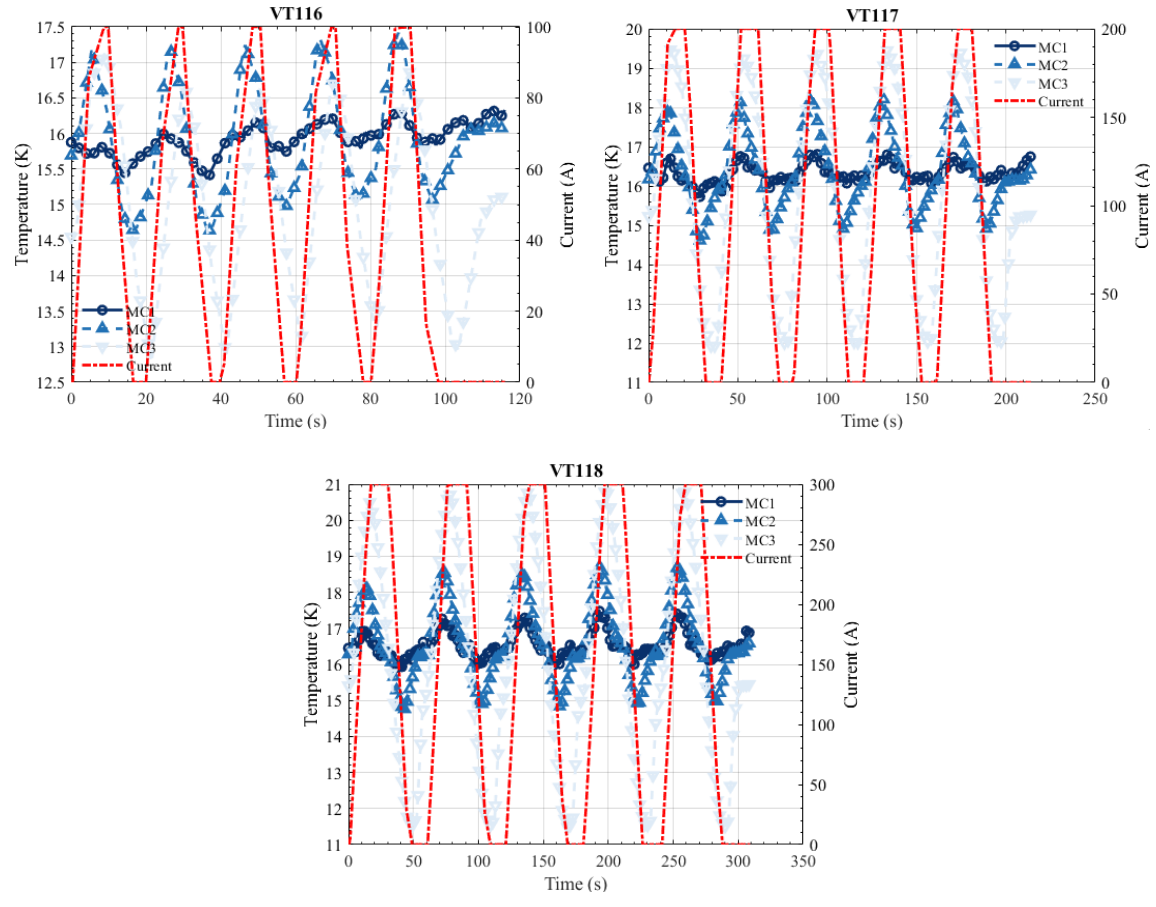


Figure 171. VT116-118 tests. A trapezoidal magnetic field (1-2-3 T) profile is applied to the magnetocaloric material with a constant inlet temperature around 15-17 K, and a constant mass flow of 10 g/min.

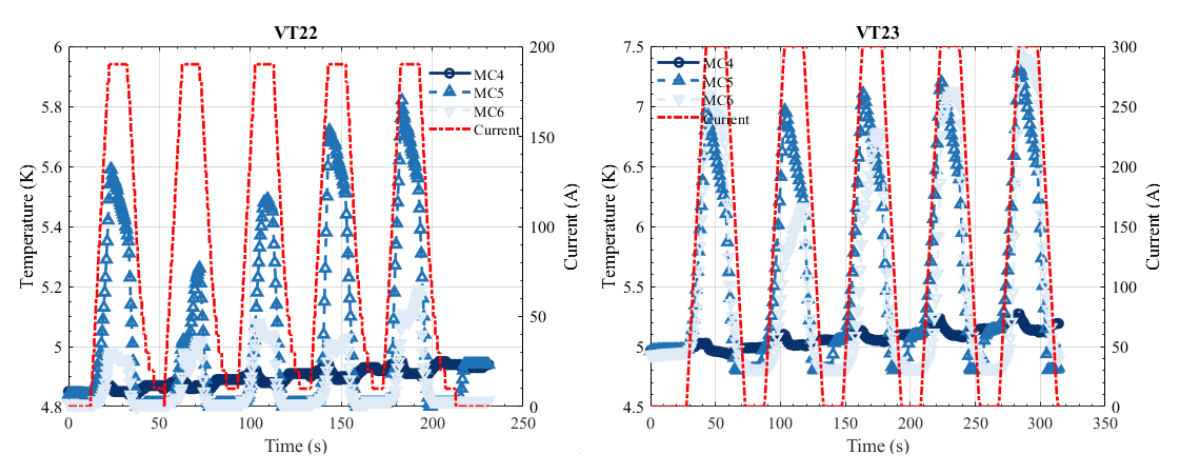


Figure 172. VT22-23 tests. A trapezoidal magnetic field (2-3 T) profile is applied to the magnetocaloric material with a constant inlet temperature around 5 K, and a constant mass flow of 6 g/min.

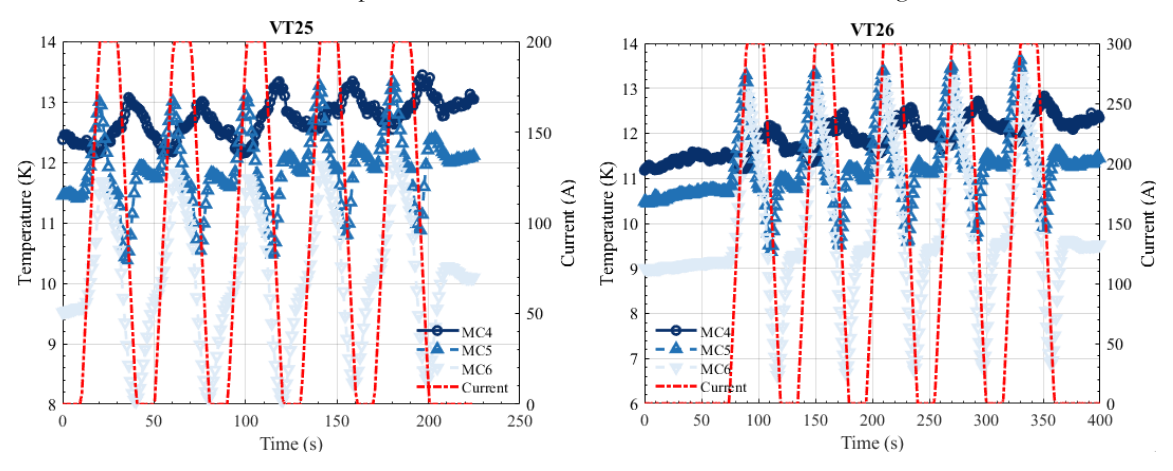


Figure 173. VT25-26 tests. A trapezoidal magnetic field (2-3 T) profile is applied to the magnetocaloric material with a constant inlet temperature around 10-12 K, and a constant mass flow of 6 g/min.

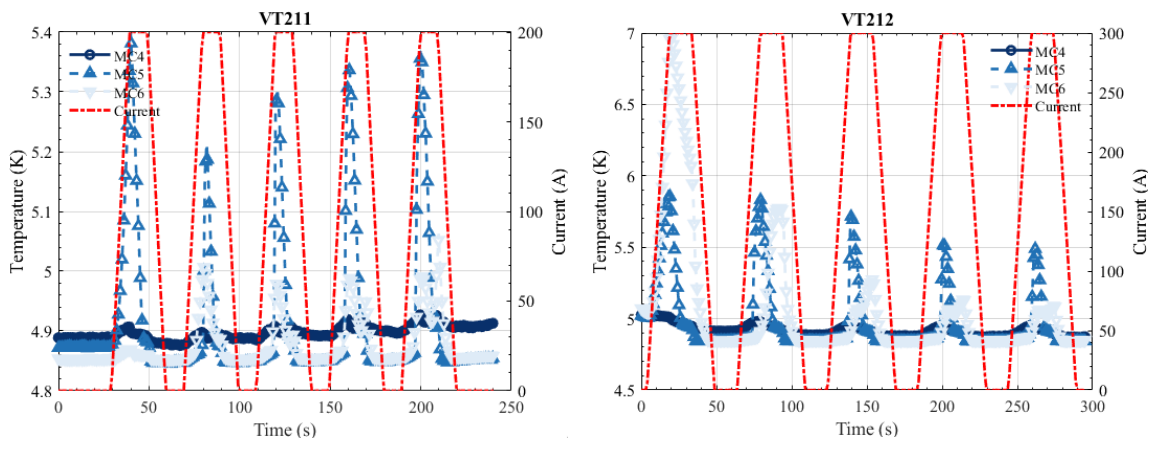


Figure 174. VT211-212 tests. A trapezoidal magnetic field (2-3 T) profile is applied to the magnetocaloric material with a constant inlet temperature around 5 K, and a constant mass flow of 10 g/min.

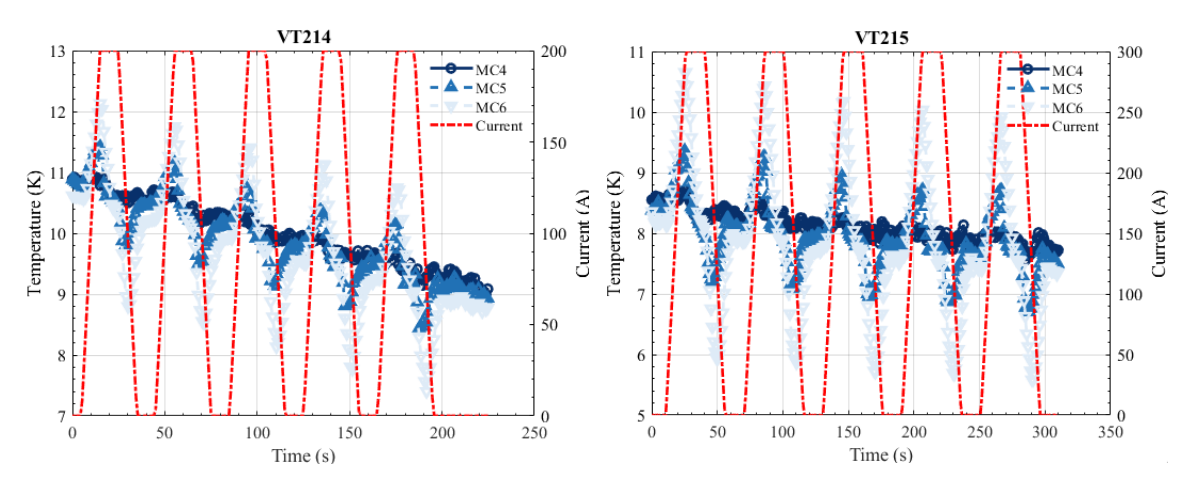


Figure 175. VT214-215 tests. A trapezoidal magnetic field (2-3 T) profile is applied to the magnetocaloric material with a constant inlet temperature around 10-12 K, and a constant mass flow of 10 g/min.

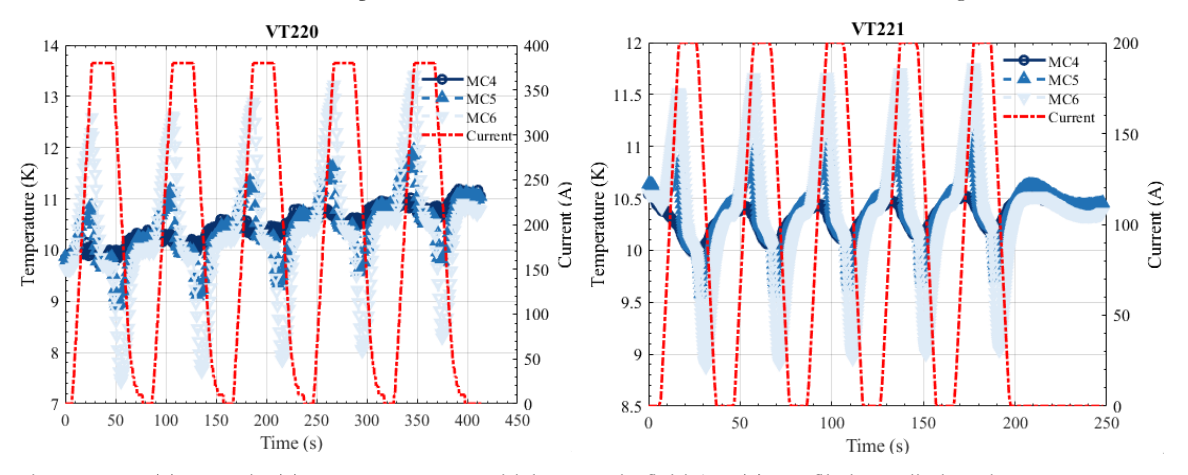


Figure 176. VT220 and VT221 tests. A trapezoidal magnetic field (4-2 T) profile is applied to the magnetocaloric material with a constant inlet temperature around 10-12 K, and a constant mass flow of 10-15 g/min.

LIST OF TABLES

TABLE 1. CRYOGENIC THERMAL DEMANDS OF SUPERCONDUCTING APPLICATIONS2
Table 2. Cryocooler cost comparison for different operational temperatures
8
Table 3. Thesis Objectives9
Table 4. Selection of compounds with giant MCE at low temperatures. Their
PROPERTIES ARE OBTAINED UNDER A MAGNETIC FIELD OF 0-5 T
Table 5. Magnetic refrigeration prototypes based on GGG operating between
4.2-20 K
Table 6. Summary of properties of selected magnetocaloric materials: $ErAl_2$
AND GGG26
Table 7. Operating conditions of the modelled AMR-Brayton cycle $\ldots 35$
Table 8. Regenerator characteristics
Table 9. Performance parameters of the AMR stage between 10-20 K39
Table 10. Objectives for the magnetocaloric test stand development49
Table 11. Summary of technical requirements for the magnetic source of the
MAGNETOCALORIC TEST STAND51
TABLE 12. PACKED BED POROSITY FOR DIFFERENT PACKING ARRANGEMENTS [112]52
Table 13. Main parameters of each test bed for the experimental test stand54
Table 14. Statistical summary of particle size distribution of ${\rm ErAL_2}$ and ${\rm GGG}$
SAMPLES
Table 15. Summary of mean geometric characteristics for $ErAl_2$ and GGG
SAMPLES
Table 16. Main parameters of each test bed for the experimental test stand60 $$
TABLE 17. SUMMARY OF TECHNICAL REQUIREMENTS FOR THE MAGNETIC SOURCE OF THE
MAGNETOCALORIC TEST STAND62
TABLE 18. MAIN ELECTROMAGNETIC PROPERTIES OF CRISA MAGNET63
TABLE 19 GEOMETRY OF CRISA MAGNET63
TABLE 20. SUPERCONDUCTOR CABLE INFORMATION
TABLE 21. OBJECTIVES FOR THE CRISA MAGNET TESTS68
TABLE 22. SUMMARY OF CRISA MAGNET TESTING RESULTS70
TABLE 23. SUMMARY OF MAIN COMPONENTS OF PUMPING CIRCUIT71
Table 24. BCs and Fluid 3 thermal targets
Table 25. Dimensionless groups for three-fluid parallel. Stream heat
EXCHANGERS WITH TWO THERMAL COMMUNICATIONS
TABLE 26 MAIN DESIGN PARAMETERS OF HEAT EXCHANGER COMPONENTS77
TABLE 27 SHELL AND MANDREL DIMENSIONS
Table 28 Preliminary heat exchanger dimensions
TABLE 29. PERCENTILE DISTRIBUTION VALUES FOR INLET TEMPERATURE AND MASS FLOW
RATE
TABLE 30. THERMAL DESIGN VALUES FOR THE 3-FLUID HX
TABLE 31. TYPE OF TEMPERATURE SENSOR USED IN HEAT EXCHANGER
CHARACTERIZATION86

TABLE	32.	Measured	BOUNDARY	CONDITIONS	DURING	LN2	HEAT	EXCHAN	I GER
				CONDITIONS					
				•••••					
				PACKED BED II					
				IGLE BLOW DA					
				FORMATION TA					
				INFORMATION					
				MATION TABLE					
				NFORMATION '					
				ATA TEST INFO					
				H TEST BED					
				INFORMATION					
				ANALYSIS INFO					
				AL ₂ SINGLE BL					
				ΓS SUMMARY TA					
				EST INFORMAT					
				A TEST INFORM					
				TEST INFORMA					
				INFORMATION					
				JLTS INFORMAT					
				LTS INFORMATI					
				ECONOMIC AN					
				COMMERCIAL (MPARISON FOR					
				MPARISON FOR MON PARAMETI					
				ET COMMON PA					
				ET COMMON PA					
				ERS FOR TI					
							•		
				IE CASCADE .					
				ING SYSTEM C					
				VEL OF ACCOM					
				L FIELD PARA					
				MAGNETIZATIO					
				ATIONS FOR T					
				XCHANGER					
				LATIONS FOR					
				XCHANGER					
				NGLE BLOW DA					
				BLOW DATA TH					
				IC BLOW DATA					
				MATION TABLE					
				NFORMATION '					
				ATA TEST INFO					

LIST OF FIGURES

FIGURE 1. CRYOGENIC APPLICATIONS AS FUNCTION OF TYPICAL COOLING TEMPERATURE
AND COOLING POWER [2]1
FIGURE 2. REFRIGERATION METHODS CLASSIFICATION [37], [38]
FIGURE 3. IMAGE AND SCHEMATIC OF A GM CRYOCOOLER5
FIGURE 4. PREFERABLE COOLING METHOD AS FUNCTION OF TEMPERATURE AND COOLING
POWER (LEFT), AND EXERGY EFFICIENCY AS FUNCTION OF REFRIGERATION
TEMPERATURE FOR SELECTED COOLING METHODS (RIGHT). RADEBAUGH ET AL [42] .5
FIGURE 5. VOLUMETRIC HEAT CAPACITY OF VARIOUS LOW TEMPERATURE REGENERATOR
MATERIALS (IN BLACK), COMPARED WITH THAT OF HELIUM AT VARIOUS PRESSURES-
0.5MPA, 1.0MPA6
FIGURE 6. CRYOGENIC SUPPLY SYSTEM (LEFT) AND CYCLOMED SUPERCONDUCTING
CYCLOTRON (RIGHT)7
FIGURE 7. ISOTHERMAL MAGNETIC ENTROPY CHANGE, IN BLUE, AND ADIABATIC
TEMPERATURE CHANGE DUE TO A VARYING MAGNETIC FIELD, IN PINK, OF A GENERIC
MAGNETOCALORIC MATERIAL. DEPICTED FROM [51]12
FIGURE 8. MAGNETIC ENTROPY DEPENDENCE ON TEMPERATURE OF A GENERIC
MAGNETOCALORIC MATERIAL. DEPICTED FROM [53]
FIGURE 9. T–S DIAGRAM OF AN MR CARNOT CYCLE
FIGURE 10. THIS FIGURE DEPICTS THE AMR CYCLE AS ADAPTED FROM [55]. THE DASHED
LINES REPRESENT THE TEMPERATURE PROFILES, HIGHLIGHTING CHANGES
OCCURRING DURING EACH STEP OF THE CYCLE. BETWEEN STEPS (B) AND (C), THE
LINEAR TEMPERATURE PROFILE IS RESTORED, A PROCESS SIMILARLY OBSERVED
BETWEEN STEPS (D) AND (A).
FIGURE 11. THE MAGNETIC FIELD PROFILES AND THE CORRESPONDING FLUID FLOW
PERIODS FOR THE AMR THERMODYNAMIC CYCLES
FIGURE 12. A SCHEMATIC DIAGRAM ILLUSTRATING VARIOUS REGENERATOR GEOMETRIES,
INCLUDING: (A) A PACKED SPHERE BED, (B) A PARALLEL PLATE MATRIX, (C) A
CIRCULAR MICRO-CHANNEL MATRIX, (D) A RECTANGULAR MICRO-CHANNEL MATRIX,
AND (E-1) AND (E-2) TOP AND SIDE VIEWS OF A PACKED SCREEN BED. IN ALL DIAGRAMS EXCEPT (E-2), THE FLOW DIRECTION IS PERPENDICULAR TO THE PLANE OF
THE DIAGRAM. THE DARK AREAS DENOTE SOLID REFRIGERANT, WHICH IS THE
MAGNETOCALORIC MATERIAL, WHILE THE REMAINING AREAS REPRESENT THE FLOW
CHANNELS. ADAPTED FROM [71]
FIGURE 13. TWO TYPES OF MAGNETIC FIELD SOURCES: SOLENOID, A TYPE OF
ELECTROMAGNET FROM NUMAZAWA ET AL [73] (LEFT) AND A HALBACH CYLINDER
MADE OF PERMANENT MAGNETS BY KIUTRA COMPANY [74] (RIGHT)
FIGURE 14. SCHEMATIC DIAGRAM OF THE 4-TO-15 K MAGNETIC REFRIGERATOR
DEVELOPED BY BARCLAY ET AL [79]
FIGURE 15. HELIUM LIQUEFIER MAGNETIC REFRIGERATOR FROM TOSHIBA DEVELOPMENT
CENTER, AND TOKYO UNIVERSITY GROUP [80] (LEFT), AND HYDROGEN LIQUEFIER
(20K) FROM JAPAN NATIONAL INSTITUTE FOR MATERIALS SCIENCE [83] (RIGHT)21
, , , , , , , , , , , , , , , , , , ,

FIGURE 16. REPRESENTATION OF FIGURE 8 IN WOOD AND POTTER [52]. SOLID LINES SHOW THE CALCULATED MAXIMUM ALLOWED MOLAR REFRIGERANT CAPACITY PER APPLIED FIELD AS A FUNCTION OF THE FIELD TO TEMPERATURE RATIO. SOLID DATA POINTS ARE CALCULATED FROM EXPERIMENTALLY DETERMINED ENTROPIES. , GD
WITH $Tc = TcOPT$; \blacktriangle , GD WITH $Tc = T0$; \times , GDCL ₃ WITH $Tc = TcOPT$; \blacklozenge , GDCL ₃ WITH $Tc = T0$; $+$, GGG WITH $Tc = T0$. Open data points are calculated from experimental refrigerator results using GGG as refrigerant. Δ , $Tc = \Delta T = \Delta $
$4.2K$ and $Ba=6.5T$; \Box , $Tc=1.8K$ or $2.1K$ and $Ba=2.5T$
TEMPERATURE AND MAGNETIC FIELD
Figure 19. Entropy of GGG as function of temperature and magnetic field; in
SOLID LINES THE RESULTS FROM THE THEORETICAL MODEL, AND THE MARKERS REPRESENT EXPERIMENTAL DATA FROM [66]–[69]
FIGURE 20. ENTROPY CHANGE (LEFT) AND SPECIFIC HEAT (RIGHT) OF GGG AS A FUNCTION OF TEMPERATURE AND MAGNETIC FIELD
FIGURE 21. ENTROPY OF ERAL ₂ DERIVED FROM THE NUMERICAL MODEL
FIGURE 23. THERMAL CONDUCTIVITY OF ErAL ₂ (LEFT) GGG (RIGHT) AS A FUNCTION OF TEMPERATURE
FIGURE 24. MAGNETIC FIELD AND PRESSURE FLOW PROFILE FOR THE APPLIED BRAYTON CYCLE
Figure 25. Establishment of the temperature profile between the magnetocaloric material at the hot and cold sides of the AMR
COLD END (X = 0), IN THE MIDDLE (X= $L/2$), AND IN THE HOT END (X= L)
FIGURE 29. COOLING POWER AND ECOP AS FUNCTION OF MAGNETIC FIELD
FIGURE 32. COOLING POWER AND ECOP FOR DIFFERENT UTILIZATION FACTORS
FIGURE 33. COMPARISON OF COOLING POWER AND ECOP BETWEEN COMPRESSIBLE AND INCOMPRESSIBLE MODELS
FIGURE 34. SCHEMATIC OF THE TEST BED BARCLAY ET AL TEST BED SHOWING THE THERMOCOUPLE POSITIONS (LEFT), AND RESPONSE OF LEAD-BALL TEST BED TO HOT-TO-COLD STEP FUNCTION (RIGHT). FIGURES ARE REPRODUCED FROM [111]
FIGURE 35. SCHEMATIC OF A PACKED BED PLACED IN THE BORE OF A SUPERCONDUCTING MAGNET
FIGURE 36. CONFIGURATION AND SCHEMATIC OF APPARATUS AND DATA ACQUISITION SYSTEM FOR THE AMBIENT TEST—PHASE 1 (LEFT) AND CRYOGENIC TEST—PHASE 2 (RIGHT). THE PORTION ENCLOSED BY DASHED LINES, IN THE RIGHT-SIDE FIGURE, IS INSIDE A CRYOSTAT

FIGURE 37. REGENERATOR POROSITY AT VARYING PACKING PRESSURE. DEPICTED FROM
[88]52
FIGURE 38. SCHEMATIC OF INSTRUMENTED GGG PACKED BED53
FIGURE 39. CONFLAT® (CF) UHV REDUCING TEE (LEFT) AND CONFLAT® (CF) CONICAL
REDUCER. 53
FIGURE 40 PRE-CRUSHED PARTICLES OF ERAL ₂ AND GGG (LEFT) AND LABORATORY SET
UP DURING MANUFACTURING (RIGHT), WHICH INCLUDES THE HYDRAULIC PRESS, A
SIEVE, A HIGH PRECISION WEIGHT SCALE AND A COMPUTER FOR DATA ACQUISITION.
54
FIGURE 41. SIEVE USED DURING MANUFACTURING PROCESS (LEFT) AND DETAILED VIEW
OF ONE SIEVE (RIGHT)55
FIGURE 42. APPLICATION OF PRESSURE TO THE PACKED BED TO ACHIEVE DESIRED
POROSITY55
FIGURE 43. MICROSCOPE IMAGE OF CRUSHED PARTICLES OF ERAL ₂ (LEFT) AND GGG
(RIGHT)56
FIGURE 44. PARTICLE SIZE DISTRIBUTION OF ERAL ₂ AND GGG SAMPLES IN THE X AND Y
DIRECTION OBTAINED THROUGH MICROSCOPE ANALYSIS
FIGURE 45. IMAGE OF AN ELLIPSOID (LEFT) AND A ERAL ₂ PARTICLE MEASURED UNDER THE
MICROSCOPE (RIGHT)57
FIGURE 46. SCHEMATIC OF AMBIENT TESTS SET UP (LEFT), AND ASSEMBLED TEST SET-UP
DURING PRESSURE DROP MEASUREMENTS INDICATING MAIN COMPONENTS OF THE
FLUID CIRCUIT58
FIGURE 47. PRESSURE DROP FOR GLASS PACKED BED, WITH DIFFERENT POROSITIES OF THE
REGENERATOR. SOLID LINES REPRESENT SIMULATION DATA, WHILE DISCONTINUOUS
LINES WITH OPEN DATA POINTS REPRESENT EXPERIMENTAL DATA
FIGURE 48. ERAL ₂ AND GGG PACKED BED HOUSING WITH INSTRUMENTATION PLACED
BEFORE INTRODUCING THE MAGNETOCALORIC MATERIAL
FIGURE 49. PACKED BED AFTER THE INTRODUCTION OF GGG PARTICLES60
FIGURE 50. COPPER GASKET WITH SOLDERED STAINLESS-STEEL MESH FOR PACKED BED
CONTAINMENT60
FIGURE 51. STAINLESS STEEL HOUSING WITH HEATER AND TEMPERATURE SENSOR IN
PLACE (LEFT), BRASS BLOCK INTRODUCED INSIDE STAINLESS STEEL HOUSING BEFORE
ENTERING THE HEATER RECIPIENT (CENTER AND RIGHT)61
FIGURE 52. FINAL ASSEMBLY OF THE TEST BED INCLUDING BRASS CONTAINER, HEATER
AND PACKED BED HOUSING
FIGURE 53. CRISA SUPERCONDUCTING MAGNET USED AS MAGNETIC SOURCE IN
MAGNETOCALORIC TEST STAND
FIGURE 54. POSITION OF THE PACKED BED HOUSING INSIDE THE CRISA MAGNET BORE. 64
FIGURE 55. MAP OF THE SIMULATED MAGNETIC FIELD IN THE YZ PLANE OF THE CRISA
MAGNET WITH BOTH PACKED BEDS PLACED INSIDE THE MAGNET BORE
FIGURE 56. SCHEMATIC OF THE ELECTRIC CIRCUIT OF THE SUPERCONDUCTING MAGNET
AND MAIN COMPONENTS VALUE
FIGURE 57. TARGET MAGNETIC CYCLE DURING TESTING
FIGURE 58. EXPECTED LOAD LINE OF THE CRISA MAGNET
FIGURE 59. QUENCH SIMULATION RESULTS USING A 0.5 OHM RESISTANCE SHOWING A)
CURRENT DECAY B) TEMPERATURE EVOLUTION C) VOLTAGE EVOLUTION. THE
SIMULATIONS WERE DONE WITH TWO CODES, ON THE LEFT THE RESULTS FROM THE
IN-HOUSE DEVELOPED CODE AND ON THE RIGHT THE RESULTS USING CIEMAT
DEVELOPED CODE
FIGURE 60. MEASURED CURRENT RAMP-UP DURING TRAINING OF CRISA
SUPERCONDUCTING MAGNET
FIGURE 61. MAGNETIC FIELD MEASUREMENT OF THE CRISA MAGNET DURING RAMPING.
69

FIGURE 62. RAMPING OF THE MAGNET TO 250 A AT DIFFERENT RAMPING RATES, FROM 5
TO 20 A/S (LEFT), TARGET CYCLE VERSUS REAL CYCLE DURING TESTING (RIGHT) 69
FIGURE 63. UPDATED SCHEMATIC OF THE EXPERIMENTAL TEST WITH PROTECTION
RESISTANCE PLACED IN SERIES
Figure 64. Protection resistance set-up. Equivalent resistance of 0.1 Ω 71
FIGURE 65. SCHEMATIC OF APPARATUS AND DATA ACQUISITION SYSTEM (LEFT), THE
PORTION ENCLOSED BY DASHED LINES IS INSIDE A CRYOSTAT. CRYOSTAT SIDE OF THE
TEST STAND (CENTER). SCHEMATIC OF THE HEAT EXCHANGER (RIGHT)72
FIGURE 66. DETAILED VIEW OF THE CROSS SECTION OF THE HEAT EXCHANGER, SHOWING
•
The heat transfer (Qout) from fluid 2 (Annular fluid) to fluid 1
(Evaporated fluid), and the heat transfer (Qin) from fluid 3 (Interior
FLUID) TO FLUID 2
FIGURE 67. BOUNDARY CONDITIONS OF THE 3-FLUID HEAT EXCHANGER73
FIGURE 68. SAMPLE COIL DENTED AT THE EXIT ANGLE. 78
FIGURE 69. ADDITION OF AN INNER WIRE SOLDERED TO THE INNER TUBE
FIGURE 70. FLOWCHART ILLUSTRATING THE ITERATIVE NUMERICAL SCHEME FOR
OPTIMIZING THE HEAT EXCHANGER LENGTH
FIGURE 71. INFLUENCE OF FLUID 1 INLET TEMPERATURE IN FLUID 2 OUTLET WITH FIXED
VALUES OF LENGTH (8 M.) AND A FLUID 1 MASS FLOW (0.1 G/S) (LEFT), AND
INFLUENCE OF MASS FLOW WITH FIXED VALUES OF LENGTH (8 M.) AND A FLUID 1
INLET TEMPERATURE (7 K) (RIGHT)80
FIGURE 72. PLACEMENT OF COPPER CYLINDER WITH HEATER FOR THE EVALUATION OF
THE HEAT TRANSFER COEFFICIENT. 81
FIGURE 73. EXPERIMENTAL VS THEORETICAL HEAT TRANSFER COEFFICIENT DURING THE
SUPERCONDUCTING MAGNET TESTS. SOLID LINES REPRESENT THEORETICAL DATA,
AND DISCONTINUOUS LINES REPRESENT EXPERIMENTAL DATA
Figure 74. Fluid 3 outlet temperature ($\xi=0$) as function of heat exchanger
LENGTH82
FIGURE 75. TEMPERATURE EVOLUTION ALONG THE HEAT EXCHANGER (LEFT), WITH A
DETAILED VIEW IN THE 0-0.6 NON-DIMENSIONAL LENGTH (RIGHT)
FIGURE 76. NTU BETWEEN FLUID 1 AND FLUID 2, DENOMINATED NTU ₁ IN THE TEXT,
EVOLUTION ALONG THE HEAT EXCHANGER (LEFT), AND PRESSURE EVOLUTION
ALONG THE HEAT EXCHANGER LENGTH (RIGHT)83
FIGURE 77. HEAT EXCHANGER AS RECEIVED WITH FIBER GLASS SEPARATORS (LEFT), AND
HEAT EXCHANGER ASSEMBLED IN CRYOSTAT (RIGHT)
FIGURE 78. GLUED COPPER HEAT EXCHANGER CONNECTOR (LEFT), AND STAINLESS-STEEL
CONNECTOR BEFORE BRAZING (RIGHT)
,
FIGURE 79. SCHEMATIC FOR THE VALIDATION OF THE HEAT EXCHANGER PERFORMANCE
(LEFT), AND FINAL TESTING ASSEMBLY FOR LIQUID NITROGEN CHARACTERIZATION
OF THE HEAT EXCHANGER (RIGHT)
FIGURE 80. UPPER (LEFT) AND LOWER (RIGHT) SIDE OF THE HEAT EXCHANGER85
FIGURE 81. TEMPERATURE SENSOR POSITION AND TYPE ALONG THE HEAT EXCHANGER. 86
FIGURE 82. POSITION OF TEMPERATURE SENSOR 4, AT THE HEAT EXCHANGER INLET
(LEFT), AND INSTRUMENTATION SENSOR SEALED WITH STYCAST (RIGHT)86
Figure 83. Fluid 2 (Left) and Fluid 3 (Right) outlet temperature ($\xi=0$) as
FUNCTION OF FLUID 2/3 MASS FLOW DURING LIQUID NITROGEN TESTING
FIGURE 84. FINAL ASSEMBLY OF THE MCE TEST STAND. THE SUPERCONDUCTING MAGNET
IS PLACED AT THE BASE OF THE CRYOSTAT INSERT, WITH THE DRY RECIPIENT IN ITS
BORE
FIGURE 85. FLUID 2 (LEFT) AND FLUID 3 (RIGHT) AT THE ENTRY OF THE
Magnetocaloric regenerator ($\xi=0$) as function of fluid 2/3 mass flow
DURING LIQUID HELIUM TESTING

FIGURE 86. SIMULATED EXAMPLE OF THE TEMPERATURE EVOLUTION DURING A SINGLE
BLOW TEST92
FIGURE 87. SIMULATED EXAMPLE OF TEMPERATURE EVOLUTION DURING A PERIODIC
BLOW TEST93
FIGURE 88. SIMULATED EXAMPLE OF A NO-LOAD TEST APPLIED TO THE ERAL ₂
MAGNETOCALORIC REGENERATOR. A TRIANGULAR MAGNETIC FIELD WAVEFORM IS
APPLIED, WHILE MEASURING THE TEMPERATURE EVOLUTION ALONG THE PACKED
BED94
FIGURE 89. SIMULATED EXAMPLE OF A RAMPING RATE TEST. A SERIES OF 5 TRAPEZOIDAL
MAGNETIC FIELD WAVEFORMS IS APPLIED TO THE REGENERATOR WHILE
MAINTAINING A CONSTANT INLET TEMPERATURE OF 6.2 K AND A CONSTANT MASS
FLOW95
FIGURE 90. SIMULATED EXAMPLE OF A RAMPING RATE TEST. A SERIES OF 5 TRAPEZOIDAL
MAGNETIC FIELD WAVEFORMS IS APPLIED TO THE REGENERATOR WHILE
MAINTAINING A CONSTANT INLET TEMPERATURE OF 6.2 K AND A CONSTANT MASS
FLOW95
FIGURE 91. ILLUSTRATION OF TESTING DAY SHOWING THE LIQUID HELIUM DEWAR
FEEDING TO THE LABORATORY CRYOSTAT96
FIGURE 92. UPPER VIEW OF THE CRYOSTAT SHOWING THE CRYOGENIC TRANSFER LINES
AND THE MANUAL VALVES USED FOR CHANGING THE FLOW DIRECTION97
FIGURE 93. SB00-SB01 TESTS MEASURED DATA: SINGLE BLOW TEST OF GLASS PACKED BED
WITH MASS FLOW OF 13.5 G/MIN99
Figure 94. SB11 test measured data: single blow test of ErAl ₂ with $m=10$
G/MIN AND B = 0 T. 100
Figure 95. SB12 test measured data: single blow test of ErAl ₂ with $m=10$
G/MIN AND B = 1 T
FIGURE 96. SB16 TEST MEASURED DATA: SINGLE BLOW TEST OF ERAL ₂ WITH $m = 6$ G/MIN
AND $B = 0 T$
FIGURE 97. SB18 TEST MEASURED DATA: SINGLE BLOW TEST OF ERAL ₂ WITH $m = 6$ G/MIN
AND $B = 2 T$
Figure 98. SB25 test measured data: single blow test of GGG with $m=6\mathrm{G/min}$
AND $B = 0$ T
Figure 99. SB25 test measured data: single blow test of GGG with $m = 6$ g/min
AND $B = 2 T$
Figure 100. PB11 test measured data: periodic blow test of $ErAl_2$ with $m = 10$
G/MIN AND B = 0 T
Figure 101. PB13 test measured data: Periodic blow test of ErAl ₂ with $m = 10$
G/MIN AND B = 2 T
,
Figure 102. PB24 test measured data: periodic blow test of GGG with $m = 6$
G/MIN AND B = 0 T. 104
Figure 103. PB26 test measured data: periodic blow test of GGG with $m=6$
G/MIN AND B = 0 T 104
FIGURE 104. NL12 AND NL23 TESTS MEASURED DATA. A TRIANGULAR MAGNETIC FIELD
PROFILE IS APPLIED TO THE PACKED BEDS. 105
FIGURE 105. NL14 AND NL24 TESTS MEASURED DATA. A TRAPEZOIDAL MAGNETIC FIELD
PROFILE IS APPLIED TO THE PACKED BEDS
FIGURE 106. RR15 TEST MEASURED DATA (ERAL ₂): A TRAPEZOIDAL MAGNETIC FIELD
PROFILE IS APPLIED WITH RAMPING RATES OF 10 A/s. STARTING TEMPERATURE IS
BETWEEN 10-12 K
FIGURE 107. RR16 TEST MEASURED DATA (ERAL ₂): A TRAPEZOIDAL MAGNETIC FIELD
PROFILE IS APPLIED WITH RAMPING RATES OF 20 A/s. STARTING TEMPERATURE IS
BETWEEN 10-12 K

FIGURE 108. RR22 TEST MEASURED DATA (GGG):. A TRAPEZOIDAL MAGNETIC FIELD PROFILE IS APPLIED WITH RAMPING RATES OF 10 A/s. STARTING TEMPERATURE IS BETWEEN 5-6 K
FIGURE 109. RR23 TEST MEASURED DATA (GGG): A TRAPEZOIDAL MAGNETIC FIELD PROFILE IS APPLIED WITH RAMPING RATES OF 20 AA/s. STARTING TEMPERATURE IS BETWEEN 5-6 K
FIGURE 110. VT111 TEST MEASURED DATA (ERAL ₂): A TRAPEZOIDAL MAGNETIC FIELD PROFILE OF 2 T IS APPLIED TO THE MAGNETOCALORIC MATERIAL WITH A CONSTANT INLET TEMPERATURE AROUND 5-7 K, AND A CONSTANT MASS FLOW OF 10 G/MIN. 109
FIGURE 111. VT115 TEST MEASURED DATA (ERAL ₂): A TRAPEZOIDAL MAGNETIC FIELD PROFILE OF 3 T IS APPLIED TO THE MAGNETOCALORIC MATERIAL WITH A CONSTANT INLET TEMPERATURE AROUND 10-12 K, AND A CONSTANT MASS FLOW OF 10 G/MIN
FIGURE 112. VT118 TEST MEASURED DATA (ERAL ₂): A TRAPEZOIDAL MAGNETIC FIELD PROFILE OF 3 T IS APPLIED TO THE MAGNETOCALORIC MATERIAL WITH A CONSTANT INLET TEMPERATURE AROUND 16-17 K, AND A CONSTANT MASS FLOW OF 10 G/MIN
FIGURE 113. VT23 TEST MEASURED DATA (GGG): A TRAPEZOIDAL MAGNETIC FIELD PROFILE OF 3 T IS APPLIED TO THE MAGNETOCALORIC MATERIAL WITH A CONSTANT INLET TEMPERATURE AROUND 5 K, AND A CONSTANT MASS FLOW OF 6 G/MIN111
FIGURE 114. VT212 TEST MEASURED DATA (GGG): A TRAPEZOIDAL MAGNETIC FIELD PROFILE OF 3 T IS APPLIED TO THE MAGNETOCALORIC MATERIAL WITH A CONSTANT INLET TEMPERATURE AROUND 5 K, AND A CONSTANT MASS FLOW OF 10 G/MIN111
FIGURE 115. VT215 TEST MEASURED DATA (GGG): A TRAPEZOIDAL MAGNETIC FIELD PROFILE OF 3 T IS APPLIED TO THE MAGNETOCALORIC MATERIAL WITH A CONSTANT INLET TEMPERATURE AROUND 9 K, AND A CONSTANT MASS FLOW OF 10 G/MIN112
FIGURE 116. VT220 TEST MEASURED DATA (GGG): A TRAPEZOIDAL MAGNETIC FIELD PROFILE OF 4 T IS APPLIED TO THE MAGNETOCALORIC MATERIAL WITH A CONSTANT INLET TEMPERATURE AROUND 10 K, AND A CONSTANT MASS FLOW OF 10 G/MIN112
FIGURE 117. MAXIMUM SLOPE OF EXIT TEMPERATURE FOR DIFFERENT NTU VALUES ASSUMING NO INFLUENCE FROM THE WALL AND NO EXTERNAL LEAKS (LEFT) AND INCLUDING WALL AND EXTERNAL LEAKS EFFECTS (RIGHT)
FIGURE 118. EXIT TEMPERATURE ATTENUATION FOR DIFFERENT NTU VALUES ASSUMING NO INFLUENCE FROM THE WALL AND NO EXTERNAL LOSSES (LEFT) EXIT TEMPERATURE ATTENUATION FOR DIFFERENT NTU VALUES ACCOUNTING FOR THE
INFLUENCE FROM THE WALL AND EXTERNAL LOSSES (RIGHT)
FIGURE 120. COMPARISON OF EXPERIMENTAL AND THEORETICAL VALUES FROM SINGLE BLOW TESTS CONDUCTED AT AMBIENT TEMPERATURE USING A GLASS PACKED BED
FIGURE 121. COMPARISON OF EXPERIMENTAL (DISCONTINUOUS LINES WITH DATA POINTS AND THEORETICAL (CONTINUOUS LINES) VALUES FROM ERAL ₂ SINGLE-BLOW TESTS
FIGURE 122. COMPARISON OF EXPERIMENTAL (DISCONTINUOUS LINES WITH DATA POINTS AND THEORETICAL (CONTINUOUS LINES) FROM GGG SINGLE-BLOW TESTS
120

FIGURE 124. COMPARISON OF EXPERIMENTAL (DISCONTINUOUS LINES WITH DATA POINTS AND THEORETICAL (CONTINUOUS LINES) VALUES FROM GGG PERIODIC-BLOW TESTS
FIGURE 125. SIMULATION OF MAGNETIC CYCLE TESTS, INDICATING THE MAGNETIC FIELD
EVOLUTION (DISCONTINUOS RED), AND THE TEMPERATURE EVOLUTION IN 3
POSITIONS OF THE PACKED BED: MC1, MC2, AND MC3. THE OUTLET (MC3) TOTAL
TEMPERATURE DIFFERENCE IS INDICATED IN THE FIGURE
FIGURE 126. SENSITIVITY OF THE MAXIMUM OUTLET TEMPERATURE DIFFERENCE AS
FUNCTION OF NTU FOR DIFFERENT EXTERNAL HEAT TRANSFER COEFFICIENTS 130
FIGURE 127. COMPARISON OF EXPERIMENTAL (DISCONTINUOUS LINES WITH DATA POINTS
AND THEORETICAL (CONTINUOUS LINES) VALUES FROM ERAL ₂ MAGNETIC TESTS 132
FIGURE 128. 3D VISUALIZATION OF TEMPERATURE EVOLUTION DURING THE LAST CYCLE
OF VT114.
FIGURE 129. CONTOUR PLOT OF TEMPERATURE EVOLUTION DURING THE LAST CYCLE OF
VT114
FIGURE 130. 3D VISUALIZATION OF TEMPERATURE EVOLUTION DURING THE LAST CYCLE
OF VT116
FIGURE 131. COMPARISON OF EXPERIMENTAL (DISCONTINUOUS LINES WITH DATA POINTS
AND THEORETICAL (CONTINUOUS LINES) VALUES FROM GGG MAGNETIC TESTS 130
FIGURE 132. THERMAL RESPONSE OF THE PACKED BED IN A SIMULATED MAGNETIC SINGLE
BLOW TEST
FIGURE 133. MAXIMUM SLOPE OF THE EXIT TEMPERATURE AS A FUNCTION OF NTU FOI
VARIOUS EXTERNAL HEAT TRANSFER VALUES (0 W/m·K to 50 W/m·K), SHOWN FOI
MAGNETIC RAMP RATES OF 0.1 T/s (LEFT) AND 0.5 T/s (RIGHT)
FIGURE 134. THERMAL RESPONSE OF THE PACKED BED IN A SIMULATED MAGNETIC
PERIODIC BLOW TEST
FIGURE 135. PHASE DIFFERENCE OF THE OUTLET FLUID TEMPERATURE RELATIVE TO THE
MAGNETIC FIELD AS A FUNCTION OF NTU FOR VARYING EXTERNAL HEAT TRANSFEI
COEFFICIENTS (0 W/m·K TO 50 W/m·K) (LEFT). SENSITIVITY OF THE MAGNETIC
PERIODIC BLOW METHOD AS A FUNCTION OF NTU FOR DIFFERENT EXTERNAL HEAT
TRANSFER COEFFICIENTS (RIGHT)
FIGURE 136. CONTOUR PLOT OF TEMPERATURE EVOLUTION DURING A SIMULATED
MAGNETIC PERIODIC BLOW TEST
FIGURE 137. PEAK TEMPERATURE POSITION AS FUNCTION OF NTU FOR DIFFERENT
MAGNETIC FIELD FREQUENCIES (LEFT), AND PEAK TEMPERATURE POSITION AS
FUNCTION OF FREQUENCY (RIGHT)
FIGURE 138. HEAT LOAD CAPACITY CURVE OF THE 2 ND STAGE OF SUMITOMO RDE-418
CRYOCOOLER
FIGURE 139. LCOEX (\$/kW·H) AS FUNCTION OF COLD SOURCE TEMPERATURE FOR
COMMERCIAL GM CRYOCOOLERS
FIGURE 140. REPRESENTATION OF THE MAGNETIC FIELD DISTRIBUTION GENERATED BY
NESTED CYLINDRICAL HALBACH DIPOLES, WITH THE MUTUAL ANGLE BETWEEN THE
INNER (BLUE ARROWS) AND OUTER (RED ARROWS) DIPOLES DETERMINING THE
RESULTING FIELD AND ORIENTATION
FIGURE 141. VARIATION OF IRREVERSIBILITY FIELD WITH TEMPERATURE FOR DIFFERENT
SUPERCONDUCTORS INCLUDING HTS, MGB ₂ , METALLIC COMPOUNDS, AND ALLOYS
THE COATED CONDUCTOR TECHNOLOGY INCLUDING APC METHODOLOGY HAS
OPENED NEW FRONTIERS OF SUPERCONDUCTIVITY APPLICATIONS IN THE TEMPERATURE RANGE OF 5-77 K. REPRODUCED FROM MATSUMOTO AND MELE [138]
1EMPERATURE RANGE OF 5-77 K. REPRODUCED FROM MATSUMOTO AND MELE [138]
FIGURE 142. CROSS SECTION VIEW OF A SUPERCONDUCTING SOLENOID
FIGURE 142. CROSS SECTION VIEW OF A SUPERCONDUCTING SOLENOID
FUNCTION OF FIELD AND TEMPERATURE
1 0 : 1 0 : 1 0 : 1 0 : 1 : 1 1 1 1 1 1

FIGURE 144. SCHEMATIC OF THE PROPOSED 2-STAGE CASCADE SYSTEM149
FIGURE 145. COOLING POWER AND EXERGY EFFICIENCY AS FUNCTION OF COLD SOURCE
TEMPERATURES IN THE ECONOMIC ANALYSIS
FIGURE 146. LCOEX (\$/kW·H) AS FUNCTION OF COLD SOURCE TEMPERATURE FOR
COMMERCIAL GM CRYOCOOLERS
FIGURE 147. GENERIC PARAMETERS OF A COMBINED GIFFORD-McMahon and Active
Magnetic Regeneration cycle in the time domain (left) and the
FREQUENCY DOMAIN (RIGHT)
FIGURE 148. VOLUMETRIC HEAT CAPACITY OF VARIOUS LOW TEMPERATURE
REGENERATOR MATERIALS (IN BLACK), ERAL ₂ (IN PURPLE), AND GGG (IN GREEN)
COMPARED WITH THAT OF HELIUM AT VARIOUS PRESSURES-0.5MPA, 1.0MPA155
FIGURE 149. TEMPERATURE DEPENDENCE OF THE DEBYE TEMPERATURE IN LAAL ₂ ,
LuAl ₂ , LaNi _{2:2} and LuNi ₂
FIGURE 150. ENTROPY OF ERAL ₂ DERIVED FROM THE NUMERICAL MODEL
FIGURE 151. SPECIFIC HEAT OF ERAL ₂ AS A FUNCTION OF TEMPERATURE AND MAGNETIC
FIELD, SOLID LINES REPRESENT MODEL RESULTS, WHILE MARKERS REPRESENT DATA
OBTAINED FROM THE LITERATURE [104] (LEFT). ENTROPY CHANGE AS FUNCTION OF
TEMPERATURE AND MAGNETIC FIELD (RIGHT)
FIGURE 152. SB00-SB01 TESTS: SINGLE BLOW TEST OF GLASS PACKED BED WITH MASS
FLOW OF 13.5 G/MIN
FIGURE 153. SB11-SB14 TESTS: SINGLE BLOW TEST OF ERAL ₂ WITH MASS FLOW OF 10
G/MIN FOR MAGNETIC FIELDS OF 0-3 T
FIGURE 154. SB05-SB08 TESTS: SINGLE BLOW TEST OF ERAL ₂ WITH MASS FLOW OF 6 G/MIN FOR MAGNETIC FIELDS OF 0-3 T
FIGURE 155. SB09-SB11 TESTS: SINGLE BLOW TEST OF GGG WITH MASS FLOW OF 10
G/MIN FOR MAGNETIC FIELDS OF 0-2
FIGURE 156. SB13-SB15 TESTS: SINGLE BLOW TEST OF GGG WITH MASS FLOW OF 6 G/MIN
FOR MAGNETIC FIELDS OF 0-2 T
FIGURE 157. PB11 AND PB13 TESTS: PERIODIC BLOW TESTS OF ERAL ₂ WITH MASS FLOW OF
10 G/MIN WITH MAGNETIC FIELDS OF 0-2 T
FIGURE 158. PB14 AND PB16 TESTS: PERIODIC BLOW TESTS OF ERAL ₂ WITH MASS FLOW OF
6 G/MIN WITH MAGNETIC FIELDS OF 0-2 T
FIGURE 159. PB21-23 TESTS: PERIODIC BLOW TESTS OF GGG WITH MASS FLOW OF 10
G/MIN WITH MAGNETIC FIELDS OF 0-1-2 T
FIGURE 160. PB21-23 TESTS: PERIODIC BLOW TESTS OF GGG WITH MASS FLOW OF 6 G/MIN
WITH MAGNETIC FIELDS OF 0-1-2 T
FIGURE 161. NL14 AND NL24 TESTS. A TRAPEZOIDAL MAGNETIC FIELD PROFILE IS
APPLIED TO THE PACKED BEDS
FIGURE 162. NL15 AND NL25 TESTS. A TRAPEZOIDAL MAGNETIC FIELD PROFILE, WITH
STOPS EVERY 100A, IS APPLIED TO THE PACKED BEDS185
FIGURE 163. NL11-13 AND NL21-23 TESTS. A TRIANGULAR MAGNETIC FIELD PROFILE IS
APPLIED TO THE PACKED BEDS. THE STARTING TEMPERATURES VARIES FROM 4 TO 15
K186
FIGURE 164. RR12 AND RR12 TESTS. A TRAPEZOIDAL MAGNETIC FIELD PROFILE IS
APPLIED WITH RAMPING RATES OF 10 AND 20 A/S. STARTING TEMPERATURE IS
BETWEEN 5-6K
FIGURE 165. RR15 AND RR16 TESTS. A TRAPEZOIDAL MAGNETIC FIELD PROFILE IS
APPLIED WITH RAMPING RATES OF 10 AND 20 A/S. STARTING TEMPERATURE IS
BETWEEN 10-12 K
FIGURE 166. RR22 AND RR23 TESTS. A TRAPEZOIDAL MAGNETIC FIELD PROFILE IS
APPLIED WITH RAMPING RATES OF 10 AND 20 A/S. STARTING TEMPERATURE IS
BETWEEN 5-6 K

FIGURE 167. RR25 AND RR26 TESTS. A TRAPEZOIDAL MAGNETIC FIELD PROFILE IS
APPLIED WITH RAMPING RATES OF 10 AND 20 A/S. STARTING TEMPERATURE IS
BETWEEN 9-11 K
Figure 168. VT18 and VT19 tests. A trapezoidal magnetic field $(2-3\ T)$ profile is
APPLIED TO THE MAGNETOCALORIC MATERIAL WITH A CONSTANT INLET
TEMPERATURE AROUND 15-20 K, AND A CONSTANT MASS FLOW OF 6 G/MIN 189
FIGURE 169. VT110-112 TESTS. A TRAPEZOIDAL MAGNETIC FIELD (1-2-3 T) PROFILE IS
APPLIED TO THE MAGNETOCALORIC MATERIAL WITH A CONSTANT INLET
TEMPERATURE AROUND 5-7 K, AND A CONSTANT MASS FLOW OF 10 G/MIN 190
FIGURE 170. VT113-115 TESTS. A TRAPEZOIDAL MAGNETIC FIELD (1-2-3 T) PROFILE IS
APPLIED TO THE MAGNETOCALORIC MATERIAL WITH A CONSTANT INLET
TEMPERATURE AROUND 10-12 K, AND A CONSTANT MASS FLOW OF 10 G/min. 191
FIGURE 171. VT116-118 TESTS. A TRAPEZOIDAL MAGNETIC FIELD (1-2-3 T) PROFILE IS
APPLIED TO THE MAGNETOCALORIC MATERIAL WITH A CONSTANT INLET
TEMPERATURE AROUND 15-17 K, AND A CONSTANT MASS FLOW OF 10 G/min. 191
FIGURE 172. VT22-23 TESTS. A TRAPEZOIDAL MAGNETIC FIELD (2-3 T) PROFILE IS APPLIED
TO THE MAGNETOCALORIC MATERIAL WITH A CONSTANT INLET TEMPERATURE
AROUND 5 K, AND A CONSTANT MASS FLOW OF 6 G/MIN
FIGURE 173. VT25-26 TESTS. A TRAPEZOIDAL MAGNETIC FIELD (2-3 T) PROFILE IS APPLIED
TO THE MAGNETOCALORIC MATERIAL WITH A CONSTANT INLET TEMPERATURE
AROUND 10-12 K, AND A CONSTANT MASS FLOW OF 6 G/MIN
FIGURE 174. VT211-212 TESTS. A TRAPEZOIDAL MAGNETIC FIELD (2-3 T) PROFILE IS
APPLIED TO THE MAGNETOCALORIC MATERIAL WITH A CONSTANT INLET
TEMPERATURE AROUND 5 K, AND A CONSTANT MASS FLOW OF 10 G/MIN 192
FIGURE 175. VT214-215 TESTS. A TRAPEZOIDAL MAGNETIC FIELD (2-3 T) PROFILE IS
APPLIED TO THE MAGNETOCALORIC MATERIAL WITH A CONSTANT INLET
TEMPERATURE AROUND 10-12 K, AND A CONSTANT MASS FLOW OF 10 G/MIN 193
Figure 176. $VT220$ and $VT221$ tests. A trapezoidal magnetic field (4-2 T) profile
IS APPLIED TO THE MAGNETOCALORIC MATERIAL WITH A CONSTANT INLET
TEMPERATURE AROUND $10-12~\mathrm{K}$, and a constant mass flow of $10-15~\mathrm{g/minF}$. $193~\mathrm{ms}$